Symbiotic diversity and mineral-associated microbial ecology in marine microbiomes

Thesis by

Kyle Shuhert Metcalfe

In Partial Fulfillment of the Requirements for

the degree of

Doctor of Philosophy

CALIFORNIA INSTITUTE OF TECHNOLOGY

Pasadena, California

2020

(Defended August 3, 2020)

Kyle Shuhert Metcalfe

ORCID: 0000-0002-2963-765X

ACKNOWLEDGEMENTS

This thesis would not have been possible if not for the opportunities afforded by my thesis advisor Victoria Orphan. Thank you, Victoria, for your inspiring drive to push the boundaries of microbial ecology, and for your boundless energy to take on any project no matter how challenging. It has been a privilege to pursue my doctorate in the Orphan Lab and under its aegis dive three thousand feet beneath the western Pacific on *Alvin* and drill nineteen thousand feet beneath the eastern Pacific on *Chikyu*. I cannot be thankful enough for your tireless work that made this thesis possible.

I would like to thank Woody Fischer for his ability to bring fresh, exciting ideas into any research question and for always pushing me to become a better scientist. The weekly meetings of the Geobiology Reading Group were a highlight of my academic career at Caltech and profoundly expanded my perspective on the breadth of disciplines within Geobiology. I also am thankful for Woody's advice and guidance in the project that became Chapter 4 of this thesis and for his thoughtful comments on the other chapters. I'd like to thank both Woody and John Grotzinger for leading expeditions to the Turks and Caicos Islands and for assembling such an incredible team to explore the microbiology and sedimentology of Little Ambergris Cay.

I would further like to thank George Rossman and Jared Leadbetter for serving on my thesis committee. George's infectious enthusiasm for mineralogy made my teaching assistantship in his Optical Mineralogy lab course a pleasure, and his advice and technical knowledge made the mineralogical analyses in Chapter 2 of this thesis possible. My first microbiology course was Jared's Microbial Physiology, where I first gained an appreciation for the incredible diversity of microbial life and gained an understanding of microbial biochemistry that was indispensible for my thesis work.

So much of the data presented here could not have been collected if not for the deep well of technical knowledge available in the Orphan Lab. First and foremost I would like to thank Stephanie Connon for her unrelenting work in curating, managing, and disseminating the technical expertise collected over many years by former and current Orphan Lab members. It cannot be understated the extent to which so much of the work in this thesis would not have been possible but for the methods developed by Orphan Lab members Anne Dekas, Elizabeth Trembath-Reichert, Kat Dawson, Hang Yu, Ranjani Murali, Benjamin Harrison, Grayson Chadwick, Shawn McGlynn,

Roland Hatzenpichler, Alice Michel, Sean Mullin, Fabai Wu, David Case, Alexis Pasulka, Abigail Green-Saxena, Masataka Aoki, and so many others.

I would further like to thank my friend, colleague, and fellow member of Team SRB, Ranjani Murali, for her many hours of lab work and discussions that contributed to Chapter 1 of this thesis. Ranjani's patience and insights were invaluable throughout the investigation of SEEP-SRB1g, particularly in our nanoSIMS analysis, which constituted an especially exciting and dynamic portion of this project.

I cannot thank enough my friends for providing support and generally being great throughout the years. Thanks to my friends from GPS, Elizabeth Trembath-Reichert, Lewis Ward, Cecilia Sanders, John Magyar, John Naviaux, Peter Martin, and many others who were always excited, supportive, and kind, and often up to get Ernie's. Thanks to my hausmates Austin Chadwick, Joe Bowkett, Alistair Hayden, Mike Citrin, and Dan Johnson for all the great times. I'm also deeply thankful to Judith Wu for her unconditional love and support.

I'd also like to thank my undergraduate thesis advisor, Bob Gaines of Pomona College, for his enthusiasm for geology, Earth history, and geomicrobiology throughout my college career that inspired me to pursue graduate studies in the earth sciences.

Finally, I could never have completed this thesis without the immeasurable support of my dad, my mom, and my brother. Thank you.

ABSTRACT

This thesis investigates ecological interactions in the seafloor between microbial taxa (Chapters 1 and 2) and between these microorganisms and their mineral hosts (Chapters 2 through 4). In seafloor sediments, electron acceptors are often limited, forcing microorganisms inhabiting these sediments to acquire symbiotic partners and/or perform extracellular electron transfer to insoluble electron acceptors. Seafloor methane seeps present an endmember case wherein extremely reducing fluids charged with methane advect through sediment. In these benthic ecosystems, anaerobic methanotrophic archaea (ANME) form symbiotic partnerships with sulfate-reducing bacteria (SRB), but it remained unclear if certain ANME exhibit a preference for certain SRB partners. In Chapter 1, I present results documenting such a pattern of partnership specificity in ANME-SRB consortia. In Chapter 2, I further examine these patterns in rare ANME taxa through development and application of a density-separation protocol refined from published work. This protocol exploits the co-association of microbial taxa on mineral surfaces to aid in the detection of novel symbioses, and further is useful to detect microbial interactions with certain minerals. In Chapter 3, I focus on the interaction between ANME-SRB consortia and authigenic silicates that have been observed on consortium exteriors, finding evidence to support that the precipitation of these silicates is actively mediated by ANME-SRB. In Chapter 4, I perform geochemical modeling benchmarked by synchrotron X-ray analysis to examine the imprint of extracellular electron transport by metal-reducing microorganisms on Precambrian manganese-rich sedimentary rocks.

PUBLISHED CONTENT AND CONTRIBUTIONS

Metcalfe, K.S., et al. (2020) "Experimentally-validated correlation analysis reveals new anaerobic methane oxidation partnerships with consortium-level heterogeneity in diazotrophy." *bioRxiv*, doi: 10.1101/2020.04.12.038331. Resubmitted with minor revisions to *The ISME Journal*.

K.S.M. conceptualized the project and performed correlation analysis, analysis of flow cytometry data, comparative genomics of SRB (in collaboration with R.M.), designed SEEP-SRB1g FISH probe, prepared SIP incubations (with R.M.), processed nanoSIMS data, and wrote the manuscript.

TABLE OF CONTENTS

LIST OF ILLUSTRATIONS AND/OR TABLES

Chapter 1

Chapter 2

Chapter 3

Chapter 4

Introduction

The geochemical dynamism of Earth's surface—unique among known terrestrial planets—is inextricably tied to the emergence and radiation of microbial life. The expansion of microbial metabolic diversity has shaped the course of Earth history, for example causing a step change in atmospheric oxygen concentrations [1], creating a pathway for the transformation of N_2 into biomass [2], and modulating the production and consumption of the powerful greenhouse gas CH_4 [3]. Microbial life in all its variegated forms directs the flow of electrons between diverse donors and acceptors, and in so doing maintains the biogeochemical cycles necessary for Earth's habitability. The numerous biochemical means by which these microorganisms transmit electrons between substrates present many opportunities for discovery, but the experimental study of these mechanisms is made more challenging by the difficulties associated with acquiring pure cultures of environmental microorganisms, the vast majority of which have not been cultured [4].

It has been proposed that the cultivation of environmental microorganisms is challenging due to the reliance of many microbial taxa upon symbiotic partnerships with other microorganisms [5]. Many microbial metabolisms important for the functioning of biogeochemical cycles are facilitated by a symbiotic relationship between microbial taxa, such as that between anaerobic methanotrophic archaea (ANME) and sulfate reducing bacteria (SRB) responsible for the anaerobic oxidation of methane (AOM) in seafloor sediments worldwide [6, 7]. In this and in many microbial symbioses, physical attachment of partner taxa facilitates the transfer of nutrients [8–10], reducing equivalents [11], and/or electrons [12–14] between partners. Study of these symbiotic relationships *in situ* has

uncovered significant diversity in the sequence identity of partner taxa [15–17], but how this diversity may influence the character of these symbioses remains largely an open question.

Evidence from the study of several different microbial symbioses indicates that the nature of a symbiotic relationship can vary between different pairings of partner taxa. In the classic mutualism between reef-building coral hosts and their *Symbiodinium* sp. endosymbionts (colloquially termed 'zooxanthellae'), coral access energy from sunlight via *Symbiodinium* sp. and in turn provide habitat to endosymbionts [18]. Study of coral hosts from a range of habitats has demonstrated that hosts exhibit preference for specific lineages of *Symbiodinium* sp. [19] which appears to have physiological implications for different host-symbiont pairings. The membership of host-symbiont pairs has been observed to predict host tolerance to thermal stress [20–22] and endosymbiont transcriptional profiles [23, 24]. Lichen, a microbial symbiosis between filamentous fungi and endosymbiotic green algae or cyanobacteria, have also been shown to exhibit specificity between partner taxa [25].

For other symbiotic relationships between microorganisms, such as that between ANME and SRB, the specificity with which certain taxa co-associate remains unclear, but may have significant implications for the physiologies of different pairs of symbiotic partners. Extensive study of ANME-SRB consortia has documented a diversity of different ANME-SRB partnerships by fluorescence *in situ* hybridization (FISH)-based microscopy [16, 17, 26] and flow cytometry [27]. However, these results largely served to catalog the ANME-SRB pairings observed in Nature but did not synthesize these datasets to examine the extent to which certain SRB lineages may preferentially associate with certain ANME.

In Chapter 1, I present evidence from an ecological survey of Costa Rica methane seep sediments for a highly specific partnership between certain ANME and SRB partners, and further present stable isotope probing evidence indicating that this specificity is important for symbiotic function.

While the results in Chapter 1 were successfully extracted from a complex dataset of many hundreds of methane seep sediment samples, detection of partnerships between more rare ANME subtypes was not possible, requiring the application of techniques to parse microbial communities at higher resolution. In Chapter 2, I present results from the application of a density-separation protocol refined from previously-published techniques [28]. By exploiting the intimate physical associations between sediment-dwelling microorganisms and minerals, I amplified the correlation signal between ANME and SRB taxa co-associating on mineral surfaces by separating minerals in methane seep sediment samples by density. These techniques circumvent the so-called 'hairball' [29] of computationally-inferred ecological interactions resulting from correlation analysis of complex sediment microbiomes. The results I present in Chapter 2 further document interactions between certain ANME-SRB consortia and certain minerals common in marine sediments, providing avenues for future study of these microbe-mineral interactions.

Such interactions between microorganisms and minerals form an interface between the geosphere and biosphere that has served to preserve a record of microbial life on Earth. AOM, mediated by microbial metabolism, drives the precipitation of carbonate minerals at sites of methane seepage [30]. Microscopy study of ANME-SRB consortia, however, documents authigenic silicate minerals associated with consortia [31, 32]. In Chapter 3, I

investigate the growth of these phases in AOM incubations from which almost all sediment had been removed, finding strong evidence for their growth from media significantly undersaturated with respect to previously-measured equilibria for precipitation of amorphous silica and clays. Together with evidence from seep carbonates, I infer that ANME-SRB consortia may mediate the precipitation of authigenic silicates, representing a means by which ANME-SRB consortia may be preserved in the rock record.

Microbial metabolism has also left an imprint on the rock record by directing redox transformations of mineral electron acceptors [33]. In Chapter 4, I present coupled synchrotron X-ray spectroscopy and geochemical modeling results that indicate Mn(III) mineral phases found in abundance in Precambrian manganese-rich sedimentary rocks were likely stabilized through microbially-mediated reduction of primary Mn oxides, rather than through abiotic means.

Spanning a range of different geomicrobiological questions, this thesis provides the groundwork for further exploration of the diverse microbial symbioses and microbe-mineral interactions that have shaped Earth's biogeochemistry. In particular, I hope future work further explores the hypothesized patterns of partnership specificity in ANME-SRB consortia presented in the first and second chapters of this dissertation. Although Chapter 1 presents a compelling argument that the partnership between ANME-2b and SEEP-SRB1g is highly specific, the degree of specificity or promiscuity in other ANME-SRB partnerships merits further quantitative exploration by FISH experiments. The partnership between ANME-2c and SEEP-SRB1a presents a particularly interesting case, in which ANME-2c, a clade consisting of multiple genera, may exhibit preference either for SEEP-SRB1a or SEEP-SRB2. Evidence for this flexibility comes from both correlation analysis

and FISH experiments performed on cold seep sediment samples in this thesis (Ch. 1) as well as FISH experiments on samples of sedimented hydrothermal vents of the Guaymas Basin in the Gulf of California [34] that show ANME-2c to preferentially associate with SEEP-SRB1a or SEEP-SRB2 in Costa Rica cold seep sediments and with SEEP-SRB2 in Guaymas Basin sedimented hydrothermal vent sites, although it will require further analysis to determine how these patterns of association relate to diversity within the ANME-2c clade. This pattern differs substantially from the high degree of preference exhibited by ANME-2b or ANME-2a for SEEP-SRB1g or SEEP-SRB1a partners, respectively. Exploring the relationship between the SRB taxon preferred by ANME-2c and the environmental parameters of the sediment from which consortia were sampled will likely yield insight into the dynamics of ANME-2c partnership specificity. Network analysis also implies that ANME-2c form intimate associations in hot seep sediments with members of the candidate phylum Atribacteria (data not shown) thought to be involved in hydrocarbon degradation [35], but the nature of this association is entirely unknown. Additionally, ANME-2c are members of consortia of diverse morphotypes (G. Chadwick, pers. comm.) and which may relate to patterns of partnership specificity. ANME-1, representing a separate order of methanotrophic archaea with multiple genera, also exhibits similar flexibility in its partnerships with SRB, as ANME-1 has been observed to associate with SEEP-SRB2 in cold seep sediments (Ch. 1) and members of the HotSeep-1 in methane-rich hydrothermal vent sediments [34]; further work could characterize the nature of ANME-1 partnerships *in situ* and further shed light on the parameters that may contribute to ANME-1 forming partnerships with different SRB partner taxa.

The discoveries described in this thesis point toward a more holistic understanding of the symbiotic relationship that lies at the heart of AOM. Previous work has primarily focused on the biochemistry of anaerobic methane oxidation within ANME, as these microorganisms presented striking similarities to methanogenic archaea. However, relatively less emphasis has been placed on investigating in detail the role of partner SRB. Although the scope of this thesis was constrained to sketching the contours of symbiotic diversity in AOM, it is my hope that future research will explore the co-evolution of ANME and their SRB partners, and in so doing shed new light on the enigma of the anaerobic oxidation of methane.

REFERENCES

1. Fischer WW, Hemp J, Johnson JE. Evolution of Oxygenic Photosynthesis. *Annu Rev Earth Planet Sci* 2016; **44**: 647–683.
2. Raymond J, Siefert JL, Staples CR, Blankenship RE. The Natural History of Nitrogen Fixation. *Mol Biol Evol* 2004; **21**: 541–554.
3. Reeburgh WS. Oceanic Methane Biogeochemistry. *Chem Rev* 2007; **107**: 486–513.
4. Steen AD, Crits-Christoph A, Carini P, DeAngelis KM, Fierer N, Lloyd KG, et al. High proportions of bacteria and archaea across most biomes remain uncultured. *ISME J* 2019; **13**: 3126–3130.
5. Schink B. Synergistic interactions in the microbial world. *Antonie Van Leeuwenhoek* 2002; **81**: 257–261.
6. Boetius A, Ravenschlag K, Schubert CJ, Rickert D, Widdel F, Gieseke A, et al. A marine microbial consortium apparently mediating anaerobic oxidation of methane. *Nature* 2000; **407**: 623.
7. Orphan VJ, House CH, Hinrichs K-U, McKeegan KD, DeLong EF. Methane-Consuming Archaea Revealed by Directly Coupled Isotopic and Phylogenetic Analysis. *Science* 2001; **293**: 484–487.
8. Dekas AE, Poretsky RS, Orphan VJ. Deep-Sea Archaea Fix and Share Nitrogen in Methane-Consuming Microbial Consortia. *Science* 2009; **326**: 422–426.
9. Schwank K, Bornemann TLV, Dombrowski N, Spang A, Banfield JF, Probst AJ. An archaeal symbiont-host association from the deep terrestrial subsurface. *ISME J* 2019; **13**: 2135–2139.
10. Heimerl T, Flechsler J, Pickl C, Heinz V, Salecker B, Zweck J, et al. A Complex Endomembrane System in the Archaeon Ignicoccus hospitalis Tapped by Nanoarchaeum equitans. *Front Microbiol* 2017; **8**: 1072.
11. Stams AJM, Plugge CM. Electron transfer in syntrophic communities of anaerobic bacteria and archaea. *Nat Rev Microbiol* 2009; **7**: 568–577.
12. Summers ZM, Fogarty HE, Leang C, Franks AE, Malvankar NS, Lovley DR. Direct exchange of electrons within aggregates of an evolved syntrophic coculture of anaerobic bacteria. *Science* 2010; **330**: 1413–5.

13. McGlynn SE, Chadwick GL, Kempes CP, Orphan VJ. Single cell activity reveals direct electron transfer in methanotrophic consortia. *Nature* 2015; **526**: 531–535.

14. Wegener G, Krukenberg V, Riedel D, Tegetmeyer HE, Boetius A. Intercellular wiring enables electron transfer between methanotrophic archaea and bacteria. *Nature* 2015; **526**: 587–590.

15. Jarett JK, Nayfach S, Podar M, Inskeep W, Ivanova NN, Munson-McGee J, et al. Single-cell genomics of co-sorted Nanoarchaeota suggests novel putative host associations and diversification of proteins involved in symbiosis. *Microbiome* 2018; **6**: 161.

16. Orphan VJ, House CH, Hinrichs K-U, McKeegan KD, DeLong EF. Multiple archaeal groups mediate methane oxidation in anoxic cold seep sediments. *Proc Natl Acad Sci* 2002; **99**: 7663–7668.

17. Knittel K, Lösekann T, Boetius A, Kort R, Amann R. Diversity and Distribution of Methanotrophic Archaea at Cold Seeps. *Appl Environ Microbiol* 2005; **71**: 467–479.

18. Baker AC. Flexibility and Specificity in Coral-Algal Symbiosis: Diversity, Ecology, and Biogeography of Symbiodinium. *Annu Rev Ecol Evol Syst* 2003; **34**: 661–689.

19. Thornhill DJ, Xiang Y, Pettay DT, Zhong M, Santos SR. Population genetic data of a model symbiotic cnidarian system reveal remarkable symbiotic specificity and vectored introductions across ocean basins. *Mol Ecol* 2013; **22**: 4499–4515.

20. Berkelmans R, van Oppen MJH. The role of zooxanthellae in the thermal tolerance of corals: a 'nugget of hope' for coral reefs in an era of climate change. *Proc R Soc B Biol Sci* 2006; **273**: 2305–2312.

21. Sampayo EM, Ridgway T, Bongaerts P, Hoegh-Guldberg O. Bleaching susceptibility and mortality of corals are determined by fine-scale differences in symbiont type. *Proc Natl Acad Sci* 2008; **105**: 10444–10449.

22. Parkinson JE, Baumgarten S, Michell CT, Baums IB, LaJeunesse TC, Voolstra CR. Gene Expression Variation Resolves Species and Individual Strains among Coral-Associated Dinoflagellates within the Genus Symbiodinium. *Genome Biol Evol* 2016; **8**: 665–680.

23. Barshis DJ, Ladner JT, Oliver TA, Palumbi SR. Lineage-Specific Transcriptional Profiles of Symbiodinium spp. Unaltered by Heat Stress in a Coral Host. *Mol Biol Evol* 2014; **31**: 1343–1352.

24. DeSalvo MK, Sunagawa S, Fisher PL, Voolstra CR, Iglesias-Prieto R, Medina M. Coral host transcriptomic states are correlated with Symbiodinium genotypes. *Mol Ecol* 2010; **19**: 1174–1186.

25. Leavitt SD, Kraichak E, Nelsen MP, Altermann S, Divakar PK, Alors D, et al. Fungal specificity and selectivity for algae play a major role in determining lichen partnerships across diverse ecogeographic regions in the lichen-forming family Parmeliaceae (Ascomycota). *Mol Ecol* 2015; **24**: 3779–3797.

26. Green-Saxena A, Dekas AE, Dalleska NF, Orphan VJ. Nitrate-based niche differentiation by distinct sulfate-reducing bacteria involved in the anaerobic oxidation of methane. *ISME J* 2014; **8**: 150–163.

27. Hatzenpichler R, Connon SA, Goudeau D, Malmstrom RR, Woyke T, Orphan VJ. Visualizing in situ translational activity for identifying and sorting slow-growing archaeal−bacterial consortia. *Proc Natl Acad Sci* 2016; **113**: E4069–E4078.

28. Harrison BK, Orphan VJ. Method for Assessing Mineral Composition-Dependent Patterns in Microbial Diversity Using Magnetic and Density Separation. *Geomicrobiol J* 2012; **29**: 435–449.

29. Röttjers L, Faust K. From hairballs to hypotheses–biological insights from microbial networks. *FEMS Microbiol Rev* 2018; **42**: 761–780.

30. Luff R, Wallmann K. Fluid flow, methane fluxes, carbonate precipitation and biogeochemical turnover in gas hydrate-bearing sediments at Hydrate Ridge, Cascadia Margin: numerical modeling and mass balances. *Geochim Cosmochim Acta* 2003; **67**: 3403–3421.

31. Dekas AE. Diazotrophy in the deep: an analysis of the distribution, magnitude, geochemical controls, and biological mediators of deep-sea benthic nitrogen fixation. *Division of Geological and Planetary Sciences* . 2013. California Institute of Technology.

32. Chen Y, Li Y-L, Zhou G-T, Li H, Lin Y-T, Xiao X, et al. Biomineralization mediated by anaerobic methane-consuming cell consortia. *Sci Rep* 2014; **4**: 1–9.

33. Johnson JE, Webb SM, Ma C, Fischer WW. Manganese mineralogy and diagenesis in the sedimentary rock record. *Geochim Cosmochim Acta* 2016; **173**: 210–231.

34. Krukenberg V, Riedel D, Gruber-Vodicka HR, Buttigieg PL, Tegetmeyer HE, Boetius A, et al. Gene expression and ultrastructure of meso- and thermophilic methanotrophic consortia. *Environ Microbiol* 2018; 20: 1651–1666.

35. Liu Y-F, Qi Z-Z, Shou L-B, Liu J-F, Yang S-Z, Gu J-D, Mu B-Z, Anaerobic hydrocarbon degradation in candidate phylum 'Atribacteria' (JS1) inferred from genomics. *ISME J* 2019; **13** 2377-2390.

Chapter 1

EXPERIMENTALLY-VALIDATED CORRELATION ANALYSIS REVEALS NEW ANAEROBIC METHANE OXIDATION PARTNERSHIPS WITH CONSORTIUM-LEVEL HETEROGENEITY IN DIAZOTROPHY

Kyle S. Metcalfe, Ranjani Murali, Sean W. Mullin, Stephanie A. Connon, and Victoria J. Orphan

Division of Geological and Planetary Sciences,
California Institute of Technology, Pasadena, California, 91125

ABSTRACT

Archaeal anaerobic methanotrophs ('ANME') and sulfate-reducing Deltaproteobacteria ('SRB') form symbiotic multicellular consortia capable of anaerobic methane oxidation (AOM), and in so doing modulate methane flux from marine sediments. The specificity with which ANME associate with particular SRB partners in situ, however, is poorly understood. To characterize partnership specificity in ANME-SRB consortia, we applied the correlation inference technique SparCC to 310 16S rRNA amplicon libraries prepared from Costa Rica seep sediment samples, uncovering a strong positive correlation between ANME-2b and members of a clade of Deltaproteobacteria we termed SEEP-SRB1g. We confirmed this association by examining 16S rRNA diversity in individual ANME-SRB consortia sorted using flow cytometry and by imaging ANME-SRB consortia with fluorescence in situ hybridization (FISH) microscopy using newly-designed probes

targeting the SEEP-SRB1g clade. Analysis of genome bins belonging to SEEP-SRB1g revealed the presence of a complete nifHDK operon required for diazotrophy, unusual in published genomes of ANME-associated SRB. Active expression of nifH in SEEP-SRB1g within ANME-2b—SEEP-SRB1g consortia was then demonstrated by microscopy using hybridization chain-reaction (HCR-) FISH targeting nifH transcripts and diazotrophic activity was documented by FISH-nanoSIMS experiments. NanoSIMS analysis of ANME-2b—SEEP-SRB1g consortia incubated with a headspace containing CH_4 and $^{15}N_2$ revealed differences in cellular ^{15}N-enrichment between the two partners that varied between individual consortia, with SEEP-SRB1g cells enriched in ^{15}N relative to ANME-2b in one consortium and the opposite pattern observed in others, indicating both ANME-2b and SEEP-SRB1g are capable of nitrogen fixation, but with consortium-specific variation in whether the archaea or bacterial partner is the dominant diazotroph.

INTRODUCTION

The partnership between anaerobic, methanotrophic Archaea (ANME) and their associated sulfate-reducing bacteria (SRB) is one of the most biogeochemically-important symbioses in the deep-sea methane cycle [1, 2]. As a critical component of methane seep ecosystems, multicellular consortia of ANME and associated SRB consume a significant fraction of the methane produced in marine sediments, using sulfate as a terminal electron acceptor to perform the anaerobic oxidation of methane (AOM) [1–4]. ANME-SRB consortia are thought to perform AOM through the direct extracellular transfer of electrons between ANME and SRB [5–7]. Along with symbiotic extracellular electron transfer, ANME-SRB consortia also exhibit other traits of mutualism such as the sharing of nutrients. For example, members of the ANME-2 clade have been reported to fix and share N with partner bacteria [8–11], but the extent to which diazotrophic capability might vary across the diverse clades of ANME and associated SRB is the focus of ongoing research.

Comparative studies of ANME [12] and associated SRB [13, 14] genomes from multiple ANME-SRB consortia have revealed significant diversity across clades, particularly for SRB genomes falling within subclades of the Desulfobacteraceae SEEP-SRB1a [14], common SRB partners to ANME [15]. However, the implications of symbiont diversity for metabolic adaptation in ANME-SRB consortia are obscured by the absence of clearly-established ANME-SRB pairings in the environment. A framework defining these pairings would address this gap in knowledge. Establishing this framework for partnership specificity in ANME-SRB consortia—being the preference that certain ANME exhibit for specific SRB partners—would shed light on the extent to which ANME or SRB physiology may differ in consortia constituted of different ANME-SRB pairs.

As an aspect of ANME or SRB physiology that may differ in different ANME-SRB pairings, nitrogen anabolism has been observed to be involved in the symbiotic relationship between partners [8, 9] and has been shown to influence niche differentiation of different ANME-SRB consortia via nitrate assimilation ability [16]. Previous evidence documenting active diazotrophy by AOM consortia from cDNA libraries of *nifH* [8] and $^{15}N_2$ stable isotope probing with FISH-nanoSIMS, indicated that the methanotrophic ANME-2 archaea fixed more nitrogen than SRB in consortia and may supply fixed nitrogen to their syntrophic partners [8–10]. The diazotrophic potential of syntrophic SRB, however, and their role in nitrogen fixation within consortia is poorly understood. Evidence from SRB genomes [14] and the expression of unidentified nitrogenase sequences in methane seep sediments [8] suggested that some seep-associated SRB may also fix nitrogen, opening up the possibility of variation in diazotrophic activity among taxonomically-distinct ANME-SRB consortia.

Previous research characterizing the diversity of partnerships in ANME-SRB consortia have employed fluorescence microscopy, magnetic separation by magneto-FISH, and single-cell sorting techniques (e.g. BONCAT-FACS) that are robust against false positives, but are often limited in statistical power. Fluorescence *in situ* hybridization (FISH) has helped to establish the diversity of ANME-bacterial associations, with ANME constituting four diverse polyphyletic clades within the Methanomicrobia: ANME-1a/b [4, 17–20], ANME-2a,b,c [3, 20–22] , ANME-2d [23, 24], and ANME-3 [20, 25, 26]. ANME-associated SRB have also observed by FISH to be diverse, representing several clades of Deltaproteobacteria including the *Desulfococcus/Desulfosarcina* (DSS) clade [3–6, 15, 19–22, 27–33], two separate subclades within the Desulfobulbaceae [16, 25, 26], a deeply-

branching group termed the SEEP-SRB2 [34], and a thermophilic clade of Desulfobacteraceae known as HotSeep-1 [34, 35]. These FISH studies documented associations for different ANME-SRB consortia, including partnerships between members of ANME-1 and SEEP-SRB2 [13] or HotSeep-1 [7, 13, 35], ANME-2a and SEEP-SRB1a [15], ANME-2c and SEEP-SRB1a [5], SEEP-SRB2 [13, 34], or Desulfobulbaceae [29], and ANME-3 and SEEP-SRB1a [15] or Desulfobulbaceae [25, 26]. Conspicuously, SRB found in consortia with ANME-2b have only been identified broadly as members of the Deltaproteobacteria targeted by the probe S-C-dProt-0495-a-A-18 (often referred to as Δ495) [5, 31, 36], leaving little known about the specific identity of this SRB partner. Visualizing ANME-SRB partnerships by FISH has been a valuable aspect of AOM research, but FISH requires the design of probes with sufficient specificity to identify partner organisms and thus will only detect partnerships consisting of taxa for which phylogenetic information is known [22]. Magneto-FISH [29, 37, 38] or BONCAT-enabled fluorescence-activated cell sorting (BONCAT-FACS) of single ANME-SRB consortia [39] complement FISH experiments by physical capture (via magnetic beads or flow cytometry, respectively) and sequencing of ANME and associated SRB from sediment samples. These studies corroborated some of the patterns observed from FISH experiments, showing associations between ANME-2 and diverse members of the DSS [39]. Magneto-FISH and BONCAT-FACS observations of ANME-SRB pairings are also highly robust against false positives but can lack the statistical power conferred by more high-throughput approaches that is necessary to establish a general framework for partnership specificity.

Recently, a number of correlation analysis techniques have been introduced in molecular microbial ecology studies, providing information about patterns of co-

occurrence between 16S rRNA OTUs (operational taxonomic units) or ASVs (amplicon sequence variants) recovered from environmental diversity surveys [40–43]. Correlation analysis performed on 16S rRNA amplicon surveys provides a complementary method to Magneto-FISH and/or BONCAT-FACS that can be used to develop hypotheses about potential microbial interactions. While predictions of co-occurrence between phylotypes from these correlation analysis techniques have been reported in a number of diverse environments, they are rarely validated through independent approaches, with a few notable exceptions (e.g. [44]).

Here, we present a framework for ANME-SRB partnership specificity, using correlation analysis of 16S rRNA amplicon sequences from a large-scale survey of seafloor methane seep sediments near Costa Rica to predict potential ANME-SRB partnerships. A partnership between ANME-2b and members of an SRB group previously not known to associate with ANME (SEEP-SRB1g) was hypothesized by correlation analysis and independently assessed by FISH and by analysis of amplicon data from Hatzenpichler and coworkers [39] of BONCAT-FACS-sorted ANME-SRB consortia. With this new framework, we were able to identify a novel partnership between ANME-2b and SEEP-SRB1g and map predicted physiological traits of SEEP-SRB1g genomes onto partnership specificity with ANME-2b. Our approach led us to formulate new hypotheses regarding how SEEP-SRB1g physiology may complement ANME-2b physiology, focusing on nitrogen fixation in SEEP-SRB1g. We demonstrate in this study that the symbiotic relationship between ANME and associated SRB can vary depending on the nature of the partner taxa and affirm the importance of characterizing individual symbiont pairings in understanding AOM symbiosis.

MATERIALS AND METHODS

Here, we present an abridged description of the methods used in this study. A full description can be found in the Supplemental Materials and Methods.

Sample origin and processing

Pushcore samples of seafloor sediment were collected by DSV Alvin during the May 20-June 11 2017 ROC HITS Expedition (AT37-13) aboard R/V Atlantis to methane seep sites southwest of Costa Rica [45–47]. After retrieval from the seafloor, sediment pushcores were extruded aboard R/V Atlantis and sectioned at 1-3 cm intervals for geochemistry and microbiological sampling using published protocols [21, 48]. Samples for DNA extraction were immediately frozen in liquid N2 and stored at -80˚C. Samples for microscopy were fixed in 2% paraformaldehyde for 24 h at 4˚C. A full list of samples used in this study can be found in Supplemental Table 1 and additional location and geochemical data can be found at https://www.bco-dmo.org/dataset/715706.

DNA extraction and Illumina 16S rRNA amplicon sequencing

DNA was extracted from 310 samples of Costa Rican methane seep sediments and seep carbonates (Supp. Table 1) using the Qiagen PowerSoil DNA Isolation Kit 12888 following manufacturer directions modified for sediment and carbonate samples [21, 49].

The V4-V5 region of the 16S rRNA gene was amplified using archaeal/bacterial primers, 515F (5'-GTGYCAGCMGCCGCGGTAA-3') and 926R (5'-CCGYCAATTYMTTTRAGTTT-3') with Illumina adapters [50]. PCR reaction mix was set up in duplicate for each sample with New England Biolabs Q5 Hot Start High-Fidelity 2x Master Mix in a 15 μL reaction volume with annealing conditions of 54°C for 30 cycles. Duplicate PCR samples were then pooled and 2.5 μL of each product was barcoded with Illumina NexteraXT index 2 Primers that include unique 8-bp barcodes. Amplification with barcoded primers used annealing conditions of 66°C and 10 cycles. Barcoded samples were combined into a single tube and purified with Qiagen PCR Purification Kit 28104 before submission to Laragen (Culver City, CA, USA) for 2 x 250 bp paired end analysis on Illumina's MiSeq platform. Sequence data were submitted to the NCBI Sequence Read Archive as Bioproject PRJNA623020. Sequence data were processed in QIIME version 1.8.0 [51] following Mason, et al. 2015 [52]. Sequences were clustered into de novo operational taxonomic units (OTUs) with 99% similarity [53], and taxonomy was assigned using the SILVA 119 database [54]. Known contaminants in PCR reagents as determined by analysis of negative controls run with each MiSeq set were also removed (see Supplemental Materials and Methods) along with rare OTUs not present in any given library at a level of at least 10 reads. The produced table of OTUs detected in the 310 methane seep sediment and seep carbonate amplicon libraries was analyzed using the correlation algorithm SparCC [41].

To examine phylogenetic placement of SRB 16S rRNA gene amplicon sequences predicted by network analysis to associate with particular ANME subgroup amplicon

sequences, a phylogeny was constructed using RAxML-HPC [55] on XSEDE [56] using the CIPRES Science Gateway [57] from full-length 16S rRNA sequences of Deltaproteobacteria aligned by MUSCLE [58]. Genomes downloaded from the IMG/M database were searched using tblastn. Chlorophyllide reductase BchX (WP011566468) was used as a query sequence for a tblastn *nifH* search using BLAST+. BchX was used as the query sequence to recover divergent *nifH* sequences covering the diversity of all *nifH* clades, following the approach of Dekas, et al., 2016. Genome trees were constructed using the Anvi'o platform [59] using HMM profiles from a subset [60] of ribosomal protein sequences and visualized in iTOL [61].

FISH Probe Design And Microscopy

A new FISH probe was designed in ARB [62]. This probe, hereafter referred to as Seep1g-1443 (Supp. Table 2), was designed to complement and target 16S rRNA sequences in a monophyletic "*Desulfococcus* sp." clade. Based on phylogenetic analysis (see below), this clade was renamed SEEP-SRB1g, following the naming scheme of Schreiber and coworkers [15]. Seep1g-1443 was ordered from Integrated DNA Technologies (Coralville, IA, USA). FISH reaction conditions were optimized for Seep1g-1443, with optimal formamide stringency found to be 35% (Supp. Fig. 1). FISH and hybridization chain reaction (HCR-) FISH was performed on fixed ANME-SRB consortia using previously published density separation and FISH protocols [22], using a selection of following FISH probes: Seep1g (Alexa488; this work), Seep1a-1441 (cy5; [15]), ANME-

2a-828 (cy3(3'); M. Aoki, pers. comm.), ANME-2b-729 (cy3; [39]), and ANME-2c-760 (cy3; [20]). FISH was performed overnight (18 hr) using modifications (G. Chadwick, pers. comm.) to previously-published protocols [29, 39, 63, 64]. Structured-illumination microscopy (SIM) was performed on FISH and HCR-FISH (see below) experiments to image ANME-SRB consortia using the Elyra PS.1 SIM platform (Zeiss, Germany) and an alpha Plan-APOCHROMAT 100X/1.46 Oil DIC M27 objective. Zen Black software (Zeiss) was used to construct final images from the structured-illumination data.

mRNA Imaging Using HCR-FISH

Hybridization chain reaction FISH (HCR-FISH) is a powerful technique to amplify signal from FISH probes [65, 66]. The protocol used here was modified from Yamaguchi and coworkers [67]. *nifH* initiators, purchased from Molecular Technologies (Pasadena, CA, USA; probe identifier "nifH 3793/D933") or designed in-house (Supp. Table 2) and ordered from Integrated DNA Technologies, were hybridized to fixed ANME-SRB consortia. Hairpins B1H1 and B1H2 with attached Alexa647 fluorophores (Molecular Technologies) were added separately to two 45 µL volumes of amplification buffer in PCR tubes and snap cooled by placement in a C1000 Touch Thermal Cycler (BioRad, Hercules, CA, USA) for 3 min at 95˚C. After 30 min at room temperature, hairpins were mixed and placed in PCR tubes along with hybridized ANME-SRB consortia. Amplification was performed for 15 min at 35˚C. Similar results were observed when the HCR-FISH v3.0 protocol established by Choi et al. [68] was used. ANME-SRB consortia subjected to

HCR-FISH experiments were imaged using the Elyra PS.1 SIM platform (Zeiss, Germany) as mentioned above. In all cases, the FITC channel was subject to a 500 ms exposure time, TRITC to 200 ms, and cy5 to 1000 ms. Colocalization of signal was analyzed in ImageJ using the Colocalization Finder and JaCoP plugin [69]. These plugins were used to compute the Pearson's cross-correlation coefficient (PC) and Manders' colocalization coefficients (M1, M2). In addition, pairwise correlations between channels were visualized using scatterplots of pixel intensity.

Stable Isotope Probing and nanoSIMS

Methane seep sediments containing abundant ANME-2b and SEEP-SRB1g consortia (Supp. Fig. 2) were used in stable isotope probing (SIP) experiments to test for diazotrophic activity by SEEP-SRB1g. SIP incubations (Supp. Table 3) were prepared by sparging source bottles and 30 mL serum bottles with N_2 and mixing 5 mL of sediment with 5 mL N_2-sparged artificial seawater without a N source. N sources were removed from the sediment slurry by washing with artificial seawater without an N source (see Supplemental Materials and Methods). Two anoxic incubations were pressurized with 2.8 bar CH_4 with 1.2 mL $^{15}N_2$ (Cambridge Isotopes, Tewksbury, MA, part # NLM-363-PK, lot # l-21065) at 1 bar, approximately equivalent to 2% headspace in 20 mL CH_4 at 2.8 bar (Supp. Table 3). Potential $^{15}NH_4^+$ contamination in $^{15}N_2$ stocks have been previously reported and can lead to spurious results in nitrogen fixation experiments. We did not test for fixed N in the specific reagent bottle used in these experiments. However, previous

comparisons of $^{15}N_2$ stocks identify those from Cambridge Isotopes as among the least-contaminated $^{15}N_2$ stocks available [70]. Positive control incubations (n = 2) were amended with 500 μM $^{15}NH_4Cl$ and were pressurized with 2.8 bar CH_4 and 1.2 mL natural-abundance N_2 at 1 bar. Incubations were periodically checked for AOM activity via sulfide production using the Cline assay [71] and were chemically fixed for FISH-nanoSIMS analysis [72] after 9 months. Samples of slurry fluid were collected, filtered using a 0.2 μm filter, and measured for dissolved ammonium concentrations using a Dionex ICS-2000 ion chromatography system (Thermo Scientific) housed at the Environmental Analysis Center at Caltech. Fixed ANME-SRB consortia were separated from the sediment matrix and concentrated following published protocols [5]. Samples were then embedded in Technovit H8100 (Kulzer GmbH, Germany) resin according to published protocols [5, 31] and semi-thin sections (2 μm thickness) were prepared using an Ultracut E microtome (Reichert AG, Austria) which were mounted on Teflon/poly-L-lysine slides (Tekdon Inc., USA). FISH reactions were performed on serial sections (n = 30) using Seep1g-1443 and ANME-2b-729 probes as described above, with the omission of 10% SDS to prevent detachment of section from slide (G. Chadwick, pers. comm.), and slides were imaged and mapped for subsequent nanoSIMS analysis using a Zeiss Elyra PS.1 platform. Sequential sections of each sample were imaged and mapped to identify the section most representative of a section through the center of ANME-SRB consortia. This allowed for the interpretation of spatial patterns correlated with distance from the exterior of the ANME-SRB consortium on the x-y plane as representative of those correlated with the unobserved x-z and y-z planes. After removal of DAPI-Citifuor mounting medium by washing in DI water following published protocols [72], individual wells on the slides were scored with a

diamond scribe and cut to fit into the nanoSIMS sample holder (~1 cm diameter) and sputter-coated with 40 nm Au using a Cressington sputter coater. Briefly, nanoSIMS analyses were performed using a Cameca NanoSIMS 50L housed in Caltech's Microanalysis Center: 512 x 512 pixel raster images of 20 μm^2 were collected for $^{12}C^-$, $^{16}O^-$, $^{12}C^{14}N^-$, $^{15}N^{12}C^-$, $^{28}Si^-$, and $^{32}S^-$ ions by sputtering with a ~1 pA primary Cs^+ ion beam current with a dwell time of 12-48 ms/pixel. Data were analyzed using look@nanoSIMS [73].

RESULTS

16S rRNA Correlation Analysis Predicts A Specific Association Between ANME-2b And SEEP-SRB1g

Correlation analysis applied to 16S rRNA gene amplicon libraries has been frequently used to identify interactions between microorganisms based on the co-occurrence of their 16S rRNA sequences in different environments or conditions [74–77]. Here, we applied correlation analysis to Illumina 16S rRNA amplicon sequences recovered from Costa Rican methane seep sediments (Supp. Table 1) to explore partnership specificity between ANME and associated SRB. QIIME processing of amplicon sequences prepared from 310 Costa Rican methane seep sediment and seep carbonate samples yielded 3,052 OTUs after filtering in R. A table of read abundances for these OTUs across the 310 samples was analyzed by SparCC to calculate correlation coefficients and significance for all possible 4,658,878 OTU pairs using 100 bootstraps (Fig. 1a). Of these pairs, 9.7% (452,377) had

pseudo-*p*-values < 0.01, indicating the coefficients for each of these correlations exceeded that calculated for that same OTU pair in any of the 100 bootstrapped datasets [41]. The taxonomic assignment of the constituent OTUs of correlations with pseudo-*p* < 0.01 were then inspected, where 18% (81,459) of correlations with pseudo-*p* < 0.01 describe those involving ANME (Fig. 1b). Of these, 32% occur between ANME and OTUs assigned to three main taxa: *Desulfococcus* sp. (renamed SEEP-SRB1g, see discussion below), SEEP-SRB1a, and SEEP-SRB2 (Fig. 1c). A complete list of significant correlations, their coefficient values, OTU identifiers, and accompanying taxonomy assignments can be found in Supplemental Table 4.

16S rRNA phylogenetic analysis revealed the SILVA-assigned "*Desulfococcus* sp." OTUs comprise a sister clade to the SEEP-SRB1a that is distinct from cultured *Desulfococcus* sp. (e.g. *D. oleovorans* and *D. multivorans*, see below). We therefore reassigned the *Desulfococcus* OTUs to a new clade we termed SEEP-SRB1g following the naming scheme outlined for seep-associated SRB in Schreiber, et al. (e.g. SEEP-SRB1a through -SRB1f) [15]. Furthermore, statistically-significant correlations between OTUs of ANME and SRB taxa suggested that ANME-SRB partnerships in the Costa Rica seep samples could be classified into the following types: ANME-1 with SEEP-SRB1a or SEEP-SRB2, ANME-2a with SEEP-SRB1a, ANME-2b with SEEP-SRB1g, ANME-2c with SEEP-SRB1a or SEEP-SRB2, and ANME-3 with SEEP-SRB1a (Fig. 1d). While physical association between different ANME lineages and Deltaproteobacterial clades SEEP-SRB1a and SEEP-SRB2 had been well-documented [5, 13, 15, 31, 34], members of

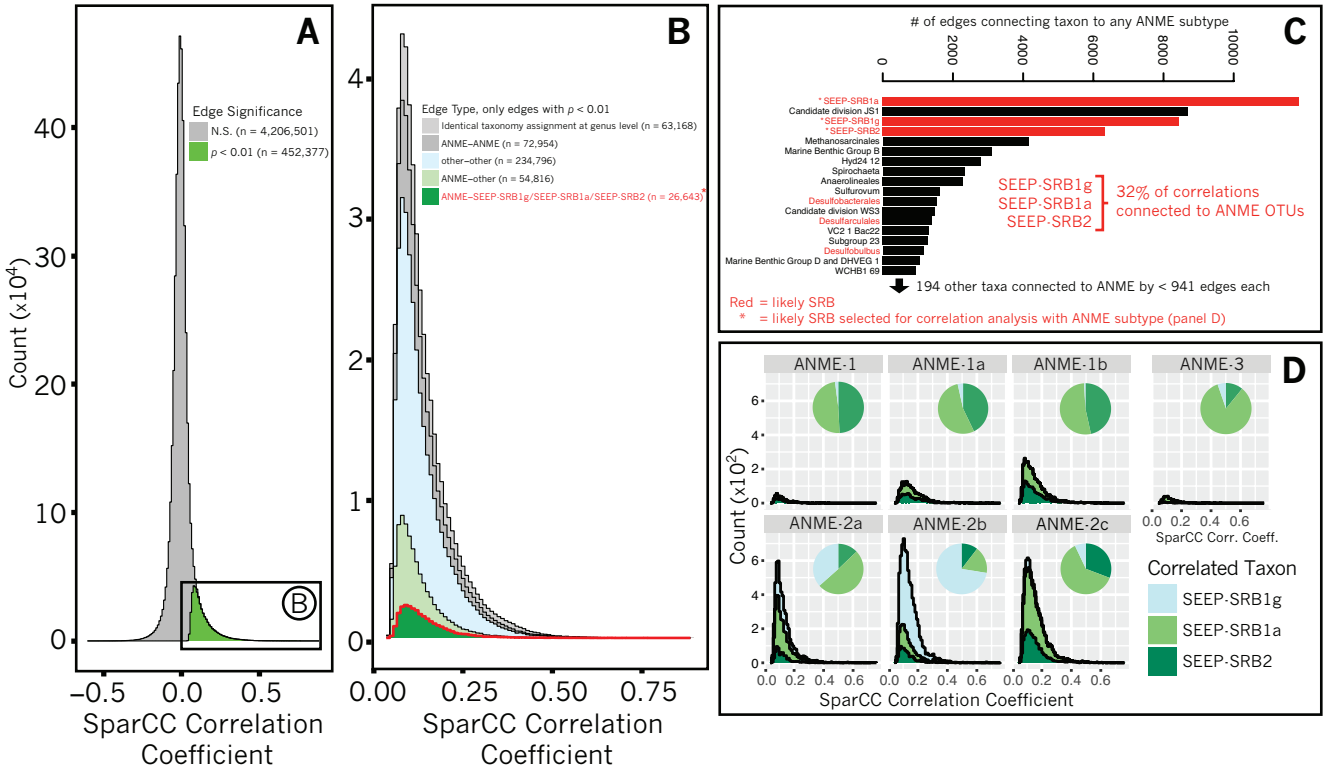

Figure 1. Analysis of SparCC-calculated correlations between 16S rRNA amplicon sequences (OTUs clustered at 99% similarity) from an ecological survey of 310 methane seep sediment samples from seafloor sites off of Costa Rica. A stacked histogram (A) illustrates the proportion of correlations deemed significant on the basis of pseudo-p-values < 0.01 calculated by comparison with 100 bootstrapped correlation tables (see Materials and Methods). Of the correlations with pseudo-p-values < 0.01, 18% include ANME with a non-ANME taxon (B). Significant correlations between OTUs with taxonomy assignments that are identical at the genus level (e.g. two Anaerolinea OTUs) are indicated by identical taxonomy assignment. 32% of correlations between ANME and non-ANME taxa are represented by OTUs assigned to three groups of sulfate-reducing bacteria: SEEP-SRB1g, SEEP-SRB1a, and SEEP-SRB2 (C). Stacked histograms of correlations between OTUs assigned to SEEP-SRB1g, SEEP-SRB1a, or SEEP-SRB2 and ANME OTUs, parsed by ANME subtype (D), highlights specific associations predicted between ANME-1 and either SEEP-SRB1a or SEEP-SRB2, ANME-2a and SEEP-SRB1a, ANME-2c and SEEP-SRB1a, and between ANME-2b and SEEP-SRB1g.

the SEEP-SRB1g had not previously been identified as a potential syntrophic partner with methanotrophic ANME.

These associations were further examined by detailed network analysis in which the table of correlations with pseudo *p*-values < 0.01 was further filtered to contain only those correlations with coefficients (a measure of correlation strength) in the 99th percentile of all significant correlations. A network diagram in which nodes represent OTUs and edges between nodes represent correlations was constructed with force-directed methods [78], where edge length varied in inverse proportion to correlation strength. A subregion of this network focused on ANME-associated OTUs is presented in Figure 2. Cohesive blocks, subsets of the graph with greater connectivity to other nodes in the block than to nodes outside [79], were calculated and revealed 3 primary blocks of ANME and SRB OTUs. Visualization of these 3 blocks by a chord diagram [80] further highlighted the taxonomic identity of ANME-SRB OTU pairs in these blocks: ANME-1 or ANME-2c (one OTU with mean read count < 10) and SEEP-SRB2, ANME-2a or ANME-2c and SEEP-SRB1a, and ANME-2b or ANME-2a and SEEP-SRB1g (Fig. 2b). The predicted associations between ANME-2c and SEEP-SRB2 and between ANME-2a and SEEP-SRB1g were relatively more rare than the other associations; only one rare ANME-2c OTU (mean read count < 10) and four uncommon ANME-2a OTUs (mean read count < 100) were predicted between SEEP-SRB2 and SEEP-SRB1g, respectively. Inferred partnership specificity in two of the blocks has been previously corroborated by FISH studies, namely associations between ANME-1 with SEEP-SRB2 [13, 34], ANME-2c with SEEP-SRB1a [5], and ANME-2a with SEEP-SRB1a [15]. The partnership between SEEP-SRB1g and ANME-2b,

however, had no precedent, as the only previous FISH descriptions of ANME-2b had placed it with a partner Deltaproteobacterium with taxonomy not known beyond the phylum level [5, 31].

Common Patterns of Association Observed in Network Analysis and in Single ANME-SRB Consortia

To test if ANME-SRB partnership specificity observed in our correlation analysis of 16S rRNA amplicon sequences from seep samples (Figs. 1, 2) was consistent with data collected from individually-sorted ANME-SRB consortia after BONCAT-FACS [39], we constructed a phylogeny with full-length and amplicon 16S rRNA sequences from ANME-associated SRB including SEEP-SRB1g (Fig. 3; Supp. Fig 5). These individual ANME-SRB sorted by BONCAT-FACS were sourced from methane seep sediment samples recovered from Hydrate Ridge off the coast of Oregon and seafloor sites in Santa Monica Basin, California, allowing us to further test whether the ANME-2b—SEEP-SRB1g partnership can be detected in seafloor sites beyond Costa Rica. 16S rRNA amplicon sequences from the network analysis (Fig. 2) and from BONCAT-FACS sorted consortia from Hydrate Ridge seeps off of Oregon and seeps from the Santa Monica Basin, CA (Fig. 3; [39]) were then annotated by ANME subtype and identity of associated phylotypes. In the BONCAT-FACS dataset, 8 out of 11 (72%) of the consortia with ANME-2b OTUs had corresponding deltaproteobacterial OTUs that belonged to the SEEP-SRB1g clade (Fig. 3). Similarly, of the Deltaproteobacteria OTU sequences from the BONCAT-FACS sorted

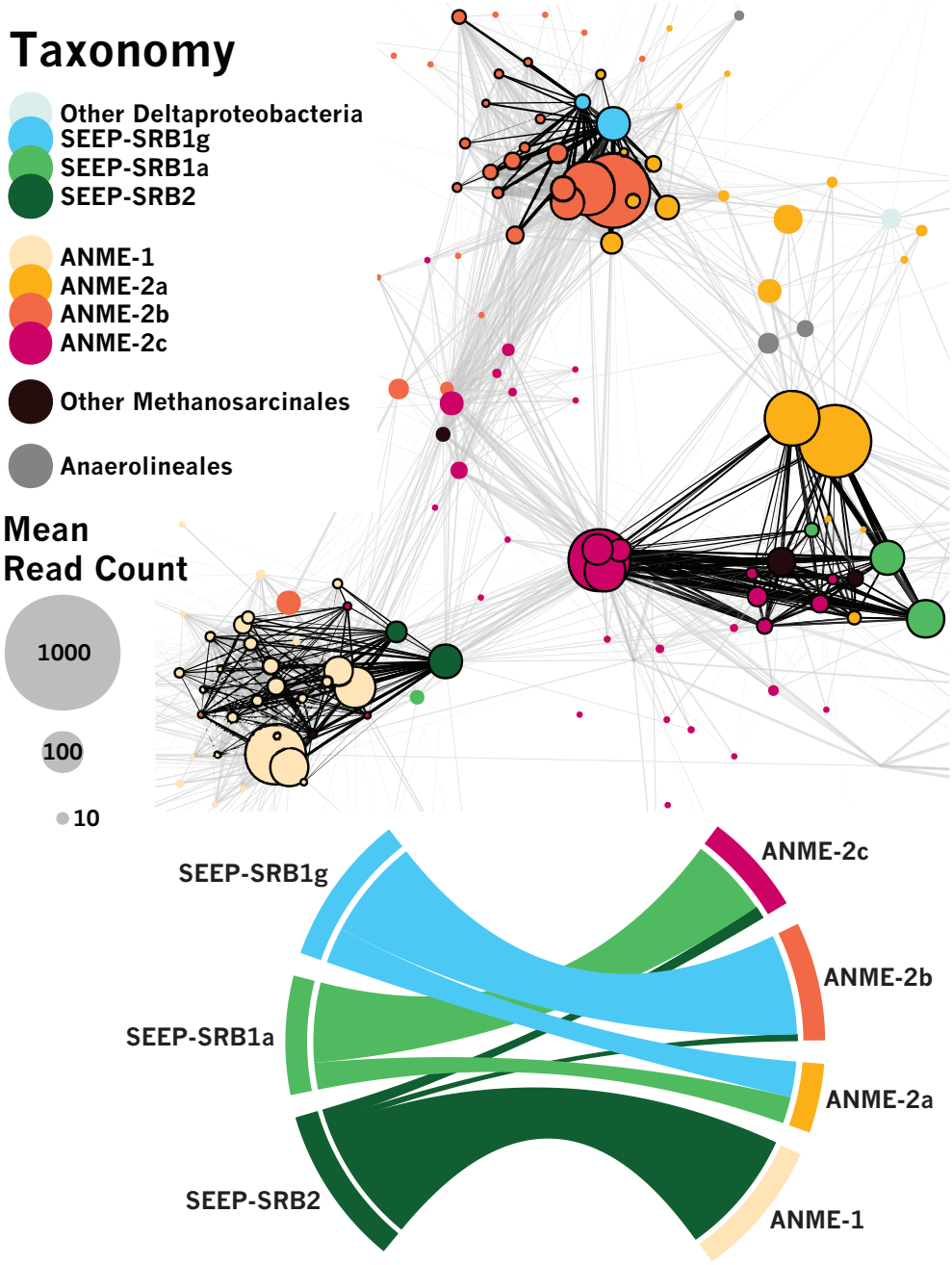

Figure 2. Network analysis of the subset of correlations between OTUs calculated by SparCC [41] that are both significant (*pseudo-p*-values < 0.01, 100 bootstraps) and strong ($\geq 99^{th}$ percentile). Edge length is inversely proportional to correlation strength and is used to visualize the network (top panel) using force-directed methods [78]. Edges are black where they belong to a set of cohesive blocks of nodes [79] and gray otherwise. Chord diagram [80] visualizing ANME-SRB partnership specificity (bottom panel), with band thickness between SRB (left) and ANME (right) proportional to the number of edges between ANME and SRB OTUs within cohesive blocks. Network analysis supports (cf. Fig. 1) previously-undescribed association between ANME-2b and SEEP-SRB1g.

consortia affiliated with SEEP-SRB1g, 89% (8/9) had ANME-2b as the archaeal partner (Fig. 3).

Notably, we found that these SEEP-SRB1g sequences were also highly-similar to published full-length 16S rRNA clone library sequences (e.g. NCBI accession AF354159) from seep sediments where ANME-2b phylotypes were also recovered [21]. A χ^2-test for independence was performed on 16S rRNA OTUs recovered from (39) to test the null hypothesis that the presence of a given SRB taxon in a FACS sort is independent of the type of ANME present in the sort. This test demonstrated that the SRB taxon found in a given sort was dependent on the ANME also present in the sort, $\chi^2 = 30.6$ (*d.f.* = 6, *n* = 30), $p < 0.001$. The pattern of association between ANME and SRB OTUs in individual BONCAT-FACS-sorted ANME-SRB consortia thus corroborated the inference from network analysis that ANME-2b and SEEP-SRB1g OTUs exhibit significant partnership specificity. On the basis of amplicon sequence associations found from the BONCAT-FACS sorting dataset (Oregon and California seeps) as well as those displayed by correlation analysis of amplicons from Costa Rica methane seeps, we designed a set of independent experiments to directly test the hypothesis that ANME-2b form syntrophic partnerships with the previously-undescribed SEEP-SRB1g deltaproteobacteria.

FISH Experiments Show SEEP-SRB1g in Association With ANME-2b

Specific oligonucleotide probes were designed and tested for the SEEP-SRB1g clade (Supp. Fig. 1) and FISH experiments were used to validate the predicted ANME-

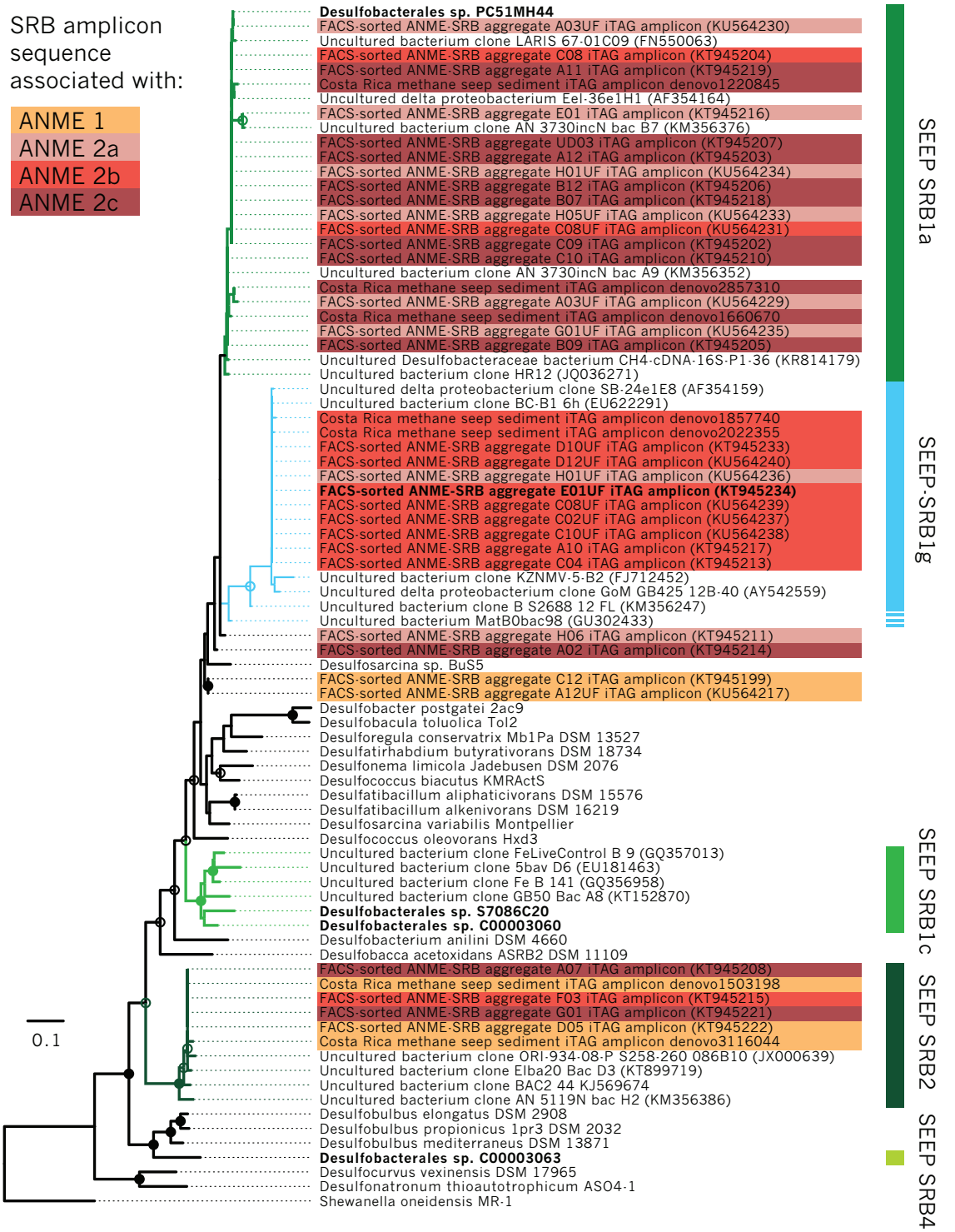
SRB amplicon sequence associated with:
ANME 1
ANME 2a
ANME 2b
ANME 2c
Desulfobacterales sp. PC51MH44
FACS-sorted ANME-SRB aggregate A03UF iTAG amplicon (KU564230)
Uncultured bacterium clone LARIS 67-01C09 (FN550063)
FACS-sorted ANME-SRB aggregate C08 iTAG amplicon (KT945204)
FACS-sorted ANME-SRB aggregate A11 iTAG amplicon (KT945219)
Costa Rica methane seep sediment iTAG amplicon denovo1220845
Uncultured delta proteobacterium Eel-36e1H1 (AF354164)
FACS-sorted ANME-SRB aggregate E01 iTAG amplicon (KT945216)
Uncultured bacterium clone AN 3730incN bac B7 (KM356376)
FACS-sorted ANME-SRB aggregate UD03 iTAG amplicon (KT945207)
FACS-sorted ANME-SRB aggregate A12 iTAG amplicon (KT945203)
FACS-sorted ANME-SRB aggregate H01UF iTAG amplicon (KU564234)
FACS-sorted ANME-SRB aggregate B12 iTAG amplicon (KT945206)
FACS-sorted ANME-SRB aggregate B07 iTAG amplicon (KT945218)
FACS-sorted ANME-SRB aggregate H05UF iTAG amplicon (KU564233)
FACS-sorted ANME-SRB aggregate C08UF iTAG amplicon (KU564231)
FACS-sorted ANME-SRB aggregate C09 iTAG amplicon (KT945202)
FACS-sorted ANME-SRB aggregate C10 iTAG amplicon (KT945210)
Uncultured bacterium clone AN 3730incN bac A9 (KM356352)
Costa Rica methane seep sediment iTAG amplicon denovo2857310
FACS-sorted ANME-SRB aggregate A03UF iTAG amplicon (KU564229)
Costa Rica methane seep sediment iTAG amplicon denovo1660670
FACS-sorted ANME-SRB aggregate G01UF iTAG amplicon (KU564235)
FACS-sorted ANME-SRB aggregate B09 iTAG amplicon (KT945205)
Uncultured Desulfobacteraceae bacterium CH4-cDNA-16S-P1-36 (KR814179)
Uncultured bacterium clone HR12 (JQ036271)
Uncultured delta proteobacterium clone SB-24e1E8 (AF354159)
Uncultured bacterium clone BC-B1 6h (EU622291)
Costa Rica methane seep sediment iTAG amplicon denovo1857740
Costa Rica methane seep sediment iTAG amplicon denovo2022355
FACS-sorted ANME-SRB aggregate D10UF iTAG amplicon (KT945233)
FACS-sorted ANME-SRB aggregate D12UF iTAG amplicon (KU564240)
FACS-sorted ANME-SRB aggregate H01UF iTAG amplicon (KU564236)
FACS-sorted ANME-SRB aggregate E01UF iTAG amplicon (KT945234)
FACS-sorted ANME-SRB aggregate C08UF iTAG amplicon (KU564239)
FACS-sorted ANME-SRB aggregate C02UF iTAG amplicon (KU564237)
FACS-sorted ANME-SRB aggregate C10UF iTAG amplicon (KU564238)
FACS-sorted ANME-SRB aggregate A10 iTAG amplicon (KT945217)
FACS-sorted ANME-SRB aggregate C04 iTAG amplicon (KT945213)
Uncultured bacterium clone KZNMV-5-B2 (FJ712452)
Uncultured delta proteobacterium clone GoM GB425 12B-40 (AY542559)
Uncultured bacterium clone B S2688 12 FL (KM356247)
Uncultured bacterium MatB0bac98 (GU302433)
FACS-sorted ANME-SRB aggregate H06 iTAG amplicon (KT945211)
FACS-sorted ANME-SRB aggregate A02 iTAG amplicon (KT945214)
Desulfosarcina sp. BuS5
FACS-sorted ANME-SRB aggregate C12 iTAG amplicon (KT945199)
FACS-sorted ANME-SRB aggregate A12UF iTAG amplicon (KU564217)
Desulfobacter postgatei 2ac9
Desulfobacula toluolica Tol2
Desulforegula conservatrix Mb1Pa DSM 13527
Desulfatirhabdium butyrativorans DSM 18734
Desulfonema limicola Jadebusen DSM 2076
Desulfococcus biacutus KMRActS
Desulfatibacillum aliphaticivorans DSM 15576
Desulfatibacillum alkenivorans DSM 16219
Desulfosarcina variabilis Montpellier
Desulfococcus oleovorans Hxd3
Uncultured bacterium clone FeLiveControl B 9 (GQ357013)
Uncultured bacterium clone 5bav D6 (EU181463)
Uncultured bacterium clone Fe B 141 (GQ356958)
Uncultured bacterium clone GB50 Bac A8 (KT152870)
Desulfobacterales sp. S7086C20
Desulfobacterales sp. C00003060
Desulfobacterium anilini DSM 4660
Desulfobacca acetoxidans ASRB2 DSM 11109
FACS-sorted ANME-SRB aggregate A07 iTAG amplicon (KT945208)
Costa Rica methane seep sediment iTAG amplicon denovo1503198
FACS-sorted ANME-SRB aggregate F03 iTAG amplicon (KT945215)
FACS-sorted ANME-SRB aggregate G01 iTAG amplicon (KT945221)
FACS-sorted ANME-SRB aggregate D05 iTAG amplicon (KT945222)
Costa Rica methane seep sediment iTAG amplicon denovo3116044
Uncultured bacterium clone ORI-934-08-P S258-260 086B10 (JX000639)
Uncultured bacterium clone Elba20 Bac D3 (KT899719)
Uncultured bacterium clone BAC2 44 KJ569674
Uncultured bacterium clone AN 5119N bac H2 (KM356386)
Desulfobulbus elongatus DSM 2908
Desulfobulbus propionicus 1pr3 DSM 2032
Desulfobulbus mediterraneus DSM 13871
Desulfobacterales sp. C00003063
Desulfocurvus vexinensis DSM 17965
Desulfonatronum thioautotrophicum ASO4-1
Shewanella oneidensis MR-1
0.1
SEEP SRB1a
SEEP-SRB1g
SEEP SRB1c
SEEP SRB2
SEEP SRB4

Figure 3. 16S rRNA phylogenetic tree of methane seep Deltaproteobacteria and other lineages, including sequences from recovered metagenome-assembled genomes (MAGs) [14], 16S rRNA amplicon sequences from BONCAT-FACS-sorted ANME-SRB consortia [39], 16S rRNA amplicon sequences from this study, and previously published full-length 16S rRNA sequences from clone libraries. Maximum likelihood phylogeny was inferred using 100 bootstraps with >70% or 90% bootstrap support of internal nodes indicated with open or closed circles, respectively. Taxa associated with SRB 16S rRNA amplicon sequences were determined from data in Hatzenpichler, et al. 2016 [39] (BONCAT-FACS-sorted ANME-SRB consortia), and by network analysis of 16S rRNA amplicon sequences from methane seep samples (cf. Fig. 2). Taxa in bold represent 16S rRNA sequences from MAG bins acquired from methane seep sediments [14] or from BONCAT-FACS-sorted ANME-SRB consortia, including associated 16S rRNA amplicon sequences [39]. The SEEP-SRB1a and -1g clades are operationally defined here by the extent of matches to the respective 16S rRNA FISH probes Seep1a-1441 and Seep1g-1443. Given the low bootstrap values for divergent sequences, the true extent of the SEEP-SRB1g clade is unclear, indicated by the dashed line (cf. Supp. Fig. 6).

FISH Experiments Show SEEP-SRB1g in Association With ANME-2b

Specific oligonucleotide probes were designed and tested for the SEEP-SRB1g clade (Supp. Fig. 1) and FISH experiments were used to validate the predicted ANME-2b—SEEP-SRB1g partnership. Simultaneous application of FISH probes targeting SEEP-SRB1a, the dominant deltaproteobacterial partner of ANME (Seep1a-1441 [15]), the newly designed SEEP-SRB1g probe (Seep1g-1443, this work), and a probe targeting ANME-2b (ANME-2b-729 [39]) demonstrated that ANME-2b form consortia with SEEP-SRB1g, appearing as large multicellular consortia in seep sediment samples from different localities at Costa Rica methane seep sites (see Supplemental Materials and Methods for site details) that also contain ANME-2a (Fig. 4b, Supp. Fig. 3) and ANME-2c (Fig. 4f, Supp. Fig. 4). Results from FISH analysis of >83 consortia from 2 subsamples of seep sediments showed that ANME-2b was not observed in association with SEEP-SRB1a (Figs. 4a, 4e), and SEEP-SRB1g was not observed in association with ANME-2a (Fig. 4d) or ANME-2c (Fig.

4h) when FISH probes ANME-2a-828 or ANME-2c-760 [20] were substituted for ANME-2b-729. Instead, SEEP-SRB1a was found in consortia with ANME-2a (Fig. 4c) and ANME-2c (Fig. 4g), consistent with previous reports [15]; (Supp. Fig. 5).

Genomic Potential for N_2 Fixation in Sulfate-reducing SEEP-SRB1g Deltaproteobacteria

Given the importance of diazotrophy in the functioning of ANME-SRB syntrophy, we screened metagenome-assembled genome bins (MAGs) of SEEP-SRB1g for the presence of the nitrogenase operon. A genome tree constructed from previously published MAGs from Hydrate Ridge and Santa Monica Basin [14, 39] revealed that two closely related MAGs (Desulfobacterales sp. C00003104, and C00003106) originally classified as belonging to the Seep-SRB1c clade [14] possessed the nitrogenase operon (Fig. 5). These MAGs did not contain 16S rRNA sequences, precluding 16S rRNA-based taxonomic identification. A more detailed look at these reconstructed genomes revealed that the nitrogenase along with a suite of other genes were unique to this subclade and missing in other SEEP-SRB1c MAGs [14], suggesting they may represent a distinct lineage. In an effort to connect these nitrogenase containing SRB MAG's with representative 16S rRNA sequences, we examined mini-metagenome data from individual BONCAT-FACS sorted ANME-SRB consortia which each contained 16S rRNA gene sequences for the ANME and bacterial partner [39]. A genome tree containing deltaproteobacterial MAGs [14] and reconstructed deltaproteobacterial genomes from the BONCAT-FACS sorts [39] revealed one SRB genome from a FACS-sorted consortium (Desulfobacterales sp.

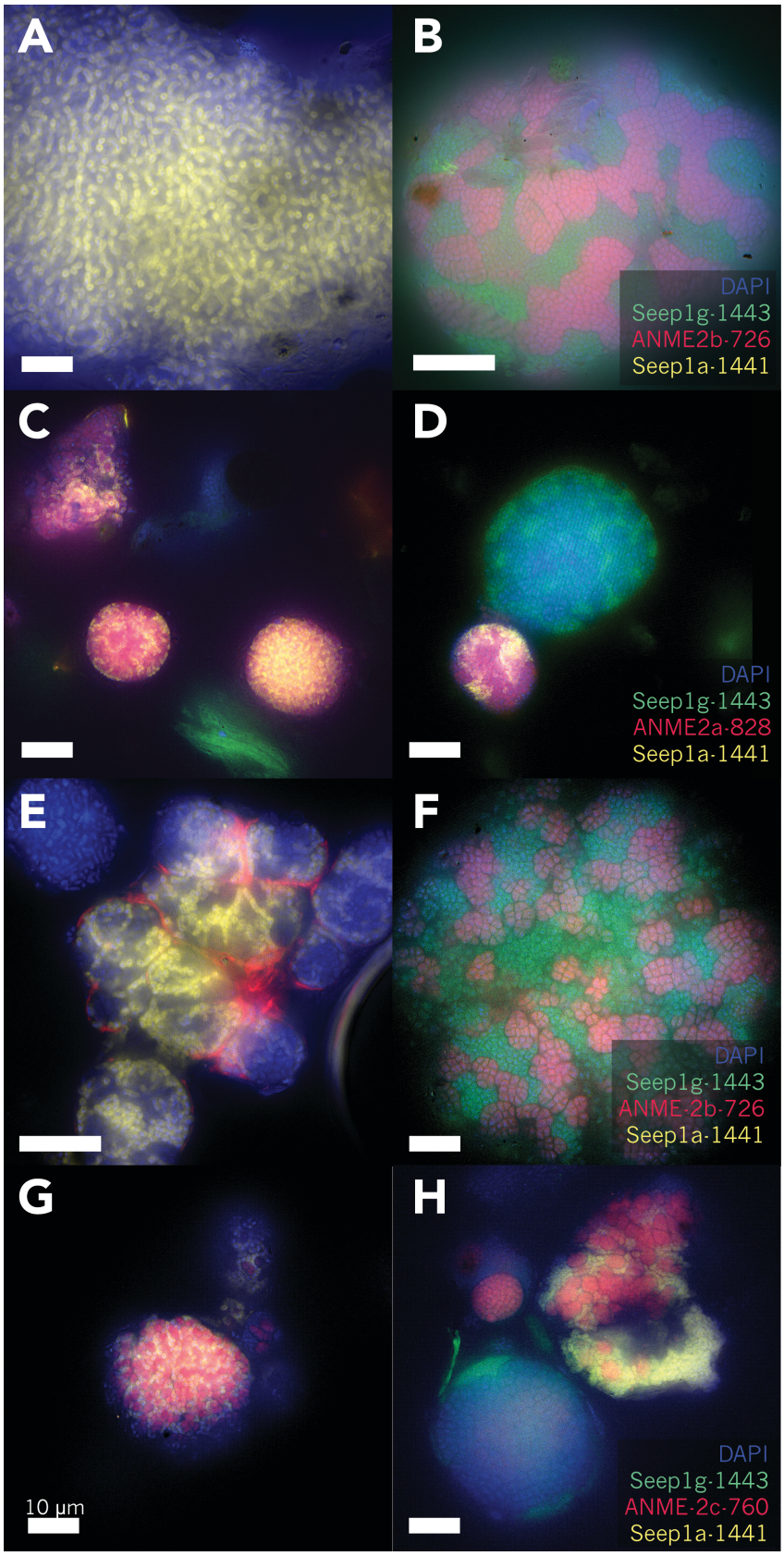
A
B
DAPI
Seep1g-1443
ANME2b-726
Seep1a-1441
C
D
DAPI
Seep1g-1443
ANME2a-828
Seep1a-1441
E
F
DAPI
Seep1g-1443
ANME-2b-726
Seep1a-1441
G
10 µm
H
DAPI
Seep1g-1443
ANME-2c-760
Seep1a-1441

Figure 4. FISH data targeting ANME-SRB consortia in seep sediment samples using oligonucleotide probes targeting ANME-2b (ANME-2b-726) and ANME-2a (ANME-2a-828); (in red), a SEEP-SRB1a (Seep1a-1443) probe (in yellow) and a newly-designed probe (Seep1g-1443) targeting the SEEP-SRB1g clade (in green) demonstrating physical association between ANME-2b and SEEP-SRB1g. DAPI counterstain is shown in blue. Seep sediments harboring ANME-2a and ANME-2b (A-D) host ANME-SRB consortia that are composed of either ANME-2a–SEEP-SRB1a or ANME-2b–SEEP-SRB1g (B, C, D). FISH analysis of ANME-SRB consortia from sediments rich in ANME-2c and ANME-2b (E-H) documented ANME-SRB consisting of ANME-2b–SEEP-SRB1g or ANME-2c–SEEP-SRB1a partnerships (F, G, H); ANME-SRB consortia positively hybridized with the SEEP-SRB1g or SEEP-SRB1a probes were not observed to hybridize with probes targeting ANME-2c (H) or ANME-2b (E), respectively. In all panels, the scale bar is 10 μm.

CONS3730E01UFb1, IMG Genome ID 3300009064) was closely related to the two putative SEEP-SRB1c MAGs containing the nitrogenase operon (Fig. 5). The 16S rRNA amplicon sequence (NCBI accession KT945234) associated with this Desulfobacterales sp. CONS3730E01UFb1 genome was used to construct a 16S rRNA phylogeny and confirmed to cluster within the SEEP-SRB1g clade, providing a link between the 16S rRNA and associated nitrogenase sequences in this lineage (Fig. 3). Given that Desulfobacterales sp. CONS3730E01UFb1, C00003104, and C00003106 genomes appeared highly similar on the genome tree (Fig. 5), we reassigned the previously published Desulfobacterales sp. C00003104 and C00003106 MAGs to the SEEP-SRB1g. Notably, the other 16S rRNA amplicon sequence sampled from the sorted consortium CONS3730E01UF (NCBI accession KT945229) was assigned to ANME-2b [39]. The detection of a *nifHDK* operon

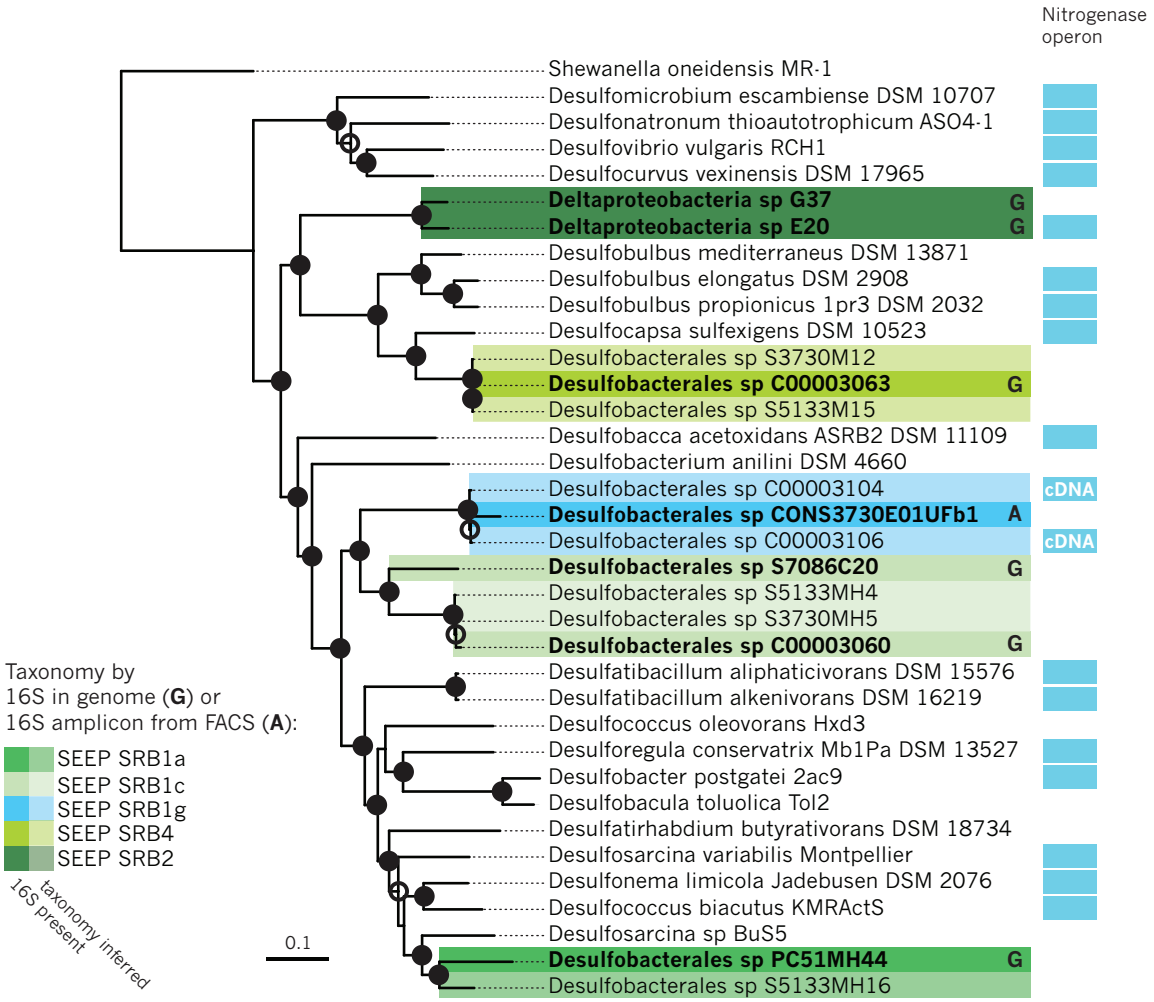

Figure 5. Genome tree of ANME-associated Deltaproteobacteria and related organisms inferred from maximum likelihood methods. Bootstrap support for internal nodes was determined using 100 bootstraps and depicted on the tree as open (>70% bootstrap support) or closed (>90%) circles. Genome bins containing a 16S rRNA gene or an associated 16S rRNA amplicon sequence are highlighted in bold and with a color corresponding to 16S taxonomy assignment. Inferred taxonomy of genome bins closely related to bins containing 16S rRNA sequences are highlighted in a lighter shade. Genome bins containing the nitrogenase operon are annotated with a blue bar. *nifH* sequences found to be expressed in methane seep sediments in cDNA clone libraries [8] are annotated by "cDNA". As noted in the text, a search of unpublished SEEP-SRB1a MAGs revealed the presence of highly-expressed [8] *nif*H sequences in several unpublished bins (Supp. Fig. 7).

involved in nitrogen fixation (Fig. 5) in the SEEP-SRB1g MAGs was of particular interest as diazotrophy had not previously been an area of focus in the analyses of ANME-associated SRB genomes. A re-analysis of published *nifH* cDNA sequences from methane seep sediments revealed sequences that were nearly identical to the SEEP-SRB1g *nifH* (NCBI accession KR020451-KR020457, [8]) suggesting active transcription of SEEP-SRB1g *nifH* under *in situ* conditions (Fig. 6, Supp. File 1). An analysis of published methane seep metaproteomic data [14] also indicated active translation of nitrogenase by SEEP-SRB1g, corroborating evidence from cDNA libraries [8]. Additionally, other *nifH* cDNA sequences in this study were found to be identical to nitrogenase sequences occurring in 18 SEEP-SRB1a unpublished metagenome bins (Supp. Fig. 7) demonstrating that at least some of the syntrophic SEEP-SRB1a SRB partners also possess and actively express *nifH*.

nifH Expression in ANME-2b–SEEP-1g Consortia Visualized by HCR-FISH

The dominant role of ANME-2 in nitrogen fixation reported in previous studies [8–10] motivated our examination of whether the sulfate-reducing SEEP-SRB1g partners of ANME-2b were also involved in diazotrophy, either in concert with the ANME-2b partner, or perhaps as the sole diazotroph in this AOM partnership. Using the *nifH* sequences from SEEP-SRB1g, we worked with Molecular Technologies to design a mRNA-targeted probe set to use in whole-cell hybridization chain reaction FISH (HCR-FISH) assays (Supp.

Figure 6. Phylogeny of *nifH* sequences extracted from *nifH* cDNA (red text) and DNA clone libraries [8], from genome bins acquired from methane seep sediments [14], and from other Deltaproteobacteria genomes using a tblastn search with chlorophyllide reductase BchX (WP011566468) as a query. This BchX sequence along with another BchX (WP012180173) were used as an outgroup to root the tree. Phylogeny was inferred by maximum likelihood methods using 100 bootstraps; bootstrap support of internal nodes is illustrated as open or closed circles, indicating >70% or >90% bootstrap support, respectively. *nifH* recovered from the BONCAT-FACS-sorted genome CONS3730E01UFb1, a bin with an accompanying 16S rRNA amplicon sequence placing it within the SEEP-SRB1g, is highlighted in teal. *nifH* groups (*sensu* Raymond et al. [97]) were assigned by comparison with Dekas, et al. 2016, and are annotated either by group number or abbreviated as follows: MSL, Methanosarcina-like; MSG, Methane Seep Group.

Table 2). HCR-FISH allows for signal amplification and improved signal-to-noise ratio compared to FISH, and has been used in single cell mRNA expression studies in select microbial studies [81–83]. Prior to this study, however, HCR-FISH had not been applied to visualize gene expression in ANME-SRB consortia from methane seep sediments. In the context of experiments with sediment-hosted ANME-SRB consortia, HCR-FISH provided adequate amplification of the signal to detect expressed mRNA above the inherent background autofluorescence in sediments. Using our HCR-FISH probes targeting SEEP-SRB1g *nifH* mRNA together with the standard 16S rRNA targeted oligonucleotide FISH probes Seep1g-1443 (targeting SEEP-SRB1g) and ANME-2b-729 (targeting ANME-2b), we successfully imaged *nifH* mRNA transcripts by SEEP-SRB1g cells in ANME-2b—SEEP-SRB1g consortia in a sediment AOM microcosm experiment (Fig. 7) in which sediments were incubated in filtered deep-sea water sampled near the seep site.

Concentrations of fixed nitrogen species in our incubations were not measured at t=0, but based on independent measurements of porewater ammonium from methane seeps ($[NH_4^+]$ = 24 – 307 μM [10]), we expect some amount (~ μM) of fixed nitrogen was carried over at the start of our microcosm experiments. We measured dissolved ammonium in the $^{15}N_2$ incubations (n = 2) approximately 3 months prior to consortia sampling for nanoSIMS (111-134 μM), and at the time of sampling for nanoSIMS (110 μM to below detection). The strongest HCR-FISH *nifH* fluorescence signal in this sample was observed to in cells identified as the SEEP-SRB1g bacterial partner by 16S rRNA FISH (n = 5), with weaker *nifH* fluorescence observed in ANME-2b stained cells, but not in co-occurring ANME-2a or -2c consortia. Negative control experiments for the HCR-FISH reaction

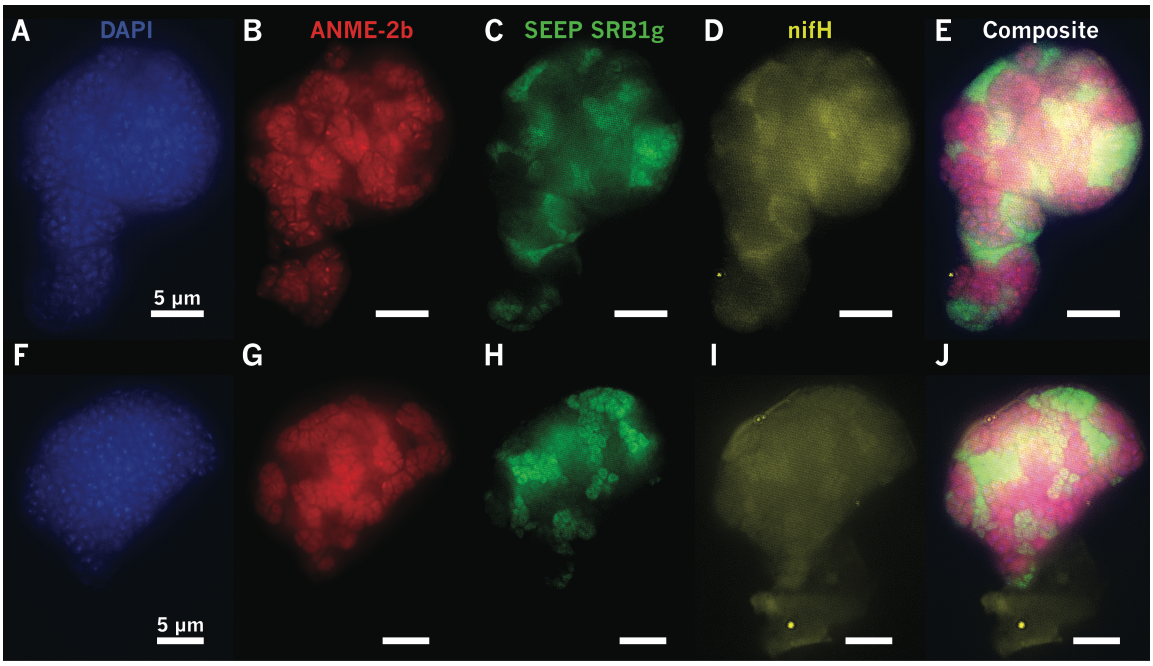

Figure 7. HCR-FISH assays show in situ expression of *nifH* in SEEP-SRB1g in association with ANME-2b in methane seep sediment incubations, scale bars in all panels are 5 µm. ANME-2b (B, G) and SEEP-SRB1g (C, H) cells labeled with FISH probes ANME-2b-729 (in red, [39]) and newly-designed Seep1g-1443 (in green) with DAPI as the DNA counterstain (A,F). HCR-FISH targeting SEEP-SRB1g *nifH* mRNA (in yellow; Supp. Table 2) demonstrated active expression of nifH transcripts localized to SEEP-SRB1g cells (D, I), supporting the hypothesis of diazotrophy by partner SRB. Control experiments omitting either HCR-FISH initiator probes targeting SEEP-SRB1g *nifH* mRNA or HCR-FISH amplifiers (Supp. Fig. 8) and colocalization analysis of these control experiments (Supp. Figs. 9, 10) excluded the possibility that positive signal for SEEP-SRB1g *nifH* was due to bleed-through of fluorescence from Alexa488 bound to the probe targeting SEEP-SRB1g 16S rRNA.

were also performed. Here, SEEP-SRB1g *nifH* initiator probes were added to the assay, but the fluorescent amplifier hairpins were excluded. In this case, there was no fluorescent signal in either the FISH-stained bacteria or archaeal partners in ANME-2b aggregates indicating that the detected *nifH* HCR-FISH signal (Fig. 7) was not due to native autofluorescence in Seep-SRB1g (Supp. Fig. 8f-j), nor due to bleed-through of fluorescence from the SEEP-SRB1g 16S rRNA probe. In a second negative control experiment, we excluded the *nifH* initiator probes that bind the mRNA but added the

fluorescent amplifier hairpins. This control showed minimal non-specific binding of the hairpins that could be readily differentiated from the positively-hybridized SEEP-SRB1g (Supp. Fig. 8a-e). Occasionally, highly localized, small spots of fluorescence from the hairpins was observed (Supp. Fig 8d) but these spots were primarily localized outside of aggregates and did not align with either bacteria or archaea in consortia (e.g. Fig. 8d). Colocalization image analysis of the control experiments revealed low correlation between FITC (SEEP-SRB1g 16S) or cy3 (ANME-2b 16S) channels with signal in the cy5 (SEEP-SRB1g *nifH*) channel (Supp. Figs. 9, 10). In contrast, a strong correlation was observed between the FITC and cy5 channels in the HCR-FISH experiment using initiator and amplifiers to detect SEEP-SRB1g *nifH* mRNA expression, producing a linear correlation in a scatterplot of pixel intensities (Supp. Fig. 11). Some correlation was also observed between the 16S rRNA ANME-2b signal (cy3) and the HCR-FISH SEEP-SRB1g *nifH* (cy5) channels, indicating that there may be a degree of non-specific binding of the SEEP-SRB1g *nifH* initiator probes to ANME-2b *nifH* mRNA, perhaps due to the conserved nature of nitrogenase sequences. Confirmation of single consortia *nifH* expression using HCR-FISH corroborated community-level evidence from cDNA libraries (Fig. 6) that SEEP-SRB1g actively express *nifH*, suggesting their potential involvement in diazotrophy in AOM consortia.

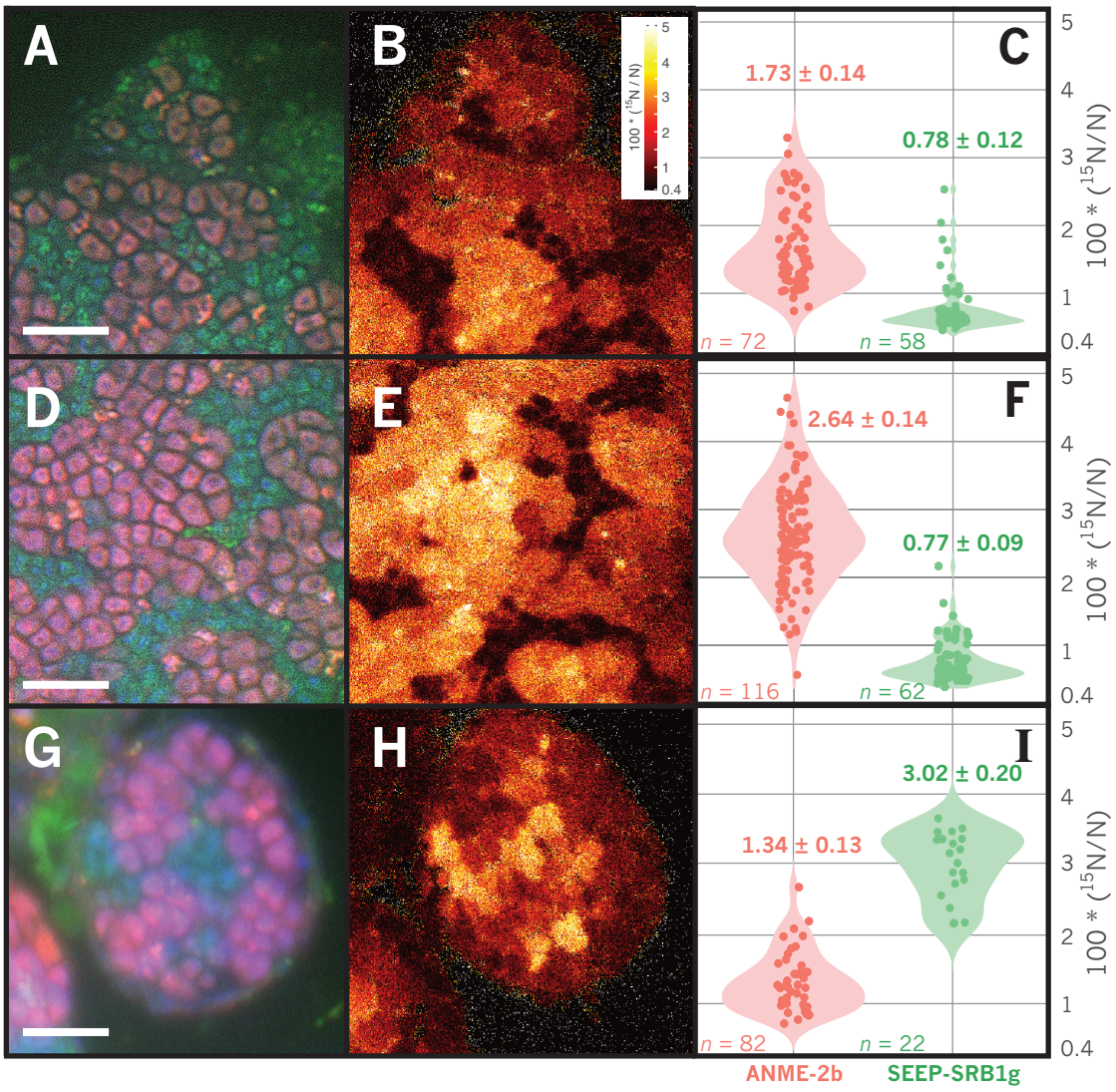

Figure 8. Correlated FISH-nanoSIMS imaging of representative ANME-2b–SEEP-SRB1g consortia demonstrating active diazotrophy by ANME-2b (B, E) and SEEP-SRB1g (H) cells through ^{15}N incorporation from $^{15}N_2$. FISH images of ANME-2b (pink) and SEEP-SRB1g (green) are shown in panels A, D, G and corresponding nanoSIMS 15N atom percent values are shown in panels B, E, and H. Scale bar is 5 µm in panels A, D, G; raster size in panels B, E, and H is 20 µm^2. Violin plots (C, F, I) of ^{15}N fractional abundance for each type of ROI, representing single ANME-2b or SEEP-SRB1g cells. The number of ROIs measured is indicated by n in each panel. Diazotrophic activity in ANME-2b cells appears to be correlated with spatial structure, evidenced by increasing 15N enrichment in cells located within consortia interiors (E, F). SEEP-SRB1g cells are also observed to incorporate ^{15}N from $^{15}N_2$, and appear to be the dominant diazotroph in the consortium shown in panels G, H, and I, with cellular ^{15}N enrichment in SEEP-SRB1g cells greater than that of the paired ANME-2b partner. Abscissa minima set to natural abundance of ^{15}N (0.36%).

$^{15}N_2$ Stable Isotope Probing and FISH-nanoSIMS Experiments Confirm Involvement of SEEP-SRB1g in N_2-fixation in Addition to ANME-2b

To test for active diazotrophy by ANME-2b-associated SEEP-SRB1g, we prepared $^{15}N_2$ stable isotope probing incubations of methane seep sediments recovered from a Costa Rica methane seep. These nitrogen-poor sediment incubations were amended with unlabeled methane and $^{15}N_2$ and maintained in the laboratory at 10ºC under conditions supporting active sulfate-coupled AOM (see Supplemental Materials and Methods). Sediments with abundant ANME-SRB consortia were sampled after 9 months of incubation and consortia were embedded, sectioned, and analyzed by FISH-nanoSIMS to measure single cell ^{15}N enrichment associated with diazotrophy within ANME-2b—SEEP-SRB1g consortia. Representative ANME-2b—SEEP-SRB1g consortia (n = 4) were analyzed by FISH-nanoSIMS and shown to be significantly (~10x) enriched in ^{15}N relative to natural abundance values (0.36%; Fig. 8). Among the consortia analyzed, the ^{15}N fractional abundance in ANME-2b cells were often higher than that measured in SEEP-SRB1g, with ANME-2b cells on the exterior of an exceptionally large consortium (Fig. 8b-c) featuring ^{15}N fractional abundance of 1.73% ± 0.14 (number of ROIs, n = 72), significantly enriched relative to that measured in SEEP-SRB1g cells in the exterior, 0.77% ± 0.09 (n = 58). In this limited dataset, ANME-2b were observed to fix more nitrogen than their SEEP-SRB1g partners, consistent with previous reports from ANME-2–DSS consortia [8–11]. Notably, however, in one of the 4 ANME-2b—SEEP-SRB1g consortia analyzed, the SEEP-SRB1g cells were more enriched in ^{15}N relative to the associated ANME-2b cells, with ANME-2b cells containing 1.34% ± 0.13 ^{15}N (n = 82) and SEEP-

SRB1g containing 3.02% ± 0.20 ^{15}N (n = 22, Fig. 8i), suggesting that under certain circumstances the sulfate-reducing partner can fix more nitrogen than their ANME-2b partners. Additionally, a gradient in ^{15}N enrichment in a large (~250 µm diameter) ANME-2b consortium was observed in which clusters of ANME-2b cells associated with the interior of the consortia, ~ 10 µm distance from the external environment, were significantly more enriched in ^{15}N (Fig. 8f, 2.64% ± 0.14; n = 116) relative to ANME-2b clusters near the aggregate exterior (Fig. 8c, 1.73% ± 0.14; n = 72). In this consortium, no equivalent ^{15}N enrichment gradient was observed in the SEEP-SRB1g partner, with SEEP-SRB1g cells in the exterior containing ^{15}N atomic percent values of 0.77% ± 0.09 (n = 58) compared with those measured on the interior, 0.78% ± 0.09 (n = 62).

DISCUSSION

The symbiotic relationship between ANME and associated SRB, originally described by Hinrichs [17], Boetius [4], and Orphan [21], has been the focus of extensive study using FISH [5, 7, 13, 15, 25, 26, 29, 34, 35], magneto-FISH [29, 37, 38], and BONCAT-FACS [39], culture-independent techniques that have provided insight into the diversity of partnerships between ANME and SRB. While these fluorescence-based approaches offer direct confirmation of physical association between taxa and are thus useful for characterizing partnership specificity, they are often constrained by sample size and are comparatively lower-throughput than sequencing-based approaches. Next-generation Illumina sequencing of 16S rRNA amplicons offers advantages in terms of throughput and has become a standard approach in molecular microbial ecology.

Correlation analysis performed on these large 16S rRNA amplicon datasets can be an effective hypothesis-generating tool for identifying microbial interactions and symbioses in the environment [77], but most studies employing this approach stop short of validating predictions. As correlation analysis of 16S rRNA amplicon data can generate false positives due to the compositional nature of 16S rRNA amplicon libraries [41, 42, 84], specific correlations predicted between taxa should be corroborated when possible by independent approaches.

In this study, we used correlation analysis of 16S rRNA amplicon sequences from 310 methane seep sediment and carbonate samples on the Costa Rican Margin to identify well-supported (pseudo-*p*-values < 0.01) positive correlations between specific OTUs commonly observed in seep ecosystems. Our analysis identified strong correlations between syntrophic partners previously described in the literature, such as that between members of the SEEP-SRB1a and ANME-2a/ANME-2c clades and between ANME-1 and SEEP-SRB2 [5, 7, 13, 15, 25, 26, 29, 34, 35], and uncovered previously unrecognized relationships between members of the ANME-2b clade and OTUs affiliated with an uncultured Desulfobacterales lineage, SEEP-SRB1g (Figs. 1-3). We then validated the specificity of the ANME-2b and SEEP-SRB1g association by FISH (Fig. 4).

The specificity of the association between ANME-2b and SEEP-SRB1g appeared to extend beyond Costa Rica methane seeps and is likely a widespread phenomenon, as this association was also recovered from BONCAT-FACS datasets originating from methane seep sites off of Oregon, USA (Hydrate Ridge) and from the Santa Monica Basin, California, USA. Our observations of ANME-2b—SEEP-SRB1g partnership specificity in

numerous samples is consistent with published observations of other ANME-SRB partnerships, where consortia composed of specific ANME and SRB clades have been observed in seep ecosystems worldwide [15]. Notably, the syntrophic relationship between ANME-2b and SEEP-SRB1g appears to be specific (Fig. 2), as FISH observations from sediment samples from multiple Costa Rica methane seep sites (Supp. Table 1) did not show ANME-2b in consortia with other bacteria besides the SEEP-SRB1g (Fig. 4, Supp. Fig. 5). In contrast, the Desulfobacteraceae SEEP-SRB1a group in these same experiments were found to form associations with both ANME-2a and ANME-2c, indicating that this SRB syntrophic lineage has the capacity to establish partnerships with members of multiple clades of ANME. Members of the diverse ANME-2c family also appeared to display partnership promiscuity in our network analysis, with positive correlations observed between ANME-2c OTUs and both SEEP-SRB1a and SEEP-SRB2 OTUs (Fig. 2). This predicted partnership flexibility in the network analysis was corroborated by our FISH observations of ANME-2c—SEEP-SRB1a consortia (Fig. 4) and additionally by prior reports of ANME-2c in association with SEEP-SRB2 from Guaymas Basin sediments [13]. Taken together, these data suggest that partnership specificity varies among different clades of ANME and SRB, which may be the result of physiological differences and/or molecular compatibility, signal exchange, and recognition among distinct ANME and SRB that shape the degree of specificity between particular ANME and SRB partners, as has been observed in other symbiotic associations [85–87]. The degree of promiscuity or specificity for a given syntrophic partner may be influenced by the co-evolutionary history of each partnership, with some ANME or SRB physiologies requiring obligate association with specific partners. A more detailed examination of the genomes of ANME-2b and SEEP-

SRB1g alongside targeted ecophysiological studies may provide clues to the underlying mechanism(s) driving specificity within this ANME-SRB consortia. Comparative investigations with ANME-2a and -2c subgroups may similarly uncover strategies enabling broader partner association, perhaps with preference for a SRB partner shaped by environmental variables rather than through pre-existing co-evolutionary relationships.

An initial genomic screening of SEEP-SRB1g offered some insight into the distinct metabolic capabilities of the SRB partner which may contribute to the association with ANME-2b. The observation of a complete nitrogenase operon in 3 different SEEP-SRB1g genome bins suggested the potential for nitrogen fixation, a phenotype not previously described for ANME-associated SRB (Fig. 5). While previous work on nitrogen utilization by ANME-SRB consortia has focused on diazotrophy performed by ANME-2 [8–10], environmental surveys of seep sediments have noted active expression of nitrogenase typically associated with Deltaproteobacteria [8, 88]. In these studies, the specific microbial taxa associated with the expressed nitrogenase in methane seep sediments were not identified, and based on this community-level analysis, it was not clear whether these putative deltaproteobacterial diazotrophs were involved in AOM syntrophy. A phylogenetic comparison of the *nifH* sequences found in SEEP-SRB1g MAGs with sequences of the expressed deltaproteobacterial-affiliated (i.e. Group III) *nifH* transcripts reported in seep sediments [8] allowed us to link the SEEP-SRB1g syntrophs with a clade of Group III nifH sequences that were among the most highly expressed in situ (Figs. 5-6). FISH-nanoSIMS performed on $^{15}N_2$ SIP incubations confirmed the potential for diazotrophic activity in SEEP-SRB1g. Of the 4 ANME-2b—SEEP-SRB1g consortia

analyzed by FISH-nanoSIMS, one showed significantly more ^{15}N enrichment in the SEEP-SRB1g partner relative to that observed in ANME-2b, while the other 3 displayed higher ^{15}N enrichment in ANME-2b cells (Fig. 8). Additional experiments are required to understand the ecological or environmental controls on N_2 fixation by ANME-2b and SEEP SRB1g; however, our results linking the nitrogenase operon in SEEP-SRB1g MAGs to highly expressed *nifH* transcripts *in situ*, evidence of nifH expression at single cell level by HCR-FISH, and demonstration of $^{15}N_2$ assimilation by FISH-nanoSIMS, all support a role for the SEEP SRB1g in nitrogen fixation as part of methane-oxidizing ANME-2b consortia. Furthermore, the FISH-nanoSIMS ^{15}N enrichment patterns within these consortia are suggestive of partner-specific variation in N_2 fixation either ANME-2b or SEEP-SRB1g, where one partner–ANME-2b or SEEP-SRB1g–fixes nitrogen in excess of the other. We also must consider the fact that the nanoSIMS measures total ^{15}N enrichment in cellular biomass, and differences observed ^{15}N enrichment between cells can also arise from variation in overall anabolic activity [5], and not exclusively from diazotrophic growth per se. Nevertheless, previous FISH-nanoSIMS data examining ^{15}N incorporation from $^{15}NH_4^+$ as a general proxy for anabolic activity revealed that SRB partners to ANME-2b tend to incorporate more ^{15}N from supplied ammonium relative to their methanotrophic partners [5], a pattern opposite to that observed in the majority of consortia incubated under a $^{15}N_2$ atmosphere. In the light of this previous work, we interpret our nanoSIMS results as indicating that factors beyond taxon-specific differences in nitrogen demand or anabolic activity determine which partner is most diazotrophically active in AOM consortia. Additionally, the observation of nitrogenase in the reconstructed genomes of members of the SEEP-SRB1a clade, consisting of the dominant syntrophic SRB partner (Supp. Fig. 7),

highlights the possibility that nitrogen fixation may extend to other syntrophic bacterial partners as well and merits further investigation. Re-examination of nitrogen fixation in these partnerships with new FISH probes and nanoSIMS analysis at single-cell resolution will further illuminate the full diversity of diazotrophic activity among ANME-SRB consortia and the associated environmental/ physiological controls.

The factors responsible for determining which partner becomes the most diazotrophically active in ANME-2b—SEEP-SRB1g consortia requires in depth study, but our preliminary data suggest this may be influenced in part by the relative position of ANME-2b or SEEP-SRB1g cells, particularly within large (>50 μm) ANME-2b—SEEP-SRB1g consortia. Previous studies of nitrogen fixation in ANME-SRB consortia found no correlation between consortia size and diazotrophic activity in consortia with diameters < 10 μm [10], but larger consortia such as those presented here have not been examined at single-cell resolution. Additionally, consortia with the morphology observed here, in which ANME-2b cells form multiple sarcinal clusters surrounded by SEEP-SRB1g (Figs. 4b, 8), have not been the specific focus of nanoSIMS analysis but appear to be the common morphotype among ANME-2b—SEEP-SRB1g consortia [31]. The frequency with which this morphotype is observed in ANME-2b—SEEP-SRB1g consortia may be related to the underlying physiology of this specific partnership, which, like other ANME-2 consortia, are assumed to be interacting syntrophically through direct interspecies electron transfer [5]. NanoSIMS analysis of a particularly large ANME-2b—SEEP-SRB1g consortium (~200 μm) with this characteristic morphology (Fig. 8a-f) revealed a gradient in diazotrophic activity in which ANME-2b cells located in the interior of the consortium

incorporated far more ^{15}N from $^{15}N_2$ than ANME-2b cells near the exterior. This pattern may be related to variations in nitrogen supply from the external environment, as similar patterns of nutrient depletion with increasing depth into microbial aggregates have been predicted in modeling studies of nitrate uptake in *Trichodesmium* sp. [89] and directly observed by SIMS in stable isotope probing studies of carbon fixation in biofilm-forming filamentous cyanobacteria [90]. In these examples, modeling and experimental results document declining nitrate or bicarbonate ion availability inwards toward the center of the aggregates resulting from nitrate or bicarbonate consumption. An analogous process may occur in large ANME-2b—SEEP-SRB1g consortia, where cells situated closer to the exterior of the consortium assimilate environmental NH_4^+, increasing nitrogen limitation for cells within the consortium core. Interestingly, the single consortium in which the SEEP-SRB1g partner fixed nitrogen in excess of the ANME-2b partner featured SEEP-SRB1g cells in the core of this consortium with ANME-2b cells toward the exterior (Fig. 8). The current nanoSIMS dataset is small and determining the biotic and environmental factors that influence which partner is most diazotrophically active in ANME-2b—SEEP-SRB1g consortia necessitates further study, but a reasonable hypothesis is that the proximity of cells in a given ANME-2b—SEEP-SRB1g consortium relative to the consortium exterior (and NH_4^+ availability in the surrounding porewater) influences the spatial patterns of diazotrophic activity by both ANME and SRB in large consortia. The concentration of ammonium in seep porewater can be highly variable over relatively small spatial scales (e.g. between 47 - 299 μM within a single 15 cm-long pushcore [10]), and rates of diazotrophy estimated from laboratory incubations of methane seep sediment samples indicate different threshold concentrations of $NH_4^+{}_{(aq)}$ above which diazotrophy

ceases, as low as 25 μM [91] to 100-1000 μM [92–94]. In the large consortia observed here, this threshold [$NH_4^+{}_{(aq)}$] may be crossed within the consortium as NH_4^+ is assimilated by cells at the consortium exterior, inducing nitrogen limitation and diazotrophy by ANME or SRB near the consortium core. The development of a simple 1D steady-state reaction-diffusion model of ammonium diffusion and assimilation supports this hypothesis, indicating that for ammonium assimilation rate constants calculated from measurements of bulk methane seep sediment, porewater ammonium concentrations of ~30 μM can produce spatial gradients in diazotrophic activity at length scales of 1 to 10 μm within AOM consortia (Supp. File 2). Given the potential importance of diazotrophy for large ANME-SRB consortia and nitrogen cycling in methane seep communities [10, 91], future work should test this hypothesis with $^{15}N_2$ incubations under variable [$NH_4^+{}_{(aq)}$].

The observed variation in diazotrophic activity in ANME-2b or SEEP-SRB1g cells may also be the result of phenotypic heterogeneity [95] within the multicellular ANME-2b—SEEP-SRB1g consortia, in which expression of the nitrogenase operon that ANME-2b and SEEP-SRB1g partners both possess is an emergent behavior resulting from the spatial organization of ANME-2b and SEEP-SRB1g cells within the consortium. On the basis of nanoSIMS observations of heterogeneous diazotrophy in clonal *Klebsiella oxytoca* cultures, phenotypic heterogeneity was inferred to confer selective advantage on microbial communities by enabling rapid response to environmental fluctuations [96]. Similar heterogeneity in *nif* expression by ANME-2b or SEEP-SRB1g cells may provide partners with resilience against changes in environmental nitrogen supply. Corroborating these observations in diverse ANME-SRB consortia and direct coupling of single-cell mRNA

expression with nanoSIMS-acquired ^{15}N enrichment would further inform the degree to which relative arrangement of the partners and spatial structure within a consortium plays a significant role in determining the mode of nutrient or electron transfer between partners.

CONCLUSIONS

Here, we present an effective approach to detect novel pairings of microbial symbionts by coupling correlation analysis of 16S rRNA amplicon data with FISH and BONCAT-FACS experiments, going beyond amplicon sequencing-based hypothesis generation to experimental validation of hypothesized partnerships using microscopy and single-cell sorting techniques. Correlation analysis performed on a 16S rRNA amplicon survey of methane seep sediments near Costa Rica uncovered a novel and highly specific ANME-SRB partnership between ANME-2b archaea and a newly described Desulfobacteraceae-affiliated SEEP-SRB1g bacteria. The partnership specificity was validated by FISH, and further corroborated by 16S rRNA amplicon sequences from BONCAT-FACS-sorted single ANME-SRB consortia from methane seep sediments near Costa Rica, Hydrate Ridge, and Santa Monica Basin in California. Preliminary genomic screening of representatives from SEEP-SRB1g uncovered potential for nitrogen fixation in these genomes. Examination of published *nifH* cDNA clone libraries [8] and transcriptomic data [14] prepared from methane seep sediments demonstrated that SEEP-SRB1g actively expresses *nifH in situ*. The colocalization of positive hybridization signal for *nifH* mRNA using HCR-FISH and SEEP-SRB1g 16S rRNA in ANME-2b—SEEP-SRB1g consortia supported the findings of in situ *nifH* transcription by SEEP-SRB1g. FISH-nanoSIMS analysis of ANME-2b—SEEP-SRB1g consortia recovered from SIP experiments with $^{15}N_2$ documented ^{15}N incorporation in SEEP-SRB1g cells, confirming that SEEP-SRB1g can fix nitrogen in addition to ANME-2b. Future work should focus on examining unique aspects of each ANME-SRB syntrophic partnership to improve our understanding of the diversity of microbial symbioses catalyzing the anaerobic oxidation of methane.

ACKNOWLEDGEMENTS

The authors acknowledge the ROC-HITS science party, R/V *Atlantis* crew and HOV *Alvin* pilots from cruise AT37-13 for their assistance with sample collection and processing. We would like to thank H. Yu for assistance with sediment incubations, and S. Lim for performing IC measurements. We are grateful to Y. Guan for his assistance with the nanoSIMS analysis, R. Hatzenpichler for early BONCAT-FACS experiments, M. Aoki (National Institute of Technology, Wakayama College, Japan) for design of the FISH probe ANME-2a-828, and M. Schwarzkopf and Molecular Technologies for designing a set of HCR-FISH probes for *nifH* mRNA. We thank G. Chadwick and three anonymous reviewers for their comments on this work. Funding for this work was provided by the US Department of Energy's Office of Science (DE-SC0020373), the SIMONS Foundation Life Sciences Collaboration on Principals of Microbial Ecosystems, the National Science Foundation BIO-OCE grant (#1634002), and a Gordon and Betty Moore Foundation Marine Microbiology Investigator grant (#3780); (all to V.J.O.). A portion of this research was performed under the Facilities Integrating Collaborations for User Science (FICUS) initiative and used resources at the DOE Joint Genome Institute and the Environmental Molecular Sciences Laboratory, which are DOE Office of Science User Facilities (#503559). Both facilities are sponsored by the Office of Biological and Environmental Research and operated under Contract Nos. DE-AC02-05CH11231 (JGI) and DE-AC05-76RL01830 (EMSL). K.S.M. was supported in part by a National Science Foundation Graduate Research Fellowship and a Schlanger Ocean Drilling Fellowship. V.J.O. is a CIFAR Fellow in the Earth 4D: Subsurface Science and Exploration Program.

REFERENCES

1. Knittel K, Boetius A. Anaerobic Oxidation of Methane: Progress with an Unknown Process. *Annu Rev Microbiol* 2009; 63: 311–334.
2. Reeburgh WS. Oceanic Methane Biogeochemistry. *Chem Rev* 2007; 107: 486–513.
3. Orphan VJ, House CH, Hinrichs K-U, McKeegan KD, DeLong EF. Methane-Consuming Archaea Revealed by Directly Coupled Isotopic and Phylogenetic Analysis. *Science* 2001; 293: 484–487.
4. Boetius A, Ravenschlag K, Schubert CJ, Rickert D, Widdel F, Gieseke A, et al. A marine microbial consortium apparently mediating anaerobic oxidation of methane. *Nature* 2000; 407: 623.
5. McGlynn SE, Chadwick GL, Kempes CP, Orphan VJ. Single cell activity reveals direct electron transfer in methanotrophic consortia. *Nature* 2015; 526: 531–535.
6. Scheller S, Yu H, Chadwick GL, McGlynn SE, Orphan VJ. Artificial electron acceptors decouple archaeal methane oxidation from sulfate reduction. *Science* 2016; 351: 703–707.
7. Wegener G, Krukenberg V, Riedel D, Tegetmeyer HE, Boetius A. Intercellular wiring enables electron transfer between methanotrophic archaea and bacteria. *Nature* 2015; 526: 587–590.
8. Dekas AE, Connon SA, Chadwick GL, Trembath-Reichert E, Orphan VJ. Activity and interactions of methane seep microorganisms assessed by parallel transcription and FISH-NanoSIMS analyses. *ISME J* 2016; 10: 678–692.
9. Dekas AE, Poretsky RS, Orphan VJ. Deep-Sea Archaea Fix and Share Nitrogen in Methane-Consuming Microbial Consortia. *Science* 2009; 326: 422–426.
10. Dekas AE, Chadwick GL, Bowles MW, Joye SB, Orphan VJ. Spatial distribution of nitrogen fixation in methane seep sediment and the role of the ANME archaea. *Environ Microbiol* 2014; 16: 3012–3029.
11. Orphan VJ, Turk KA, Green AM, House CH. Patterns of 15N assimilation and growth of methanotrophic ANME-2 archaea and sulfate-reducing bacteria within structured syntrophic consortia revealed by FISH-SIMS. *Environ Microbiol* 2009; 11: 1777–1791.

12. Evans PN, Boyd JA, Leu AO, Woodcroft BJ, Parks DH, Hugenholtz P, et al. An evolving view of methane metabolism in the Archaea. *Nat Rev Microbiol* 2019; 17: 219–232.
13. Krukenberg V, Riedel D, Gruber‐Vodicka HR, Buttigieg PL, Tegetmeyer HE, Boetius A, et al. Gene expression and ultrastructure of meso- and thermophilic methanotrophic consortia. *Environ Microbiol* 2018; 20: 1651–1666.
14. Skennerton CT, Chourey K, Iyer R, Hettich RL, Tyson GW, Orphan VJ. Methane-Fueled Syntrophy through Extracellular Electron Transfer: Uncovering the Genomic Traits Conserved within Diverse Bacterial Partners of Anaerobic Methanotrophic Archaea. *mBio* 2017; 8: e00530-17.
15. Schreiber L, Holler T, Knittel K, Meyerdierks A, Amann R. Identification of the dominant sulfate-reducing bacterial partner of anaerobic methanotrophs of the ANME-2 clade. *Environ Microbiol* 2010; 12: 2327–2340.
16. Green-Saxena A, Dekas AE, Dalleska NF, Orphan VJ. Nitrate-based niche differentiation by distinct sulfate-reducing bacteria involved in the anaerobic oxidation of methane. *ISME J* 2014; 8: 150–163.
17. Hinrichs K-U, Hayes JM, Sylva SP, Brewer PG, DeLong EF. Methane-consuming archaebacteria in marine sediments. *Nature* 1999; 398: 802.
18. Hallam SJ, Girguis PR, Preston CM, Richardson PM, DeLong EF. Identification of Methyl Coenzyme M Reductase A (mcrA) Genes Associated with Methane-Oxidizing Archaea. *Appl Environ Microbiol* 2003; 69: 5483–5491.
19. Michaelis W, Seifert R, Nauhaus K, Treude T, Thiel V, Blumenberg M, et al. Microbial Reefs in the Black Sea Fueled by Anaerobic Oxidation of Methane. *Science* 2002; 297: 1013–1015.
20. Knittel K, Lösekann T, Boetius A, Kort R, Amann R. Diversity and Distribution of Methanotrophic Archaea at Cold Seeps. *Appl Environ Microbiol* 2005; 71: 467–479.
21. Orphan VJ, Hinrichs K-U, Ussler W, Paull CK, Taylor LT, Sylva SP, et al. Comparative Analysis of Methane-Oxidizing Archaea and Sulfate-Reducing Bacteria in Anoxic Marine Sediments. *Appl Environ Microbiol* 2001; 67: 1922–1934.

22. Orphan VJ, House CH, Hinrichs K-U, McKeegan KD, DeLong EF. Multiple archaeal groups mediate methane oxidation in anoxic cold seep sediments. *Proc Natl Acad Sci* 2002; 99: 7663–7668.
23. Raghoebarsing AA, Pol A, Pas-Schoonen KT van de, Smolders AJP, Ettwig KF, Rijpstra WIC, et al. A microbial consortium couples anaerobic methane oxidation to denitrification. *Nature* 2006; 440: 918.
24. Haroon MF, Hu S, Shi Y, Imelfort M, Keller J, Hugenholtz P, et al. Anaerobic oxidation of methane coupled to nitrate reduction in a novel archaeal lineage. *Nature* 2013; 500: 567–570.
25. Niemann H, Lösekann T, Beer D de, Elvert M, Nadalig T, Knittel K, et al. Novel microbial communities of the Haakon Mosby mud volcano and their role as a methane sink. *Nature* 2006; 443: 854.
26. Lösekann T, Knittel K, Nadalig T, Fuchs B, Niemann H, Boetius A, et al. Diversity and Abundance of Aerobic and Anaerobic Methane Oxidizers at the Haakon Mosby Mud Volcano, Barents Sea. *Appl Environ Microbiol* 2007; 73: 3348–3362.
27. Manz W, Eisenbrecher M, Neu TR, Szewzyk U. Abundance and spatial organization of Gram-negative sulfate-reducing bacteria in activated sludge investigated by in situ probing with specific 16S rRNA targeted oligonucleotides. *FEMS Microbiol Ecol* 1998; 25: 43–61.
28. Nauhaus K, Albrecht M, Elvert M, Boetius A, Widdel F. In vitro cell growth of marine archaeal-bacterial consortia during anaerobic oxidation of methane with sulfate. *Environ Microbiol* 2007; 9: 187–196.
29. Pernthaler A, Dekas AE, Brown CT, Goffredi SK, Embaye T, Orphan VJ. Diverse syntrophic partnerships from deep-sea methane vents revealed by direct cell capture and metagenomics. *Proc Natl Acad Sci U S A* 2008; 105: 7052–7057.
30. Vigneron A, Cruaud P, Pignet P, Caprais J-C, Cambon-Bonavita M-A, Godfroy A, et al. Archaeal and anaerobic methane oxidizer communities in the Sonora Margin cold seeps, Guaymas Basin (Gulf of California). *ISME J* 2013; 7: 1595–1608.
31. McGlynn SE, Chadwick GL, O'Neill A, Mackey M, Thor A, Deerinck TJ, et al. Subgroup Characteristics of Marine Methane-Oxidizing ANME-2 Archaea and Their

Syntrophic Partners as Revealed by Integrated Multimodal Analytical Microscopy. *Appl Environ Microbiol* 2018; 84: e00399-18.

32. Treude T, Krüger M, Boetius A, Jørgensen BB. Environmental control on anaerobic oxidation of methane in the gassy sediments of Eckernförde Bay (German Baltic). *Limnol Oceanogr* 2005; 50: 1771–1786.
33. Girguis PR, Orphan VJ, Hallam SJ, DeLong EF. Growth and Methane Oxidation Rates of Anaerobic Methanotrophic Archaea in a Continuous-Flow Bioreactor. *Appl Environ Microbiol* 2003; 69: 5472–5482.
34. Kleindienst S, Ramette A, Amann R, Knittel K. Distribution and in situ abundance of sulfate-reducing bacteria in diverse marine hydrocarbon seep sediments. *Environ Microbiol* 2012; 14: 2689–2710.
35. Holler T, Widdel F, Knittel K, Amann R, Kellermann MY, Hinrichs K-U, et al. Thermophilic anaerobic oxidation of methane by marine microbial consortia. *ISME J* 2011; 5: 1946–1956.
36. Loy A, Lehner A, Lee N, Adamczyk J, Meier H, Ernst J, et al. Oligonucleotide Microarray for 16S rRNA Gene-Based Detection of All Recognized Lineages of Sulfate-Reducing Prokaryotes in the Environment. *Appl Environ Microbiol* 2002; 68: 5064–5081.
37. Trembath-Reichert E, Case DH, Orphan VJ. Characterization of microbial associations with methanotrophic archaea and sulfate-reducing bacteria through statistical comparison of nested Magneto-FISH enrichments. *PeerJ* 2016; 4: e1913.
38. Trembath-Reichert E, Green-Saxena A, Orphan VJ. Chapter Two - Whole Cell Immunomagnetic Enrichment of Environmental Microbial Consortia Using rRNA-Targeted Magneto-FISH. In: DeLong EF (ed). *Methods in Enzymology*. 2013. Academic Press, pp 21–44.
39. Hatzenpichler R, Connon SA, Goudeau D, Malmstrom RR, Woyke T, Orphan VJ. Visualizing in situ translational activity for identifying and sorting slow-growing archaeal−bacterial consortia. *Proc Natl Acad Sci* 2016; 113: E4069–E4078.
40. Degnan PH, Ochman H. Illumina-based analysis of microbial community diversity. *ISME J* 2012; 6: 183–194.

41. Friedman J, Alm EJ. Inferring Correlation Networks from Genomic Survey Data. *PLOS Comput Biol* 2012; 8: e1002687.
42. Kurtz ZD, Müller CL, Miraldi ER, Littman DR, Blaser MJ, Bonneau RA. Sparse and Compositionally Robust Inference of Microbial Ecological Networks. *PLOS Comput Biol* 2015; 11: e1004226.
43. Schwager E, Mallick H, Ventz S, Huttenhower C. A Bayesian method for detecting pairwise associations in compositional data. *PLOS Comput Biol* 2017; 13: e1005852.
44. Lima-Mendez G, Faust K, Henry N, Decelle J, Colin S, Carcillo F, et al. Determinants of community structure in the global plankton interactome. *Science* 2015; 348.
45. Bohrmann G, Heeschen K, Jung C, Weinrebe W, Baranov B, Cailleau B, et al. Widespread fluid expulsion along the seafloor of the Costa Rica convergent margin. *Terra Nova* 2002; 14: 69–79.
46. Mau S, Sahling H, Rehder G, Suess E, Linke P, Soeding E. Estimates of methane output from mud extrusions at the erosive convergent margin off Costa Rica. *Mar Geol* 2006; 225: 129–144.
47. Sahling H, Masson DG, Ranero CR, Hühnerbach V, Weinrebe W, Klaucke I, et al. Fluid seepage at the continental margin offshore Costa Rica and southern Nicaragua. *Geochem Geophys Geosystems* 2008; 9.
48. Glass JB, Yu H, Steele JA, Dawson KS, Sun S, Chourey K, et al. Geochemical, metagenomic and metaproteomic insights into trace metal utilization by methane-oxidizing microbial consortia in sulphidic marine sediments. *Environ Microbiol* 2014; 16: 1592–1611.
49. Case DH, Pasulka AL, Marlow JJ, Grupe BM, Levin LA, Orphan VJ. Methane Seep Carbonates Host Distinct, Diverse, and Dynamic Microbial Assemblages. *mBio* 2015; 6.
50. Parada AE, Needham DM, Fuhrman JA. Every base matters: assessing small subunit rRNA primers for marine microbiomes with mock communities, time series and global field samples. *Environ Microbiol* 2016; 18: 1403–1414.

51. Caporaso JG, Kuczynski J, Stombaugh J, Bittinger K, Bushman FD, Costello EK, et al. QIIME allows analysis of high-throughput community sequencing data. *Nat Methods* 2010; 7: 335–336.
52. Mason OU, Case DH, Naehr TH, Lee RW, Thomas RB, Bailey JV, et al. Comparison of Archaeal and Bacterial Diversity in Methane Seep Carbonate Nodules and Host Sediments, Eel River Basin and Hydrate Ridge, USA. *Microb Ecol* 2015; 70: 766–784.
53. Edgar RC. Search and clustering orders of magnitude faster than BLAST. *Bioinformatics* 2010; 26: 2460–2461.
54. Quast C, Pruesse E, Yilmaz P, Gerken J, Schweer T, Yarza P, et al. The SILVA ribosomal RNA gene database project: improved data processing and web-based tools. *Nucleic Acids Res* 2013; 41: D590–D596.
55. Stamatakis A. RAxML version 8: a tool for phylogenetic analysis and post-analysis of large phylogenies. *Bioinformatics* 2014; 30: 1312–1313.
56. Towns J, Cockerill T, Dahan M, Foster I, Gaither K, Grimshaw A, et al. XSEDE: Accelerating Scientific Discovery. *Comput Sci Eng* 2014; 16: 62–74.
57. Miller MA, Pfeiffer W, Schwartz T. Creating the CIPRES Science Gateway for inference of large phylogenetic trees. *2010 Gatew. Comput. Environ. Workshop GCE*. 2010. pp 1–8.
58. Edgar RC. MUSCLE: multiple sequence alignment with high accuracy and high throughput. *Nucleic Acids Res* 2004; 32: 1792–1797.
59. Eren AM, Esen ÖC, Quince C, Vineis JH, Morrison HG, Sogin ML, et al. Anvi'o: an advanced analysis and visualization platform for 'omics data. *PeerJ* 2015; 3: e1319.
60. Campbell BJ, Yu L, Heidelberg JF, Kirchman DL. Activity of abundant and rare bacteria in a coastal ocean. *Proc Natl Acad Sci* 2011; 108: 12776–12781.
61. Letunic I, Bork P. Interactive Tree Of Life (iTOL) v4: recent updates and new developments. *Nucleic Acids Res* 2019; 47: W256–W259.
62. Ludwig W, Strunk O, Westram R, Richter L, Meier H, Yadhukumar, et al. ARB: a software environment for sequence data. *Nucleic Acids Res* 2004; 32: 1363–1371.

63. Daims H, Stoecker K, Wagner M, Stoecker K, Wagner M. Fluorescence in situ hybridization for the detection of prokaryotes. *Molecular Microbial Ecology*. https://www.taylorfrancis.com/. Accessed 15 Jul 2019.
64. Glöckner FO, Fuchs BM, Amann R. Bacterioplankton Compositions of Lakes and Oceans: a First Comparison Based on Fluorescence In Situ Hybridization. *Appl Environ Microbiol* 1999; 65: 3721–3726.
65. Dirks RM, Pierce NA. Triggered amplification by hybridization chain reaction. *Proc Natl Acad Sci* 2004; 101: 15275–15278.
66. Choi HMT, Beck VA, Pierce NA. Next-Generation in Situ Hybridization Chain Reaction: Higher Gain, Lower Cost, Greater Durability. *ACS Nano* 2014; 8: 4284–4294.
67. Yamaguchi T, Kawakami S, Hatamoto M, Imachi H, Takahashi M, Araki N, et al. In situ DNA-hybridization chain reaction (HCR): a facilitated in situ HCR system for the detection of environmental microorganisms. *Environ Microbiol* 2015; 17: 2532–2541.
68. Choi HMT, Schwarzkopf M, Fornace ME, Acharya A, Artavanis G, Stegmaier J, et al. Third-generation in situ hybridization chain reaction: multiplexed, quantitative, sensitive, versatile, robust. *Development* 2018; 145.
69. Bolte S, Cordelières FP. A guided tour into subcellular colocalization analysis in light microscopy. J Microsc 2006; 224: 213-232.
70. Dabundo R, Lehmann MF, Treibergs L, Tobias CR, Altabet MA, Moisander PA, Granger J. The contamination of commercial 15N2 gas stocks with 15N-labeled nitrate and ammonium and consequences for nitrogen fixation measurements. PLoS ONE 2014; 9: e110335.
71. Cline JD. Spectrophotometric Determination of Hydrogen Sulfide in Natural Waters1. *Limnol Oceanogr* 1969; 14: 454–458.
72. Dekas AE, Orphan VJ. Chapter Twelve - Identification of Diazotrophic Microorganisms in Marine Sediment via Fluorescence In Situ Hybridization Coupled to Nanoscale Secondary Ion Mass Spectrometry (FISH-NanoSIMS). In: Klotz MG (ed). *Methods in Enzymology*. 2011. Academic Press, pp 281–305.

73. Polerecky L, Adam B, Milucka J, Musat N, Vagner T, Kuypers MMM. Look@NanoSIMS--a tool for the analysis of nanoSIMS data in environmental microbiology. *Environ Microbiol* 2012; 14: 1009–1023.
74. Berry D, Widder S. Deciphering microbial interactions and detecting keystone species with co-occurrence networks. *Front Microbiol* 2014; 5.
75. David LA, Maurice CF, Carmody RN, Gootenberg DB, Button JE, Wolfe BE, et al. Diet rapidly and reproducibly alters the human gut microbiome. *Nature* 2014; 505: 559–563.
76. Leone V, Gibbons SM, Martinez K, Hutchison AL, Huang EY, Cham CM, et al. Effects of Diurnal Variation of Gut Microbes and High-Fat Feeding on Host Circadian Clock Function and Metabolism. *Cell Host Microbe* 2015; 17: 681–689.
77. Ruff SE, Biddle JF, Teske AP, Knittel K, Boetius A, Ramette A. Global dispersion and local diversification of the methane seep microbiome. *Proc Natl Acad Sci* 2015; 112: 4015–4020.
78. Fruchterman TMJ, Reingold EM. Graph drawing by force-directed placement. *Softw Pract Exp* 1991; 21: 1129–1164.
79. Moody J, White DR. Structural Cohesion and Embeddedness: A Hierarchical Concept of Social Groups. *Am Sociol Rev* 2003; 68: 103–127.
80. Gu Z, Gu L, Eils R, Schlesner M, Brors B. Circlize implements and enhances circular visualization in R. *Bioinformatics* 2014; 30: 2811–2812.
81. Nikolakakis K, Lehnert E, McFall-Ngai MJ, Ruby EG. Use of Hybridization Chain Reaction-Fluorescent In Situ Hybridization To Track Gene Expression by Both Partners during Initiation of Symbiosis. *Appl Environ Microbiol* 2015; 81: 4728–4735.
82. DePas WH, Starwalt-Lee R, Sambeek LV, Kumar SR, Gradinaru V, Newman DK. Exposing the Three-Dimensional Biogeography and Metabolic States of Pathogens in Cystic Fibrosis Sputum via Hydrogel Embedding, Clearing, and rRNA Labeling. *mBio* 2016; 7.
83. Imachi H, Nobu MK, Nakahara N, Morono Y, Ogawara M, Takaki Y, et al. Isolation of an archaeon at the prokaryote–eukaryote interface. *Nature* 2020; 577: 519–525.

84. Gloor GB, Macklaim JM, Pawlowsky-Glahn V, Egozcue JJ. Microbiome Datasets Are Compositional: And This Is Not Optional. *Front Microbiol* 2017; 8.
85. Sampayo EM, Ridgway T, Bongaerts P, Hoegh-Guldberg O. Bleaching susceptibility and mortality of corals are determined by fine-scale differences in symbiont type. *Proc Natl Acad Sci* 2008; 105: 10444–10449.
86. Parkinson JE, Baumgarten S, Michell CT, Baums IB, LaJeunesse TC, Voolstra CR. Gene Expression Variation Resolves Species and Individual Strains among Coral-Associated Dinoflagellates within the Genus Symbiodinium. *Genome Biol Evol* 2016; 8: 665–680.
87. Barshis DJ, Ladner JT, Oliver TA, Palumbi SR. Lineage-Specific Transcriptional Profiles of Symbiodinium spp. Unaltered by Heat Stress in a Coral Host. *Mol Biol Evol* 2014; 31: 1343–1352.
88. Kapili BJ, Barnett SE, Buckley DH, Dekas AE. Evidence for phylogenetically and catabolically diverse active diazotrophs in deep-sea sediment. *ISME J* 2020; 14: 971–983.
89. Klawonn I, Eichner MJ, Wilson ST, Moradi N, Thamdrup B, Kümmel S, et al. Distinct nitrogen cycling and steep chemical gradients in Trichodesmium colonies. *ISME J* 2020; 14: 399–412.
90. Petroff AP, Wu T-D, Liang B, Mui J, Guerquin-Kern J-L, Vali H, et al. Reaction–diffusion model of nutrient uptake in a biofilm: Theory and experiment. *J Theor Biol* 2011; 289: 90–95.
91. Dekas AE, Fike DA, Chadwick GL, Green‐Saxena A, Fortney J, Connon SA, et al. Widespread nitrogen fixation in sediments from diverse deep-sea sites of elevated carbon loading. *Environ Microbiol* 2018; 20: 4281–4296.
92. Knapp AN. The sensitivity of marine N2 fixation to dissolved inorganic nitrogen. *Front Microbiol* 2012; 3.
93. Bertics VJ, Löscher CR, Salonen I, Dale AW, Gier J, Schmitz RA, et al. Occurrence of benthic microbial nitrogen fixation coupled to sulfate reduction in the seasonally hypoxic Eckernförde Bay, Baltic Sea. *Biogeosciences* 2013; 10: 1243–1258.

94. Gier J, Sommer S, Löscher CR, Dale AW, Schmitz RA, Treude T. Nitrogen fixation in sediments along a depth transect through the Peruvian oxygen minimum zone. *Biogeosciences* 2016; 13: 4065–4080.

95. Ackermann M. A functional perspective on phenotypic heterogeneity in microorganisms. *Nat Rev Microbiol* 2015; 13: 497–508.

96. Schreiber F, Littmann S, Lavik G, Escrig S, Meibom A, Kuypers MMM, et al. Phenotypic heterogeneity driven by nutrient limitation promotes growth in fluctuating environments. *Nat Microbiol* 2016; 1: 1–7.

97. Raymond J, Siefert JL, Staples CR, Blankenship RE. The Natural History of Nitrogen Fixation. *Mol Biol Evol* 2004; 21: 541–554.

SUPPLEMENTAL TABLES, FIGURES, AND FILES

Supplemental Table 1. (not shown) Samples of methane seep sediment used in this study to produce 16S rRNA amplicon libraries. This file is available in a preprint version of this manuscript, doi: 10.1101/2020.04.12.038331v1

Probe	Specificity	Sequence (5' -> 3')	Position	% FA	Hits in target group	Outgroup hits (#)
S-F-SP1g-1443-a-A-23 (Seep1g-1443)	Methane seep SEEP-SRB1g	CCTCTCGCATAAAGCGAGTTAGC	1443 – 1465	35	4/5 (80%)	*Desulfatiglans* sp. (1), *Latescibacteria* sp. (1), SEEP SRB1a (1), *Desulfobulbus* sp. (1), SEEP SRB4 (1)
nifH_Seep1g_43-73_set1a	Seep1g nifH transcripts	**GAGGAGGGCAGCAAACGG**aaCTGTGTTGTCGTGGA	43 – 73	35	N/A	N/A
nifH_Seep1g_43-73_set1b	Seep1g nifH transcripts	GGCCTGCGACCGTATTta**GAAGAGTCTTCCTTTACG**	43 – 73	35	N/A	N/A
nifH_Seep1g_80-110_set2a	Seep1g nifH transcripts	**GAGGAGGGCAGCAAACGG**aaTTTTCTTTCCCATTT	80 – 110	35	N/A	N/A
nifH_Seep1g_80-110_set2b	Seep1g nifH transcripts	ACAGCCTACGACCATAAta**GAAGAGTCTTCCTTTACG**	80 – 110	35	N/A	N/A
nifH_Seep1g_120-150_set3a	Seep1g nifH transcripts	**GAGGAGGGCAGCAAACGG**aaCCCTCCGAGAAGCAAA	120 – 150	35	N/A	N/A
nifH_Seep1g_120-150_set3b	Seep1g nifH transcripts	CCCTCCGAGAAGCAAAta**GAAGAGTCTTCCTTTACG**	120 – 150	35	N/A	N/A
nifH_Seep1g_160-190_set4a	Seep1g nifH transcripts	**GAGGAGGGCAGCAAACGG**aaCTTCCTCCCTCAGGGT	160 – 190	35	N/A	N/A
nifH_Seep1g_160-190_set4b	Seep1g nifH transcripts	CTTCCTCCCTCAGGGTta**GAAGAGTCTTCCTTTACG**	160 – 190	35	N/A	N/A
nifH_Seep1g_320-350_set5a	Seep1g nifH transcripts	**GAGGAGGGCAGCAAACGG**aaAGGCGCCCAGGGACT	320 – 350	35	N/A	N/A
nifH_Seep1g_320-350_set5b	Seep1g nifH transcripts	CCCTCGGATTCCTCGTta**GAAGAGTCTTCCTTTACG**	320 – 350	35	N/A	N/A

Supplemental Table 2. Newly-designed FISH probe (Seep1g-1443) and nifH mRNA HCR-FISH probe for labeling ANME-associated members of SEEP-SRB1g or SEEP-SRB1g nifH transcripts, respectively. Bolded sequence is complementary to HCR-FISH amplifier B1; nonbolded sequence is complementary to SEEP-SRB1g 16S rRNA or nifH RNA. Matches determined by comparison with ARB/SILVA SSU release 128 [54].

Supplemental Table 3. (not shown) Stable isotope probing incubation conditions, sample sources and sulfide concentration measurements as a proxy for sulfate reduction activity. This file is available in a preprint version of this manuscript, doi: 10.1101/2020.04.12.038331v1

Supplemental Table 4. (not shown) SparCC-calculated correlations (pseudo-p < 0.01) between OTUs, detailing coefficients, OTU identifiers, and taxonomy assignments. This file is available in a preprint version of this manuscript, doi: 10.1101/2020.04.12.038331v1

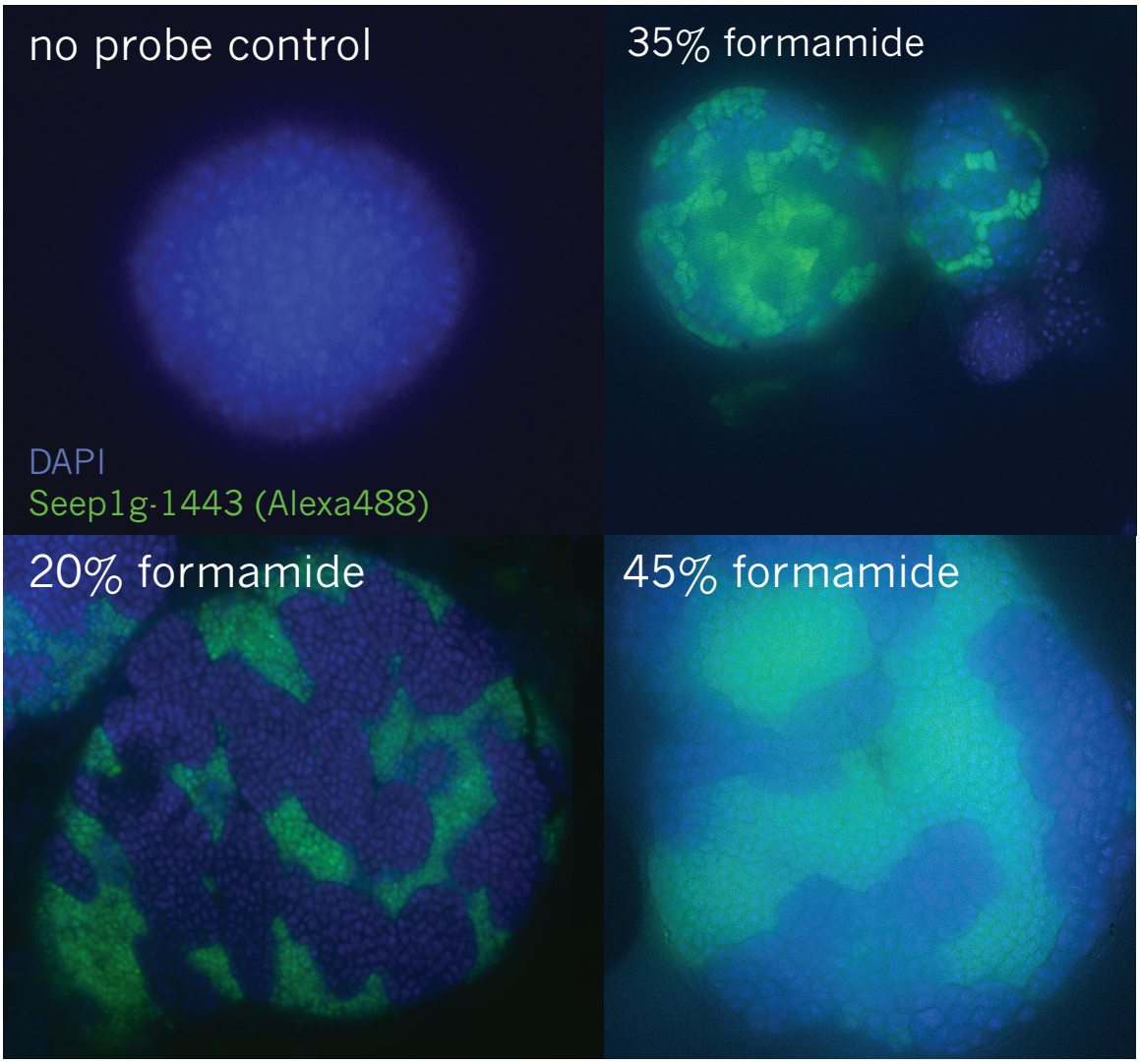

Supplemental Figure 1. Optimization of the newly designed Seep1g-1443 probe by FISH hybridization of ANME-2b—SEEP-SRB1g consortia at a range of formamide concentrations.

Supplemental Figure 2. Krona chart depicting relative abundance of taxa in Costa Rica seep sediment sample #10073 (Fig. 7) as measured by 16S rRNA amplicon sequencing.

Supplemental Figure 3. Krona chart depicting relative abundance of taxa in Costa Rica seep sediment sample #9279 (Fig. 4) as measured by 16S rRNA amplicon sequencing.

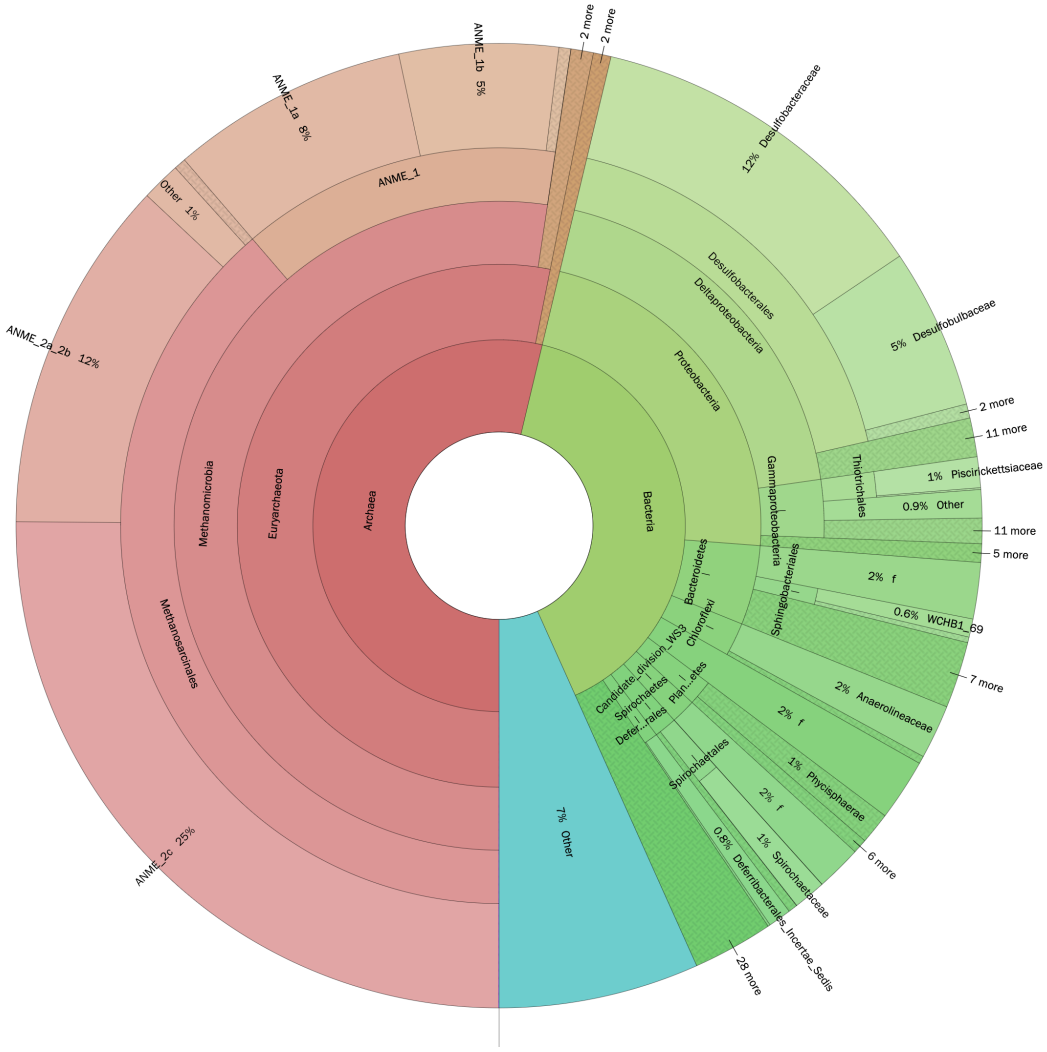

Supplemental Figure 4. Krona chart depicting relative abundance of taxa in Costa Rica seep sediment sample #9112 (Fig. 4) as measured by 16S rRNA amplicon sequencing.

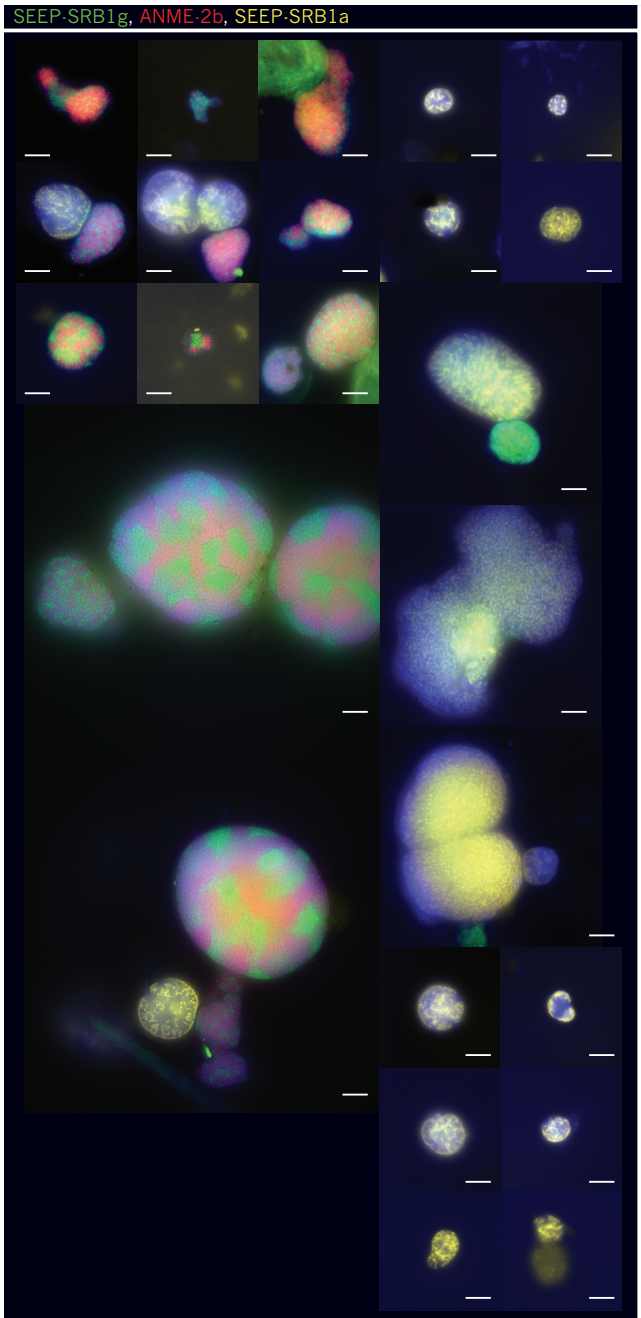

	SEEP-SRB1g	SEEP-SRB1a
ANME-2b	18	0
DAPI only	0	19

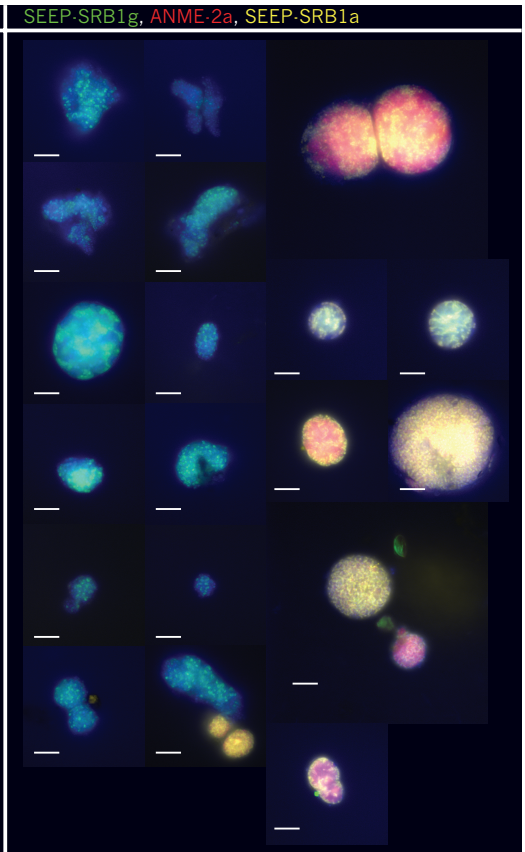

	SEEP-SRB1g	SEEP-SRB1a
ANME-2a	0	7
DAPI only	13	2

Supplemental Figure 5. Quantification of ANME-SRB partnership pairings in Costa Rica seep sediment sample #9279 using 16S rRNA FISH experiments, using probes Seep1g-1443, ANME-2b-729, and SEEP-SRB1a (left panel) and a complementary experiment (right panel) in which the ANME-2b probe was exchanged for ANME-2a-828. DAPI signal appears as blue in all images. Scale bar (white) for all images is 10 μm. Tabulation of consortia comprised of each pairing is presented at the bottom of each column, showing highly specific pairing between ANME-2b and SEEP-SRB1g.

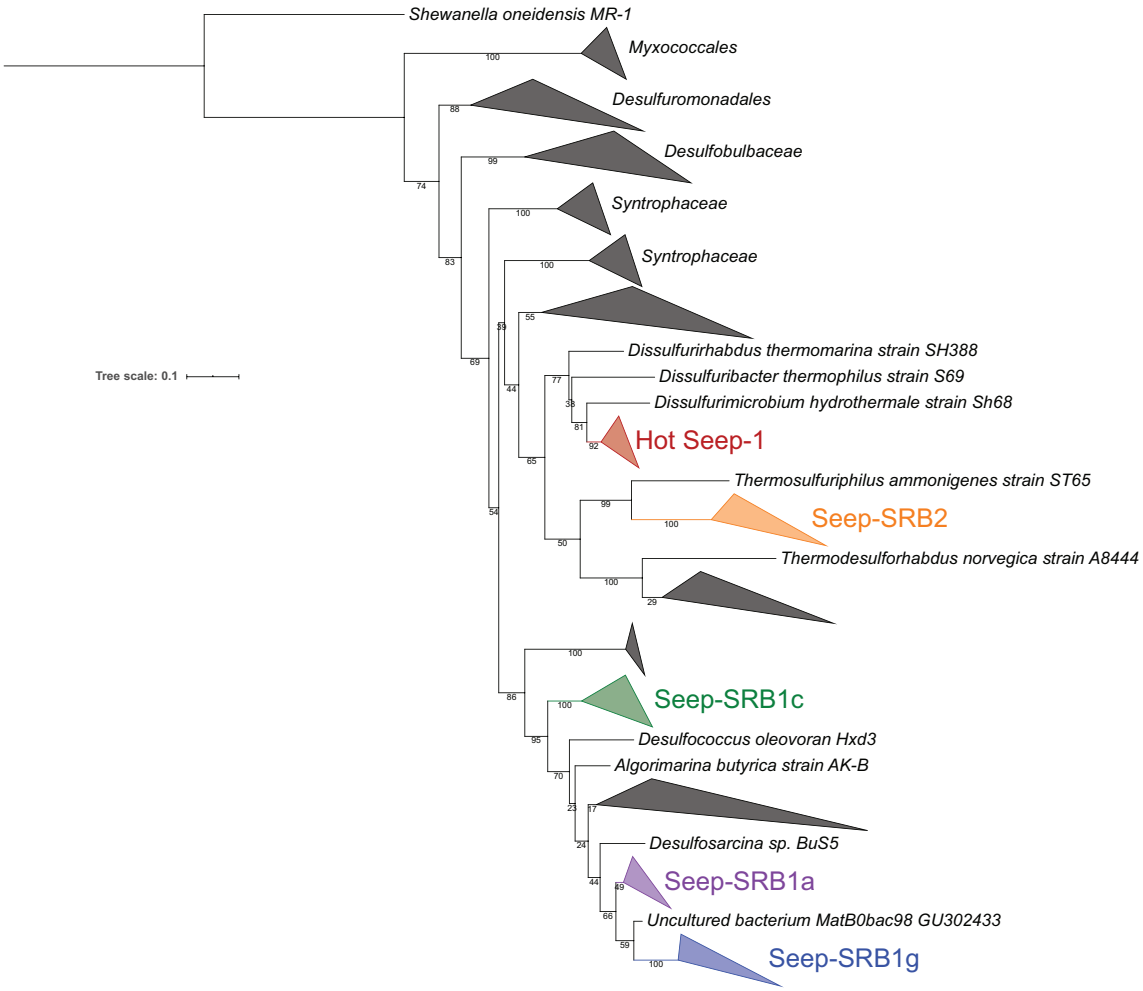

Supplemental Figure 6. 16S rRNA phylogeny inferred from maximum-likelihood methods using only full-length 16S rRNA sequences. Tree topology shown here is congruent with the phylogeny shown in Figure 3 constructed using a mix of shorter 16S rRNA amplicon and full-length 16S sequences.

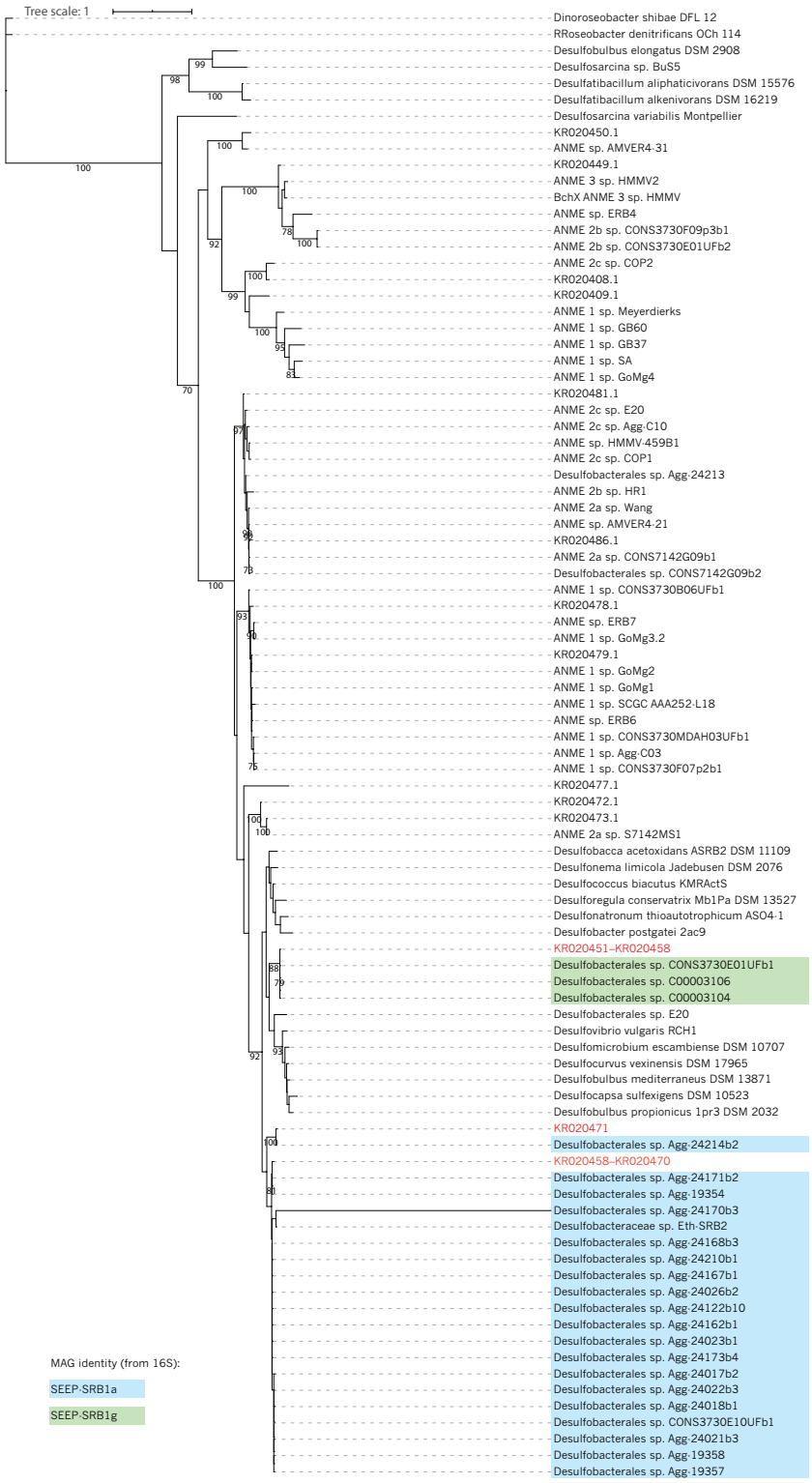

Supplemental Figure 7. Extended *nifH* tree including unpublished SEEP-SRB1a MAGs possessing nifH sequences nearly identical to some recovered in environmental cDNA libraries (Dekas, et al. 2016).

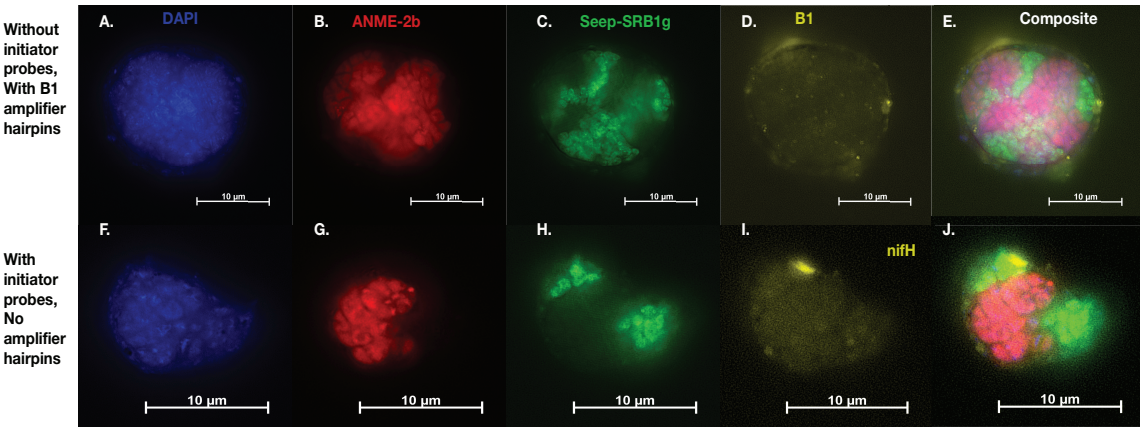

Supplemental Figure 8. Representative images for the negative control experiments for visualizing mRNA expression by HCR-FISH (A-E). Images of ANME-2b—SEEP-SRB1g consortia in the DAPI, TRITC, FITC, and cy5 channels as well as the composite of images from all the channels, These images were from an experiment without *nifH*-targeted initiator probes but with just B1 fluorescent hairpins in order to visualize potential non-specific binding of B1 hairpins (F-J). These images were from an experiment with *nifH*-targeted initiator probes but without B1 fluorescent hairpins in order to visualize the background fluorescence in the samples.

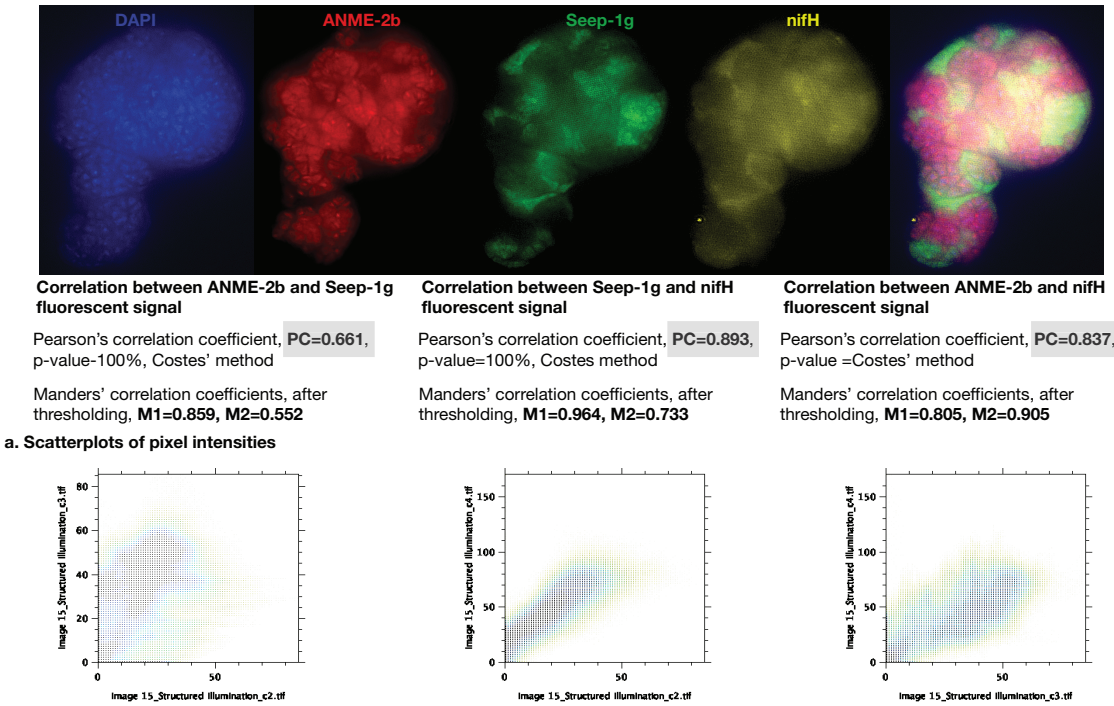

Supplemental Figure 9. Colocalization analysis of HCR-FISH experimental data to investigate nitrogenase expression by nifH targeted probes. ANME-2b is stained in the cy3 channel, Seep-1g in the FITC channel and the B1 amplifiers binding nifH initiator probes are visualized in the cy5 channel a. Scatterplots of pixel intensities of the FITC, cy3 and cy5 channel suggest that there is correlation between the Seep-1g signal and nifH signal, as well as correlation between ANME-2b and the nifH signal. However, there appears to be more noise in the latter, rather than just a linear correlation between the ANME-2b and *nifH* signals. An equally high PC between between Seep-1g and nifH, and ANME-2b and nifH is suggestive of nifH expression in ANME-2b as well. This is not an observation that is visually obvious and the lower intensity signal could come from nifH probes designed to target Seep-1g, binding ANME-2b *nifH* with lower efficiency. The Manders' coefficients suggest that almost all of the SEEP-SRB1g cells correlate with *nifH* signal while the same is not true of the colocalization of nifH signal with ANME-2b.

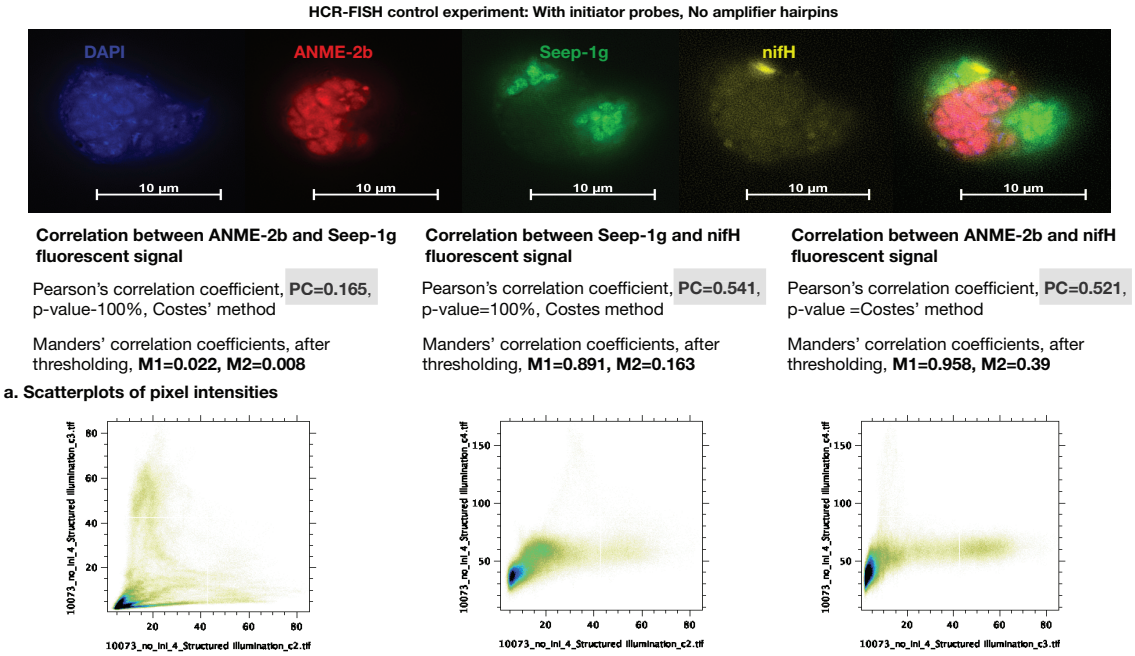

Supplemental Figure 10. Colocalization analysis of HCR-FISH control experiment with initiator probes and without amplifier hairpins. ANME-2b is stained in the cy3 channel, SEEP-SRB1g in the FITC channel. No dyes fluorescing in the cy5 channel are present in this experiment a. Scatterplots of pixel intensities of the FITC, cy3 and cy5 channel suggest there is some bleed through in both the cy3 and FITC channels.Neither the Pearson's correlation coefficient which measures covariance between the channels in proportion to their standard deviation nor Manders' correlation coefficients M1 and M2, which better correct for differences in intensity, are high enough to indicate significant cross-correlation.

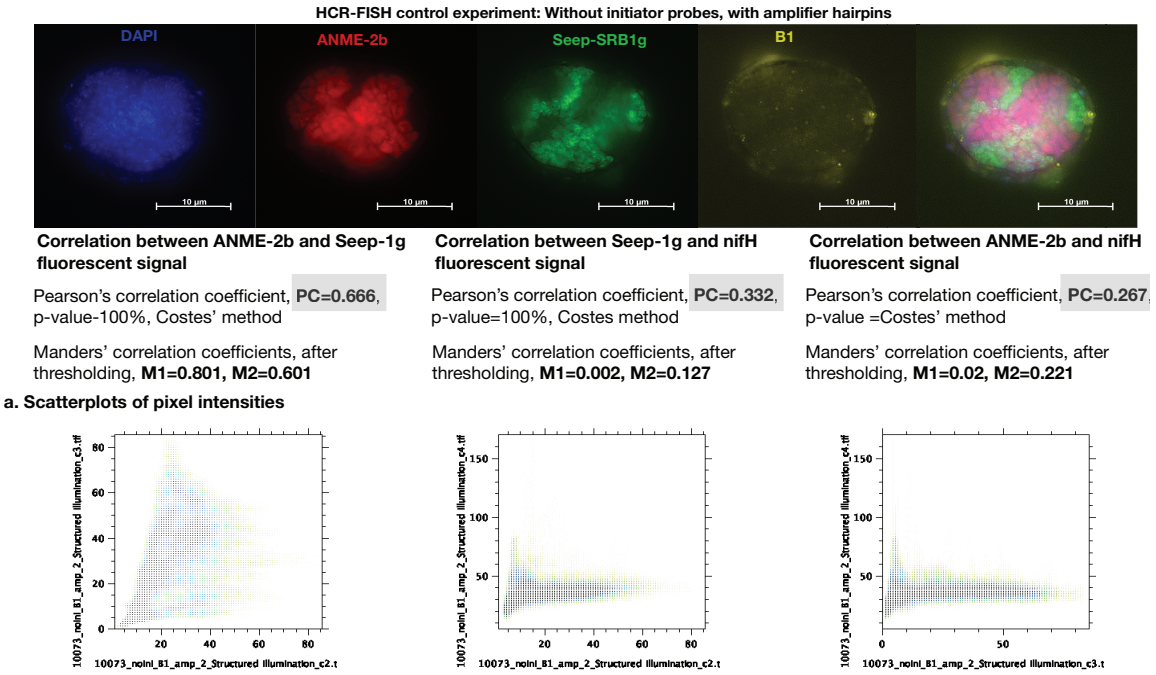

Supplemental Figure 11. Colocalization analysis of HCR-FISH experimental data to investigate nitrogenase expression by nifH-targeted probes. ANME-2b is stained in the cy3 channel, Seep-1g in the FITC channel and the B1 amplifiers binding nifH initiator probes are visualized in the cy5 channel.

Supplemental File 1. (not shown) FASTA file containing the translated amino acid sequences for nifH included in Figure 6 in select ANME and SRB genomes (Chadwick, et al., in prep) and transcripts [8]. This file is available in a preprint version of this chapter, doi: 10.1101/2020.04.12.038331v1

Supplemental File 2

In [1]:
```
import numpy as np
from numpy import ma
import matplotlib
import matplotlib.pyplot as plt
from matplotlib import cm
```

We hypothesize that preference for ammonium assimilation over nitrogen fixation consumed ammonium diffusing inwards into the ANME-SRB consortia shown in Figure 8, forcing cells in the consortium interior to fix additional nitrogen from $^{15}N_2$ to compensate for the decrease in N source from ammonium uptake. Here, we model ammonium diffusion into an ANME-SRB consortium and simultaneous ammonium assimilation as a classic 1D diffusion problem with boundary conditions describing continuous input at a fixed location (x = 0) with decay:

$$\frac{\partial C}{\partial t} = D\frac{\partial^2 C}{\partial t^2} - kC$$

where C is the concentration of ammonium at time t, D is the diffusivity for dissolved ammonium, and k is the first-order rate constant for ammonium assimilation.

Solving this differential equation at steady state $\left(\frac{\partial C}{\partial t} = 0\right)$ gives:

$$C = C_0 \exp\left(-\sqrt{\frac{k}{D}}x\right)$$

where C_0 is the concentration of ammonium in the porewater and thus the concentration at the exterior of the consortium.

Re-arranging to solve for x yields

$$x = \frac{-\ln\left(\frac{C}{C_0}\right)}{\sqrt{\frac{k}{D}}}$$

In our approach, we explore $x(C_0, D)$ holding C constant at 25 μM, the threshold value of ammonium concentration above which diazotrophy is inhibited in incubations of methane seep sediments (Dekas, et al. 2018). $x(C_0, D)$ will thus describe the depth within a consortium at which ammonium will be depleted sufficiently to induce diazotrophy, described in the figure below as 'diazotrophy frontier depth'. We have calculated k = 0.0004-0.0009 hr^{-1} from time-series measurements of ammonium concentration in methane seep sediment incubations under ammonium-replete (≥ 25 μM) conditions (Dekas, et al. 2018, Fig. S5, "Mat-774", "Mat-794").

In [2]:
```
C = 25
k = 0.0004
```

We explore a range of C_0 between 0.01 and 316 μM, representative of porewater ammonium concentrations measured *in situ* (Dekas, et al. 2018).

In [3]:
```
C_0 = np.logspace(-2, 2.5, 1000)
```

We use an estimate for the diffusivity of ammonium derived from the literature (Krom and Berner, 1980) of D = 3.5 * 10^6 to constrain maximum possible diffusivity, and explore a range of parameter values for D down to 10^1, representing the limitations on diffusion imposed by diffusion between cells within the consortium. A large range of values for D was employed here to reflect the challenges of measuring this parameter within ANME-SRB consortia.

In [4]:
```
D = np.logspace(1, 6.7, 1000)
```

In [5]:
```
c_0, d = np.meshgrid(C_0, D)
x = np.zeros((1000, 1000))
x = -np.log(25/c_0) * 1/np.sqrt(k/d)
```

In [7]:
```
fig, ax = plt.subplots()

x = ma.masked_where(x <= 0, x)
norm = cm.colors.LogNorm()
cs = ax.contourf(c_0, d, x, 50,
                 norm = norm)
cbar = fig.colorbar(cs)
plt.xlim(25, c_0.max())
plt.xlabel('Porewater [NH$_4$$^+$] (μM)')
ax.set_yscale('log')
ax.set_xscale('log')
ax.set_xticks([30, 50, 100, 300])
ax.get_xaxis().set_major_formatter(matplotlib.ticker.ScalarFormatter())
plt.ylabel('Diffusivity (μm$^2$ h$^{-1}$)')
cbar.set_label('Diazotrophy frontier depth (μm)')
plt.rcParams['figure.figsize'] = [10, 10]
plt.rcParams['font.size'] = 12
plt.show()
```

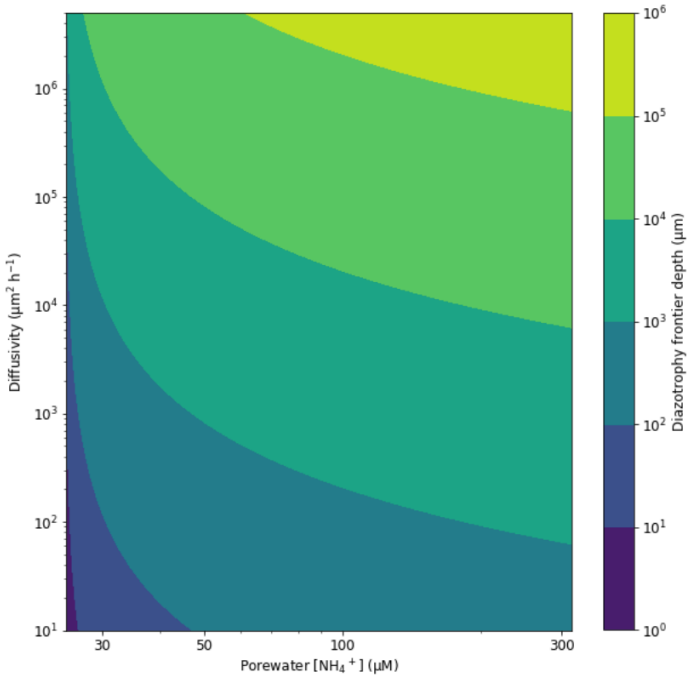

Plotting the results, we see that the depth at which we observe significant ^{15}N incorporation and thus diazotrophic activity in our consortia (1 to 10 μm into consortia, Fig. 8) is possible at diffusivities near that measured for bulk marine sediment (≈10^6 μm^2 hr^{-1}) for porewater ammonium concentrations that approach 25 μm. Thus, the simple model presented here broadly supports our hypothesized mechanism for the observed gradient in diazotrophic activity presented in Figure 8.

Supplemental File 2. Jupyter Notebook describing the 1D steady-state reaction-diffusion model calculating the depth inside of an ANME-SRB consortia at which ammonium assimilation depletes ammonium concentrations below the measured threshold for induction of diazotrophic activity in methane seep sediments. This file will be available upon publication of this chapter in the *ISME Journal.*

SUPPLEMENTAL MATERIALS AND METHODS

Sample collection

Pushcore samples of seafloor sediment were collected by DSV *Alvin* during the May 20-June 11 2017 ROC HITS Expedition (AT37-13) aboard R/V *Atlantis* (operated by Woods Hole Oceanographic Institute, Woods Hole, MA, USA) to methane seep sites southwest of Costa Rica [1–3]. After retrieval from the seafloor, sediment pushcores were extruded aboard R/V *Atlantis* and sectioned at 1-3 cm intervals for geochemistry and microbiological sampling using published protocols [4, 5]. Subsamples for DNA extraction and microscopy were recovered using sterile cutoff 1 mL syringes (BD, Franklin Lakes, NJ, USA). Samples of seep carbonates and xenophyophores collected proximal to seafloor seep sites were also used for DNA extraction. Sediment, seep carbonate, and xenophyophore samples for DNA extraction were immediately frozen in liquid N_2 and stored at -80˚C. Samples for microscopy were fixed in a filter-sterile (0.2 μm) 3X phosphate-buffered saline solution, pH 7.4 (145 mM NaCl, 1.4 mM NaH_2PO_4, 8 mM Na_2HPO_4, Sigma-Aldrich Corporation, St. Louis, MO, USA) with 2% paraformaldehyde (Electron Microscopy Sciences, Hatfield, PA, USA) for 24 h at 4˚C. Samples were subsequently washed with 1X PBS after centrifugation at 10000xg for 2 min. 1X PBS wash was removed after a second centrifugation and the resulting sediment pellet was resuspended in a 50:50 solution of ethanol and 1X PBS solution and stored at -20˚C.

Remaining sediment not used for DNA extraction or microscopy was placed in Mylar bags with filtered seawater, sparged with Ar, and stored at 4˚C after pressurization to ~2 atm with CH_4. Upon return to the laboratory, Mylar bags were unsealed and decanted into 1L Pyrex bottles (Corning Life Sciences, Tewksbury, MA, USA) while being sparged with N_2. Bottles were sealed with butyl stoppers and pressurized to ~2 atm with CH_4. These incubations were stored in the dark at 4˚C for 1.5 yr before sampling, with spent media replaced every 3 months with fresh N_2-sparged filter-sterilized seawater and methane. Mud from these incubations was also sampled for FISH and HCR-FISH by fixation in 4% paraformaldehyde at room temperature for 30 min. A full list of samples used in this study can be found in Supplementary Table 1.

DNA Extraction and Illumina MiSeq sequencing of 16S rRNA gene

DNA was extracted from 310 samples of Costa Rican methane seep sediments and seep carbonates (Supp. Table 1) using the Power Soil DNA Isolation Kit 12888 following manufacturer (Qiagen, Germantown, MD, USA) directions modified for sediment and carbonate samples [4, 6]. The V4-V5 region of the 16S rRNA gene was amplified using archaeal/bacterial primers [7] with Illumina (San Diego, CA, USA) adapters on 5' end (515F: 5'-TCGTCGGCAGCGTCAGATGTGTATAAGAGACAG-GTGYCAGCMGCCGCGGTAA-3', 926R: 5'-GTCTCGTGGGCTCGGAGATGTGTATAAGAGACAG-CCGYCAATTYMTTTRAGTTT-3'). PCR reaction mix was set up in duplicate for each

sample with Q5 Hot Start High-Fidelity 2x Master Mix (New England Biolabs, Ipswich, MA, USA) in a 15 µL reaction volume according to manufacturer's directions with annealing conditions of 54°C for 30 cycles. Duplicate PCR samples were then pooled and 2.5 µL of each product was barcoded with Illumina NexteraXT index 2 Primers that include unique 8-bp barcodes (P5 5'-AATGATACGGCGACCACCGAGATCTACAC-XXXXXXXX-TCGTCGGCAGCGTC-3' and P7 5'-CAAGCAGAAGACGGCATACGAGAT-XXXXXXXX-GTCTCGTGGGCTCGG-3'). Amplification with barcoded primers used the same conditions as above, except for a volume of 25 µL, annealing at 66°C and 10 cycles. Products were purified using Millipore-Sigma (St. Louis, MO, USA) MultiScreen Plate MSNU03010 with vacuum manifold and quantified using ThermoFisherScientific (Waltham, MA, USA) QuantIT PicoGreen dsDNA Assay Kit P11496 on the BioRad CFX96 Touch Real-Time PCR Detection System. Barcoded samples were combined in equimolar amounts into single tube and purified with Qiagen PCR Purification Kit 28104 before submission to Laragen (Culver City, CA, USA) for 2 x 250 bp paired end analysis on Illumina's MiSeq platform with PhiX addition of 15-20%.

Processing of 16S rRNA gene MiSeq sequences

Sequence data were processed in QIIME version 1.8.0 [8] following Mason, et al. 2015 [9]. Raw sequence pairs were joined and quality-trimmed using the default parameters in QIIME. Sequences were clustered into *de novo* operational taxonomic units

(OTUs) with 99% similarity using UCLUST open reference clustering protocol and the most abundant sequence was chosen as representative for each *de novo* OTU [10]. Taxonomic identification for each representative sequence was assigned using the Silva-119 database [11] clustered at 99% similarity. This SILVA database had been appended with 1,197 in-house high-quality, methane seep-derived bacterial and archaeal full-length 16S rRNA sequences. Any sequences with pintail values > 75 were removed. The modified SILVA database is available upon request from the corresponding authors. Further taxonomic assignment of OTUs assigned to the SEEP-SRB1 clade was performed by aligning these 411 bp amplicon sequences to the Silva 119 database in ARB [12] and construction of a phylogenetic tree from full-length and amplicon 16S rRNA sequences of SEEP-SRB1 and sister clades to delineate SEEP-SRB1 subgroups [13]. Known contaminants in PCR reagents as determined by analysis of negative controls run with each MiSeq set were also removed [14] along with rare OTUs not present in any given library at a level of at least 10 reads.

Correlation analysis of 16S rRNA amplicon libraries

A QIIME-produced table of OTUs detected in the 310 methane seep sediment and seep carbonate amplicon libraries was further analyzed using the correlation algorithm SparCC [15]. A bash shell script (sparccWrapper.sh, written by Karoline Faust) was used to call SparCC Python scripts SparCC.py, MakeBootstraps.py, and PseudoPvals.py. First, SparCC.py calculated correlations between OTUs. MakeBootstraps.py then produced 100

shuffled OTU tables by random sampling from the real data with replacement and SparCC.py was used to calculate correlations in each of these 100 shuffled OTU tables. Finally, PseudoPvals.py calculated pseudo-*p* values for OTU correlations in the real dataset by comparison to correlations calculated in the shuffled OTU tables. As described by Friedman and Alm, 2012 [15], pseudo-*p*-values represent the fraction of correlation coefficients for a given pair of OTUs calculated from the 100 shuffled datasets that are greater than that calculated from the real datasets. Thus, a *pseudo*-p-values < 0.01 for a given pair of OTUs indicates that no correlation coefficient from any given shuffled dataset was greater than that calculated from our real data. Subsequent analysis of the produced tables describing magnitude and significance for OTU correlations was performed in R versions 3.3.3 and 3.5.0 [16], using visualization packages igraph [17], circlize [18], ggplot2 [19], and RColorBrewer [20]. In this study, only positive correlations (correlation coefficient > 0) between OTUs were used to examine potential ANME-SRB pairings. Analysis of cohesive blocks of OTUs (represented as nodes) in a force-directed network diagram [17, 21, 22] calculated from a filtered table of OTU correlations was interpreted to generate hypotheses of ANME-SRB pairings.

Phylogenetic analysis of 16S rRNA amplicon sequences

To examine phylogenetic placement of SRB 16S rRNA gene amplicon sequences predicted by network analysis to associate with particular ANME subgroup amplicon sequences, a phylogeny was constructed using RAxML-HPC [23] on XSEDE [24] using

the CIPRES Science Gateway [25] from full-length 16S rRNA sequences of Deltaproteobacteria aligned by MUSCLE [26]. Although amplicon sequences contain significantly less information than full-length 16S rRNA sequences, they were used in phylogeny construction to allow direct comparison between amplicon and full length 16S sequences. 16S rRNA sequences were sourced from NCBI for published full-length 16S sequences [27], from 99% consensus OTU sequences produced by QIIME from amplicon libraries prepared from methane seep sediments (this work) and from genome contig files downloaded from the US Department of Energy Joint Genome Institute's Integrated Microbial Genomes and Microbiomes (IMG/M) [72] of individual ANME-SRB consortia isolated by fluorescence-activated cell sorting of BONCAT-labeled consortia (BONCAT-FACS [27]). The latter was acquired either by direct download of 16S rRNA genes detected in genome bins or by tblastn (e-value < 1^{-10}) searches of genome contig files using the 16S rRNA sequence from genome *Desulfosarcina* sp. BuS5 (IMG Genome ID 2513237157), closely related to known SEEP-SRB1a [28], as query. RAxML was run in parallel using raxmlHPC-HYBRID with the following settings: 100 bootstraps, 25 distinct rate categories, bootstrapping model GTRCAT, rapid bootstrapping, random seed for parsimony and for rapid bootstrapping set to 12345, and the Lewis ascertainment bias correction (called as raxmlHPC-HYBRID -T 4 -n result -s infile.txt -c 25 -m GTRCAT -p 12345 -k -f a -N 100 -x 12345 --asc-corr lewis). The resulting tree was exported and visualized using iTOL [29].

FISH probe design for new ANME-associated SRB group SEEP-SRB1g

A new FISH probe was designed in ARB using a modified version of the Silva 132 database (available on request). This new probe, named S-F-SP1g-1443-a-A-23 following published conventions [30] and hereafter referred to as Seep1g-1443 (5'-CCTCTCGCATAAAGCGAGTTAGC-3', Supp. Table 2), was designed to complement and target 16S rRNA sequences in a monophyletic "*Desulfococcus* sp." clade, which, based on phylogenetic analysis (see below), was renamed SEEP-SRB1g. Seep1g-1443 was ordered from Integrated DNA Technologies (Coralville, IA, USA) with fluor-dye Alexa488 attached to the 5' end, prepared for use by dilution to 50 ng/μL, and frozen at -20˚C. FISH reaction conditions were optimized for Seep1g-1443 by performing a series of FISH reactions at a range of formamide concentrations between 20% to 45% vol/vol. In this range, signal was specific to the SRB partner with little observed cross-hybridization; optimal intensity and specificity at 35% (Supp. Fig. 1).

FISH sediment sample preparation and imaging

FISH and hybridization chain reaction (HCR-) FISH was performed on paraformaldehyde-fixed samples ANME-SRB consortia extracted from Costa Rican methane seep sediments using previously published density separation and FISH protocols [31]. Two samples of fixed sediment with abundant 16S iTAG amplicon reads of ANME-2a and -2b (sample 9279) or ANME-2c and -2b (sample 9112) were prepared for downstream FISH labeling and microscopy (Supp. Fig. 2). For each sample, 50 μL of

fixed sediment was diluted with 950 µL 0.2 µm filter-sterilized 1X PBS in a 2 mL Eppendorf tube. After cooling for 10 min on ice, the diluted sediment was sonicated using a Branson Sonifier 150 (Branson Ultrasonics Corporation, Danbury, CT, USA). Sonication was performed with three 10 s pulses of the sonicator, set at 4 W output, with 10 s intervals between pulses. The 1 mL of sonicated sediment slurry was then pipetted onto 500 µL of Percoll (Sigma-Aldrich) and centrifuged at 16100 x G for 20 min at 4˚C. The supernatant with consortia was recovered and pipetted into 250 mL filter-sterile 1X PBS in a filter tower. This solution was filtered through a 5 µm polyethersulfone (PES) filter until ~50 mL solution remained in the tower. The filter was then washed with 200 mL 1X PBS while on the filter tower. Washing the remaining sample was repeated three times, with the final filtration step yielding a 1 mL aliquot. This 1mL aliquot was slowly concentrated onto a 0.2 µm GTTP white polycarbonate filter (Millipore-Sigma), keeping the filtered sample within a circular area of 0.5 mm-diameter. This area of the filter was then cut out with a razor blade and placed in a 250 µL PCR tube for FISH labeling.

FISH was performed overnight (18 hr) using the following modifications (G. Chadwick, pers. comm.) to previously-published protocols [27, 32]. A hybridization buffer at appropriate stringency was prepared along with accompanying wash buffer [33, 34] and pre-warmed to 46˚C and 48˚C in a hybridization oven and a water bath, respectively. 5 µL each of FISH probe stocks (50 ng/µL) Seep1g-1443 (this work), Seep1a-1441 [13], ANME-2a-828 (M. Aoki, pers. comm., 5'-GGTCGCACCGTGTCTGACACCT-3'), ANME-2b-729 [27], and ANME-2c-760 [35]. Four FISH experiments were performed, in which 5 µL each of 3 FISH probe stocks (at

concentration 50 ng/μL) were added to 35 μL hybridization buffer in 200 μL PCR tubes along with the filter sections. Two experiments were performed at 20% formamide stringency on sample 9279, both using Seep1g-1443 (Alexa488) and Seep1a-1441 (cy5), and ether ANME-2b-729 (cy3) or ANME-2a-828 (cy3). Two similar experiments were performed at 45% formamide stringency on sample 9112 using instead either ANME-2b-729 (cy3) or ANME-2c-760 (cy3) and both Seep1g-1443 (Alexa488) and Seep1a-1441 (cy5). After 18 hr hybridization, filters were removed and incubated for 20 min at 48˚C in 200 μL wash buffer. Filter sections were then removed and briefly dipped in deionized water and placed on Superfrost Plus slides (Thermo Fischer Scientific, Waltham, MA, USA) to dry at room temperature in the dark. 10 μL 4,6-diamidino-2-phenylindole (DAPI, Sigma-Aldrich) dissolved in Citifluor (Electron Microscopy Sciences) was applied to filter sections and left to incubate for 15 min in the dark. A cover slip (No. 1.5, VWR, Radnor, PA, USA) was then placed on each filter.

Structured-illumination microscopy (SIM) was performed on FISH and HCR-FISH (see below) experiments to image ANME-SRB consortia at resolutions beyond that of traditional microscopy. After Immersol 518F immersion oil (Zeiss, Jena, Germany) was placed onto sample cover slips, FISH-labeled samples were examined using a Zeiss Elyra PS.1 SIM platform. Samples illuminated by Elyra laser lines (405 nm, 488 nm, 561 nm, 642 nm) and viewed through an alpha Plan-APOCHROMAT 100X/1.46 Oil DIC M27 objective and filter set (BP420-480+LP750, BP495-550+LP750, BP570-620+LP750, LP655) were imaged using a pco.edge sCMOS camera (PCO, Kelheim,

Germany). Zen Black software (Zeiss) was used to construct final images from structured-illumination data.

Imaging of nifH mRNA by HCR-FISH

Hybridization chain reaction FISH (HCR-FISH) is a powerful technique to amplify signal from bound FISH probes by inducing polymerization of additional fluorophores to the bound probes [36, 37]. The protocol was modified from Yamaguchi and coworkers [38] and adapted to use lower probe concentrations (50 nM vs. 500 nM) and amplifier (300 nM) concentrations. In contrast to the published protocol, here, HCR-FISH was performed on white polycarbonate filters rather than directly on glass slides. HCR-FISH was performed using the same filter preparation protocol described above. This hybridization mix also included 5 µL each of 16S rRNA-targeted FISH probes Seep1g-1443 and ANME-2b-729 and a mix of HCR-FISH initiator probes (final concentration 50 nM) in the modified hybridization buffer (35% formamide stringency: 40 µL of 1M TRIS at pH 8 , 360 µL of 5M NaCL, 10 µL of 10% SDS, 700 µL of 100% formamide, 400 µL of 50% dextran sulfate, 4 µL of 50X Denhardt's Solution, 486 µL of deionized water) designed to target SEEP-SRB1g *nifH* mRNA transcripts (Supp. Table 2). After 18 hr hybridization at 46˚C, filters were removed and placed in 200 µL wash buffer (4 µL 1M pH 8 TRIS, 3.2 µL 5M NaCl, 1 µL 10% SDS, 191.8 µL deionized water). Immediately after, an amplification buffer solution was prepared (200 µL 0.5 M NaH_2PO_4, 360 µL 5M NaCl, 2 µL 10% SDS, 400 µL 50% dextran sulfate, 4 µL 50X

Denhardt's Solution, 1034 µL deionized water). 5 µL each of hairpins B1H1 and B1H2 (3 µM stock) with attached Alexa647 fluorophores (Molecular Technologies, Pasadena, CA, USA) were added separately to two 45 µL volumes of amplification buffer in PCR tubes and snap cooled by placement in a C1000 Touch Thermal Cycler (BioRad, Hercules, CA, USA) for 3 min at 95˚C. Hairpins in amplification buffer were then left to cool at room temperature for 30 min. After the elapsed time, hairpins in amplification buffer were mixed and placed in PCR tubes. Filters were removed from wash buffer and placed in the mixed amplification buffer, and amplification was performed by placement of PCR tubes in a 35˚C water bath. After 15 min, filters were removed and placed into pre-chilled 1X PBS at 4˚C for 10 min. Filters were then removed and dipped in deionized water briefly before placement on Superfrost Plus slides to dry at room temperature in the dark. 10 µL DAPI in Citifluor was applied and No. 1.5 VWR coverslips were placed on filters. The HCR-FISH reaction with *nifH* probes was also performed in accordance with published protocols [39]. HCR-FISH v3.0 uses a different buffer system and longer incubation times during hybridization and amplification stages of the protocol but we observed similar results with both protocols.

Comparative genomics of SEEP-SRB1g

Genomes downloaded from the IMG/M database were searched using tblastn (e-value<1^{-10}) for sequences matching reference NifD (NCBI Accession WP012698833), NifK (WP012698832), AprA (WP027353074), and DsrB (WP027352568) sequences. A

reference sequence for chlorophyllide reductase BchX (WP011566468) was used as a reference sequence for a tblastn *nifH* search using BLAST+ on the command line [40]. The *nifH* search also included a set of cDNA sequences cloned from methane seep sediments using primers specific to *nifH* [40]. Phylogenetic trees of MUSCLE-aligned tblastn hits were calculated using RAxML on XSEDE through the CIPRES Science Gateway, using the following settings for RAxML: raxmlHPC-HYBRID_8.2.12_comet -n result -s infile.txt -c 25 -p 12345 -m PROTCATDAYHOFF -k -f a -N 100 -x 12345 --asc-corr lewis. Output was viewed in iTOL.

Genome trees were constructed using the Anvi'o platform [41] using HMM profiles from a subset of sequences from Campbell, et al. [42] consisting of only ribosomal proteins. HMM hits to these profiles were then concatenated, aligned in MUSCLE, and used as input in RAxML to generate genome trees (called with identical settings as those for individual gene trees).

Stable isotope probing incubations with $^{15}N_2$

Incubated Costa Rica methane seep sediments from samples with abundant ANME-2b and SEEP-SRB1g (Supp. Fig. 4) were maintained in the laboratory under conditions supporting AOM and subsequently subsampled to test for diazotrophic activity in SEEP-SRB1g by stable isotope probing (SIP). SIP incubations (Supp. Table 3) were prepared by sparging source bottles and 30 mL serum bottles with N_2 and mixing 5 mL of sediment with 5 mL N_2-sparged artificial seawater without a N source (per L, 9.474 g

$MgCl_2 \cdot 6H_2O$, 0.2 g $CaCl_2 \cdot 2H_2O$, 26.7 g NaCl, 0.522 g KCl, 1.42 g Na_2SO_4, 0.174 g K_2HPO_4, 1 mL L1 trace elements solution, 100 mL 250 mM pH 7.5 HEPES, 5 mL 1M $NaHCO_3$, from a published medium composition [43]). Bottles were capped with butyl stoppers and overpressurized with CH_4. Over the course of three days, 9 mL of artificial seawater supernatant was removed and replaced with 9 mL additional artificial seawater to remove residual $NH_4^+{}_{(aq)}$. After pressurization to 2.8 bar CH_4, two incubations were further pressurized with 1.2 mL $^{15}N_2$ at 1 bar, approximately equivalent to 2% headspace in 20 mL CH_4 at 2.8 bar. Two positive control incubations were inoculated with 20 μL 500 mM $^{15}NH_4Cl$ ($^{15}NH_4Cl/NH_4Cl = 0.1$) and were further pressurized with 1.2 mL natural-abundance N_2 at 1 bar. Incubations were sampled for microbial community analysis and geochemistry and refreshed every 3 months and samples for nanoSIMS were recovered after 9 months. Sulfate reduction activity was assayed using the published protocols [44].

FISH-NanoSIMS

Incubations were sampled for FISH-nanoSIMS [45] following fixation procedures described above. After fixation and Percoll separation, samples were embedded in 3% Difco Noble Agar (BD, USA) on a 5 μm polycarbonate filter, peeled off, dehydrated in an ethanol series, and embedded using Technovit H8100 Embedding kit (Kulzer GmbH, Wehrheim, Germany). 2 μm thin sections were cut using an Ultracut E microtome (Reichert AG, Wein, Austria) and mounted on Teflon/poly-L-lysine slides (Tekdon Inc.,

FL, USA) by placement on 50 µL H_2O. FISH reactions were performed using Seep1g-1443 and ANME-2b-729 probes as described above, with the omission of 10% SDS to prevent detachment of section from slide (G. Chadwick, pers. comm.), and slides were imaged using a Zeiss Elyra PS.1 platform. After removal of DAPI-Citifuor by washing, slides were cut to fit into nanoSIMS sample holders and sputter-coated with 40 nm Au using a Cressington sputter coater. Spatially-resolved secondary-ion mass spectroscopy was then performed on sectioned ANME-SRB consortia using a Cameca NanoSIMS 50L housed in Caltech's Microanalysis Center. Pre-sputtering of samples was performed using a 1 nA Cs^+ ion beam until $^{12}C^{15}N^-$ ion counts stabilized. 512 x 512 pixel raster images of 20 μm^2 were then collected for $^{12}C^-$, $^{16}O^-$, $^{12}C^{14}N^-$, $^{15}N^{12}C^-$, $^{28}Si^-$, and $^{32}S^-$ ions by sputtering with a ~1 pA primary Cs^+ ion beam current with a dwell time of 12-48 ms/pixel. Mass calibration was performed once an hour for all masses. NanoSIMS data were processed using look@nanoSIMS [46] to determine ^{15}N fractional abundance, $^{15}N/(^{15}N+^{14}N)$. Regions of interest (ROIs) for ANME-2b and SEEP-SRB1g in consortia were drawn with Adobe Draw using secondary electron images of sectioned consortia compared with FISH images of the same section collected prior to nanoSIMS. ROIs annotated as ANME-2b or SEEP-SRB1g were then used as input for a MATLAB script used to extract ^{15}N fractional abundance from ROIs.

REFERENCES FOR SUPPLEMENTAL MATERIALS AND METHODS

1. Bohrmann G, Heeschen K, Jung C, Weinrebe W, Baranov B, Cailleau B, et al. Widespread fluid expulsion along the seafloor of the Costa Rica convergent margin. *Terra Nova* 2002; **14**: 69–79.

2. Mau S, Sahling H, Rehder G, Suess E, Linke P, Soeding E. Estimates of methane output from mud extrusions at the erosive convergent margin off Costa Rica. *Mar Geol* 2006; **225**: 129–144.

3. Sahling H, Masson DG, Ranero CR, Hühnerbach V, Weinrebe W, Klaucke I, et al. Fluid seepage at the continental margin offshore Costa Rica and southern Nicaragua. *Geochem Geophys Geosystems* 2008; **9**.

4. Orphan VJ, Hinrichs K-U, Ussler W, Paull CK, Taylor LT, Sylva SP, et al. Comparative Analysis of Methane-Oxidizing Archaea and Sulfate-Reducing Bacteria in Anoxic Marine Sediments. *Appl Environ Microbiol* 2001; **67**: 1922–1934.

5. Glass JB, Yu H, Steele JA, Dawson KS, Sun S, Chourey K, et al. Geochemical, metagenomic and metaproteomic insights into trace metal utilization by methane-oxidizing microbial consortia in sulphidic marine sediments. *Environ Microbiol* 2014; **16**: 1592–1611.

6. Case DH, Pasulka AL, Marlow JJ, Grupe BM, Levin LA, Orphan VJ. Methane Seep Carbonates Host Distinct, Diverse, and Dynamic Microbial Assemblages. *mBio* 2015; **6**.

7. Parada AE, Needham DM, Fuhrman JA. Every base matters: assessing small subunit rRNA primers for marine microbiomes with mock communities, time series and global field samples. *Environ Microbiol* 2016; **18**: 1403–1414.

8. Caporaso JG, Kuczynski J, Stombaugh J, Bittinger K, Bushman FD, Costello EK, et al. QIIME allows analysis of high-throughput community sequencing data. *Nat*

Methods 2010; **7**: 335–336.

9. Mason OU, Case DH, Naehr TH, Lee RW, Thomas RB, Bailey JV, et al. Comparison of Archaeal and Bacterial Diversity in Methane Seep Carbonate Nodules and Host Sediments, Eel River Basin and Hydrate Ridge, USA. *Microb Ecol* 2015; **70**: 766–784.

10. Edgar RC. Search and clustering orders of magnitude faster than BLAST. *Bioinformatics* 2010; **26**: 2460–2461.

11. Quast C, Pruesse E, Yilmaz P, Gerken J, Schweer T, Yarza P, et al. The SILVA ribosomal RNA gene database project: improved data processing and web-based tools. *Nucleic Acids Res* 2013; **41**: D590–D596.

12. Ludwig W, Strunk O, Westram R, Richter L, Meier H, Yadhukumar, et al. ARB: a software environment for sequence data. *Nucleic Acids Res* 2004; **32**: 1363–1371.

13. Schreiber L, Holler T, Knittel K, Meyerdierks A, Amann R. Identification of the dominant sulfate-reducing bacterial partner of anaerobic methanotrophs of the ANME-2 clade. *Environ Microbiol* 2010; **12**: 2327–2340.

14. Salter SJ, Cox MJ, Turek EM, Calus ST, Cookson WO, Moffatt MF, et al. Reagent and laboratory contamination can critically impact sequence-based microbiome analyses. *BMC Biol* 2014; **12**: 87.

15. Friedman J, Alm EJ. Inferring Correlation Networks from Genomic Survey Data. *PLOS Comput Biol* 2012; **8**: e1002687.

16. R Core Team. R: A Language and Environment for Statistical Computing. 2017. R Foundation for Statistical Computing, Vienna, Austria.

17. Csardi G, Nepusz T. The igraph software package for complex network research. *InterJournal* 2006; **Complex Systems**: 1695.

18. Gu Z, Gu L, Eils R, Schlesner M, Brors B. Circlize implements and enhances circular visualization in R. *Bioinformatics* 2014; **30**: 2811–2812.

19. Wickham H. ggplot2: Elegant Graphics for Data Analysis. 2009. Springer-Verlag New York.

20. Neuwirth E. RColorBrewer: ColorBrewer Palettes. 2014.

21. Fruchterman TMJ, Reingold EM. Graph drawing by force-directed placement. *Softw Pract Exp* 1991; **21**: 1129–1164.

22. Moody J, White DR. Structural Cohesion and Embeddedness: A Hierarchical Concept of Social Groups. *Am Sociol Rev* 2003; **68**: 103–127.

23. Stamatakis A. RAxML version 8: a tool for phylogenetic analysis and post-analysis of large phylogenies. *Bioinformatics* 2014; **30**: 1312–1313.

24. Towns J, Cockerill T, Dahan M, Foster I, Gaither K, Grimshaw A, et al. XSEDE: Accelerating Scientific Discovery. *Comput Sci Eng* 2014; **16**: 62–74.

25. Miller MA, Pfeiffer W, Schwartz T. Creating the CIPRES Science Gateway for inference of large phylogenetic trees. *2010 Gatew. Comput. Environ. Workshop GCE*. 2010. pp 1–8.

26. Edgar RC. MUSCLE: multiple sequence alignment with high accuracy and high throughput. *Nucleic Acids Res* 2004; **32**: 1792–1797.

27. Hatzenpichler R, Connon SA, Goudeau D, Malmstrom RR, Woyke T, Orphan VJ. Visualizing in situ translational activity for identifying and sorting slow-growing archaeal−bacterial consortia. *Proc Natl Acad Sci* 2016; **113**: E4069–E4078.

28. Skennerton CT, Chourey K, Iyer R, Hettich RL, Tyson GW, Orphan VJ. Methane-Fueled Syntrophy through Extracellular Electron Transfer: Uncovering the Genomic Traits Conserved within Diverse Bacterial Partners of Anaerobic Methanotrophic

Archaea. *mBio* 2017; **8**: e00530-17.

29. Letunic I, Bork P. Interactive Tree Of Life (iTOL) v4: recent updates and new developments. *Nucleic Acids Res* 2019; **47**: W256–W259.

30. Alm EW, Oerther DB, Larsen N, Stahl DA, Raskin L. The oligonucleotide probe database. *Appl Environ Microbiol* 1996; **62**: 3557–3559.

31. Orphan VJ, House CH, Hinrichs K-U, McKeegan KD, DeLong EF. Multiple archaeal groups mediate methane oxidation in anoxic cold seep sediments. *Proc Natl Acad Sci* 2002; **99**: 7663–7668.

32. Daims H, Stoecker K, Wagner M, Stoecker K, Wagner M. Fluorescence in situ hybridization for the detection of prokaryotes. *Molecular Microbial Ecology*. https://www.taylorfrancis.com/. Accessed 15 Jul 2019.

33. Pernthaler J, Glöckner F-O, Schönhuber W, Amann R. Fluorescence in situ hybridization (FISH) with rRNA-targeted oligonucleotide probes. *Methods in Microbiology*. 2001. Academic Press, pp 207–226.

34. Glöckner FO, Fuchs BM, Amann R. Bacterioplankton Compositions of Lakes and Oceans: a First Comparison Based on Fluorescence In Situ Hybridization. *Appl Environ Microbiol* 1999; **65**: 3721–3726.

35. Knittel K, Lösekann T, Boetius A, Kort R, Amann R. Diversity and Distribution of Methanotrophic Archaea at Cold Seeps. *Appl Environ Microbiol* 2005; **71**: 467–479.

36. Dirks RM, Pierce NA. Triggered amplification by hybridization chain reaction. *Proc Natl Acad Sci* 2004; **101**: 15275–15278.

37. Choi HMT, Beck VA, Pierce NA. Next-Generation in Situ Hybridization Chain Reaction: Higher Gain, Lower Cost, Greater Durability. *ACS Nano* 2014; **8**: 4284–4294.

38. Yamaguchi T, Kawakami S, Hatamoto M, Imachi H, Takahashi M, Araki N, et al. In situ DNA-hybridization chain reaction (HCR): a facilitated in situ HCR system for the detection of environmental microorganisms. *Environ Microbiol* 2015; **17**: 2532–2541.

39. Choi HMT, Schwarzkopf M, Fornace ME, Acharya A, Artavanis G, Stegmaier J, et al. Third-generation in situ hybridization chain reaction: multiplexed, quantitative, sensitive, versatile, robust. *Development* 2018; **145**.

40. Dekas AE, Connon SA, Chadwick GL, Trembath-Reichert E, Orphan VJ. Activity and interactions of methane seep microorganisms assessed by parallel transcription and FISH-NanoSIMS analyses. *ISME J* 2016; **10**: 678–692.

41. Eren AM, Esen ÖC, Quince C, Vineis JH, Morrison HG, Sogin ML, et al. Anvi'o: an advanced analysis and visualization platform for 'omics data. *PeerJ* 2015; **3**: e1319.

42. Campbell BJ, Yu L, Heidelberg JF, Kirchman DL. Activity of abundant and rare bacteria in a coastal ocean. *Proc Natl Acad Sci* 2011; **108**: 12776–12781.

43. Scheller S, Yu H, Chadwick GL, McGlynn SE, Orphan VJ. Artificial electron acceptors decouple archaeal methane oxidation from sulfate reduction. *Science* 2016; **351**: 703–707.

44. Cline JD. Spectrophotometric Determination of Hydrogen Sulfide in Natural Waters1. *Limnol Oceanogr* 1969; **14**: 454–458.

45. Dekas AE, Orphan VJ. Chapter Twelve - Identification of Diazotrophic Microorganisms in Marine Sediment via Fluorescence In Situ Hybridization Coupled to Nanoscale Secondary Ion Mass Spectrometry (FISH-NanoSIMS). In: Klotz MG (ed). *Methods in Enzymology*. 2011. Academic Press, pp 281–305.

46. Polerecky L, Adam B, Milucka J, Musat N, Vagner T, Kuypers MMM. Look@NanoSIMS--a tool for the analysis of nanoSIMS data in environmental

microbiology. *Environ Microbiol* 2012; **14**: 1009–1023.

47. Dekas AE, Poretsky RS, Orphan VJ. Deep-Sea Archaea Fix and Share Nitrogen in Methane-Consuming Microbial Consortia. *Science* 2009; **326**: 422–426.

48. Dekas AE, Chadwick GL, Bowles MW, Joye SB, Orphan VJ. Spatial distribution of nitrogen fixation in methane seep sediment and the role of the ANME archaea. *Environ Microbiol* 2014; **16**: 3012–3029.

49. Orphan VJ, Turk KA, Green AM, House CH. Patterns of 15N assimilation and growth of methanotrophic ANME-2 archaea and sulfate-reducing bacteria within structured syntrophic consortia revealed by FISH-SIMS. *Environ Microbiol* 2009; **11**: 1777–1791.

Chapter 2

MINERAL-ASSOCIATED MICROBIAL ECOLOGY OF METHANE SEEP SEDIMENTS INVESTIGATED BY DENSITY SEPARATION

Kyle S. Metcalfe and Victoria J. Orphan

Division of Geological and Planetary Sciences,
California Institute of Technology, Pasadena, California, 91125

ABSTRACT

Minerals host subseafloor microbiomes, but it remains unknown if certain minerals provide niches for certain microbial taxa. Recent work has demonstrated that conductive minerals in particular may provide important conduits for extracellular electron transfer, a process central to the physiology of many syntrophic microorganisms that inhabit seafloor sediments. Multicellular consortia of anaerobic methanotrophic archaea (ANME) and partner sulfate-reducing bacteria (SRB) are a prominent example of syntrophic EET in marine sediments, but little is known about the extent to which these consortia associate with conductive minerals *in situ*. Here, we report the optimization of a heavy-liquids separation protocol and results from its application to methane seep sediment samples, which revealed preferential association between members of the ANME-3 and magnetite and/or pyrite mineral surfaces. We further demonstrate the capacity for this new protocol to improve detection of ecological interactions between microbial taxa.

INTRODUCTION

Marine sediments comprise one of Earth's most energy-poor biomes. High-energy electron acceptors such as oxygen or nitrate diffusing downward into seafloor sediments from an aerobic water column are rapidly consumed by respiring microorganisms that inhabit sediments near the sediment-water interface (Froelich et al., 1979; Van Cappellen and Wang, 1996). In the subsurface biosphere, the presence of a mineral matrix reduces the rate at which electron acceptors can be replenished by diffusion or advection as occurs in the water column, leaving many subsurface microbial communities reliant upon lower-energy electron acceptors to survive (Kallmeyer et al., 2012; Bowles et al., 2014). Organic carbon deposited on the seafloor provdes an abundant source of electrons for microbial communities buried in seafloor sediment, which in most coastal environments exceeds the supply of high-potential electron donors such as oxygen and nitrate (Jørgensen, 2000). The energetic challenge posed by this excess of electron donor is particularily acute in sediments proximal to seafloor methane seeps, where highly reducing, methane-charged fluid advects upwards from depth, inducing anoxia in sediment pore water within as little as a few millimeters beneath the sediment-water interface (Grünke et al., 2012).

The selective pressure imposed on microorganisms inhabiting highly reducing subseafloor environments has driven the evolution of adaptations that exploit diverse and unique electron acceptors or employ biochemical mechanisms of extracellular electron transfer (EET). Among these are sulfate ions as well as insoluble iron and manganese oxyhydroxides/oxides (Froelich et al., 1979; Van Cappellen and Wang, 1996) and humic substances (Lovley et al., 1996). Fe- or Mn-reducing microorganisms must pass electrons

to an insoluble acceptor, presenting a physiological challenge in which the acceptor cannot be transported into the cell (Lovley, 1991), requiring these microorganisms to perform EET. EET is also thought to facilitate energy-poor syntrophic metabolisms important in the marine subsurface, such as the anaerobic oxidation of methane (AOM, (McGlynn et al., 2015; Wegener et al., 2015)), in which anaerobic methanotrophic archaea (ANME) couple methane oxidation to sulfate reduction in a syntrophic partnership with sulfate-reducing bacteria (SRB, (Boetius et al., 2000; Orphan et al., 2001b)). EET can facilitate both syntrophic partnerships and reduction of insoluble electron acceptors, in some instances in the same metabolism, such as the reduction of iron and manganese oxides during AOM syntrophy (Beal et al., 2009). Several biochemical mechanisms for EET to insoluble electron acceptors and/or syntrophic partners have been proposed, including conductive pili (El-Naggar et al., 2010; Summers et al., 2010; Pfeffer et al., 2012), cytochromes (McGlynn et al., 2015; Skennerton et al., 2017), and/or electron shuttles (Marsili et al., 2008; Scheller et al., 2016). EET through conductive pili and/or cytochromes requires direct physical contact with insoluble electron acceptors or syntrophic partners, and thus can be significantly influenced by the substrates to which cells employing EET are attached (Lovley, 2017).

Defining the inorganic matrix within which the marine subsurface microbiome is embedded, minerals hinder the diffusion of high-energy electron acceptors into the subsurface microbiome but also my provide conduits for EET to some sediment-dwelling microorganisms. Semiconductive minerals such as hematite (Fe_2O_3), magnetite (Fe_3O_4), greigite (Fe_3S_4), and pyrite (FeS_2) are mineral components of marine sediments and are

increasingly considered ecologically important for sediment-dwelling microorganisms (Rowe et al., 2015; Shi et al., 2016) by facilitating EET to mineral electron acceptors (Liu et al., 2015) and/or syntrophic partners (Kato et al., 2012b, 2012a; Li et al., 2015; Liu et al., 2015; Tang et al., 2016; Rotaru et al., 2018). The stimulation of syntrophic EET by magnetite specifically has been repeatedly demonstrated in cultured and uncultured microorganisms. Syntrophic acetoclastic methanogenesis, an important but underappreciated methanogenic process in seafloor sediments (Beulig et al., 2018), has been shown to be stimulated by magnetite amendments in incubations of rice paddy soil (Kato et al., 2012a) or marine sediments (Rotaru et al., 2018), by increasing the rate of EET between *Geobacter* sp. and *Methanosarcina* sp. partners. Defined *Geobacter metallireducens*/*Methanosarcina barkeri* co-cultures have corroborated these observations (Tang et al., 2016), and other studies have shown that magnetite stimulates syntrophic oxidation of acetate by nitrate in *Geobacter sulfurreducens*/*Thiobacillus denitrificans* co-cultures (Kato et al., 2012b) and syntrophic oxidation of ethanol by fumarate in *G. metallireducens*/*G. sulfurreducens* co-cultures (Liu et al., 2015). It remains unknown, however, if related microorganisms or other syntrophs such as ANME-SRB consortia associate physically with conductive minerals *in situ* in methane seep sediments, where syntrophic EET modulates the flux of methane to the sediment-water interface (Reeburgh, 2007; Knittel and Boetius, 2009).

We sought to uncover *in situ* associations between microbial taxa and conductive minerals in marine sediments, targeting methane seep sediments—habitats for syntrophic microorganisms that are also rich in conductive minerals— as source material. In these

sediments, syntrophic ANME-SRB consortia perform AOM, and in so doing mediate the precipitation of authigenic carbonate (Aloisi et al., 2000; Luff and Wallmann, 2003; Naehr et al., 2007) and iron sulfide minerals. Of these, iron sulfide minerals such as pyrite (FeS_2) and pyrrhotite ($Fe_{(1-x)}S$, $x = 0 – 0.2$) are of particular interest, given their conductive nature (Sato and Mooney, 1960) and thus their potential involvement in microbial EET. Pyrite in particular is found in abundance at the SMTZ, the interface between sulfate-rich and methane-rich porewaters (Garming et al., 2005; Riedinger et al., 2005; März et al., 2008; Shi et al., 2017) where AOM rates are highest, precipitating from reaction of sulfide produced by AOM with dissolved Fe^{2+} or with detrital iron oxides (e.g. hematite, magnetite) present in seep sediments (Roberts, 2015). We focused on methane seep sediments, given their abundance of conductive minerals and syntrophic ANME-SRB consortia, to explore potential interactions between syntrophic EET and conductive minerals.

Here, we present methods we optimized to separate minerals in marine sediments by density and the insights into mineral-associated microbial ecology obtained from our methods building on previous work by Harrison and Orphan (Harrison and Orphan, 2012). The dense nature of conductive minerals such as pyrite and magnetite ($\rho >> 2.9$ g/cc) relative to the silicate clays ($\rho \approx 2.0 – 2.5$ g/cc) that comprise most of marine sediments by mass enables separation based on mass. Carbonate minerals are also somewhat more dense than silicate clays ($2.4 < \rho < 2.9$ g/cc), allowing for their separation from bulk sediments. Although not the focus of the current study, microbially-mediated carbonate precipitation is an important process in methane seep sediments, where it is responsible for the

emplacement of large authigenic carbonate edifices and extensive pavements (Treude et al., 2007; Marlow et al., 2014; Case et al., 2015), and thus we designed our protocol to also separate carbonate minerals out of sediments. We obtained several density-separated fractions of methane seep sediment samples, and applied next-generation 16S rRNA amplicon sequencing (Degnan and Ochman, 2012) to these fractions to profile the microbial communities present in each minerallogically-distinct fraction (Fig. 1). This work revealed a novel association between members of a clade of anaerobic methanotrophic archaea termed ANME-3 and a dense sediment fraction enriched in pyrite and magnetite as well as trace clay minerals. We further hypothesize from correlation analysis that ANME-3 form a novel partership with SEEP-SRB1c, potentially co-associating on the surfaces of the conductive minerals magnetite and pyrite.

MATERIALS AND METHODS

Density Separation Using Sodium Metatungstate

To separate minerals in methane seep sediments, we used heavy-liquids initially based upon previously- published methods (Harrison and Orphan, 2012). We used sodium metatungstate hydrate ($Na_6W_{12}O_{39} \cdot xH_2O$) given its non-toxic nature and the high densities that solutions of sodium metatungstate (SMT) can achieve without reaching saturation (up to ~3.1 g/mL). SMT and the related compound sodium polytungstate have previously been used to partition marine sediments by density to extract cells from

sediment (Morono et al., 2013) and to isolate mineralogically-distinct density fractions (Harrison and Orphan, 2012). Here we present further development of these techniques to

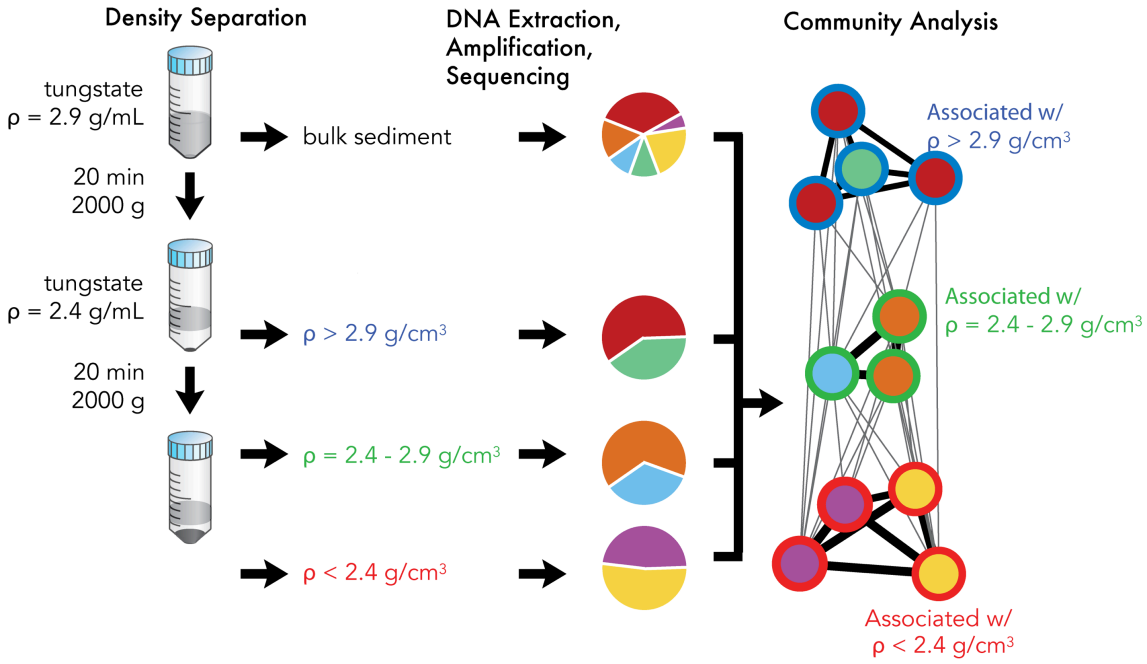

Figure 1. Schematic depiction of heavy-liquids mineral separation for mineral-associated microbial ecology. Density separation using sodium metatungstate recovered mineralogically-distinct density fractions (demonstrated using XRD and FTIR) from which DNA was extracted and sequenced using high-throughput platforms. Downstream community analysis revealed taxa associated with particular minerals and amplifies correlations between taxa co-associating on mineral surfaces.

increase the mineralogical purity and reproducability of density fractions, as assayed by x-ray diffractometry (XRD) and fourier transform infrared spectroscopy (FTIR), and to prepare density fractions for downstream microbial community profiling by 16S rRNA amplicon sequencing using an Illumina platform. The density separation technique is presented in detail for ease of future application of this technique:

Density Separation Protocol

1. 250 g SMT powder (Sigma-Aldrich #377341) was mixed with deionized water at a ratio of 250 g/55.0 mL in a 100 mL beaker with a stir bar. To increase the rate of SMT dissolution, this beaker was placed on a hot plate at 50˚ C for 1 hr. Higher temperatures decompose SMT.

2. When all SMT was dissolved, SMT was sterilized using a 0.2 µm filter flask. The filtrate SMT was decanted into sterile 60 mL serum vials sealed with butyl stoppers.

3. SMT in serum vials was placed under UV-C light (254 nm wavelength) for 2 hr to remove DNA contamination. 125 mL filter-sterile (0.2 µm) DI water was simultaneously UV sterilized.

4. After UV irradiation, butyl stoppers were removed and serum vials placed on scales to measure SMT density, target density ρ = 2.9 g/mL. 1 mL SMT was removed with a sterile 2 mL pipette and the mass deficit measured for the serum vial used to estimate SMT density. After density measurement, SMT was pipetted back into the serum vial and pipette was discarded. If density was too high, appropriate volume of DI was added, using this formula:

$$V_w = V_0 \frac{\rho_f - \rho_0}{\rho_w - \rho_f}$$

   where V_w is the volume of added to SMT, V_0 is the current volume of SMT, ρ_f = 2.9 g/mL, ρ_i is the measured current density of SMT, and $\rho_w \approx 1$ g/mL. If density was too low, SMT decanted into clean nonsterile beaker for evaporative densification (see step 23 below), followed by resterilization and density measurement (repeat steps 2-4).

5. With ρ = 2.9 g/mL achieved, SMT was decanted into 6 sterile 5 mL Eppendorf Tubes® (Cat. No. 0030119401), with 4 mL SMT into each tube.

6. Remaining SMT was diluted with filter- and UV-sterile DI from step 3 to achieve ρ = 1.5 g/mL, volume determined by use of formula above.

7. A ~ 10 mL sample of methane seep sediment slurry were extracted from incubations while maintaining anaerobic conditions in incubations, and placed in two 50 mL Falcon centrifuge tubes.

8. Samples were centrifuged for 10 min at 2000× g in a Beckman-Coulter Allegra X-14 set to room temperature. After centrifugation, supernatant was either frozen immediately at -20 ˚C for downstream DNA extraction or discarded. Dissolved calcium readily reacts with SMT to form insoluble precipitates that cannot be recovered (Krukowski, 1988), and therefore caution should be taken to avoid any contact between

seawater and SMT solution. Dissolved sulfides can also reduce tungstate, producing a blue solution, which can be remedied by re-oxidation of the solution using H_2O_2 (Krukowski, 1988).

9. Pellets were mixed with SMT w/ ρ = 1.5 g/mL in a slurry at a ratio of 1 mL sediment per 2 mL ρ = 1.5 g/mL SMT. Samples were vortexed and shaken to produce a slurry.

10. 10 x 1 mL of SMT-sediment slurry was sampled into 2 mL tubes for downstream DNA extraction, constituting samples of the 'bulk' sediment, effectively control samples for use in downstream community analysis. Exposure to 1.5 g/mL SMT was important for these control samples, as SMT can interact with downstream PCR (Harrison and Orphan, 2012).

11. Samples of SMT-sediment slurry were diluted with nonsterile DI and pelleted by centrifugation for 30 s at 10000× g. Supernatant was decanted into a 500 mL Pyrex bottle used later to recycle SMT (steps **22-23**).

12. The following wash steps were performed simultaneously with step 13 below. Three washes of the pellets were then performed by addition of 1.5 mL 1X PBS to tubes and repeated centrifugation at 10000× g for 30 s. After washing, samples were frozen at -20˚C for DNA extraction, fixed for 1 hr in 2% paraformaldahyde (PFA) at RT for FISH, or washed in DI and air dried for mineralogical analysis. PFA-fixed samples were washed 3 times with 1X PBS after fixing and resuspended in 1:1 1X PBS:EtOH and stored at -20˚ C.

13. 1 mL of SMT-sediment slurry was overlain on the 4 mL ρ = 2.9 g/mL SMT added to each 5 mL tube.

14. Density separation was then performed by centrifugation using a Beckman-Coulter Allegra X-14 at 2000× g for 2 min at RT. 2 min was determined as a sufficient centrifugation time that maximizes the proportion of pelleted material while minimizing time of exposure of microorganisms to SMT solution (Supp. Fig. 1).

15. Supernatant sediment, forming a cohesive layer, was pipetted out of 5 mL tubes and into new sterile 5 mL tubes using a 5000 µL pipette, with the first 5 mm of the pipette tip cut off using a razor blade. This modification enables removal of the cohesive layer without perturbing the density gradient, improving the reproducability and mineralogical purity of the separation.

16. After the cohesive layer is pipetted into new 5 mL tubes, the remaining SMT solution was pipetted out of the original tubes and into the new tubes along with the cohesive layer, taking care to not disturbe the pellet in the original tubes.

17. 1 mL filter- and UV-sterilized DI was then added to each of the new tubes, which diluted the SMT to ρ = 2.4 g/mL.

18. Simultaneously, the new tubes with SMT ρ = 2.4 g/mL were centrifuged as in step 14 and the original tubes (containing pellets w/ ρ > 2.9 g/cc) were washed and frozen following step 12, with the modification that samples were pooled in one 2 mL tube.

19. After centrifugation, supernatant sediment in new tubes with SMT ρ = 2.4 g/mL (sediment fraction with 2.4 g/cc < ρ < 2.9 g/cc) were removed by 5000 µL pipette as in step 15 and pipetted into 2 mL tubes for subsequent washing as in step 12.

20. At the same time, pelleted material (ρ < 2.4 g/cc) was carefully pipetted out into 2 mL tubes for washing following step 12.

21. Remaining SMT and contaminating sediment was decanted into the 500 mL Pyrex bottle to be used for SMT recycling.

22. SMT recycling was performed by decanting sediment-contaminated SMT along with the remaining 1.5 g/mL SMT from step 6 into the 0.2 µm filter flask used in step 2.

23. After vacuum filtration, SMT filtrate $\rho \approx$ 2.4 g/mL was densified by evaporation, by decanting filtrate into a 500 mL Pyrex bottle with stir bar placed on a hot plate set to 50˚ C. Densification then proceeded for the next ~4 hr by evaporation, assisted by flow of compressed air passed through a 0.2 µm filter at the end of a hose directed into the Pyrex bottle. Subsamples were taken every ~1 hr to track SMT density by pipetting out 1 mL SMT into 1 mL nonsterile DI in a weighed 2 mL tube, taking care to pipette up and down several times into DI to ensure all SMT was successfully pipetted out. The 2 mL tube was then weighed to assay SMT density.

24. After SMT was successfully redensified to ρ = 2.9 g/mL, filter and UV sterilization was performed as in steps 2-3. SMT can be recycled many times but the formation of insoluble calcium tungstate will eventually remove enough tungstate to require purchase of new SMT powder.

Application of this protocol to incubations of methane seep sediment maintained under AOM conditions in the laboratory (see below) yielded three density fractions, the bulk sediment control, and the porewater fraction from initial centrifugation of sediment samples. For each sediment sample, seven replicate separations were performed for statistical robustness in downstream community analysis. Fractions from five of the separations were frozen at -20˚C for DNA extraction, fractions from the fourth separation

were not frozen but washed in DI and dried for mineralogical analysis, and fractions from the fifth separation was fixed for 1 hr with 2% PFA. Every separation yielded 2 replicate samples in each fraction. Thus, the five replicate separations for downstream DNA extraction yielded dense (ρ > 2.9 g/cc, n = 5), intermediate (2.4 < ρ < 2.9 g/cc, n = 10), and light (ρ < 2.4 g/cc, n = 10) fractions as well as samples of the bulk control (n = 10). Only 5 samples of the dense fraction were acquired as the small mass of dense minerals in these samples required pooling for successful PCR amplification.

Sample Collection, Processing, and Incubation

Sediment samples analyzed in this study were collected by push core using the ROV *Doc Ricketts* of the R/V *Western Flyer* during a cruise in October 2013 and the ROV *JASON* II of the R/V *Atlantis* in September 2011 (AT18-10) to seafloor methane seep sites in Santa Monica Basin, California, and Hydrate Ridge North, Oregon, respectively. Push core (PC) samples were recovered from seafloor methane seep sites in Santa Monica Basin (PC-KD: 33.640056, -118.800278, 898 mbsl) and Hydrate Ridge North (sample 5133: 44° 40.03N, 125° 6.00W, 600 mbsl). PC-KD, a long (24 cm) push core sample, was homogenized shipboard by preparation of a sediment slurry, and was sealed an Ar-sparged mylar bag and stored at 4˚ C for laboratory-based incubation experiments. Sample 5133 was derived from a PC sectioned by sediment depth horizons that were subsequently transferred to Pyrex bottles, slurried with filtered seawater, sparged with CH_4, and sealed with butyl stoppers (Skennerton et al., 2016). Seawater samples were collected proximal to

methane seep sites with Niskin bottles, and collected seawater was filter-sterilized on board and placed in sterile 2 L Pyrex bottles. Laboratory incubation experiments were performed by mixing N_2-sparged filter-sterile seawater with sediment samples at a ~2:1 sediment to seawater ratio in sterile 500 mL Pyrex bottles continuously sparged with N_2 to maintain anoxia. Incubations were sealed with butyl stoppers and pressurized with CH_4 to maintain AOM conditions. Every ~6 months, water from the bottle incubations was removed and were refreshed with filter-sterilized N_2-sparged seawater to maintain a steady supply of sulfate and prevent buildup of sulfide.

X-ray Diffractometry

The mineralogy of density-separated methane seep sediments was characterized in part by use of X-ray diffractometry (XRD). Air-dried samples of mineral fractions and the bulk control were resuspended in 1000 µL DI and 200 µL each were spotted onto round glass slides (diameter 1.5 cm) for fitting into the XRD holder. After air drying, samples were analyzed by a PANalytical X-Pert Pro (Malvern Panalytical, Malvern, UK) housed in the Department of Applied Physics and Materials Science at Caltech. Scans were performed between 3.5 – 65˚ 2θ with a step size of 0.008˚ 2θ and step time of 1 s. The a Cu anode source was set to 45 kV and 40 mA. Peak-matching to JCPDS mineral standards was performed on XRD spectra using X'Pert Highscore software (Malvern Panalytical). Peak-matching was performed by first using the "Search Peaks" function with parameters: minimum significance = 25, minimum tip width = 0.5, peak base width = 1.5, method =

minimum 2nd derivative. The "Search & Match" function was then used, with the following settings: minimum score = 20, search sensitivity = 1.8, smoothing range = 1.5, threshold factor = 3.

Fourier Transform Infrared Spectroscopy

Samples analyzed by XRD were then measured by attenuated total reflectance Fourier transform infrared spectroscopy (ATR-FTIR) for further mineralogical characterization. Samples adhered by air drying to glass slides were inverted and placed onto an ATR diamond plate in a SensIR Durascope (SensIR Technologies, Danbury, CT) accessory mounted inside a Thermo Nicolet Magna 860 FTIR (Thermo Fischer Scientific, Waltham, MA, USA) housed in the Rossman Laboratory in the Division of Geological and Planetary Sciences at Caltech. Spectra were acquired at a resolution of 4 cm^{-1} between 4000 to 400 cm^{-1}. Comparison to mineral standards was then performed using the RRUFF database (rruff.info, (Lafuente et al., 2016)) and FTIR spectra aqcuired from API clay mineral standards by Prof. Rossman (http://minerals.gps.caltech.edu/FILES/ATR/myweb5/clay.htm).

Scanning Electron Microscopy

Sediment fractions were imaged by scanning electron microscopy (SEM) and analyzed for elemental composition by energy-dispersive X-ray spectroscopy (EDS). The

remaining 800 μL of each mineral fraction suspended in DI prior to XRD and FTIR analysis (see 'Sample Collection, Processing, and Incubation' above) was concentrated into a ~1 mm diameter area on a 0.2 μm EMD Millipore white polycarbonate filter (code GTTP) using a pipette. The concentrated mineral sample was cut out of the filter using a razor blade and adhered to carbon tape attached to an SEM stand. Samples were then Pd-coated (10 nm thickness) using a Cressington Sputter Coater 208HR. Samples were imaged by a Zeiss 1550VP Field Emission SEM equipped with an Oxford INCA Energy 300 X-ray EDS system housed in the Division of Geological and Planetary Sciences at Caltech. SEM images were acquired using an electron beam energy of 10 eV and EDS point spectra were acquired with a 15 eV electron beam.

DNA Extraction and Illumina MiSeq sequencing of 16S rRNA gene

DNA was extracted from samples of methane seep sediments using the Power Soil DNA Isolation Kit 12888 following manufacturer (Qiagen, Germantown, MD, USA) directions modified for sediment samples (Orphan et al., 2001a; Case et al., 2015). The V4-V5 region of the 16S rRNA gene was amplified using archaeal/bacterial primers (Parada et al., 2016) with Illumina (San Diego, CA, USA) adapters on 5' end (515F: 5'-TCGTCGGCAGCGTCAGATGTGTATAAGAGACAG-GTGYCAGCMGCCGCGGTAA-3', 926R: 5' GTCTCGTGGGCTCGGAGATGTGTATAAGAGACAG-CCGYCAATTYMTTTRAGTTT-3'). PCR reaction mix was set up in duplicate for each

sample with Q5 Hot Start High-Fidelity 2x Master Mix (New England Biolabs, Ipswich, MA, USA) in a 15 μL reaction volume according to manufacturer's directions with annealing conditions of 54°C for 30 cycles. Duplicate PCR samples were then pooled and 2.5 μL of each product was barcoded with Illumina NexteraXT index 2 Primers that include unique 8-bp barcodes (P5 5'-AATGATACGGCGACCACCGAGATCTACAC-XXXXXXXX-TCGTCGGCAGCGTC-3' and P7 5'-CAAGCAGAAGACGGCATACGAGAT-XXXXXXXX-GTCTCGTGGGCTCGG-3'). Amplification with barcoded primers used the same conditions as above, except for a volume of 25 μL, annealing at 66°C and 10 cycles. Products were purified using Millipore-Sigma (St. Louis, MO, USA) MultiScreen Plate MSNU03010 with vacuum manifold and quantified using ThermoFisherScientific (Waltham, MA, USA) QuantIT PicoGreen dsDNA Assay Kit P11496 on the BioRad CFX96 Touch Real-Time PCR Detection System. Barcoded samples were combined in equimolar amounts into single tube and purified with Qiagen PCR Purification Kit 28104 before submission to Laragen (Culver City, CA, USA) for 2 x 250 bp paired end analysis on Illumina's MiSeq platform with PhiX addition of 15-20%.

Processing of 16S rRNA gene MiSeq sequences

Sequence data was processed in QIIME version 1.8.0 (Caporaso et al., 2010) following published methods (Mason et al., 2015). Raw sequence pairs were joined and quality-trimmed using the default parameters in QIIME. Sequences were clustered into *de*

novo operational taxonomic units (OTUs) with 99% similarity using UCLUST open reference clustering protocol and the most abundant sequence was chosen as representative for each *de novo* OTU (Edgar, 2010). Taxonomic identification for each representative sequence was assigned using the Silva-119 database (Quast et al., 2013) clustered at 99% similarity. This SILVA database had been appended with 1,197 in-house high-quality, methane seep-derived bacterial and archaeal full-length 16S rRNA sequences. Any sequences with pintail values > 75 were removed. The modified SILVA database is available upon request from the corresponding authors. Further taxonomic assignment of OTUs assigned to the SEEP-SRB1 clade was performed by aligning these 411 bp amplicon sequences to the Silva 119 database in ARB (Ludwig et al., 2004) and construction of a phylogenetic tree from full-length and amplicon 16S rRNA sequences of SEEP-SRB1 and sister clades to delineate SEEP-SRB1 subgroups (Schreiber et al., 2010). Known contaminants in PCR reagents as determined by analysis of negative controls run with each MiSeq set were also removed (Salter et al., 2014) along with rare OTUs not present in any given library at a level of at least 10 reads.

16S rRNA Amplicon Community Analysis

The QIIME-produced table of OTUs detected in the bulk control and density-separated fractions of methane seep sediment was then analyzed using community ecology packages in R versions 3.3.3 and 3.5.0 (R Core Team, 2017). Dissimilarity matrices for samples of bulk control and density-separated fractions were calculated using the Bray-

Curtis dissimilarity metric (Legendre and Legendre, 1998) by the R package *vegan* (Oksanen et al., 2009). Non-metric multidimensional scaling (NMDS) was applied to ordinate samples based on Bray-Curtis pairwise sample dissimilarities. OTUs differentially abundant in microbial communities associated with dense ($\rho > 2.9$ g/cc) sediment fractions were detected using the R package *ANCOM* (Mandal et al., 2015), selected here for its low false discovery rate (Weiss et al., 2017). OTUs identified by ANCOM were used to explore the differential abundance of other OTUs of the same taxonomy assignment by regression of OTU relative abundances onto NMDS space using the *envfit* function in *vegan*, with statistical significance ($p < 0.05$) calculated by 999 permutations. Many additional analyses were performed to provide robustness to these results (see Supplemental File 1 for code)

Correlation analysis of 16S rRNA amplicon libraries

A QIIME-produced table of OTUs detected in the density-separated fractions of methane seep sediment (excluding bulk controls) was further analyzed using the correlation algorithm SparCC (Friedman and Alm, 2012). A bash shell script (sparccWrapper.sh, written by Karoline Faust) was used to call SparCC Python scripts SparCC.py, MakeBootstraps.py, and PseudoPvals.py. First, SparCC.py calculated correlations between OTUs. MakeBootstraps.py then produced 100 shuffled OTU tables by random sampling from the real data with replacement and SparCC.py was used to calculate correlations in each of these 100 shuffled OTU tables. Finally, PseudoPvals.py calculated pseudo-*p* values for OTU correlations in the real dataset by comparison to

correlations calculated in the shuffled OTU tables. As described by Friedman and Alm, 2012, pseudo-*p*-values represent the fraction of correlation coefficients for a given pair of OTUs calculated from the 100 shuffled datasets that are greater than that calculated from the real datasets. Thus, a *pseudo*-p-values < 0.01 for a given pair of OTUs indicates that no correlation coefficient from any given shuffled dataset was greater than that calculated from our real data. Subsequent analysis of the produced tables describing magnitude and significance for OTU correlations was performed in R versions 3.3.3 and 3.5.0, using visualization packages *igraph* (Csardi and Nepusz, 2006), *circlize* (Gu et al., 2014), *ggplot2* (Wickham, 2009), and *RColorBrewer* (Neuwirth, 2014). In this study, only positive correlations (correlation coefficient > 0) between OTUs were used.

Fluorescence in situ Hybridization

To confirm the presence of microbial taxa in density-separated sediment fractions, as inferred by analysis of 16S rRNA amplicon datasets, we performed fluorescence *in situ* hybridization (FISH) using the following modification of previously published protocols (Orphan et al., 2002). Density-separated sediment fractions fixed by PFA were concentrated onto ~1 mm diameter areas on 0.2 μm white polycarbonate filters. This area of the filter was then cut out with a razor blade and placed in a 200 μL PCR tube for FISH labeling. FISH was performed overnight (18 hr) using the following modifications (G. Chadwick, pers. comm.) to previously-published protocols. A hybridization buffer at appropriate stringency was prepared along with accompanying wash buffer [33, 34] and

pre-warmed to 46˚C and 48˚C in a hybridization oven and a water bath, respectively. 5 µL of FISH probe stock (50 ng/µL) ANME-3-125 with cy3 dye (K. Dawson, pers. comm. 5'- TCCTAAGGGCAGGTTATCCA-3') and either Eub338 mix (Daims et al., 1999) or probe Seep1c-1309 (Schreiber et al., 2010) in cy5 was added to 40 µL hybridization buffer along with filter sections. After 18 hr hybridization, filters were removed and incubated for 20 min at 48˚C in 200 µL wash buffer. Filter sections were then removed and briefly dipped in deionized water and placed on Superfrost Plus slides (Thermo Fischer Scientific) to dry at room temperature in the dark. 10 µL 4,6-diamidino-2-phenylindole (DAPI, Sigma-Aldrich) dissolved in Citifluor (Electron Microscopy Sciences) was applied to filter sections and left to incubate for 15 min in the dark. A cover slip (No. 1.5, VWR, Radnor, PA, USA) was then placed on each filter. Hybridized samples were illuminated using an XCite Series 120Q fluorescence source and imaged with a Qimage QIClick camera attached to an Olympus BX51 epifluorescence microscope with 60x (Olympus PlanApo N Oil, N.A. 1.42) and 100x (Olympus UPlan FL N Oil, N.A. 1.30) objectives. Imaging software cellSens Dimension was used to acquire images. Composites of epifluorescence images were produced using the image processing software Q-Capture Pro 7.

RESULTS

Density Separation by SMT Yields Three Mineralogically-Distinct Fractions

The efficacy of the density-separation protocol presented here was assayed by characterizing the mineralogy of density fractions. Methane seep sediment samples from both Hydrate Ridge North (sample 5133) and Santa Monica Basin (sample PC-KD) were

both separated by density and analyzed in parallel by XRD, FTIR, and SEM to identify mineral constituents of each fraction and by 16S rRNA amplicon sequencing to characterize the microbial communities present in each fraction. Here, we present mineralogical data from density separation of sample 5133 and microbial community data from sample PC-KD. Mineralogical data from only sample 5133 are presented here, as samples of fractions from PC-KD originally intened for mineralogical analysis were instead used for 16S rRNA amplicon sequencing to increase the size of the sequencing dataset. Sequencing data from sample 5133 as well as samples of seep sediment from Costa Rica (samples 10073, 10003-10007) are not shown as our separation protocol did not yield insight into microbial communities found in fractions rich in conductive minerals.

XRD analysis of dense (ρ > 2.9 g/cc), intermediate (2.4 < ρ < 2.9 g/cc), and light (ρ < 2.4 g/cc) density fractions of methane seep sediment sample 5133 documented distinct mineralogical compositions in each fraction. Automated analysis of XRD spectra identified magnetite and pyrite in the dense fraction (Fig. 2, Table 1). Several significant peaks were not identified by X'Pert Highscore, most notably (counts > 30) those at 2θ = 8.4˚, 10.2˚, 12.2˚, 17.4˚ (Table 1). XRD analysis of the intermediate fraction catalogued peaks assigned to quartz and calcite (Fig. 2, Table 2), and several without a peak assignment, including those at 2θ = 8.8˚, 12.4˚, 21.9˚, 24.1˚, 27.8˚ (Table 2). XRD analysis of the light fraction identified only quartz and halite, with peaks not identified also observed with peak maxima at 2θ = 8.6˚, 12.3˚, 18.6˚, 19.5˚, 21.8˚, 23.5˚, 27.6˚, and 29.6˚ (Table 3). A large, broad peak not detected by the automated peak identification algorithm was also observed in the light fraction at 2θ ≈ 6˚ (Fig. 2).

Spectra collected by FTIR performed on of density-separated methane seep sediment samples complemented XRD analysis, revealing three mineralogically-distinct fractions. FTIR spectra collected from the dense fraction displayed absorbance peaks at 454, 509, 1012, 1451, 1636, 3424, and 3601 cm^{-1}. Comparison to FTIR spectra from the RRUFF database (Lafuente et al., 2016) corroborated XRD characterization of this fraction as FTIR of pyrite (RRUFF ID R050070) and magnetite (R080025) closely matching a patten of increasing absorbance at wavenumbers >1200 cm^{-1} (Fig. 3). FTIR detected clays in this fraction not observed in XRD spectra, with peaks at 454, 509, and 1012 cm^{-1} matching a FTIR spectrum of illite (H-36, Morris, Illinois) closely (Fig. 3). The XRD spectrum for this fraction did not detect clay minerals, but this may have been a result of the absence of extensive clay mineral standards in the X'Pert Highscore database or the inherent challenges of characterizing clay minerals, the identification by XRD of which can require specialized techniques (Moore and Reynolds, 1997).

FTIR spectroscopy performed on the intermediate density fraction further corroborated XRD analysis of that fraction, with promenent absorbance peaks at 880 cm^{-1} and 1422 cm^{-1} matching absorbance peaks from a FTIR spectrum collected from a calcite sample (Fig. 3). FTIR spectra of this fraction also displayed spectroscopic features possibly indicating the presence of other Ca carbonates dolomite or aragonite, such as a shoulder to the 1418 cm^{-1} peak in the sample spectrum at 1460 cm^{-1} (Supp. Fig. 2); dolomite or aragonite was not detected by automated peak matching for XRD scans. There also appeared to be significant clay in this fraction, demonstrated by a close match between the sample spectrum and that of an illite standard (Fig. 3).

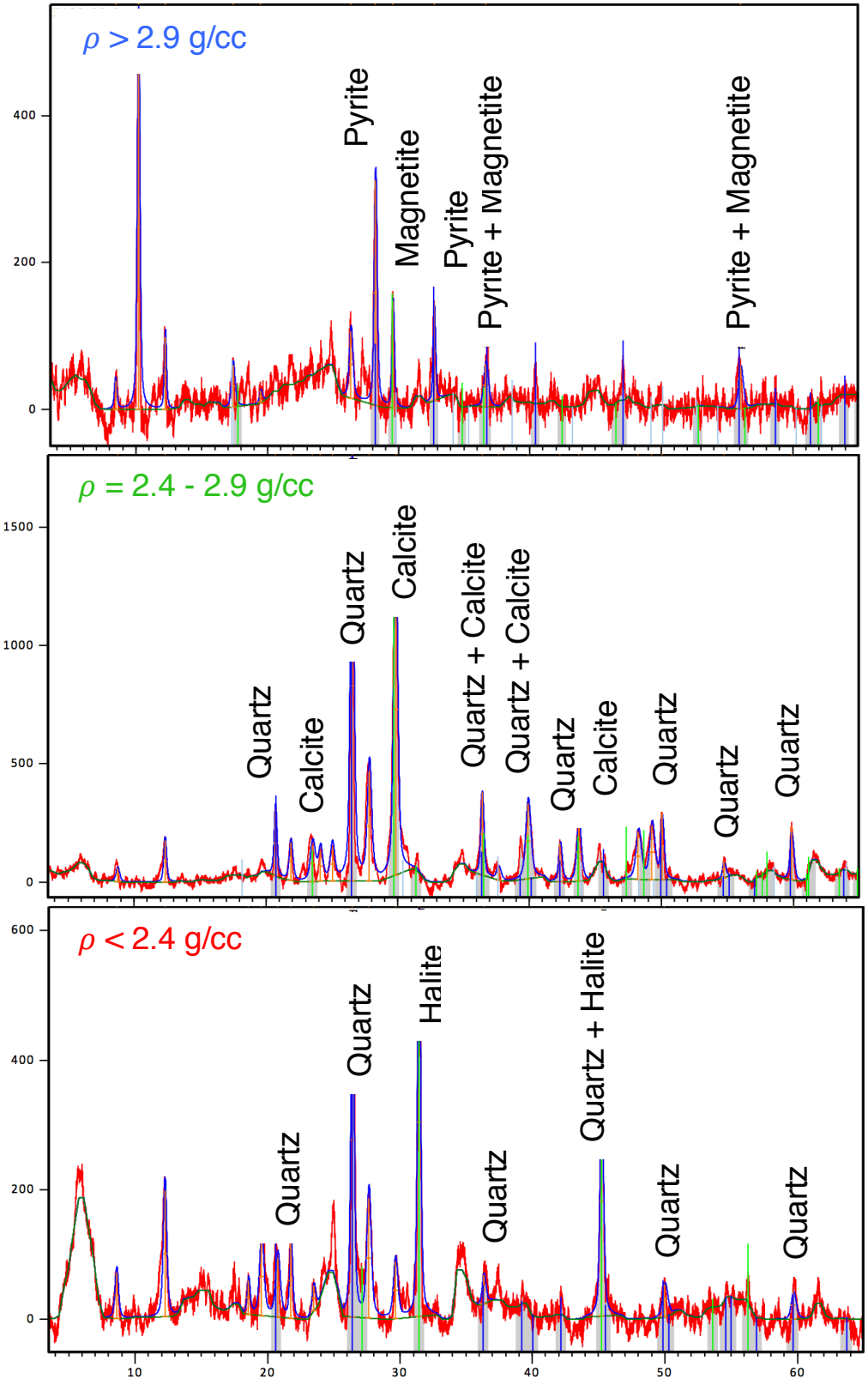
ρ > 2.9 g/cc
Pyrite
Magnetite
Pyrite
Pyrite + Magnetite
Pyrite + Magnetite
400
200
0
ρ = 2.4 - 2.9 g/cc
Quartz
Calcite
Quartz
Calcite
Quartz + Calcite
Quartz + Calcite
Quartz
Calcite
Quartz
Quartz
Quartz
1500
1000
500
0
ρ < 2.4 g/cc
Quartz
Quartz
Halite
Quartz
Quartz + Halite
Quartz
Quartz
600
400
200
0
10
20
30
40
50
60

Figure 2. Representative X-ray diffraction (XRD) spectrum of the dense (*top*, $\rho > 2.9$ g/cc), intermediate (*middle*, $2.4 < \rho < 2.9$ g/cc), and light (*bottom,* $\rho < 2.4$ g/cc) mineral fraction sfrom density-separated methane seep sediment, with peaks identified and annotated by best-fit mineral from powder-diffraction standards.

FTIR spectroscopy corroborated XRD observations for the light density fraction, with prominent absorbances at 419, 524, 1000, 1461, and 1644 cm^{-1}, and a broad peak at ~3430 cm^{-1}, all matching equivalent absorbances from a montmorillonite standard (H-24, Otay, California; Fig. 3). While automated analysis XRD spectrum of this sample did not detect clay minerals, possibly for the same reasons discussed above for the intermediate density fraction, we inferred the presence of clays from the XRD spectrum in this fraction by the observation of a broad peak at $2\theta \approx 6^{\circ}$ (Fig. 2), approximately equivalent to the basal 001 reflection for montmorillonite between $2\theta = 6.3^{\circ} – 6.6^{\circ}$ (rruff.info, R110053).

Taken together, the XRD and FTIR data supported the inference that our density-separation protocol yielded three fractions of sediment distinguished by mineralogy. The dense fraction was composed of pyrite and magnetite with minor (only observed by FTIR) clays, the intermediate fraction consisted of calcite and minor clays, and the light fraction contained only clays. We thus concluded that we could apply our protocol to acquire three mineralogically-distinct fractions: a silicate-rich fraction ($\rho < 2.4$ g/cc), a carbonate-rich fraction ($2.4 < \rho < 2.9$ g/cc), and a fraction rich in iron sulfides and oxides ($\rho > 2.9$ g/cc). We used this nomenclature to describe the fractions for the remainder of the study.

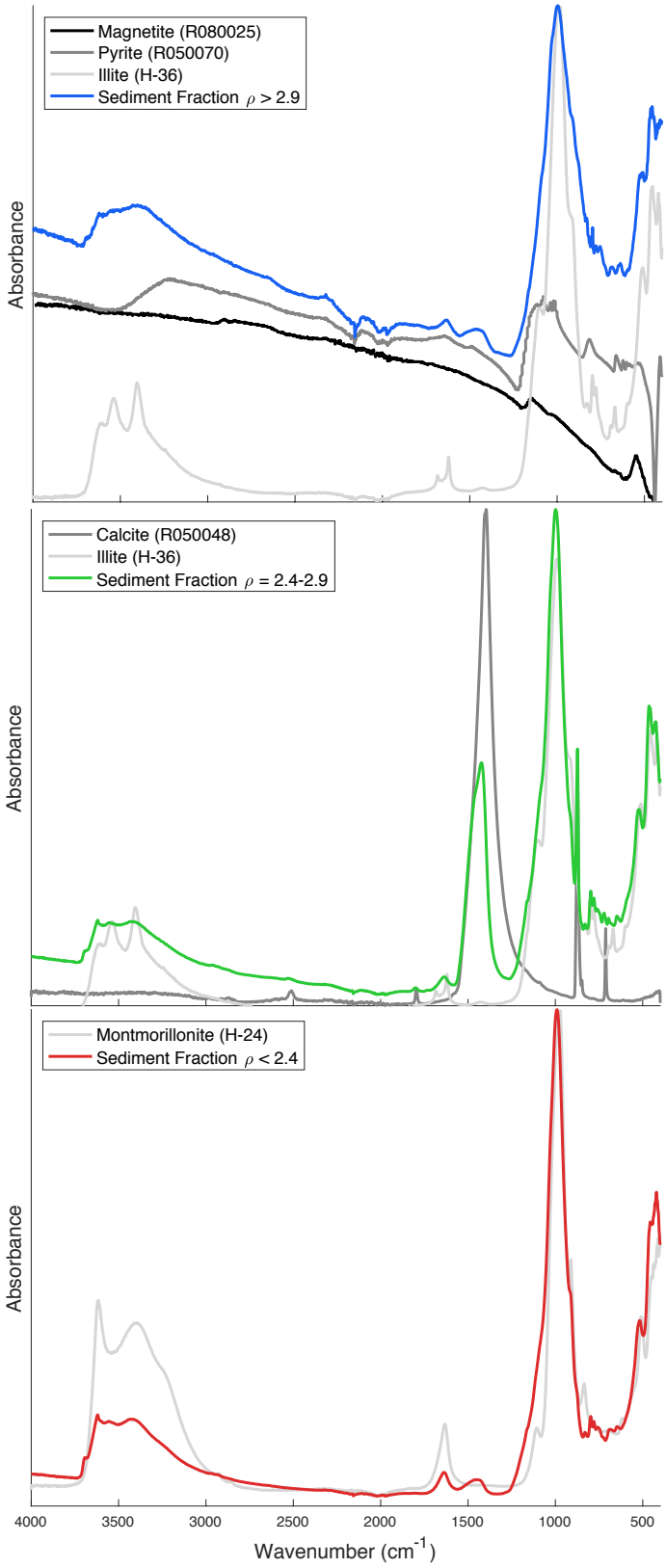
Magnetite (R080025)
Pyrite (R050070)
Illite (H-36)
Sediment Fraction ρ > 2.9
Absorbance
Calcite (R050048)
Illite (H-36)
Sediment Fraction ρ = 2.4-2.9
Absorbance
Montmorillonite (H-24)
Sediment Fraction ρ < 2.4
Absorbance
4000
3500
3000
2500
2000
1500
1000
500
Wavenumber (cm-1)

Figure 3. Representative FTIR spectra of the dense (*top*, blue), intermediate (*middle*, green), and light (*bottom*, red) fractions of density-separated methane seep sediment. Spectra were normalized to maximum absorbance equal to 1. Spectra from minerals in the RRUFF database (Lafuente et al., 2016) and from API clay mineral standards are underlain for comparison; minerals were selected on the basis of their identification in XRD spectra collected from thesame density fractions (Fig. 2).

Given our successful enrichment of conductive minerals magnetite and pyrite in the iron sulfide/oxide-rich fraction, we wanted to characterize the microscale nature of this fraction by SEM. Optical microscopy performed on this fraction documented abundant 10-25 μm diameter clusters of ~2-5 μm diameter framboidal solid phases that appeared highly reflective under reflected light (Fig. 4). Epifluorescent imaging using a DAPI stain documented ~1 μm diameter signal colocalized with outer surfaces of reflective framboids (Fig. 4). Subsequent correlated SEM imaging revealed DAPI signal to be correlated with ~1 μm rods adhered to framboid surfaces. EDS point spectra characterized the framboidal phases as Fe and S rich (data not shown). Together with the FTIR and XRD data, we inferred from our correlated fluorescence and electron microscopy observations that the iron sulfide/oxide-rich fraction contained abundant pyrite framboids with adhered microbial cells.

16S rRNA Amplicon Sequencing of Density Fractions Reveals Mineral-Associated Microbial Communities

Application of the density separation protocol to methane seep sediments from Santa Monica Basin (sample PC-KD) yielded 5 iron sulfide/oxide-rich fractions, 10

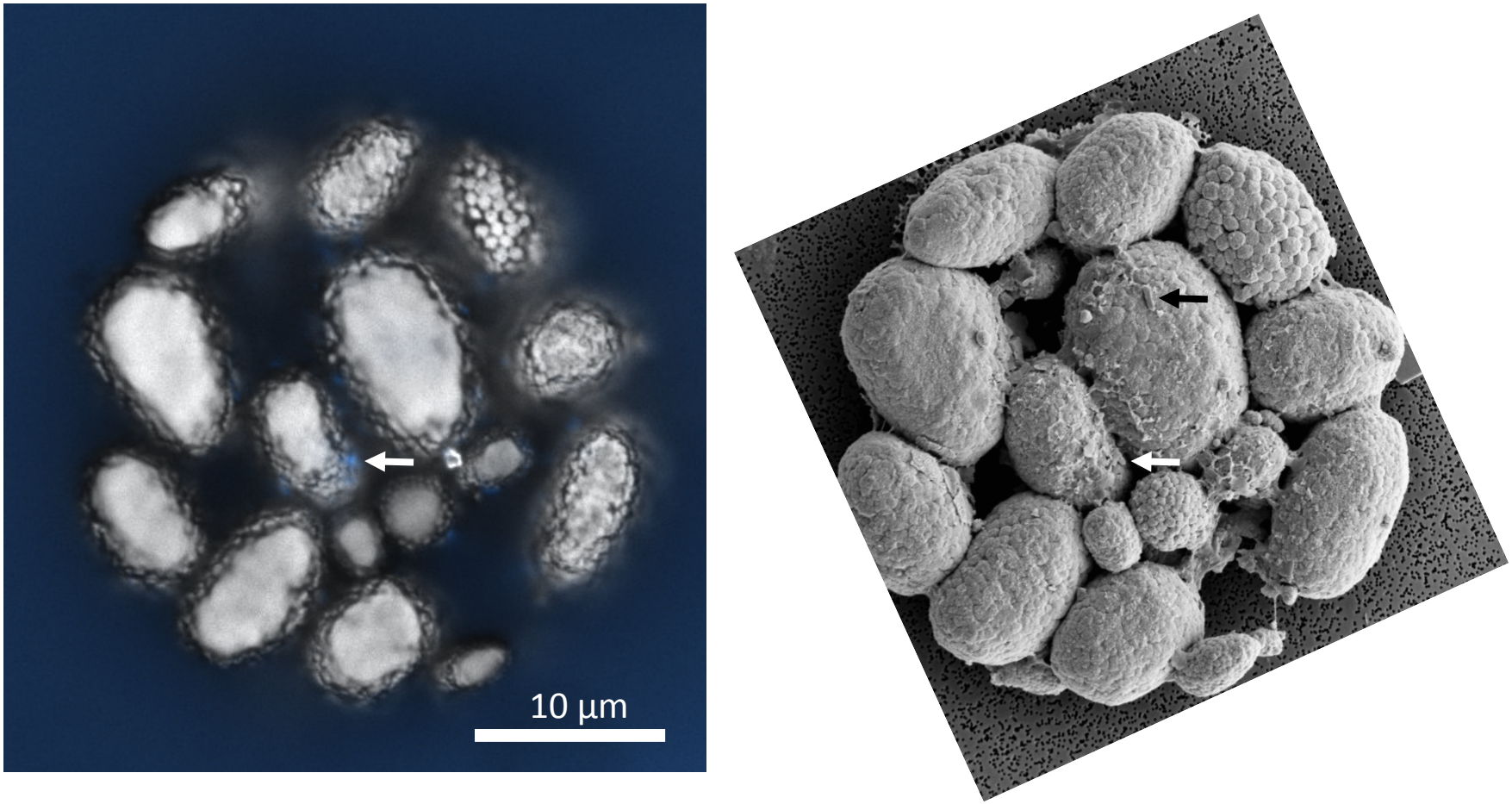

Figure 4. Correlated epifluorescence (left) and scanning elecctron microscopy (to scale, right) imaging documenting an aggregate of Fe sulfides (composition confirmed by EDS, data not shown) in a sample of the dense (ρ > 2.9 g/cc) sediment fraction, featuring attached cells visible by DAPI stain and under SEM (arrows).

carbonate-rich fractions, 10 silicate-rich fractions, and 10 bulk control samples. Of these, PCR amplification all using 30 PCR cycles was successful in all 5 iron sulfide/oxide-rich fractions, 9 carbonate-rich fractions, 9 silicate-rich fractions, and 7 bulk sediment controls. QIIME processing of amplicon sequences prepared from these 30 samples yielded 875 OTUs after filtering in R.

16S rRNA amplicon sequencing of the bulk sediment controls revealed a microbial community in the bulk sediment controls dominated by ANME subtypes ANME-2a/b, ANME-2c and ANME-3 (Fig. 5). OTUs assigned to the common ANME partner SEEP-SRB1 (Schreiber et al., 2010) were found to be the second-most-abundant group of OTUs. OTUs assigned to archaeal Marine Benthic Groups B and D, the bacterial SEEP SRB2 clade, and to the deeply-branching Atribacteria were observed to be minor members of the bulk community.

Comparison of 16S rRNA community profiles between the bulk sediment controls and the iron sulfide/oxide-rich fraction revealed ANME-3 OTUs to be differentially abundant in this fraction. ANME-3 OTUs constitute a larger portion of the total number of reads in the iron sulfide/oxide-rich fraction, comprising 15 ± 2.6% of all reads in this fraction compared to only ~2.5% of the reads in the bulk sediment controls (Fig. 5). Comparison of the relative abundance of the 78 ANME-3 OTUs across all density fractions documented higher ANME-3 OTU abundance correlated with fraction density (Fig. 6), with the ANME-3 OTU population dominated (~80% of ANME-3 reads) by 4 OTUs.

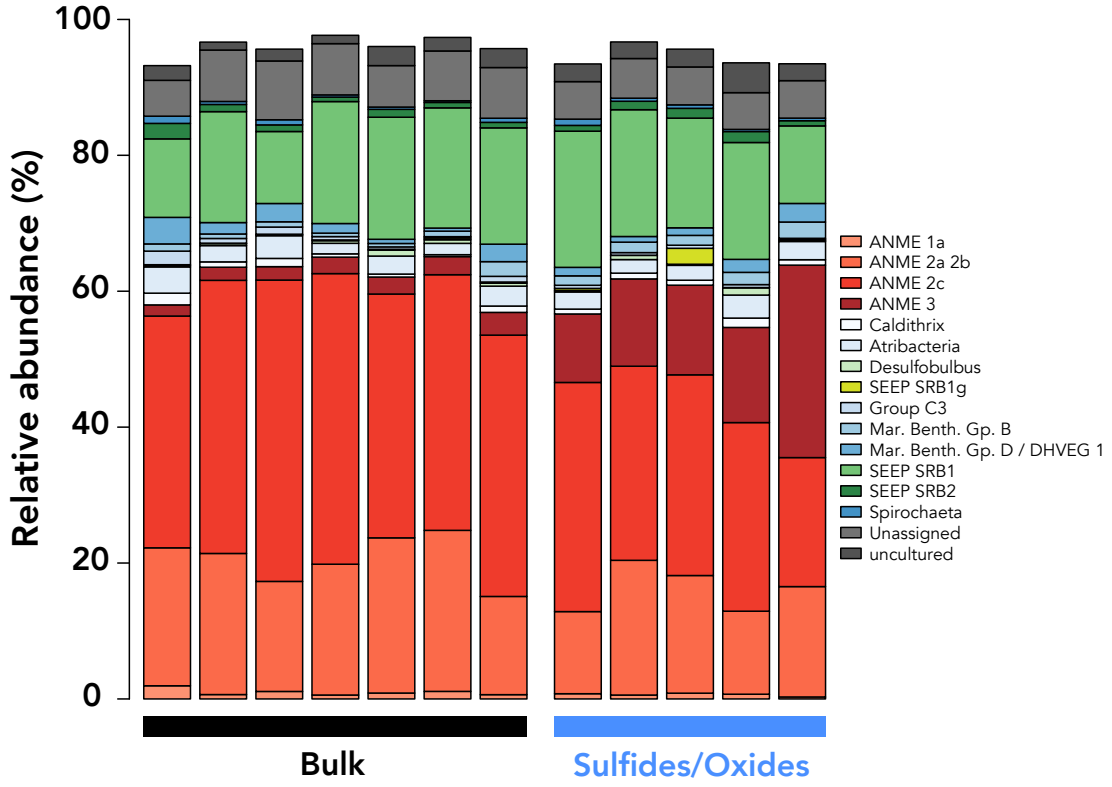

Figure 5. Stacked bar plot comparing relative abundance of OTUs, clustered by taxonomy assignment at a family level according to NCBI taxonomy assignments in Silva-119 (Quast et al., 2013), between bulk sediment controls and density-separated fractions rich in iron sulfides and iron oxides. Bars are replicate samples, and are ordered on increasing abundance of ANME-3 OTUs.

Silicate-rich density fractions, with average density lower than that of the bulk sediment, were shown to have fewer ANME-3 reads than bulk sediment controls (Fig. 6). Ordination of sample pairwise dissimilarity by NMDS identified the 16S rRNA community profiles for the iron sulfide/oxide-rich fraction to be more dissimilar to the bulk controls than other density fractions (Fig. 7). Regression of OTU relative abundance onto the NMDS ordination revealed all significant ($p < 0.05$) ANME-3 OTU vectors were correlated with iron sulfide/oxide-rich fractions (Fig. 7). Consistent with the observation that ANME-3

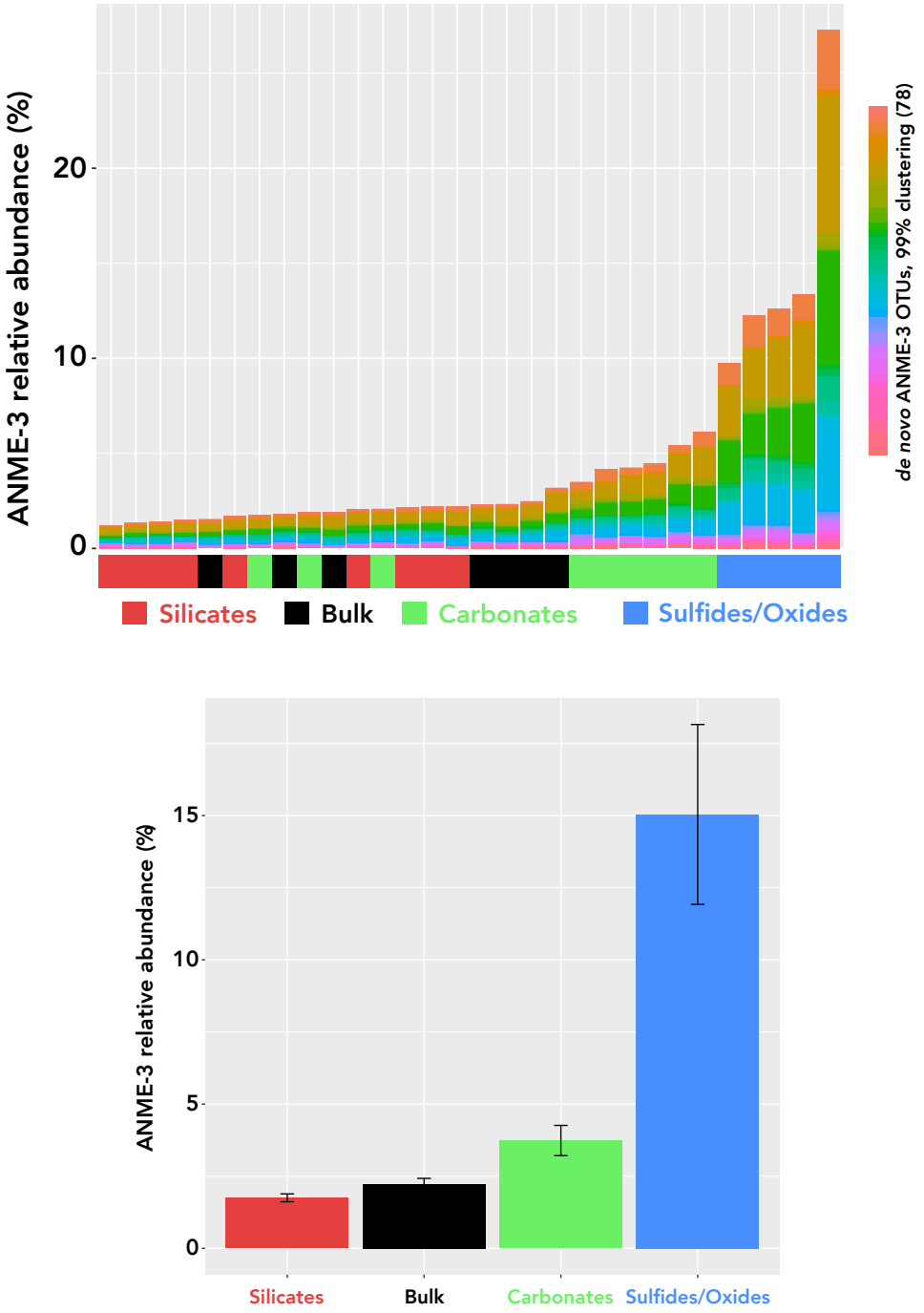

Figure 6. *Top,* stacked bar plots comparing relative abundance of ANME-3 OTUs across all density-separated sediment fractions, with each bar representing a replicate sample. Samples are ordered by increasing total abundance of ANME-3 OTUs and are annotated by density fraction. *Bottom,* mean relative abundance of all ANME-3 OTUs in density-separated fractions ordered by ANME-3 OTU abundance.

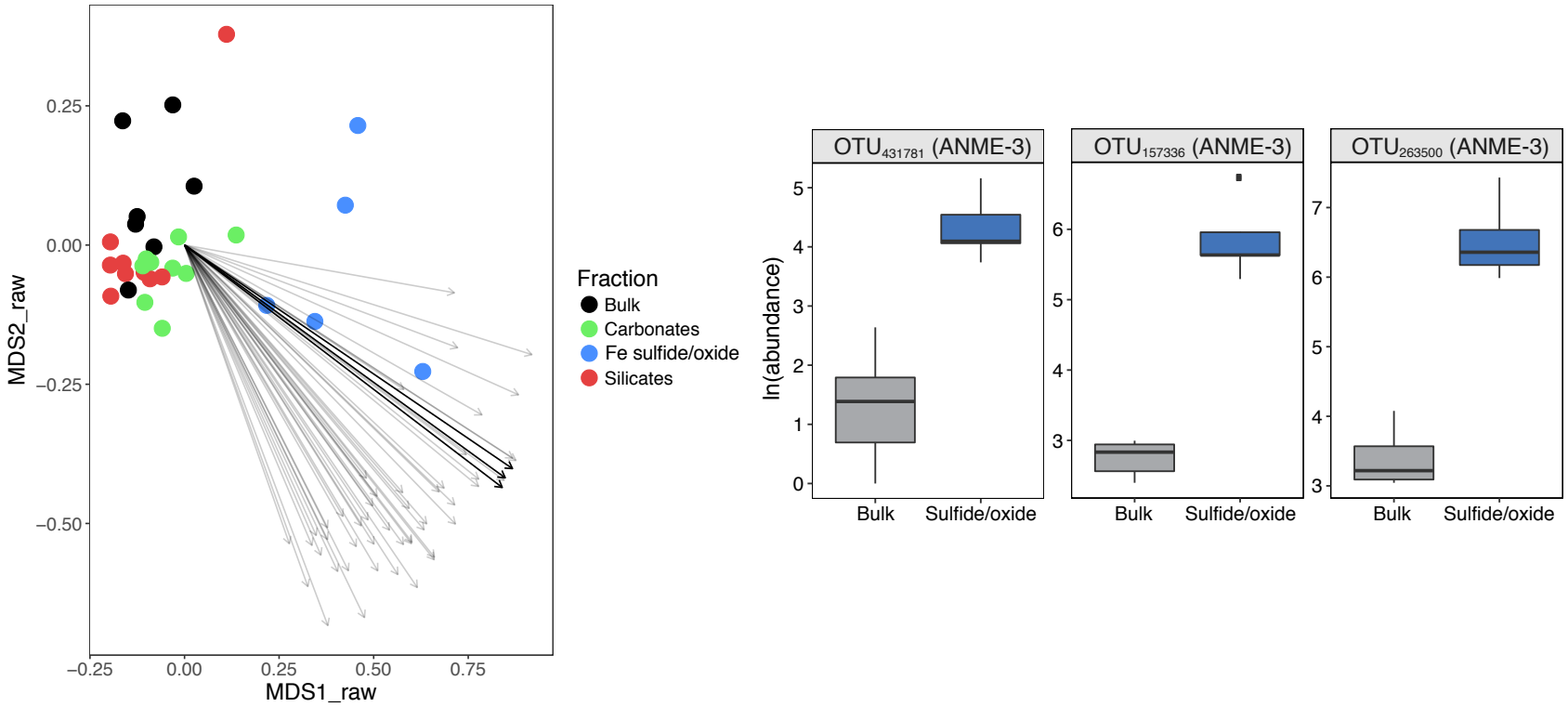

Figure 7. *Left*, NMDS plot displaying differences in 16S rRNA community composition of density-separated methane seep samples from Santa Monica basin, as measured by Bray-Curtis dissimilarity. Replicates are colored by the XRD- and FTIR-identified mineralogy of the density fraction from which DNA was extracted and amplified. Arrows represent regressions (using *envfit*) of ANME-3 OTU relative abundance onto Bray-Curtis NMDS space; light arrows are *envfit* regressions ($p < 0.05$) and dark arrows are *envfit* regressions for OTUs detected to be differentially abundant by ANCOM ($p < 0.05$, Mann-Whitney *U* test, B-H adjusted). *Right*, subset of OTUs detected to be differentially abundant in ($p < 0.05$, Mann-Whitney *U* test, B-H adjusted) the dense, sulfide/oxide-rich fraction relative to the bulk control.

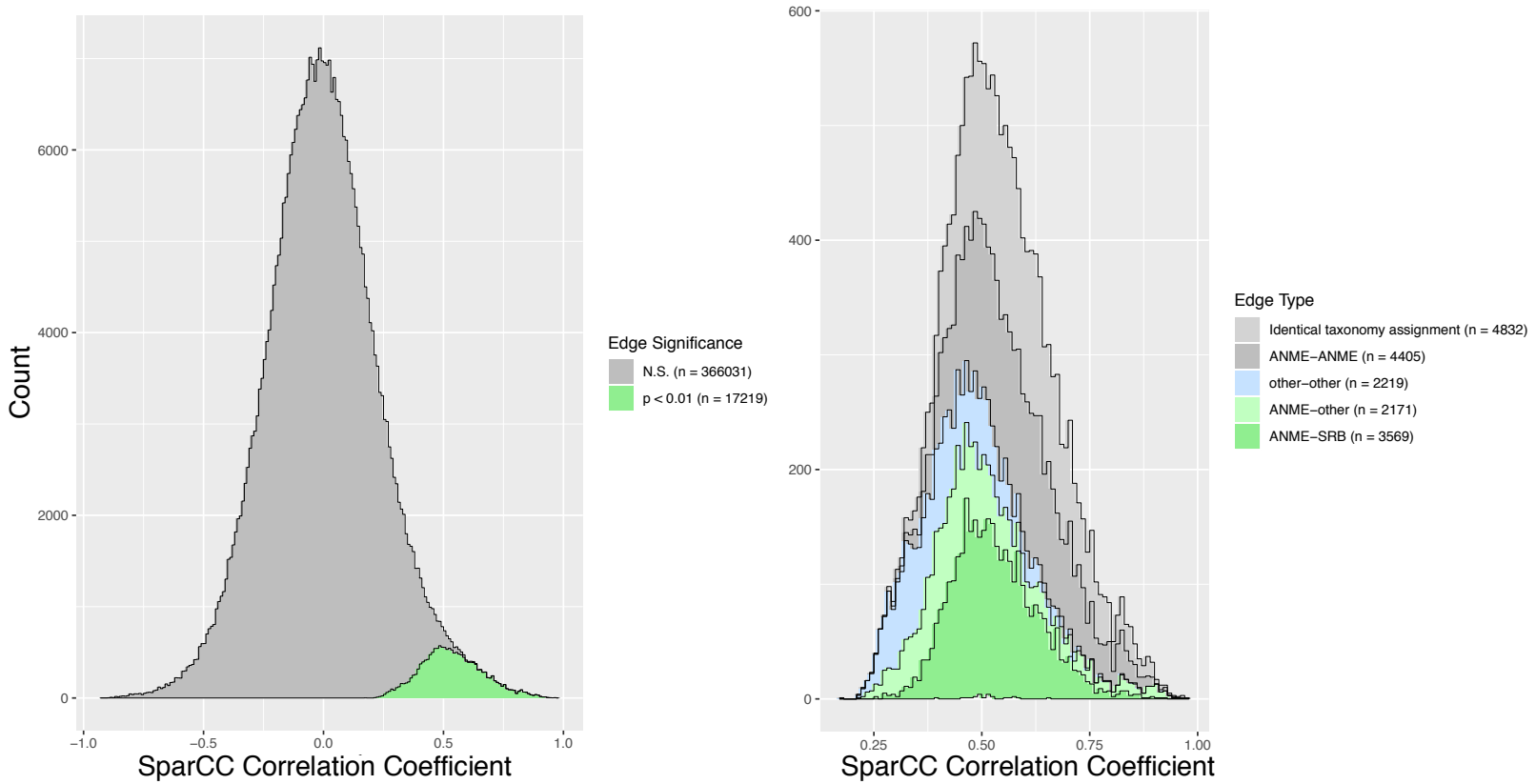

Figure 8. Stacked histograms illustrating the distribution of SparCC-calculated correlations between 16S rRNA amplicon sequences from all density-separated fractions, excluding bulk sediment controls. *Left*, comparison of correlations deemed significant on the basis of bootstrap-calculated pseudo-*p*-values < 0.01 (green) with those not calculated to be significant (*'N.S.'*, in gray). *Right*, significant correlations broken down by the taxonomy assignment of each OTU in the pair. 'SRB' are considered those taxa with assignments of known ANME-partner SRB (e.g. SEEP-SRB1) or any Deltaproteobacteria with genus-level taxonomy assignment containing the string 'Desulf' (e.g. *Desulfococcus* sp.).

OTU relative abundance is correlated with fraction density (Fig. 6), carbonate-rich fractions lie in NMDS space between iron sulfide/oxide-rich fractions and those of the bulk sediment controls (Fig. 7). The differential abundance R package ANCOM was then applied to detect differentially-abundant OTUs between the bulk sediment control and the iron sulfide/oxide-rich fraction. ANCOM detected 3 OTUs, all ANME-3, that were differentially-abundant in the iron sulfide/oxide-rich fraction ($p < 0.05$, Mann-Whitney *U* test, B-H adjusted; Fig. 7), supporting the inference from *envfit* regression that ANME-3 OTUs are preferentially found associated with magnetite and pyrite in our samples of Santa Monica Basin methane seep sediment.

Correlation Analysis of Density-Separated Methane Seep Sediment Reveals Associations Between Microbial Taxa

With the association between ANME-3 OTUs and magnetite/pyrite established by community analysis, we turned to investigate the potential partnerships between ANME-3 and different bacterial SRB clades that could possibly be detected with higher fidelity due to their co-association on pyrite and/or magnetite surfaces. We applied the correlation tool SparCC (Friedman and Alm, 2012) to the 30 16S rRNA amplicon datasets prepared from density-separated methane seep sediments, calculating 383,250 pairwise correlations between the 875 OTUs detected in our 30 samples. Of these pairs, 4.4% (17,196) had pseudo-*p*-values < 0.01, indicating the coefficients for each of these correlations exceeded that calculated for that same OTU pair in any of the 100 bootstrapped datasets (Fig. 8). The

taxonomic assignment of the constituent OTUs of correlations with pseudo-$p < 0.01$ were then inspected: 33% (5,740) of correlations with pseudo-$p < 0.01$ describe those involving ANME.

From this set of significant correlations, a network diagram was constructed to identify the OTUs correlated with ANME-3 OTUs, representing the microbial community adhered to conductive mineral surfaces that may be interacting with ANME-3 via co-attachement to these minerals. Examination of clusters of OTUs within this network revealed two primary communities of OTUs (Fig. 9). Of these communities, one consisted of ANME-2c, ANME-2a/b, and SEEP-SRB1 OTUs and the other centered on ANME-3 and SEEP-SRB1 OTUs (Fig. 9). SEEP-SRB1 OTU representative sequences were extracted and compared with SEEP-SRB1 full-length 16S rRNA sequences used by Schreiber and coworkers to assign subtype taxonomy (e.g. SEEP-SRB1a, SEEP-SRB1c) to these sequences (data not shown). This analysis revealed SEEP-SRB1 OTUs associated with ANME-3 OTUs in network analysis are predominantly SEEP-SRB1c, while those associated with ANME-2a/b and -2c in the network are a mix of SEEP-SRB1a and SEEP-SRB1c. Additionally, ANME-3 associate with other non-SRB taxa in the network, including several OTUs assigned to the Atribacteria and Marine Benthic Group B (now referred to as Lokiarchaeota).

FISH Documents ANME-3 in Iron Sulfide/Oxide-rich Fractions

To validate the presence of ANME-3 consortia in the iron sulfide/oxide-rich fraction, we performed fluorescence *in situ* hybridization (FISH). Epifluorescence microscopy of an aliquot of the iron sulfide/oxide-rich fraction documented several ANME-3 consortia of ~10 μm diameter (Fig. 10). Other microbial aggregates stained only by DAPI counterstain (deemed to be putative ANME-SRB consortia) were also observed, but quantification of the relative abundance of ANME-3 consortia as a proportion of total consortia was precluded given the small sample size, with total consortia observed ≤ 25. The propensity for the SMT density matrix to form precipitates via reaction with $Ca^{2+}_{(aq)}$ presented significant challenges for our FISH experiments, as these precipitates, often forming ~100 μm long crystals (data not shown), interfered significantly with FISH reactions. Reflected light microscopy revealed several ANME-3 consortia with reflective domains inferred to be reflective pyrite or magnetite on the basis that iron sulfides with composition confirmed by EDS (Fig. 4) appeared reflective. These consortia were typically ~10-15 μm in diameter, and featured ANME-3 cocci forming aggregates with a shell-type morphology similar to that previously observed for ANME-3 consortia (Lösekann et al., 2007). Application of FISH probes targeting bacterial 16S rRNA did not successfully hybridize to cells in consortia, but DAPI staining of non-ANME-3 cells in consortia suggested that bacterial cells were likely present but not labeled.

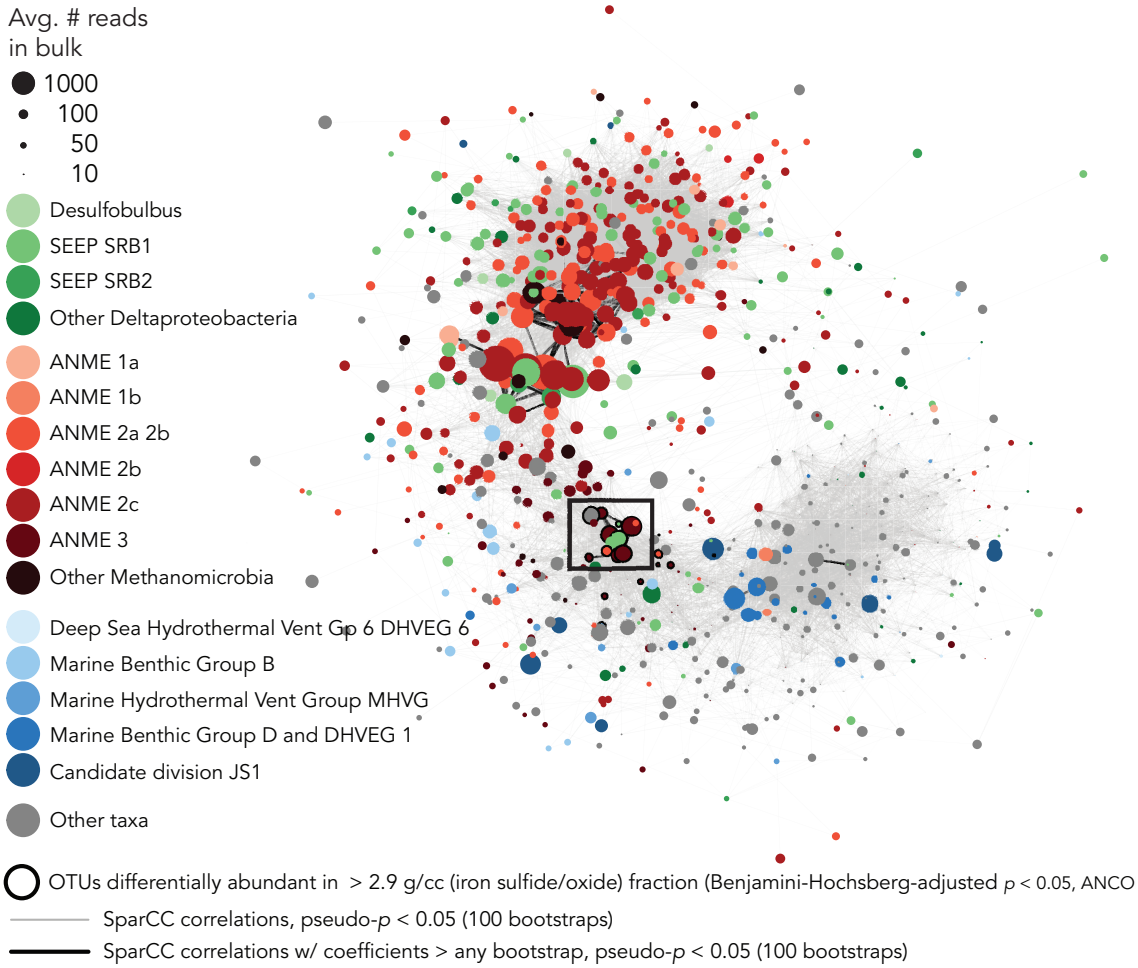
Avg. # reads
in bulk
1000
100
50
10
Desulfobulbus
SEEP SRB1
SEEP SRB2
Other Deltaproteobacteria
ANME 1a
ANME 1b
ANME 2a 2b
ANME 2b
ANME 2c
ANME 3
Other Methanomicrobia
Deep Sea Hydrothermal Vent Gp 6 DHVEG 6
Marine Benthic Group B
Marine Hydrothermal Vent Group MHVG
Marine Benthic Group D and DHVEG 1
Candidate division JS1
Other taxa
OTUs differentially abundant in > 2.9 g/cc (iron sulfide/oxide) fraction (Benjamini-Hochsberg-adjusted p < 0.05, ANCO
SparCC correlations, pseudo-p < 0.05 (100 bootstraps)
SparCC correlations w/ coefficients > any bootstrap, pseudo-p < 0.05 (100 bootstraps)

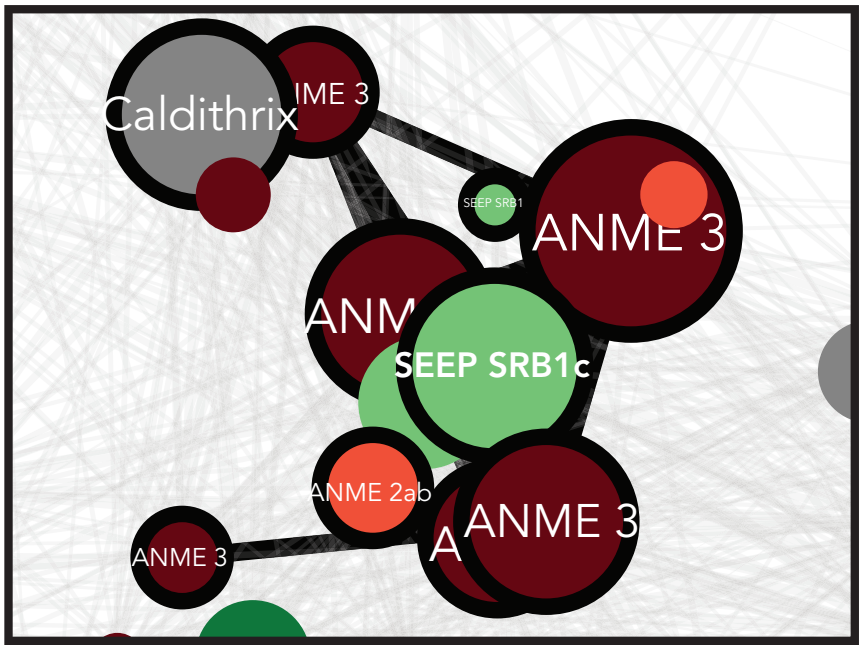
Caldithrix
IME 3
SEEP SRB1
ANME 3
ANM
SEEP SRB1c
ANME 2ab
ANME 3
A
ANME 3

Figure 9. Network diagrams constructed from SparCC-calculated (pseudo-$p < 0.01$) pairwise correlations between OTUs in density-separated methane seep sediment. *Top*, network diagram with vertices (OTUs) colored by taxonomy assignment. OTUs found to be particularily highly-correlated include ANME-3 OTUs that were found to be differentially-abundant in the iron sulfide/oxide-rich fraction (*bottom inset*); these OTUs are correlated with specific SEEP-SRB1 OTUs that fall within the SEEP-SRB1c lineage as previously defined (Schreiber et al., 2010).

DISCUSSION

Associations between sediment-dwelling microorganisms and minerals have proven challenging to parse, but are likely are important for the physiology of these microorganisms given the observations from cultures (Kato et al., 2012b; Liu et al., 2015; Tang et al., 2016) and environmental incubations (Kato et al., 2012a; Rotaru et al., 2018) that conductive minerals stimulate syntrophic EET. Previous methods and results to examine mineral-associated microbial ecology in marine sediments reported by Harrison and Orphan described density-separation protocols using SMT to yield a dense ($\rho > 2.8$ g/cc) and a light ($\rho < 2.8$ g/cc) fraction from methane seeps, but the mineralogical purity of these fractions was only examined by the elemental composition of these fractions using EDS, and microbial communities in each fraction were identified by terminal restriction fragment length polymorphism (Harrison and Orphan, 2012). Other work has used SMT to separate marine sediments by density and characterized the mineralogical purity of density fractions by XRD (Poppe et al., 1991; Poppe and Commeau, 1992; Totten et al., 2002), but no work to date has used SMT separation in tandem with next-generation Illumina sequencing of 16S rRNA amplicon libraries to reveal *in situ* microbe-mineral associations in marine sediments.

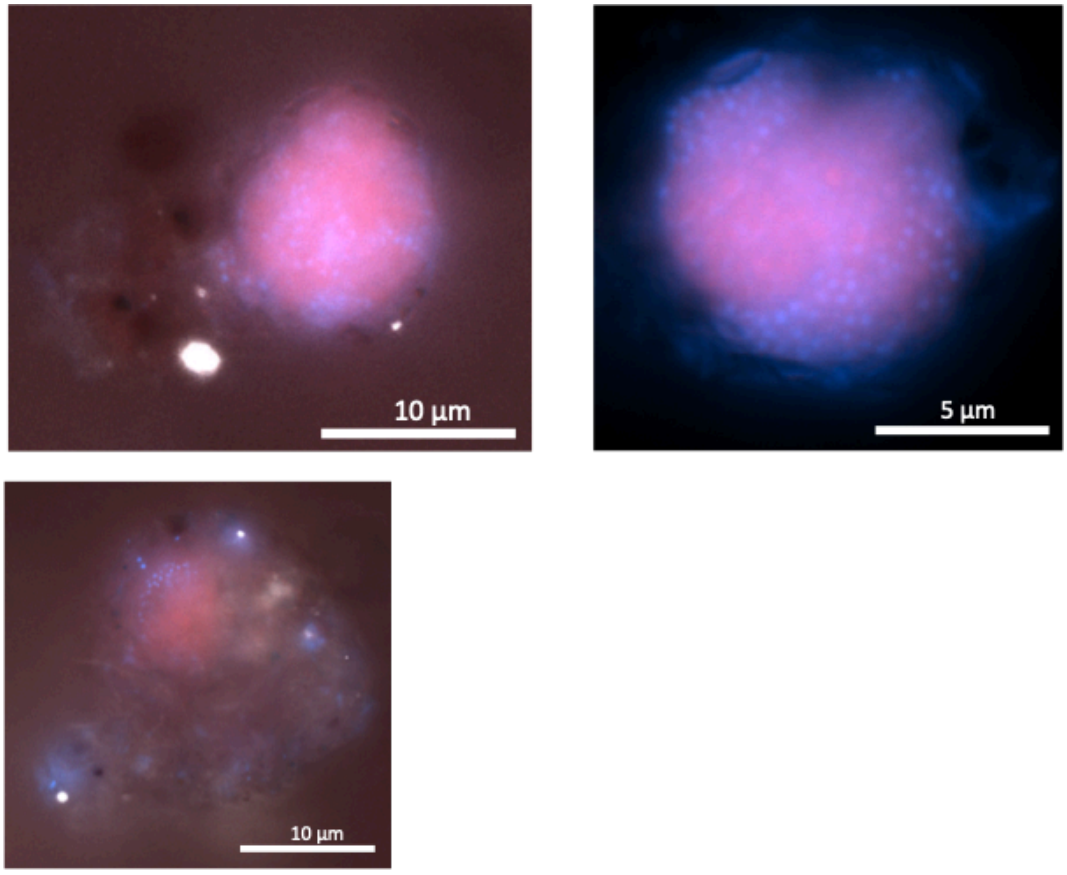

Figure 10. Reflected light and epifluorescent microscopy imaging of ANME-3—SRB consortia extracted from the iron sulfide/oxide-rich fraction. ANME-3 were labeled using FISH probe ANME-3-125 (K. Dawson, pers. comm.). Reflective domains embedded in the extracellular matrix appear as white from reflected light.

Here, we present the successful enrichment of iron sulfide/oxide-rich and carbonate-rich mineral fractions from methane seep sediments by application of SMT-based density separation to methane seep sediments. XRD (Fig. 2) and FTIR (Fig. 3) spectra acquired from the dense (ρ > 2.9 g/cc) fraction were fit by pyrite and magnetite standards. FTIR spectroscopy of the intermediate-density fraction, in contrast, documented spectra from this fraction well-matched by calcite standards (Fig. 3), corroborating XRD measurements (Fig. 2). FTIR spectra of these fraction also contained features characteristic of clay minerals, indicating either the presence of particularily dense illite (Totten et al., 2002) and/or lower-density clays adhered to magnetite or pyrite surfaces. However, we inferred that clays were significantly less abundant in these fractions in comparison with the light fraction, as XRD spectra of the dense and intermediate fractions did not detect the peak at $2\theta \approx 6^{\circ}$ observed in the light fraction (Fig. 2), interpreted as reflective of clays at significant abundance to produce prominent signal at low 2θ. Successful enrichment of these mineral fractions by density separation not only made possible downstream ecological study of mineral-associated microbial communities, but may also prove useful for future geochemical study of carbonate and sulfide mineral authigenesis in methane seep sediments.

16S rRNA amplicon sequencing of the density fractions revealed a particularily unique community associated with the iron sulfide/oxide-rich fraction. Differential abundance analysis by ANCOM detected 3 OTUs, all assigned to the ANME-3, that were significantly abundant relative to the bulk sediment (Fig. 7); no other OTUs were detected as differentially abundant in any other fraction relative to the bulk sediment control. As an

enrichment rather than purification technique, density separation using SMT results in some cross-contamination across density fractions; the elevated abundance of ANME-3 in the carbonate-rich fraction (Figs. 9, 10) is likely a consequence of this. An interpretation of the differential abundance of ANME-3 in the dense fraction to be a result of intracellular minerals such as magnetosomes that have been observed in some SRB partners to ANME-2 (McGlynn et al., 2018) seems less likely, as the volume of magnetite or pyrite adhered to or inside of a given cell must be >86-90% of the volume of the cell to achieve mean particle density > 2.9 g/cc. However, given the exceedingly high salinity of SMT solutions, dehydration could significantly reduce cell volumes during density separation. Further EM examination of ANME-3 associated with the dense fraction will be required to characterize the nature of the association.

ANME-3, first discovered in the Haakon Mosby mud volcano in the Barents Sea (Niemann et al., 2006), have also been observed at methane seep sites in the Congo Basin (Pop Ristova et al., 2012) and the Eel River Basin (Orphan et al., 2001a), but relatively less is known about their physiology compared to more common ANME subtypes such as ANME-2a. Given their preferential association with the iron sulfide/oxide-rich fraction, which by mass constituted only a small percentage (~1%) of the total mass of the bulk sediment, we inferred that ANME-3 may appear rare when characterizing the microbial community in bulk samples due to their preference for an ecological niche provided by relatively rare magnetite or pyrite grains. We speculated that this niche may provide a condiut for EET and facilitate survival in electron-donor poor AOM sediments, aiding electron transport from ANME-3 to syntrophic partners or to other electron acceptors. In a

similar manner as that observed for in syntrophic co-cultures of *Geobacter* sp. and *Methanosarcina* sp. (Rotaru et al., 2018), conductive minerals may aid in the transfer of electrons in AOM. Future research should leverage insights from recent work indicating that magnetite in particular stimulates syntrophic EET and focus on extracting magnetic minerals from marine sediments, as has been attempted previously (Harrison and Orphan, 2012. While magnetic mineral concentrations are depleted at the SMTZ relative to their concentration in sediments above and below due to diagenetic reduction of magnetite by sulfide (Roberts, 2015), these trace minerals may still host local populations of microorganisms employing mineral-facilitated EET. Anaerobic extraction methods for magnetite from marine sediments developed in this thesis (see Appendix A) were moderately successful, but future work could build on these methods to extract live microbial communities attached to magnetic minerals for downstream culturing and molecular work.

Density separation of methane seep sediments also provided new hypotheses about microbe-microbe interactions. By extracting fractions of sediment enriched in a particular mineral, density separation amplified ecological signals resulting from the co-association of certain microbial taxa on mineral surfaces. Here, we observed improved signal from correlation analysis performed on density fractions from Santa Monica Basin seep sediments (Fig. 8) relative to that observed from application of the same analysis to a ecological survey of Costa Rica seep sediments (Ch. 1, Fig . 1A, 1B). In the density-separated samples, correlation analysis detects fewer total significant correlations but those correlations have higher coefficients, indicating improved ecological signal. Microbial

communities are readily detected in density-separated samples, requiring no further thresholding of the correlation analysis to obtain insights; in contrast, performing the same analysis on ecological survey data requries a much larger dataset (~300 vs 30 samples) and more post-analysis processing to obtain ecological insights. Furthermore, ecological insights from density separation techniques describe microscale niche differentiation within a single sample, critical information for the investigation of microbial ecology *in situ*. Here, we infer a preferential association between ANME-3 and SEEP-SRB1c in the iron sulfide/oxide fraction, notable as previous microscopy study had not observed SEEP-SRB1c in association with ANME (Schreiber et al., 2010). Attempted FISH labeling of SEEP-SRB1c using published probe Seep1c-1309 (Schreiber et al., 2010) was unsuccessful, but we inferred this failure did not reflect the absence of association between ANME-3 and SEEP-SRB1c but rather a failure of the probe, designed on the basis of 8 full-length 16S rRNA sequences, to hybridize SEEP-SRB1c 16S rRNA in our samples resulting either from sequence divergence or interference from SMT. Future work should identify the SRB partner for ANME-3, which has been identified in different seep environments as SEEP-SRB1a (Schreiber et al., 2010), SEEP-SRB1c (hypothesized in this study), *Desulfobulbus* sp. (Lösekann et al., 2007), or SEEP-SRB4 (Ruff et al., 2015).

CONCLUSIONS

Here, we demonstrate statistically-significant associations between certain 16S rRNA amplicon sequences and specific minerals by application of a heavy-liquids protocol to separate minerals in marine sediments by density compatible with downstream molecular analyses. Application of this protocol to samples of methane seep sediment yielded three mineralogically-distinct fractions of methane seep sediment, with mineralogy of each fraction validated by XRD and FTIR. Community analysis of each density fraction documented a statistically-significant association between ANME-3 OTUs and a density fraction rich in magnetite and pyrite. The presence of ANME-3 in this fraction was then confirmed by FISH microscopy, and the microbial community correlated with ANME-3 in this fraction was detected by analysis of a network constructed from the using the correlation analysis tool SparCC (Friedman and Alm, 2012). Comparison of the correlation analysis results from density-separated seep sediments to those from an ecological survey of seep sediments demonstrated the capacity for this method to amplify ecological signal from microorganisms co-associating on mineral surfaces. The future application of this technique to other sediments and soils holds promise to reveal the microscale interactions between microorganisms and minerals as well as those between microorganisms.

ACKNOWLEDGEMENTS

The authors are grateful to G. Rossman for use of the FTIR and for aid in characterizing the mineralogy of the density fractions. We would further like to thank E. Trembath-Reichert for helpful discussions and advice in methods development. We also acknowledge K. Dawson for design of the FISH probe ANME-3-125 and for establishing incubation of sediment push core sample PC-KD. Funding for this work was provided by the National Science Foundation Graduate Research Fellowship and the Schlanger Ocean Drilling Fellowship (both to K.S.M.) and by the NSF Center for Dark Energy and Biosphere Investigations (to V.J.O.).

REFERENCES

Aloisi, G., Pierre, C., Rouchy, J.-M., Foucher, J.-P., and Woodside, J. (2000). Methane-related authigenic carbonates of eastern Mediterranean Sea mud volcanoes and their possible relation to gas hydrate destabilisation. *Earth Planet. Sci. Lett.* 184, 321–338. doi:10.1016/S0012-821X(00)00322-8.

Beal, E. J., House, C. H., and Orphan, V. J. (2009). Manganese- and Iron-Dependent Marine Methane Oxidation. *Science* 325, 184–187. doi:10.1126/science.1169984.

Beulig, F., Røy, H., Glombitza, C., and Jørgensen, B. B. (2018). Control on rate and pathway of anaerobic organic carbon degradation in the seabed. *Proc. Natl. Acad. Sci.* 115, 367–372. doi:10.1073/pnas.1715789115.

Boetius, A., Ravenschlag, K., Schubert, C. J., Rickert, D., Widdel, F., Gieseke, A., et al. (2000). A marine microbial consortium apparently mediating anaerobic oxidation of methane. *Nature* 407, 623. doi:10.1038/35036572.

Bowles, M. W., Mogollón, J. M., Kasten, S., Zabel, M., and Hinrichs, K.-U. (2014). Global rates of marine sulfate reduction and implications for sub–sea-floor metabolic activities. *Science* 344, 889. doi:10.1126/science.1249213.

Caporaso, J. G., Kuczynski, J., Stombaugh, J., Bittinger, K., Bushman, F. D., Costello, E. K., et al. (2010). QIIME allows analysis of high-throughput community sequencing data. *Nat. Methods* 7, 335–336. doi:10.1038/nmeth.f.303.

Case, D. H., Pasulka, A. L., Marlow, J. J., Grupe, B. M., Levin, L. A., and Orphan, V. J. (2015). Methane Seep Carbonates Host Distinct, Diverse, and Dynamic Microbial Assemblages. *mBio* 6. doi:10.1128/mBio.01348-15.

Csardi, G., and Nepusz, T. (2006). The igraph software package for complex network research. *InterJournal* Complex Systems, 1695.

Daims, H., Brühl, A., Amann, R., Schleifer, K.-H., and Wagner, M. (1999). The Domain-specific Probe EUB338 is Insufficient for the Detection of all Bacteria: Development and Evaluation of a more Comprehensive Probe Set. *Syst. Appl. Microbiol.* 22, 434–444. doi:10.1016/S0723-2020(99)80053-8.

Degnan, P. H., and Ochman, H. (2012). Illumina-based analysis of microbial community diversity. *ISME J.* 6, 183–194. doi:10.1038/ismej.2011.74.

Edgar, R. C. (2010). Search and clustering orders of magnitude faster than BLAST. *Bioinformatics* 26, 2460–2461. doi:10.1093/bioinformatics/btq461.

El-Naggar, M. Y., Wanger, G., Leung, K. M., Yuzvinsky, T. D., Southam, G., Yang, J., et al. (2010). Electrical transport along bacterial nanowires from Shewanella oneidensis MR-1. *Proc. Natl. Acad. Sci.* 107, 18127. doi:10.1073/pnas.1004880107.

Friedman, J., and Alm, E. J. (2012). Inferring Correlation Networks from Genomic Survey Data. *PLOS Comput. Biol.* 8, e1002687. doi:10.1371/journal.pcbi.1002687.

Froelich, P. N., Klinkhammer, G. P., Bender, M. L., Luedtke, N. A., Heath, G. R., Cullen, D., et al. (1979). Early oxidation of organic matter in pelagic sediments of the eastern equatorial Atlantic: suboxic diagenesis. *Geochim. Cosmochim. Acta* 43, 1075–1090. doi:10.1016/0016-7037(79)90095-4.

Garming, J. F. L., Bleil, U., and Riedinger, N. (2005). Alteration of magnetic mineralogy at the sulfate–methane transition: Analysis of sediments from the Argentine continental slope. *Phys. Earth Planet. Inter.* 151, 290–308. doi:10.1016/j.pepi.2005.04.001.

Grünke, S., Lichtschlag, A., Beer, D. de, Felden, J., Salman, V., Ramette, A., et al. (2012). Mats of psychrophilic thiotrophic bacteria associated with cold seeps of the Barents Sea. *Biogeosciences* 9, 2947–2960. doi:https://doi.org/10.5194/bg-9-2947-2012.

Gu, Z., Gu, L., Eils, R., Schlesner, M., and Brors, B. (2014). Circlize implements and enhances circular visualization in R. *Bioinformatics* 30, 2811–2812.

Harrison, B. K., and Orphan, V. J. (2012). Method for Assessing Mineral Composition-Dependent Patterns in Microbial Diversity Using Magnetic and Density Separation. *Geomicrobiol. J.* 29, 435–449. doi:10.1080/01490451.2011.581327.

Jørgensen, B. B. (2000). "Bacteria and Marine Biogeochemistry," in *Marine Geochemistry*, eds. H. D. Schulz and M. Zabel (Berlin, Heidelberg: Springer), 173–207. doi:10.1007/978-3-662-04242-7_5.

Kallmeyer, J., Pockalny, R., Adhikari, R. R., Smith, D. C., and D'Hondt, S. (2012). Global distribution of microbial abundance and biomass in subseafloor sediment. *Proc. Natl. Acad. Sci.* 109, 16213. doi:10.1073/pnas.1203849109.

Kato, S., Hashimoto, K., and Watanabe, K. (2012a). Methanogenesis facilitated by electric syntrophy via (semi)conductive iron-oxide minerals. *Env. Microbiol* 14, 1646–54. doi:10.1111/j.1462-2920.2011.02611.x.

Kato, S., Hashimoto, K., and Watanabe, K. (2012b). Microbial interspecies electron transfer via electric currents through conductive minerals. *Proc. Natl. Acad. Sci.* 109, 10042. doi:10.1073/pnas.1117592109.

Knittel, K., and Boetius, A. (2009). Anaerobic Oxidation of Methane: Progress with an Unknown Process. *Annu. Rev. Microbiol.* 63, 311–334. doi:10.1146/annurev.micro.61.080706.093130.

Krukowski, S. T. (1988). Sodium Metatungstate: A New Heavy-Mineral Separation Medium for the Extraction of Conodonts from Insoluble Residues. *J. Paleontol.* 62, 314–316.

Lafuente, B., Downs, R. T., Yang, H., and Stone, N. (2016). The power of databases: The RRUFF project. *Highlights Mineral. Crystallogr.*, 1–29. doi:10.1515/9783110417104-003.

Legendre, P., and Legendre, L. (1998). *Numerical Ecology*. 2nd ed. Amsterdam: Elsevier.

Li, H., Chang, J., Liu, P., Fu, L., Ding, D., and Lu, Y. (2015). Direct interspecies electron transfer accelerates syntrophic oxidation of butyrate in paddy soil enrichments. *Environ. Microbiol.* 17, 1533–47. doi:10.1111/1462-2920.12576.

Liu, F., Rotaru, A. E., Shrestha, P. M., Malvankar, N. S., Nevin, K. P., and Lovley, D. R. (2015). Magnetite compensates for the lack of a pilin-associated c-type cytochrome in extracellular electron exchange. *Env. Microbiol* 17, 648–55. doi:10.1111/1462-2920.12485.

Lösekann, T., Knittel, K., Nadalig, T., Fuchs, B., Niemann, H., Boetius, A., et al. (2007). Diversity and Abundance of Aerobic and Anaerobic Methane Oxidizers at the Haakon Mosby Mud Volcano, Barents Sea. *Appl. Environ. Microbiol.* 73, 3348–3362. doi:10.1128/AEM.00016-07.

Lovley, D. R. (1991). Dissimilatory Fe(III) and Mn(IV) reduction. *Microbiol. Rev.* 55, 259–287.

Lovley, D. R. (2017). Syntrophy Goes Electric: Direct Interspecies Electron Transfer. *Annu. Rev. Microbiol.* 71, 643–664. doi:10.1146/annurev-micro-030117-020420.

Lovley, D. R., Coates, J. D., Blunt-Harris, E. L., Phillips, E. J. P., and Woodward, J. C. (1996). Humic substances as electron acceptors for microbial respiration. *Nature* 382, 445–448. doi:10.1038/382445a0.

Ludwig, W., Strunk, O., Westram, R., Richter, L., Meier, H., Yadhukumar, et al. (2004). ARB: a software environment for sequence data. *Nucleic Acids Res.* 32, 1363–1371. doi:10.1093/nar/gkh293.

Luff, R., and Wallmann, K. (2003). Fluid flow, methane fluxes, carbonate precipitation and biogeochemical turnover in gas hydrate-bearing sediments at Hydrate Ridge, Cascadia Margin: numerical modeling and mass balances. *Geochim. Cosmochim. Acta* 67, 3403–3421. doi:10.1016/S0016-7037(03)00127-3.

Mandal, S., Van Treuren, W., White, R. A., Eggesbø, M., Knight, R., and Peddada, S. D. (2015). Analysis of composition of microbiomes: a novel method for studying microbial composition. *Microb. Ecol. Health Dis.* 26, 27663. doi:10.3402/mehd.v26.27663.

Marlow, J. J., Steele, J. A., Ziebis, W., Thurber, A. R., Levin, L. A., and Orphan, V. J. (2014). Carbonate-hosted methanotrophy represents an unrecognized methane sink in the deep sea. *Nat. Commun.* 5, 5094. doi:10.1038/ncomms6094.

Marsili, E., Baron, D. B., Shikhare, I. D., Coursolle, D., Gralnick, J. A., and Bond, D. R. (2008). Shewanella secretes flavins that mediate extracellular electron transfer. *Proc. Natl. Acad. Sci.* 105, 3968–3973. doi:10.1073/pnas.0710525105.

März, C., Hoffmann, J., Bleil, U., de Lange, G. J., and Kasten, S. (2008). Diagenetic changes of magnetic and geochemical signals by anaerobic methane oxidation in sediments of the Zambezi deep-sea fan (SW Indian Ocean). *Mar. Geol.* 255, 118–130. doi:10.1016/j.margeo.2008.05.013.

Mason, O. U., Case, D. H., Naehr, T. H., Lee, R. W., Thomas, R. B., Bailey, J. V., et al. (2015). Comparison of Archaeal and Bacterial Diversity in Methane Seep Carbonate Nodules and Host Sediments, Eel River Basin and Hydrate Ridge, USA. *Microb. Ecol.* 70, 766–784. doi:10.1007/s00248-015-0615-6.

McGlynn, S. E., Chadwick, G. L., Kempes, C. P., and Orphan, V. J. (2015). Single cell activity reveals direct electron transfer in methanotrophic consortia. *Nature* 526, 531–535. doi:10.1038/nature15512.

McGlynn, S. E., Chadwick, G. L., O'Neill, A., Mackey, M., Thor, A., Deerinck, T. J., et al. (2018). Subgroup Characteristics of Marine Methane-Oxidizing ANME-2 Archaea and Their Syntrophic Partners as Revealed by Integrated Multimodal Analytical Microscopy. *Appl. Environ. Microbiol.* 84, e00399-18. doi:10.1128/AEM.00399-18.

Moore, D. M., and Reynolds, R. C. (1997). *X-Ray Diffraction and the Identification and Analysis of Clay Minerals*. New York: Oxford University Press Available at: https://www.cambridge.org/core/article/div-class-title-m-span-class-sc-oore-span-d-m-andamp-r-span-class-sc-eynolds-span-r-c-jr-1997-span-class-italic-x-ray-diffraction-and-the-identification-and-analysis-of-clay-minerals-span-2nd-ed-xviii-378-pp-oxford-new-york-oxford-university-press-price-27-95-spiral-bound-paperback-isbn-0-19-508713-5-div/36DBF262516EC65CD0665FE59E361B57.

Morono, Y., Terada, T., Kallmeyer, J., and Inagaki, F. (2013). An improved cell separation technique for marine subsurface sediments: applications for high-throughput analysis using flow cytometry and cell sorting. *Environ. Microbiol.* 15, 2841–2849. doi:10.1111/1462-2920.12153.

Naehr, T. H., Eichhubl, P., Orphan, V. J., Hovland, M., Paull, C. K., Ussler, W., et al. (2007). Authigenic carbonate formation at hydrocarbon seeps in continental margin sediments: A comparative study. *Deep Sea Res. Part II Top. Stud. Oceanogr.* 54, 1268–1291. doi:10.1016/j.dsr2.2007.04.010.

Neuwirth, E. (2014). *RColorBrewer: ColorBrewer Palettes*. Available at: https://CRAN.R-project.org/package=RColorBrewer.

Niemann, H., Lösekann, T., Beer, D. de, Elvert, M., Nadalig, T., Knittel, K., et al. (2006). Novel microbial communities of the Haakon Mosby mud volcano and their role as a methane sink. *Nature* 443, 854. doi:10.1038/nature05227.

Oksanen, J., Kindt, R., Legendre, P., Hara, B., Simpson, G., Solymos, P., et al. (2009). The vegan Package.

Orphan, V. J., Hinrichs, K.-U., Ussler, W., Paull, C. K., Taylor, L. T., Sylva, S. P., et al. (2001a). Comparative Analysis of Methane-Oxidizing Archaea and Sulfate-Reducing Bacteria in Anoxic Marine Sediments. *Appl. Environ. Microbiol.* 67, 1922–1934. doi:10.1128/AEM.67.4.1922-1934.2001.

Orphan, V. J., House, C. H., Hinrichs, K.-U., McKeegan, K. D., and DeLong, E. F. (2001b). Methane-Consuming Archaea Revealed by Directly Coupled Isotopic and Phylogenetic Analysis. *Science* 293, 484–487. doi:10.1126/science.1061338.

Orphan, V. J., House, C. H., Hinrichs, K.-U., McKeegan, K. D., and DeLong, E. F. (2002). Multiple archaeal groups mediate methane oxidation in anoxic cold seep sediments. *Proc. Natl. Acad. Sci.* 99, 7663–7668. doi:10.1073/pnas.072210299.

Parada, A. E., Needham, D. M., and Fuhrman, J. A. (2016). Every base matters: assessing small subunit rRNA primers for marine microbiomes with mock communities, time series and global field samples. *Environ. Microbiol.* 18, 1403–1414. doi:10.1111/1462-2920.13023.

Pfeffer, C., Larsen, S., Song, J., Dong, M., Besenbacher, F., Meyer, R. L., et al. (2012). Filamentous bacteria transport electrons over centimetre distances. *Nature* 491, 218. doi:10.1038/nature11586.

Pop Ristova, P., Wenzhöfer, F., Ramette, A., Zabel, M., Fischer, D., Kasten, S., et al. (2012). Bacterial diversity and biogeochemistry of different chemosynthetic habitats of the REGAB cold seep (West African margin, 3160 m water depth). *Biogeosciences* 9, 5031–5048. doi:https://doi.org/10.5194/bg-9-5031-2012.

Poppe, L. J., and Commeau, J. A. (1992). Mineralogy of the silt fraction in surficial sediments from the United States mid-Atlantic shelf, slope and rise. *Mar. Geol.* 103, 185–197. doi:10.1016/0025-3227(92)90015-A.

Poppe, L. J., Commeau, J. A., and Valentine, P. C. (1991). Mineralogy of the silt fraction in surficial sediments from the outer continental shelf off southeastern New England. *J. Sediment. Res.* 61, 54–64. doi:10.1306/D4267686-2B26-11D7-8648000102C1865D.

Quast, C., Pruesse, E., Yilmaz, P., Gerken, J., Schweer, T., Yarza, P., et al. (2013). The SILVA ribosomal RNA gene database project: improved data processing and web-based tools. *Nucleic Acids Res.* 41, D590–D596. doi:10.1093/nar/gks1219.

R Core Team (2017). *R: A Language and Environment for Statistical Computing*. Vienna, Austria: R Foundation for Statistical Computing Available at: https://www.R-project.org/.

Reeburgh, W. S. (2007). Oceanic Methane Biogeochemistry. *Chem. Rev.* 107, 486–513. doi:10.1021/cr050362v.

Riedinger, N., Pfeifer, K., Kasten, S., Garming, J. F. L., Vogt, C., and Hensen, C. (2005). Diagenetic Alteration of Magnetic Signals by Anaerobic Oxidation of Methane Related to a Change in Sedimentation Rate. *Geochim. Cosmochim. Acta* 69, 4117–4126. doi:10.1016/j.gca.2005.02.004.

Roberts, A. P. (2015). Magnetic mineral diagenesis. *Earth-Sci. Rev.* 151, 1–47. doi:10.1016/j.earscirev.2015.09.010.

Rotaru, A.-E., Calabrese, F., Stryhanyuk, H., Musat, F., Shrestha, P. M., Weber, H. S., et al. (2018). Conductive Particles Enable Syntrophic Acetate Oxidation between Geobacter and Methanosarcina from Coastal Sediments. *mBio* 9. doi:10.1128/mBio.00226-18.

Rowe, A. R., Chellamuthu, P., Lam, B., Okamoto, A., and Nealson, K. H. (2015). Marine sediments microbes capable of electrode oxidation as a surrogate for lithotrophic insoluble substrate metabolism. *Front. Microbiol.* 5. doi:10.3389/fmicb.2014.00784.

Ruff, S. E., Biddle, J. F., Teske, A. P., Knittel, K., Boetius, A., and Ramette, A. (2015). Global dispersion and local diversification of the methane seep microbiome. *Proc. Natl. Acad. Sci.* 112, 4015–4020. doi:10.1073/pnas.1421865112.

Sahin, M., Ayranci, K., Kosun, E., and Ayranci, E. (2009). Density, sound velocity and viscosity properties of aqueous sodium metatungstate solutions and an application of these solutions in heavy mineral separations. *Chem. Geol.* 264, 96–100. doi:10.1016/j.chemgeo.2009.02.016.

Salter, S. J., Cox, M. J., Turek, E. M., Calus, S. T., Cookson, W. O., Moffatt, M. F., et al. (2014). Reagent and laboratory contamination can critically impact sequence-based microbiome analyses. *BMC Biol.* 12, 87. doi:10.1186/s12915-014-0087-z.

Sato, M., and Mooney, H. M. (1960). The electrochemical mechanism of sulfide self-potentials. *Geophysics* 25, 226–249. doi:10.1190/1.1438689.

Scheller, S., Yu, H., Chadwick, G. L., McGlynn, S. E., and Orphan, V. J. (2016). Artificial electron acceptors decouple archaeal methane oxidation from sulfate reduction. *Science* 351, 703–707. doi:10.1126/science.aad7154.

Schreiber, L., Holler, T., Knittel, K., Meyerdierks, A., and Amann, R. (2010). Identification of the dominant sulfate-reducing bacterial partner of anaerobic methanotrophs of the ANME-2 clade. *Environ. Microbiol.* 12, 2327–2340. doi:10.1111/j.1462-2920.2010.02275.x.

Shi, L., Dong, H., Reguera, G., Beyenal, H., Lu, A., Liu, J., et al. (2016). Extracellular electron transfer mechanisms between microorganisms and minerals. *Nat. Rev. Microbiol.* 14, 651–662. doi:10.1038/nrmicro.2016.93.

Shi, M., Wu, H., Roberts, A. P., Zhang, S., Zhao, X., Li, H., et al. (2017). Tectonic, climatic, and diagenetic control of magnetic properties of sediments from Kumano Basin,

Nankai margin, southwestern Japan. *Mar. Geol.* 391, 1–12. doi:10.1016/j.margeo.2017.07.006.

Skennerton, C. T., Chourey, K., Iyer, R., Hettich, R. L., Tyson, G. W., and Orphan, V. J. (2017). Methane-Fueled Syntrophy through Extracellular Electron Transfer: Uncovering the Genomic Traits Conserved within Diverse Bacterial Partners of Anaerobic Methanotrophic Archaea. *mBio* 8, e00530-17. doi:10.1128/mBio.00530-17.

Skennerton, C. T., Haroon, M. F., Briegel, A., Shi, J., Jensen, G. J., Tyson, G. W., et al. (2016). Phylogenomic analysis of Candidatus 'Izimaplasma' species: free-living representatives from a Tenericutes clade found in methane seeps. *ISME J.* 10, 2679–2692. doi:10.1038/ismej.2016.55.

Summers, Z. M., Fogarty, H. E., Leang, C., Franks, A. E., Malvankar, N. S., and Lovley, D. R. (2010). Direct exchange of electrons within aggregates of an evolved syntrophic coculture of anaerobic bacteria. *Science* 330, 1413–5. doi:10.1126/science.1196526.

Tang, J., Zhuang, L., Ma, J., Tang, Z., Yu, Z., and Zhou, S. (2016). Secondary Mineralization of Ferrihydrite Affects Microbial Methanogenesis in Geobacter-Methanosarcina Cocultures. *Appl. Environ. Microbiol.* 82, 5869–5877. doi:10.1128/AEM.01517-16.

Totten, M. W., Hanan, M. A., Knight, D., and Borges, J. (2002). Characteristics of mixed-layer smectite/illite density separates during burial diagenesis. *Am. Mineral.* 87, 1571–1579. doi:10.2138/am-2002-11-1207.

Treude, T., Orphan, V., Knittel, K., Gieseke, A., House, C. H., and Boetius, A. (2007). Consumption of Methane and CO2 by Methanotrophic Microbial Mats from Gas Seeps of the Anoxic Black Sea. *Appl. Environ. Microbiol.* 73, 2271–2283. doi:10.1128/AEM.02685-06.

Van Cappellen, P., and Wang, Y. (1996). Cycling of iron and manganese in surface sediments; a general theory for the coupled transport and reaction of carbon, oxygen, nitrogen, sulfur, iron, and manganese. *Am. J. Sci.* 296, 197–243. doi:10.2475/ajs.296.3.197.

Wegener, G., Krukenberg, V., Riedel, D., Tegetmeyer, H. E., and Boetius, A. (2015). Intercellular wiring enables electron transfer between methanotrophic archaea and bacteria. *Nature* 526, 587–590. doi:10.1038/nature15733.

Weiss, S., Xu, Z. Z., Peddada, S., Amir, A., Bittinger, K., Gonzalez, A., et al. (2017). Normalization and microbial differential abundance strategies depend upon data characteristics. *Microbiome* 5, 27. doi:10.1186/s40168-017-0237-y.

Wickham, H. (2009). *ggplot2: Elegant Graphics for Data Analysis*. Springer-Verlag New York Available at: http://ggplot2.org.

Pos. [°2θ]	Height [cts]	FWHM Left [°2θ]	d-spacing [Å]	Rel. Int. [%]	Tip Width	Matched by
8.6211	71.39	0.3149	10.25700	11.86	0.3779	
12.2542	194.17	0.3149	7.22293	32.25	0.3779	
18.5588	52.08	0.2519	4.78103	8.65	0.3023	
19.5450	120.24	0.3779	4.54197	19.97	0.4534	
20.7623	90.62	0.4093	4.27834	15.05	0.4912	01-089-1961
21.7652	117.54	0.2519	4.08342	19.52	0.3023	
23.4771	38.52	0.3149	3.78939	6.40	0.3779	
26.3782	547.67	0.2676	3.37885	90.97	0.3212	01-089-1961
27.6269	184.78	0.3779	3.22890	30.69	0.4534	
29.6342	87.23	0.3779	3.01460	14.49	0.4534	
31.4440	602.03	0.2676	2.84510	100.00	0.3212	00-005-0628
36.3486	44.62	0.3149	2.47167	7.41	0.3779	01-089-1961
45.2137	353.49	0.2834	2.00553	58.72	0.3401	01-089-1961
						00-005-0628
49.9841	49.85	0.4408	1.82473	8.28	0.5290	01-089-1961
59.6788	42.63	0.3779	1.54940	7.08	0.4534	01-089-1961

Ref. Code	Score	Compound Name	Displacement [°2Th.]	Scale Factor	Chemical Formula
01-089-1961	70	Silicon Oxide	-0.199	0.850	SiO_2
00-005-0628	55	Sodium Chloride	-0.219	0.949	NaCl

Table 3. Peaks detected (*top*) and corresponding mineralogical identification (*bottom*) by X'Pert Highscore from a representative XRD spectra collected from a sample of the light ($\rho < 2.4$ g/cc) fraction of density-separated methane seep sediment (Fig. 2).

Pos. [°2θ]	Height [cts]	FWHM Left [°2θ]	d-spacing [Å]	Rel. Int. [%]	Tip Width	Matched by
8.7742	57.33	0.3149	10.07834	3.47	0.3779	
12.3601	174.51	0.2519	7.16130	10.55	0.3023	
20.7157	277.06	0.2519	4.28786	16.75	0.3023	01-089-1961
21.8928	159.28	0.3149	4.05990	9.63	0.3779	
23.5424	152.92	0.4408	3.77903	9.24	0.5290	01-086-2341
24.1270	127.08	0.3779	3.68878	7.68	0.4534	
25.0271	143.98	0.3779	3.55811	8.70	0.4534	
26.5142	1654.45	0.3149	3.36183	100.00	0.3779	01-089-1961
27.8307	461.98	0.3779	3.20572	27.92	0.4534	
29.8100	1396.58	0.3464	2.99722	84.41	0.4156	01-086-2341
36.4232	349.49	0.2519	2.46678	21.12	0.3023	01-089-1961
						01-086-2341
37.6643	54.39	0.3779	2.38830	3.29	0.4534	
39.9014	318.50	0.4408	2.25941	19.25	0.5290	01-089-1961
						01-086-2341
42.3318	164.52	0.2834	2.13515	9.94	0.3401	01-089-1961
43.7411	244.94	0.3779	2.06957	14.80	0.4534	01-086-2341
48.2544	198.28	0.4408	1.88602	11.98	0.5290	
49.2895	228.52	0.4408	1.84881	13.81	0.5290	
50.0550	280.77	0.2519	1.82232	16.97	0.3023	01-089-1961
54.7251	69.45	0.2519	1.67734	4.20	0.3023	01-089-1961
59.8555	222.53	0.2834	1.54525	13.45	0.3401	01-089-1961

Ref. Code	Score	Compound Name	Displacement [°2Th.]	Scale Factor	Chemical Formula
01-089-1961	76	Silicon Oxide	-0.094	0.990	SiO_2
01-086-2341	52	Calcium Carbonate	0.501	0.731	$Ca(CO_3)$

Table 2. Peaks detected (*top*) and corresponding mineralogical identification (*bottom*) by X'Pert Highscore from a representative XRD spectra collected from a sample of the intermediate ($2.4 < \rho < 2.9$ g/cc) fraction of density-separated methane seep sediment (Fig. 2).

Pos. [°2θ]	Height [cts]	FWHM Left [°2θ]	d-spacing [Å]	Rel. Int. [%]	Tip Width	Matched by
8.4469	38.59	0.2204	10.46805	7.75	0.2645	
10.1959	497.73	0.2362	8.67596	100.00	0.2834	
12.2320	97.94	0.1889	7.23598	19.68	0.2267	
17.3895	57.20	0.3149	5.09980	11.49	0.3779	
19.4890	15.92	0.2519	4.55488	3.20	0.3023	
26.3485	91.17	0.3149	3.38259	18.32	0.3779	
28.2200	307.19	0.2519	3.16237	61.72	0.3023	00-024-0076
29.5466	145.63	0.1889	3.02334	29.26	0.2267	01-089-0950
32.7266	133.66	0.1889	2.73647	26.85	0.2267	00-024-0076
36.6646	58.47	0.3779	2.45110	11.75	0.4534	00-024-0076 01-089-0950
56.0246	58.28	0.3779	1.64148	11.71	0.4534	00-024-0076 01-089-0950

Ref. Code	Score	Compound Name	Displacement [°2Th.]	Scale Factor	Chemical Formula
00-024-0076	56	Iron Sulfide	-0.322	0.353	FeS_2
01-089-0950	34	Iron Oxide	-0.559	0.280	Fe_3O_4

Table 1. Peaks detected (*top*) and corresponding mineralogical identification (*bottom*) by X'Pert Highscore from a representative XRD spectra collected from a sample of the dense (ρ > 2.9 g/cc) fraction of density-separated methane seep sediment (Fig. 2).

SUPPLEMENTAL FIGURES

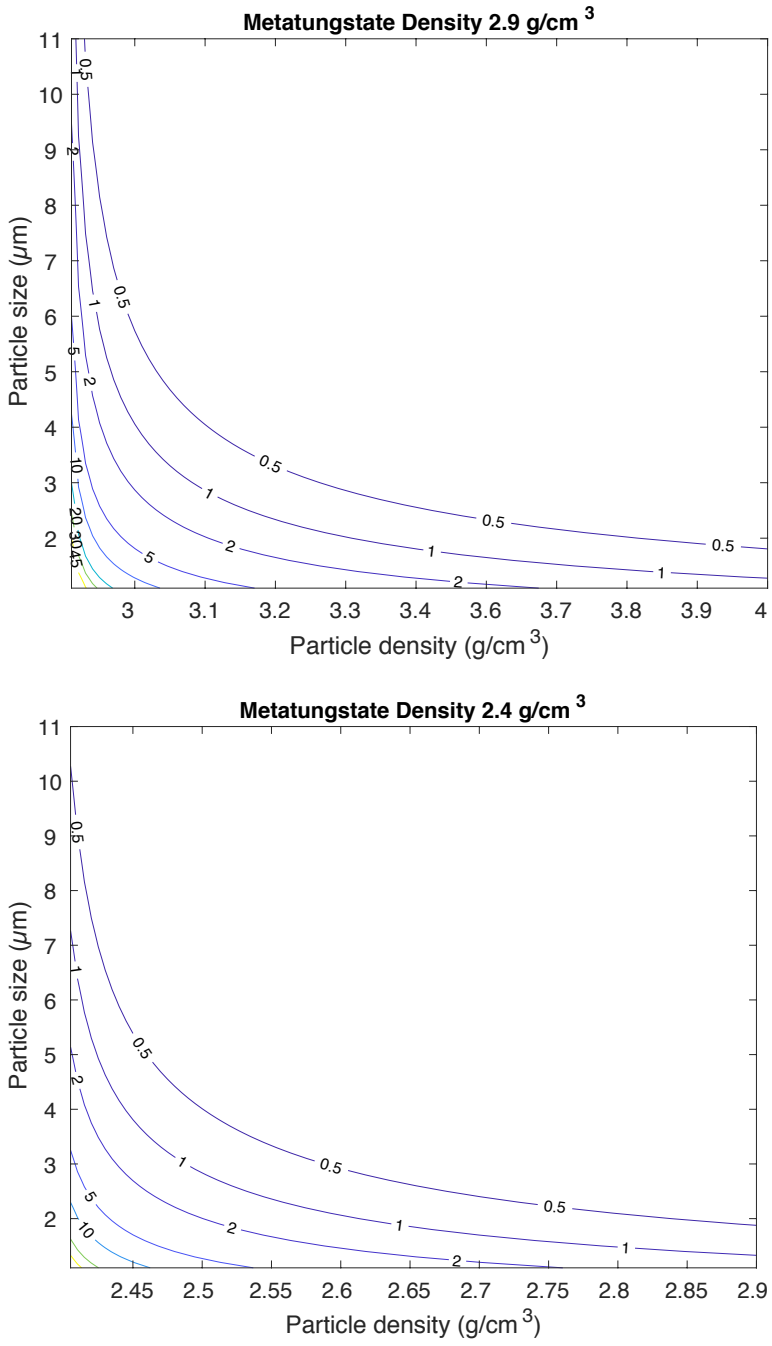

Supplemental Figure 1. Spherical paricle size pelleted from a 2 min spin at 2000× g as a function of the density of that particle and the density and viscosity of different SMT solutions, showing the time in minutes (contours) required for a particle of given diameter to pellet at the bottom of a 5 mL tube, assuming Stokes' settling. Viscosities for different SMT densities were adapted from the literature (Sahin et al., 2009).

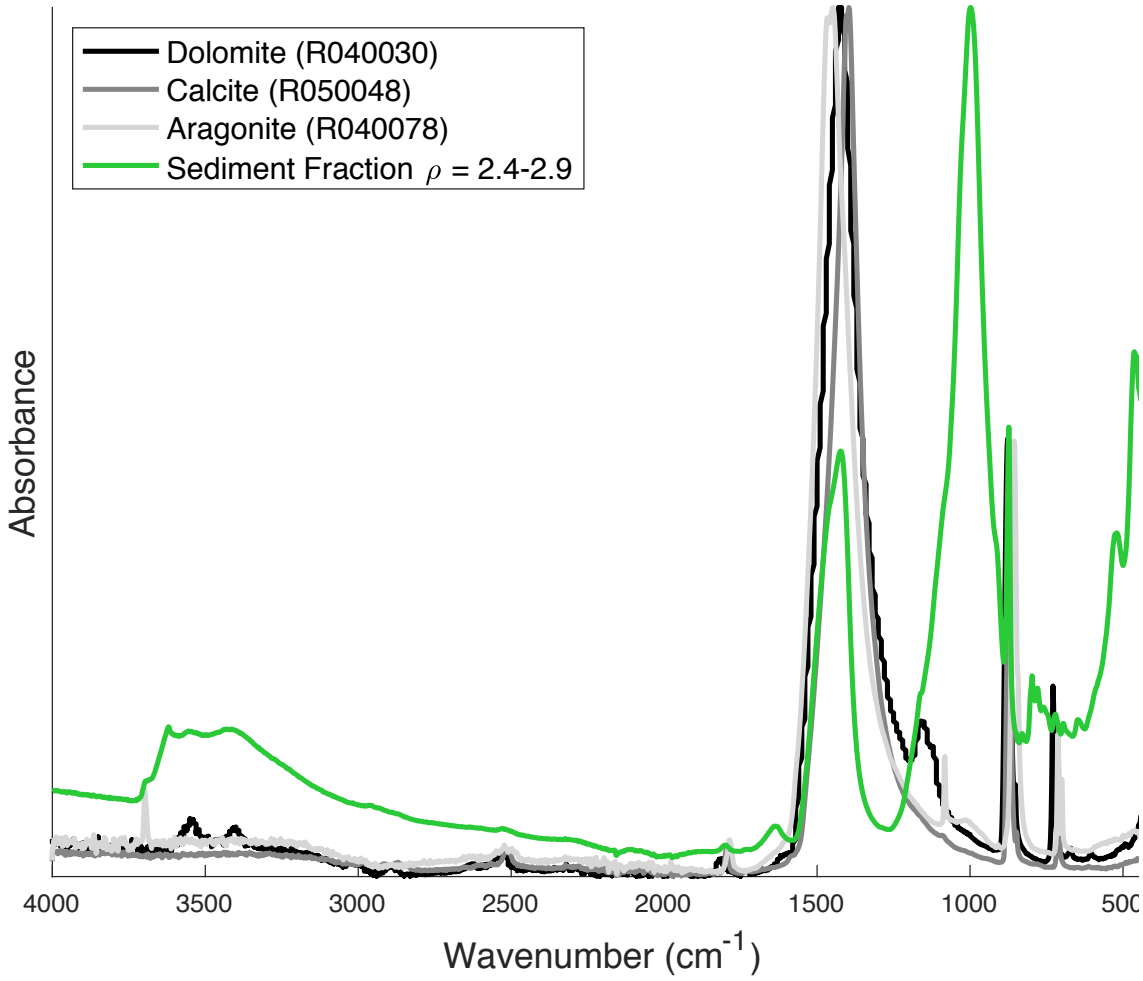

Supplemental Figure 2. FTIR spectrum collected from the intermediate density fraction comparing this sample spectrum to those of several carbonate standards (cf. Fig. 3).

Chapter 3

SILICATE PRECIPITATION MEDIATED BY ANME-SRB CONSORTIA

Kyle S. Metcalfe[1], Daniela Osorio Rodríguez[1], Hank Yu[1], Anne E. Dekas[2], Shawn E. McGlynn[3], John P. Grotzinger[1], and Victoria J. Orphan[1]

[1] Division of Geological and Planetary Sciences,
California Institute of Technology, Pasadena, California, 91125

[2] Department of Earth System Science,
Stanford University, Stanford, California, 94305

[3] Earth-Life Science Institute,
Tokyo Institute of Technology, Ookayama, Meguro, Tokyo, 152-8550, Japan

ABSTRACT

Prokaryotic silicate biomineralization in solutions undersaturated with respect to amorphous silica—representative of conditions in most shallow sediment pore waters—is poorly understood, but may be significant for the preservation of microfossils and soft tissues in the rock record by early silicate cementation. Recent work reported the presence of authigenic silicates (clays) attached to the exteriors of consortia of anaerobic methane-oxidizing archaea (ANME) and sulfate-reducing bacteria (SRB). However, it remains uncertain whether the association between ANME-SRB consortia and silicates occurs through biogenetic precipitation or represent passive attachment if detrital sedimentary particles. In this study, we addressed the null hypothesis of abiotic silicate attachment and/or precipitation to consortium surfaces by characterizing the texture and composition of ANME-SRB consortium-attached silicates sourced directly from deep-sea methane seep

sediments and from 3-year-long sediment-free enrichments of methane-oxidizing ANME-SRB consortia in Si-poor artificial seawater. Compositional data from both field-collected and sediment-free consortia demonstrates statistically significant ($p < 0.01$) Si enrichment in consortium-attached silicates over detrital silicates drawn from the same sample. The texture of silicate phases attached to ANME-SRB consortia maintained anaerobically in sediment-free conditions is distinct from that observed *in situ* and suggests the growth of these phases concomitant with AOM consortia growth over a 3 year period at 10˚ C. ICP-MS measurements of media [Si] in sediment-free incubations preclude Si enrichment via abiotic silica precipitation or Si adsorption to clays. Instead, these laboratory controlled incubations suggest AOM consortia mediate silicate biomineralization in conditions undersaturated with respect to precipitation of amorphous silica as well as equilibrium silicon adsorption onto clays, and thus may point to a previously underexamined mode of biomineralization by microorganisms abundant in methane-rich marine sediments.

INTRODUCTION

The anaerobic oxidation of methane (AOM) is an important, microbially-driven process modulating methane flux from coastal sediments worldwide. AOM consumes 80-90% of CH_4 produced in marine sediments (Reeburgh, 2007; Knittel and Boetius, 2009), oxidizing methane to bicarbonate via the reduction of sulfate to sulfide:

$$CH_4 + SO_4^{2-} \rightarrow HCO_3^- + HS^- + H_2O \qquad \Delta G = -10 \text{ to } -40 \text{ kJ mol}^{-1}.$$

The scant energy produced by this reaction, barely sufficient for ATP synthesis (Schink, 1997), is harnessed by multicellular methane-oxidizing archaea (ANME) and sulfate-reducing bacteria (SRB) consortia common in methane seep ecosystems, reaching maximum abundances on the order of 10^7 consortia per cm^3 of sediment (Boetius et al., 2000; Orphan et al., 2001b, 2002). ANME-SRB cell aggregation likely enables direct interspecies electron transfer between ANME and SRB (McGlynn et al., 2015; Wegener et al., 2015). Experimental evidence demonstrating the capacity for ANME-SRB consortia to reduce solid phase iron and manganese oxides (Beal et al., 2009; Cai et al., 2018; Leu et al., 2020) supports this model and further suggests interactions between ANME-SRB consortia and mineral electron acceptors in the environment.

Traditionally, studies of the interactions between ANME-SRB consortia and minerals have focused on the precipitation of authigenic carbonates resulting from alkalinity production via AOM. The production of bicarbonate and sulfide ion increases porewater alkalinity in zones of AOM activity, driving the precipitation of carbonate minerals (Luff and Wallmann, 2003). Extensive seafloor pavements observed proximal to

sites of CH_4 seepage are thought to be the result of pervasive cementation of terrigenous clastic sediment by AOM-induced carbonate precipitation (Aloisi et al., 2000; Luff and Wallmann, 2003; Teichert et al., 2005; Naehr et al., 2007). Geochemical modeling of seep carbonate porewaters (Luff and Wallmann, 2003) and nonequilibrium clumped isotope signatures in modern and ancient seep carbonates imply rapid carbonate precipitation rates during early diagenesis (Loyd et al., 2016; Thiagarajan et al., 2020), suggesting interactions between ANME-SRB consortia and authigenic mineral precipitation at seeps. Indeed, many studies demonstrate the presence of viable ANME consortia and active AOM in association with seep carbonates and carbonate concretions (Marlow et al., 2014; Case et al., 2015; Mason et al., 2015), in some cases forming large 'reefs' in which a carbonate pillar protruding from the seafloor is coated in ANME microbial mats (Michaelis et al., 2002; Treude et al., 2007). Given these observations, one might expect carbonate minerals to associate with EPS coatings on ANME-SRB consortia, as SRB cell surface and/or EPS chemistry has been suggested to catalyze carbonate precipitation (Visscher et al., 2000; Braissant et al., 2007; Decho, 2010; Krause et al., 2012).

It is therefore surprising that silicate phases are more commonly found intimately associated with ANME-SRB consortia than carbonate phases (Pernthaler et al., 2008; Dekas, 2013; Chen et al., 2014). These observations were initially collected by correlated fluorescence in situ- hybridization (FISH), scanning electron microscopy (SEM), and nanoscale secondary ion mass spectroscopy (nanoSIMS) analysis (for Si), which revealed the common presence of a Si-rich phase surrounding consortia sourced directly from sediments. Initial energy-dispersive spectroscopy (EDS) analysis characterized this silicate

phase as an aluminosilicate clay (Dekas, 2013). Further SEM-EDS analysis revealed the presence of a texturally-massive Si-rich phase between Al-rich phases within the silicate shell, interpreted as a silica cement binding detrital aluminosilicate clays to ANME-SRB consortium exteriors (Chen et al., 2014). Alkalinity produced by AOM was proposed to drive diatom frustule dissolution via increased pH of porewater, followed by Si precipitation on ANME-SRB consortium exteriors due to interactions with adsorbed metal cations such as Al (Chen et al., 2014).

The hypothesis that silica precipitation on ANME-SRB consortia is enhanced by alkalinity-driven silica leaching is notable in that it implies prokaryotic silica biomineralization occurring in porewater undersaturated with respect to amorphous silica, an understudied process about which little is known. Previous research on prokaryotic silica and silicate biomineralization has focused predominantly on phases precipitated from solutions supersaturated with respect to amorphous silica (Phoenix et al., 2002, 2003; Yee et al., 2003; Lalonde et al., 2005; Hugo et al., 2011) or on cell-associated clay or clay-like phases rich in Fe and Al (Ferris et al., 1987; Konhauser et al., 1993, 1994; Mera and Beveridge, 1993; Köhler et al., 1994, 1999; Urrutia and Beveridge, 1994; Konhauser and Urrutia, 1999; Fein et al., 2002). Experimental work examining precipitation from supersaturated Si solutions demonstrated most precipitation to occur in solution abiotically, independent of the presence of bacterial cells (Yee et al., 2003) (Phoenix et al., 2003; Yee et al., 2003). In experiments examining silicate precipitation in solutions undersaturated with respect to amorphous silica, the coating of *Bacillus subtilis* cell surfaces by synthetic iron oxides was required to adsorb significant Si to cells (Fein et al., 2002), producing

silicate precipitates rich in Fe and/or Al on cell surfaces, similar to some phases observed attached to cells sampled from sediments (Konhauser et al., 1993, 1994; Köhler et al., 1994; Konhauser and Urrutia, 1999). However, in these experiments, control incubations in which the iron oxide coating was added alone removed significant Si from solution, indicating the interaction between Fe and Si occuring at the cell surface is unlikely to have any biotic influence. These experimental results are consistent with previous work demonstrating that in the presence of Al or Fe oxides or clay minerals, Si solubility is considerably reduced from Si solubility with respect to amorphous silica (Siever and Woodford, 1973; Iler, 1979).

Surprisingly, silicate phases observed on ANME-SRB consortium exteriors are Fe- and Al-poor (Dekas, 2013; Chen et al., 2014), and sediment porewaters are often below theoretical silica saturation (~1170 μM at pH 8, 4˚ C (Gunnarsson and Arnórsson, 2000)) due to interactions with Al from detrital clays (Van Cappellen and Qiu, 1997; Dixit et al., 2001; Michalopoulos and Aller, 2004; Tréguer and De La Rocha, 2013). For context, methane seep sediment porewater [Si] has been measured at ~400 μM (Zabel et al., 2008). Any model explaining precipitation of Si-rich silicate phases on ANME-SRB consortium exteriors must therefore depart from current understandings of prokaryotic silicate biomineralization developed through examination of cell-associated Fe- and/or Al-rich clay-like phases or silicate precipitation occurring under conditions supersaturated with respect to amorphous silica.

To date, observations of silicate phases adhered to ANME-SRB consortia have been acquired from samples isolated directly from clay-rich seep sediments (Dekas et al.,

2009; Zhang et al., 2010, 2011; Dekas, 2013; Chen et al., 2014), preventing clear discrimination of active, biologically-mediated precipitation from passive attachment of phases to cell exteriors. The latter process is a null hypothesis at once important and challenging to reject, as passive abiotic attachment can result in intimate spatial association between minerals and cell exteriors (Glasauer et al., 2001), confounding textural analysis in the absence of additional geochemical or microbiological constraints on porewater composition or cell growth.

Here we attempted to investigate the proposed hypotheses (Dekas, 2013; Chen et al., 2014) of ANME-SRB consortium-mediated silicate precipitation through direct microscopy and analysis of the exteriors of active ANME-SRB consortia separated from methane seep sediments and maintained in laboratory incubations in media with [Si] below the threshold for abiotic silica precipitation or Si adsorption to preexisting, consortium-attached aluminosilicates. We found the growth of abundant Si-rich phases embedded in EPS and attached to ANME-SRB consortium exteriors with compositions (1) significantly Si-enriched relative to the Si content of the original source sediment and (2) similar to those of silicate phases found adhered to ANME-SRB consortia sourced directly from diverse seep sediment. These observations demonstrated de novo growth of a Si-rich silicate phase from solutions undersaturated with respect to amorphous silica, and suggestive of bona fide silicate biomineralization mediated by ANME-SRB consortia both in culture experiments and in a diversity of methane seep sediments.

MATERIALS AND METHODS

Sample Collection and Processing

Sediment samples analyzed in this study were collected by push coring using the submersible HOV *Alvin* of the R/V *Atlantis* from 2 seafloor methane seep sites, in the Eel River Basin (AT 15-11, October 2006) and off the coast of Costa Rica (AT 37-13, May 2017), and by the ROV *Doc Ricketts* of the R/V *Western Flyer* from a seafloor methane seep site in Santa Monica Basin (October 2013). Push core (PC) samples PC14 and PC15 from *Alvin* dive AD4254 (AT 15-11) were collected from a microbial mat proximal to an active methane seep site 520 m below sea level (mbsl) on the Northern Ridge of Eel River Basin (40.786533, -124.5951). Samples from the Costa Rica Margin (AT 37-13) were obtained during *Alvin* dive AD4912 from a microbial mat (PC 6) collected at 1811 mbsl in the Jacó Scar submarine landslide (9.1163, -84.8372). Samples from Santa Monica Basin were covered in a microbial mat at a seafloor methane seep site (33.788835, -118.668298) at 863 mbsl during DR 459 (PC 43). In all cases, samples were processed shipboard by extruding sediment upward from the push core liner and sectioning sediment at 3 cm intervals. Subsamples of sediment were frozen at -80˚ C, PFA-fixed for microscopy, or sealed in Ar-sparged mylar bags and stored at 4˚ C for laboratory-based microcosm experiments.

Carbonate rock samples analyzed in this study were collected using the robotic arm of HOV *Alvin* from a seafloor methane seep site in the Jacó Scar off the coast of Costa Rica during the R/V *Atlantis* cruise AT42-03. Sample #10860 was collected from a warm (6˚ C) seep site at 1784 mbsl (9.117783, -84.839512), and processed shipboard by placing in a

mylar bag filled with Ar-sparged, filter-sterile seawater collected by Niskin bottle. The mylar bag was supplied with CH_4 and stored at 4˚ C for laboratory-based microcosm experiments.

Percoll Separation

Using a modified protocol from (Orphan et al., 2001a), separation of ANME-SRB consortia from bulk sediment for downstream microscopy or cultivation was performed using a Percoll (Sigma-P1644) density gradient on an aliquot of seep sediment. Cells for microscopy were initially fixed by incubating a 1mL aliquot of sediment with 4% glutaraldehyde overnight at 4˚ C, and were subsequently disaggregated from bulk sediment by sonication for 3 x 10-second intervals on ice using a Branson Sonifier 50 with a power output of 4 W. Cells for downstream sediment-free incubation were not fixed but were also sonicated. A 1 mL aliquot of sonicated sediment was then pipetted onto 500µL of a 100% Percoll density gradient and centrifuged at 18000 x G for 30 minutes at 10˚ C using a Beckman-Coulter Microfuge 18 centrifuge. The supernatant (~1 mL) was then pipetted into 250 mL 1X PBS in a filter tower and vacuumed through a 5 µm polyethersulfone (PES) filter until ~50 mL solution remained in the tower, which was then diluted by ~200 mL 1X PBS added to the tower. Repeated filtration and dilution by 1X PBS was performed 3 times. We calculated this dilution and filtration to remove 99.2% of the 500 µL Percoll (initially containing 0.43 µmol Si (G.E. Healthcare Life Sciences, 2018)) present in the density separation supernatant, with the final filtration step yielding a 1 mL aliquot used for

downstream microscopy. Final [Si] from Percoll was calculated to equal 3.4 μM. Inoculum for the sediment-free incubation experiments was prepared from source sediment using the consortium extraction protocol described above, with the omission of the initial glutaraldehyde fixation step. Percoll separation for sediment-free incubation experiments was performed in a Coy anaerobic chamber with an 97% N_2, 3% H_2 atmosphere.

Bottle Incubations

To enrich for ANME-SRB consortia, seep sediments were homogenized with 0.2 μm filter-sterilized, Ar-sparged deep seawater sampled at to the sampling site and placed in N_2-sparged Pyrex bottles sealed with butyl rubber stoppers. Aliquots from anaerobic Percoll separation to enrich ANME-SRB consortia for sediment-free incubation (see above) were mixed with N_2-sparged artificial seawater (media composition from Scheller, et al. 2016) and placed in N_2-sparged serum vials with butyl rubber stoppers. Carbonate samples were also placed in Pyrex bottles together with filter-sterile N_2-sparged seawater. All incubations were supplied with a CH_4 headspace pressurized to ~2 atm. These anoxic incubations were maintained in the dark at 10˚ C with partial exchange of spent media with the addition of 0.2 μm filter-sterilized Ar-sparged seawater and CH_4 every 3 months. Sediment-free incubations were maintained in these conditions over the course of ~3 years. Sulfate-reducing activity during the course of the incubations was measured using a modified Cline assay (Cline, 1969).

Fluorescence in situ Hybridization and Epifluorescence Microscopy

Conventional fluorescence in situ hybridization (FISH) with a single fluorophore on the 5' end was used to identify ANME-SRB consortia for analysis of consortium exteriors. Here, Percoll-separated AOM consortia were filtered onto 0.2 μm (25 mm) EMD Millipore white polycarbonate filters (Code GTTP) and incubated in 50 μL hybridization buffer for 24 hr at the appropriate formamide stringency, following published protocols (Pernthaler et al., 2001). Percoll separation was only performed on samples from sediment-bearing incubations. Carbonate samples were cut by a rock saw for downstream microscopy. In this study, we used probes targeting Archaea (Arch915; (Stahl and Amann, 1991)), ANME-2 (Eel932; (Boetius et al., 2000)), ANME-2a/b (Treude et al., 2005), and SRB (DSS658; (Boetius et al., 2000)). 4',6-diamino-2-phenylindole (DAPI) was applied as a counterstain, and hybridized samples were illuminated using an XCite Series 120Q fluorescence source and imaged with a Qimage QIClick camera attached to an Olympus BX51 epifluorescence microscope with 60x (Olympus PlanApo N Oil, N.A. 1.42) and 100x (Olympus UPlan FL N Oil, N.A. 1.30) objectives. Imaging software (cellSens Dimension) was used to acquire images. Composites of epifluorescence images were produced using the image processing software Q-Capture Pro 7.

Scanning Electron Microscopy

Scanning electron microscopy (SEM) and energy-dispersive X-ray spectroscopy (EDS) of ANME-SRB consortia from sediment-free incubations immobilized on white

polycarbonate filters or present in situ in carbonate crusts was performed and correlated with optical microscopy. Additionally, sediment samples representing a range of diverse seep sites were filtered onto 0.2 μm EMD Millipore white polycarbonate filters (Code GTTP). Samples were Pd-coated (10 nm thickness) using a Cressington Sputter Coater 208HR and examined using a Zeiss 1550VP Field Emission SEM equipped with an Oxford INCA Energy 300 X-ray EDS system. After SEM image acquisition, EDS mapping of consortia was performed to characterize the spatial distribution of consortium-adhered phases, and EDS point spectra were collected to determine the composition of consortium-adhered phases. EDS data were also collected from non-consortium-associated phases as a comparison. as well as the sediment from which these consortia were separated. SEM images were acquired using an electron beam energy of 10 eV and EDS mapping and spectra were acquired with an electron beam of 15 eV. Subsequent statistical analysis of EDS-acquired compositional data was performed in R.

Transmission Electron Microscopy

ANME-SRB consortia were embedded in Technovit 8200 resin following published protocols (McGlynn et al., 2018), and sectioned using a Leica Ultracut UCT ultramicrotome fitted with a diamond knife. Sections were stained using the contrasting agent osmium tetraoxide and subsequently imaged at UCSD using a FEI Spirit transmission electron microscope operated at 120 kV with a Tietz TemCam F224 2K by 2K CCD camera.

Silicate Grain Size Estimate

TEM micrographs depicting silicates attached to ANME-SRB consortia maintained in sediment-free conditions were processed in Fiji/ImageJ 1.0 to estimate the size distribution of these silicates. A TEM micrograph panorama was constructed using Photoshop from 13 TEM micrographs (20 μm2 each) of a cluster of ANME-SRB consortia. Pixels representing consortium-attached silicates from the TEM micrograph panorama were isolated in Fiji/ImageJ 1.0 by thresholding a grayscale TEM micrograph panorama to only capture pixels of value 0-131 (9.15% of pixels). The thresholded micrograph was further processed using watershed analysis to quantify particle areas in the image with areas 10-1000 μm^2 and circularity 0.5-1. Particle areas were used to estimate particle diameters by assuming the particles approximated spheres, consistent with SEM observations.

The diameter distribution of the 6060 identified particles from the micrograph was used to estimate the true diameter distribution of consortium-attached silicates maintained under sediment-free conditions. A Markov-Chain Monte Carlo approach implemented in MATLAB was used to estimate the true distribution of particle diameters by simulating observed particle diameters produced by random cross-sections of spherical particles assuming a Gaussian size distribution. Particle diameter mean and variance were used as input parameters by the Monte Carlo model which simulated an observed distribution of particle cross-sections and compared these iteratively (10^5 Monte Carlo samples) to the distribution observed via ImageJ in the TEM micrograph panorama. The model converged

on a particle size distribution of maximum likelihood by maximizing the log-likelihood function for the Gaussian distribution.

Focused Ion Beam and Electron Dispersive Spectroscopy

Consortium cross-sections were prepared using a focused Ga^+ ion beam (FEI Nova-600) at the Kavli Nanoscience Institute, Caltech followed by EDS analysis of FIB-sectioned consortia to acquire cross-sectional compositional variability of consortium-attached silicates and consortium interiors.

Inductively Coupled Plasma Mass Spectrometry

[Si] was measured using an Agilent 8800 Triple Quadrupole ICP-MS . A Si standard from Sigma-Aldrich (#15747) was used to calibrate the ICP-MS measurements through a serial dilution procedure. This calibration curve was used to acquire precise measurements for [Si] which were subsequently compared with calculated amorphous silica saturation at temperature and pH conditions corresponding to those of present in sediment-free conditions, using MATLAB and the equations of (Drever, 1988; Gunnarsson and Arnórsson, 2000). Additionally, [Si] was compared to experimentally-determined equilibria describing adsorption of Si to various aluminosilicate clays (Siever and Woodford, 1973).

Comparative Genomics

To explore potential mechanisms for mediation of silicate precipitation by members of ANME-SRB consortia, metagenomes acquired from ANME-SRB consortia (Skennerton et al., 2017) were used as a database to search for predicted proteins possibly involved in condensation of orthosilicic acid to form the observed precipitate attached to ANME-SRB consortia. An approach similar to that of (Scheffel et al., 2011) was used, in which a metagenomic database is searched for predicted proteins possessing a sequence of amino acids with residue frequencies suggestive of involvement in orthosilicic acid condensation. Here, the python module biopython (Cock et al., 2009) was used to parse a metagenomic database for proteins containing ≥ 25% serine and ≥ 20% lysine or arginine residues in a sliding 30 amino-acid-long window, a criterion inspired by the amino acid composition of a spore coat protein from *Bacillus cereus* known to be involved in silica precipitation (Motomura et al., 2016). Candidate proteins selected by this criterion were then further filtered using BLASTp for extracellular membrane-associated proteins. PSORTb 3.0 (Yu et al., 2010) was used to predict signal peptide sequences in candidate proteins.

RESULTS

FISH-EM Imaging Reveals Silicates Attached to ANME-SRB Consortia

Correlated epifluorescence microscopy, SEM, and elemental mapping via EDS (Figs. 1, S1) documented the presence of silicate phases on the exteriors of ANME-SRB

consortia extracted directly from methane seep sediment samples (Fig. 1A-C) and additionally revealed the presence of silicates distributed between consortia grown under sediment-free conditions (Fig. 1D-O). Silicates appearing on consortia extracted directly from sediments collected from seafloor methane seep sites of the Santa Monica Basin (Fig. 1B) were often difficult to distinguish under SEM from C-rich domains but were apparent when elemental maps documenting the spatial distribution of C and Si were constructed (Fig. 1C). Si-rich domains attached to ANME-SRB consortia extracted from methane seep sediment samples appeared as massive phases intergrown with consortium exteriors (Fig. 1B). Occasionally, Fe- and S-rich domains with framboidal textures (putative pyrite) appeared embedded in Si-rich domains (Fig. 1C).

AOM-active ANME-SRB consortia maintained in the laboratory for 3 years under sediment-free conditions harbored biomass consisting of multiple clusters of ANME-SRB consortia within EPS matrix (Figs. 1D-O, S1). Correlated epifluorescence FISH microscopy and SEM-EDS revealed these intergrown cell clusters were embedded in a matrix containing Si-rich phases and C (Figs. 1G-N, S1). These silicate phases were attached to the exteriors of consortia and differed in appearance from those observed on consortia sampled directly from sediment in their botryoidal habit, appearing as ~200 nm spheres forming intergrown Si-rich masses (Figs. 1G-N). These masses display a range of textural attributes, encrusting consortium exteriors (Fig. 2A,C), grading into smoother features of lower porosity (Fig. 2A,B), occasionally hosting framboidal Fe- and S-rich phases (Fig. 1N,O), and nearly or entirely enveloping consortia (Figs. 2A, S1H).

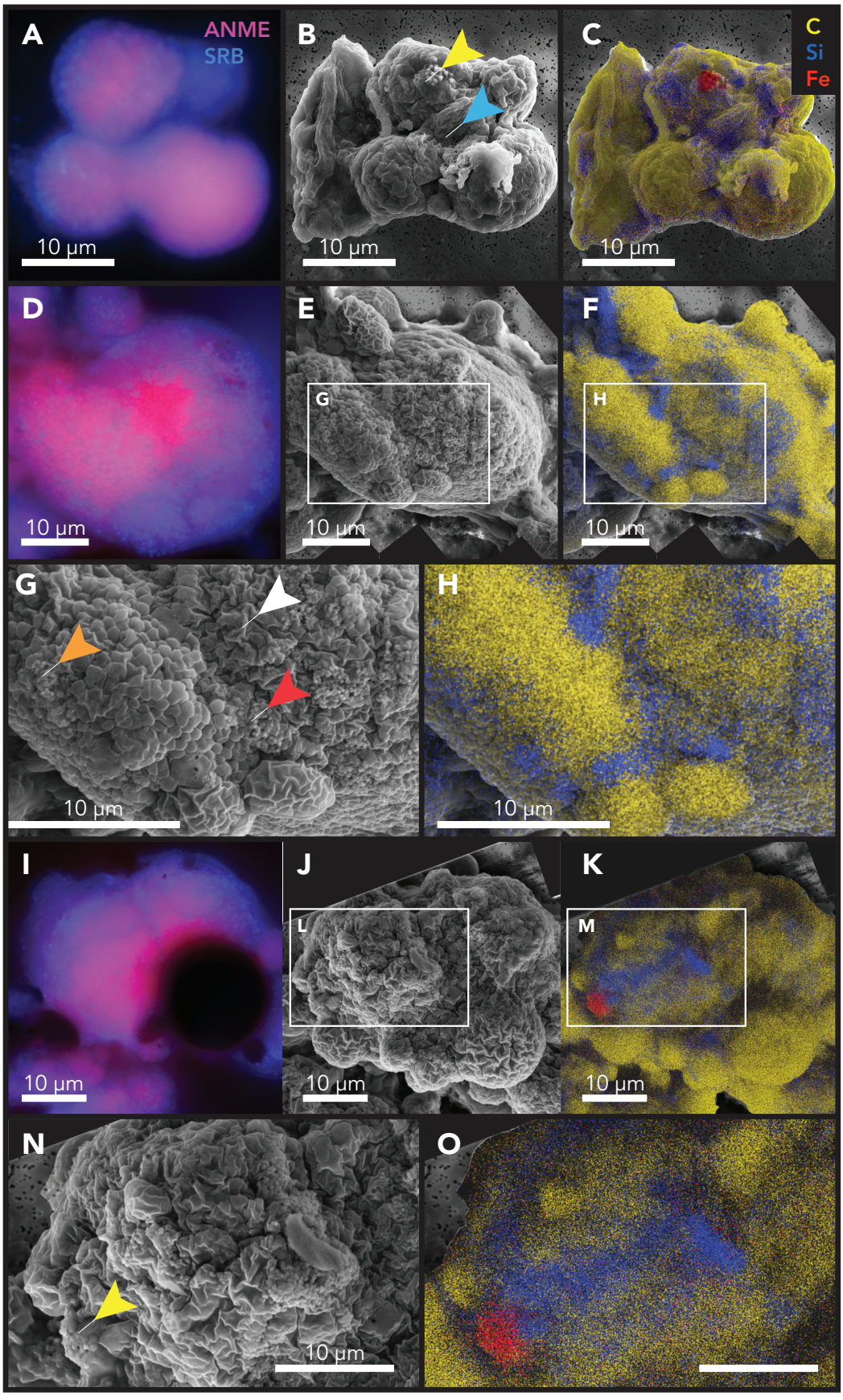
A
ANME
SRB
10 µm
B
10 µm
C
C
Si
Fe
10 µm
D
10 µm
E
G
10 µm
F
H
10 µm
G
10 µm
H
10 µm
I
10 µm
J
L
10 µm
K
M
10 µm
N
10 µm
O

Figure 1. Correlated epifluorescence (using FISH; A,D,I), SEM (B,E,G,J,N), and EDS (C,F,H,K,M) images documenting the presence of silicate phases attached to ANME-SRB consortium exteriors extracted from methane seep sediments from Santa Monica Basin (A-C), or from sediment-free AOM consortia incubations (D-O). In ANME-SRB consortia extracted directly from methane seep sediment samples, Si-rich domains between consortia are intergrown with consortia exteriors (B, *blue arrow*). In the sediment-free incubation, silicates are present between consortia which appear as clusters of dozens of ANME-SRB consortia, and have botryoidal, authigenic textures (G, *red arrow*) and encrust ANME exteriors (G, *orange arrow*). These botryoidal silicates were distinguishable from the rugose, C-rich consortium exteriors (*white arrow*) they encrust. Additionally, Fe- and S- rich domains observed via EDS (C, O) correlate with framboidal textures observed in SEM imagery (B, N, *yellow arrows*).

An ultrathin section of consortia biomass imaged by TEM (Fig. 2D) further revealed the textural characteristics of Si-rich phases with a particle size distribution of 230±62 nm (n = 6060) by image processing and Monte Carlo simulations. These sub-micron scale Si spheres were localized between multiple ANME-SRB consortia, embedded in the less coherent mineral-organic matrix adhering consortia to each other in a larger (~200 μm) biofilm.

Silicate Composition via EDS and FIB-EDS

EDS was used to compare the elemental composition of consortium-attached phases to free silicate phases (predominantly, clay particles) in the sediments from which ANME-SRB consortia were extracted. Elemental compositions, reported as weight percent of each element, were converted to atom percent to aid in phase identification. Phases attached to consortia extracted from both sediment-containing and sediment-free incubations are typically ~5-20 atom % Si, ~0-5% Al, and ~0-5% Fe (Fig. S2), but the raw atom % calculated from EDS data underrepresents Si, Al, and Fe due to high C and O

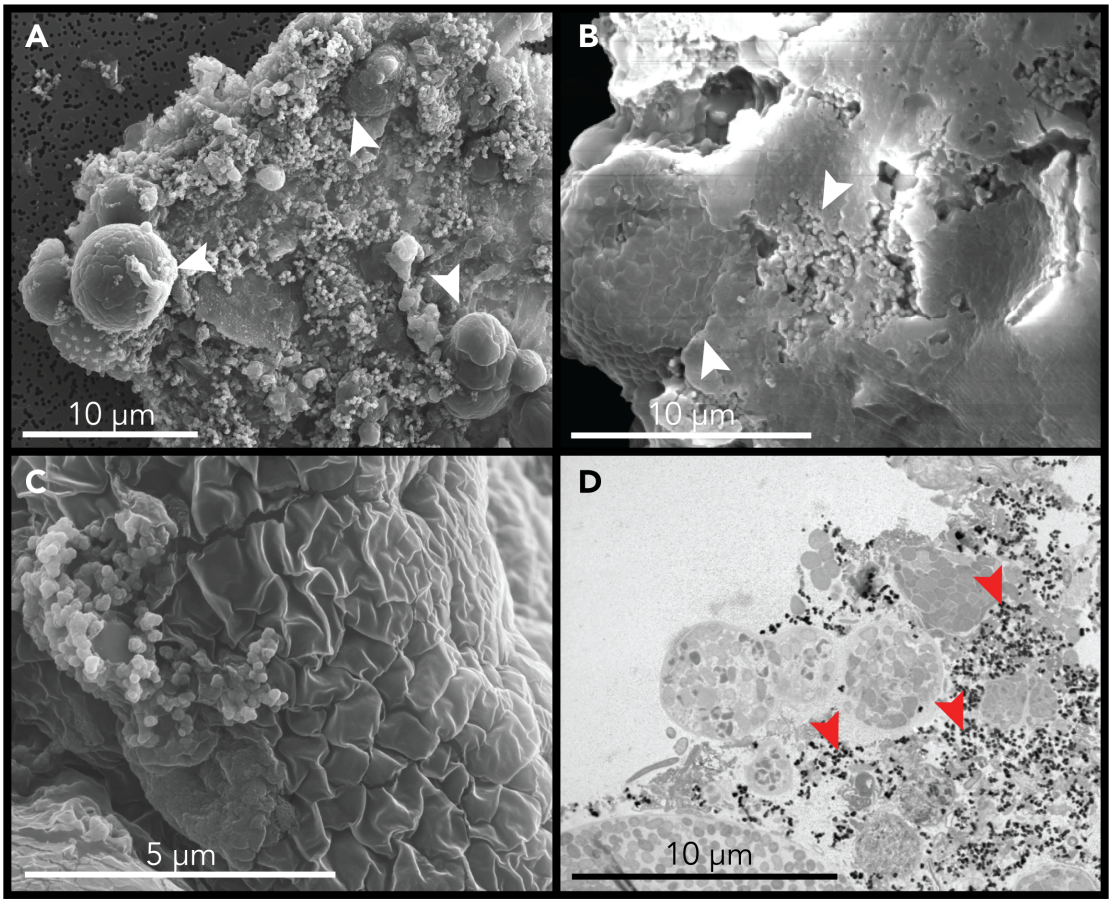

Figure 2. SEM imagery documenting the texture of silicate phases attached to ANME-SRB consortia grown under sediment-free conditions reveals the common appearance of these phases as ~200 nm botryoidal subspherical particles intergrown (A-B, *white arrows*) and encrusting consortia (A,C, *white arrows*). TEM imagery of a cross-section of a consortium cluster (D) demonstrates the distribution of this phase between consortia (*red arrows*), allowing for a quantitative estimation of sphere particle size (230±62 nm; Fig. S7).

signal from the associated biomass. To reduce this analytical bias, the data were analyzed as elemental ratios (atom % per atom %) which are unbiased by an abundance of C or O due to proximity to biomass (Fig. 3). The ratio of elements typically found in octahedral sites (Mg + Al + Fe) of clays to Si was also calculated, and revealed most consortium-attached phases to have more than 2 Si per octahedral cation. A one-way ANOVA test determined the elemental ratios between consortium-attached phases and the sediment

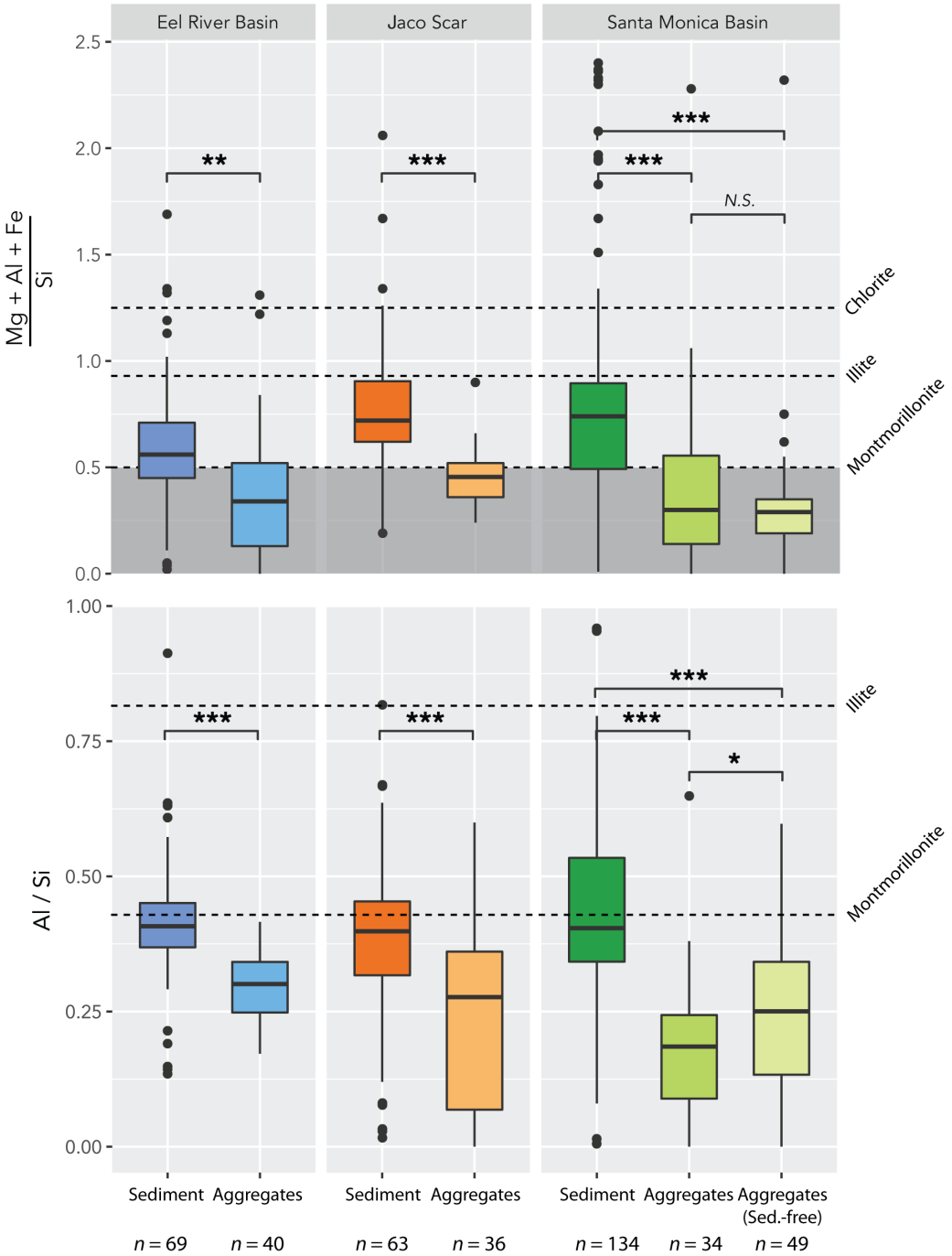

Figure 3. EDS-acquired compositional data of ANME-SRB consortium-attached silicates extracted directly from sediments or grown under sediment-free conditions compared with the range of compositions of silicates in the sediment from which the samples were drawn demonstrates the statistical significance (One-way ANOVA test, ***: $p<0.001$, **: $p<0.01$, *: $p<0.05$, *N.S.*: $p>0.05$) of compositional differences between consortium-attached silicates and source sediment due to significant Si enrichment in consortium-attached silicates. This enrichment is incompatible with the precipitation of stoichiometric clay, shown in the upper panel, which should have an octahedral cation : Si ratio greater than 0.5. Reference ideal clay mineral compositions taken from (Moore and Reynolds, 1997); chlorite omitted from bottom panel as ideal chlorite Al/Si ≥ 1.25.

samples from which consortia were extracted were all statistically significant in all samples (Fig. 3). Notable, elemental compositions of phases attached to consortia grown under sediment-free conditions (originally extracted from Santa Monica Basin methane seep sediments) were compositionally similar to those found attached to consortia recovered directly from those sediments by several elemental ratios ($p > 0.05$).

Using a focused ion beam (FIB), a cross-section through the center of a FISH-identified ANME-2—DSS consortium was prepared and subsequently analyzed by EDS. Data showed organic-rich interior with abundant C and N, with a Si-enriched phase on consortia exteriors in cross-section (Fig. 4). Si, Al, and Fe atom % measurements on the consortium exterior are comparable to those measured in non-sectioned consortia. Additionally, (Mg + Al + Fe) : Si measured on silicates attached to the FIB-sectioned consortium were similar to the measurements of this ratio on non-sectioned consortia, ranging between 0.25-0.29, or greater than 4 Si per octahedral cation.

ICP-MS

Si concentrations in the seawater media from the sediment-free incubations were low (1.22 ± 0.19 μM), as measured by ICP-MS (Fig. S5). Calculations of silica solubility at the pH (buffered to pH 8) and temperature (10˚ C) conditions present in sediment-free incubations demonstrated the sediment-free incubation media to be significantly undersaturated with respect to amorphous silica and equilibrium adsorption of Si to clay minerals.

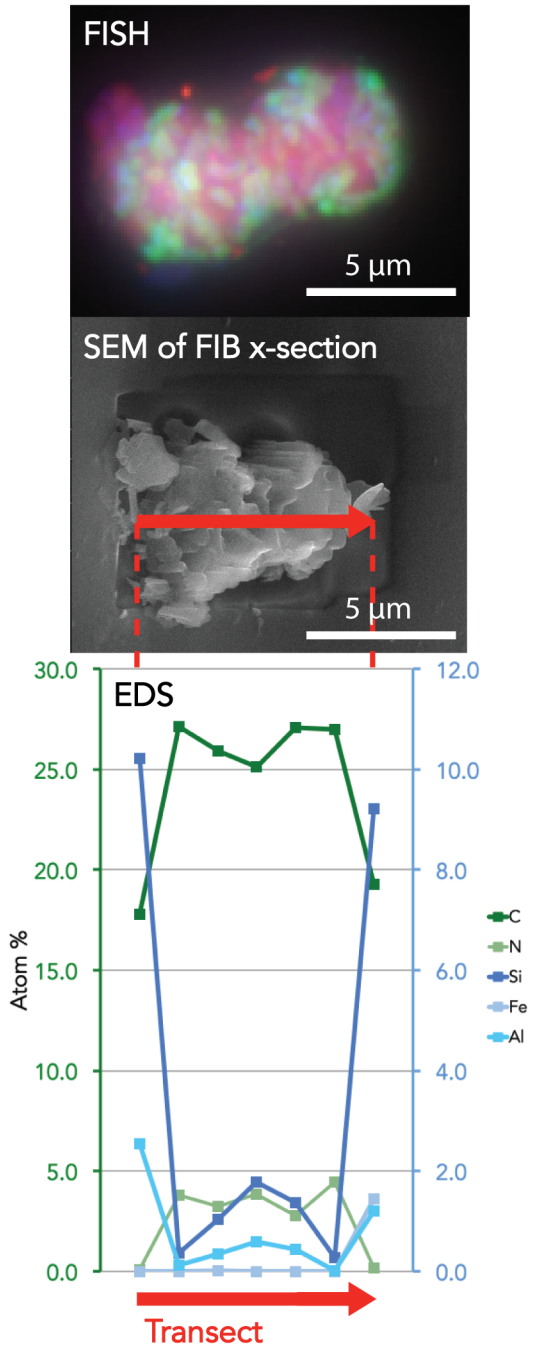

Figure 4. Correlated FISH and SEM micrographs of an ANME-SRB consortium (ANME-2, pink, stained by probe Eel 932; SRB, green, probe DSS 658) sectioned subsequent to epifluorescence microscopy by Ga^{+} FIB (after Dekas, 2013). Chemical analysis of a transect of this cross-section reveals consortium-attached silicate compositions similar to those measured on non-sectioned consortia, with Si enrichment relative to the source sediment inconsistent with stoichiometric clay compositions (octahedral cation : Si ≈ 1 : 4).

Seep Carbonates Contain C-rich Domains with Si-rich Margins

Epifluorescence microscopy and SEM imaging of a sample of seep carbonate recorded ~10-20 μm diameter aggregates of cocci stained by DAPI (Fig. 5A). FISH hybridization of these aggregates failed, potentially due to high background fluorescence from the carbonate matrix. These aggregates were common in the carbonate matrix, appearing particularly concentrated near or in vugs, cracks, or other porous features within the seep carbonate. These aggregates displayed a similar morphology to one another, with a bimodal distribution of cell sizes, larger cells located in the center of aggregates, and smaller cells near aggregate margins. SEM imaging of this seep carbonate sample documented electron-dense domains with similar morphology and spatial distribution to that observed for the DAPI-stained aggregates (Fig. 5B), although correlated fluorescence microscopy and SEM was not performed. EDS analysis of these electron-dense domains revealed them to be more C-rich than the carbonate matrix, and also surrounded by elevated Si concentrations (Fig. 5C-E).

Community Analysis

To determine the microbial community composition in the Si precipitating-AOM incubations, 16S rRNA amplicon sequencing was performed. 16S rRNA amplicon sequencing data from the sediment-free AOM incubation after 3 years of enrichment revealed a high proportion of reads (OTUs clustered at a 97% similarity) affiliated with ANME-2a/b (40% of total reads) and previously-established partner organism SEEP-SRB1

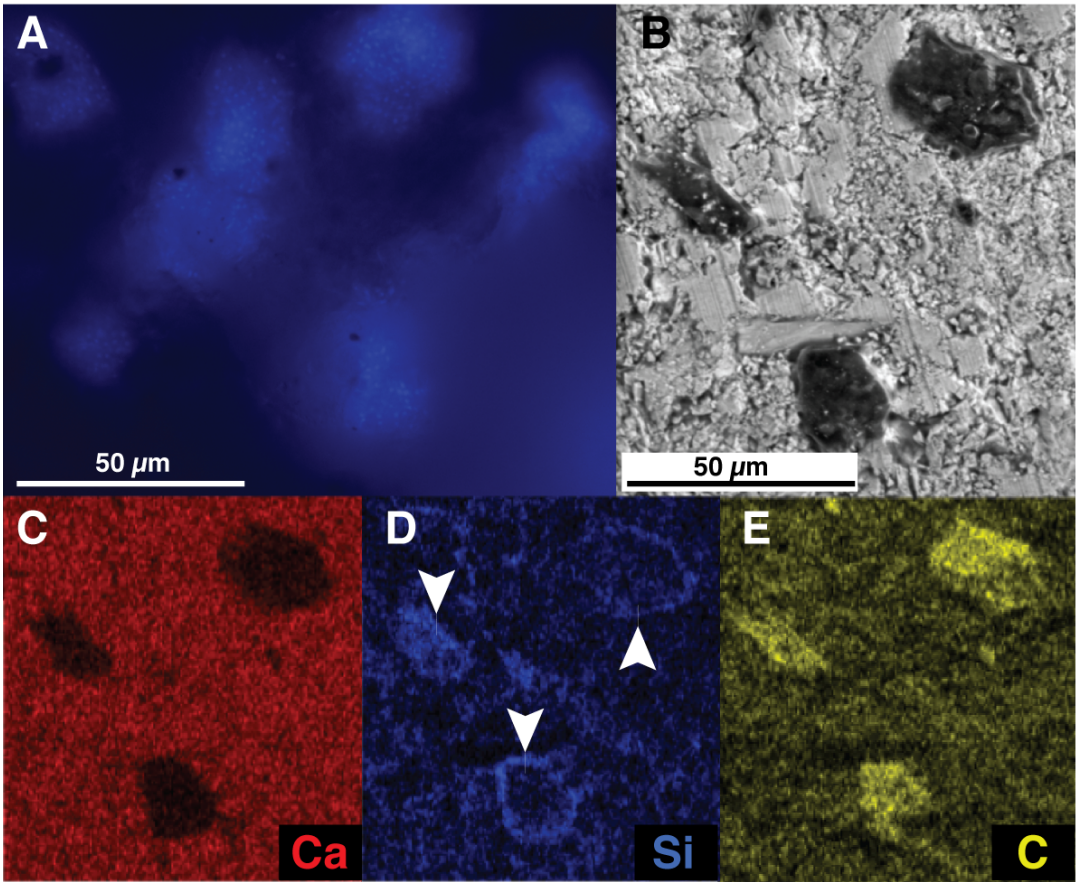

Figure 5. Epifluorescence microscopy (A) and SEM-EDS (B-E) imaging of putative ANME-SRB consortia embedded in seep carbonate. Microscopy (A) revealed the presence of many DAPI-stained microbial aggregates with morphology highly similar to that previously observed for ANME-SRB consortia embedded in carbonate (cf. Marlow, et al. 2014). SEM imaging of this seep carbonate sample documented the presence of several electron-dense (B) domains of similar size, morphology, and distribution as those of putative ANME-SRB consortia as observed by epifluorescence microscopy, although direct correlative imaging was not performed. EDS mapping of these putative ANME-SRB consortia revealed high Si concentrations localized to the exterior of these putative consortia (D, *white arrows*).

(15%; Figure S6). Other SRB detected in these incubations include SEEP-SRB2 (0.7% of total reads) and Desulfobacula (0.8% of total reads). While ANME-2a/b were the dominant archaeal group detected, minor contributions from methanogenic Methanococcoides (2% of archaeal reads) and from members of the class Thermoplasmata (6% of archaeal reads)

were also detected, while bacterial lineages associated with the the Chloroflexi (1% of total reads), heterortophic MBGD, and the Planctomycetes (2% of total reads).

Comparative Genomics

A search for predicted proteins containing serine- and lysine-/arginine-rich sequences was performed using a database of ANME and SRB genomes, followed by a search for similar proteins using BLASTp. The first part of the search was implemented in Python, using a sliding window of variable size to search for domains of any given ORF within the genome with a count of serine, lysine, and/or arginine residues within this window above a threshold. Of many candidate proteins uncovered during this search process, one predicted protein (NCBI Accession OEU44463) associated with metagenome-assembled genome bin from Santa Monica Basin (Desulfobacterales sp. S7086C20 (Skennerton et al., 2017)) affiliated with the SEEP-SRB1, clade of sulfate-reducing partners of ANME (Schreiber et al., 2010; Skennerton et al., 2017) with a particularly serine- and arginine-rich C-terminal sequence was found. Further analysis via BLAST revealed the identity of this protein as a member of the DUF3300 family of hypothetical membrane proteins, and was also predicted by PSORTb 3.0 (Yu et al., 2010) to have a signal peptide suggesting extracellular localization.

DISCUSSION

Previous research documented the presence of silicates with authigenic textures on the exterior of ANME-SRB consortia (Dekas, 2013; Chen, et al., 2014), but it was not clear to what extent these phases represented the product of active microbially-mediated precipitation as has been suggested, rather than passive attachment of silicates to ANME-SRB consortia by abiotic processes. To investigate this, we examined silicates attached to the exterior of ANME-SRB consortia grown under sediment-free conditions and compared these phases with those attached to ANME-SRB consortia extracted from methane seep sediments. Correlated epifluorescence microscopy and SEM-EDS imaging revealed the presence associated with Si-rich phases on ANME-SRB consortia (Fig. 1). These phases appeared intimately associated with consortium exteriors, sometimes intergrown with a C-rich matrix between consortia interpreted extracellular polymers. EDS-acquired compositional data of these Si-rich phases display compositions consistent with the interpretation of these phases as a silicate precipitate. Notably, consortium-attached silicates differ significantly (one-way ANOVA test, $p < 0.01$) from the composition of detrital silicates in the sediments from which they were sourced (Fig. 3) due to the Si-enriched nature of the consortium-attached silicates. When the elemental composition of consortium-attached silicates was examined using the ratio of elements typically found in octahedral sites of clay minerals (Mg, Al, Fe) to Si, it is clear that a majority of consortium-attached silicates are more enriched in Si than known clay mineral compositions. The most Si-rich clay possible (e.g. montmorillonite, $(Na,Ca)_{0.33}(Al, Mg)_2(Si_4O_{10})(OH)_2 \cdot nH_2O$), in which the ratio of tetrahedral to octahedral sheets is 2:1 and Si occupies all tetrahedral sites, could only have a octahedral cation to Si ratio of 0.5 (Moore and Reynolds, 1997);

however, most consortium-attached silicates have octahedral cation: Si ratios < 0.5 (0.40 ± 0.39, Fig. 3). In contrast, most compositional measurements of terrigenous detrital silicates in methane seep sediment samples from which consortia were extracted have octahedral cation : Si ratios of ~0.75 (0.82 ± 0.51), consistent with clay minerals. Notably, the silicates attached to ANME-SRB consortia from our work are significantly more Si-rich than cell-attached silicates previously used as a model for silicate precipitation aided by Fe or Al adsorption on cell walls ((Konhauser and Urrutia, 1999); Fig. S3). EDS performed along a transect of a FIB-sectioned ANME-SRB consortium corroborated observations of silicates attached to intact consortia recovered directly from seep sediments (Fig. 4). EDS elemental analysis along the transect supports the presence of silicates attached to external surfaces, as Si enrichment at consortium edges transitions to C and N-rich domains toward consortium interiors.

These observations, consistent with previous study of silicate phases attached to ANME-SRB exteriors, demonstrate to a high degree of statistical significance that ANME-SRB consortia extracted directly from seep sediments recruit Si to consortium exteriors, producing authigenic Si-rich silicate precipitates significantly Si-enriched relative to the silicates present in their host sediment. The Si-rich compositions of these phases stand in contrast to silicates observed attached to microbial exteriors in previous experiments in which Fe or Al adsorption to cell surfaces recruits Si from solutions rich in dissolved Si (≥150 μM), producing Fe- and/or Al-rich phases (Fig. S3 (Ferris et al., 1987; Konhauser et al., 1993, 1994; Mera and Beveridge, 1993; Köhler et al., 1994, 1999; Urrutia and Beveridge, 1994; Konhauser and Urrutia, 1999; Fein et al., 2002)). Previous work

describing ANME-SRB consortium-attached silicates, postulated a role for Al adsorption to ANME-SRB cell exteriors in mediating silicate precipitation (Chen et al., 2014), a mechanism which has only been shown to produce Fe- and/or Al-rich phases attached to cell exteriors (Urrutia and Beveridge, 1994; Konhauser and Urrutia, 1999). Additionally, Al-adsorption to cell exteriors has only been demonstrated to interact with silicate precipitation in media with sufficient dissolved Si ([Si] ≥ 150 μM) to drive abiotic silicate precipitation, obscuring the degree of biologically-mediated silicate precipitation (Urrutia and Beveridge, 1994; Konhauser and Urrutia, 1999). The significant compositional difference between Si-rich silicates observed here attached to ANME-SRB consortia and that of cell-attached silicates produced by interactions between Fe and/or Al adsorbed to cell surfaces (Fig. S3; (Konhauser and Urrutia, 1999)) suggests other processes may be involved in the precipitation of Si-rich silicates on ANME-SRB consortium exteriors. However, the degree to which silicate precipitation onto ANME-SRB consortia sourced directly from sediments is biologically controlled was difficult to assess without additional constraints on porewater geochemistry, as sufficiently high [Si] could possibly catalyze abiotic precipitation of authigenic silicates. Previous observations of ANME-SRB consortium-attached silicates from the South China Sea (Chen et al., 2014) were collected from incubation samples with no constraints on porewater [Si] (Zhang et al., 2010, 2011).

We were able to test the hypothesis that ANME-SRB consortia are capable of removing Si preferentially from solution, producing Si-rich silicate precipitates on consortium exteriors by analyzing a sediment-free incubation of ANME-2b—DSS consortia anaerobically prepared from methane seep sediments of Santa Monica Basin

using Percoll-based density separation. After 3 years of sediment-free incubation under AOM conditions enriching for the growth of ANME-SRB consortia, correlated epifluorescence microscopy and SEM-EDS analysis documented large clusters consisting of dozens of ANME-SRB consortia embedded in a Si-rich matrix that, under SEM, consisted of ~200 nm Si spheres intergrown with rugose, C-rich domains interpreted as EPS (Figs. 1G,H, 1N,O, 2A-C, S1). Occasionally, framboidal Fe- and S-rich domains were observed in this matrix, likely framboidal pyrite or other iron sulfide phases produced during active, sulfate-coupled AOM. The growth habit of clusters of many AOM consortia held together by a mineral-organic matrix contrasts with the appearance of consortia extracted directly from sediment by standard sonication- and density separation-based techniques, the latter typically appearing in epifluorescence microscopy as single consortia of 50-5000 cells (Boetius et al., 2000; Orphan et al., 2001b, 2002). Notably, the polyconsortium clusters observed here (Figs. 1D-O, 2, S1, S4), sourced from sediment-free incubations were observed without the sonication, density separation, and filtration steps necessary to extract consortia directly from sediment, steps that may bias observations against such clusters in situ. TEM observations of consortia grown under sediment-free conditions corroborated SEM-EDS images, revealing the presence of abundant 230±62 nm-diameter subspherical particles between consortia, and confirming the presence of these silicate phases throughout consortium clusters (Fig. 2D). We were initially concerned that some portion of these phases may represent Percoll contamination, but calculations based on the abundance of consortium-attached silicates and estimated total ANME-SRB biomass in these incubations precluded the introduced Si from Percoll as a sufficient source of Si for the consortium-attached silicates. Additionally, the size distribution of these subspherical

silicate particles eliminates the possibility of significant Percoll contamination which is represented by colloidal silica particles of diameter 15-30 nm (G.E. Healthcare Life Sciences, 2018).

Observations of silicates distributed between consortia grown under sediment-free conditions are consistent with previous observations (Chen et al., 2014), which were collected from consortia sampled directly out of sediment without use of Percoll density separation, suggesting this silicate precipitation to be a biological phenomenon of ANME-SRB consortia, rather than an artifact of the consortia enrichment procedure. We further analyzed the process of silicate precipitation by ANME-SRB consortia using a model describing growth of consortia within EPS using consortium doubling times of 3-9 months taken from the literature (Girguis et al., 2005; Nauhaus et al., 2007; Dekas et al., 2009; Meulepas et al., 2009; Orphan et al., 2009). Assuming consortia clusters observed after 3 years of incubation had increased exponentially from a small number of starting consortia, the consortium counts in a larger cluster from epifluorescence data (Fig. S4) were used to constrain the maximum number of consortia present at $t = 0$ that could have produced the observed consortium number after 3 years of incubation (Fig. 6). The model demonstrates that significant consortium growth over 3 years is required for even the longest generation times (9 months). Therefore, the Si-rich phases observed in the extracellular matrix between consortia must have developed subsequent to inoculation, as the majority of consortia embedded within these phases are required by reasonable doubling times to have grown subsequent to inoculation. Measurement of [Si] in sediment-free incubation media post-incubation via ICP-MS, 1.2 ± 0.2 μM, precluded abiotic mechanisms of Si enrichment

of consortium-attached silicates, as a [Si] of 1.2 µM was below concentrations previously reported to drive was too low to drive either amorphous silica precipitation (~1000 µM) or Si adsorption on pre-existing consortium-attached silicates (≥200 µM (Siever and Woodford, 1973); Fig. S5). Silicon concentrations in sediment-free incubations are also inconsistent with silicate precipitation associated with the initial gradient separation, as such precipitation again would only occur with Percoll-introduced [Si] above Si clay adsorption equilibria (Siever and Woodford, 1973), far above the ~3 µM of Percoll-associated [Si] estimated to be introduced during the initial gradient separation.

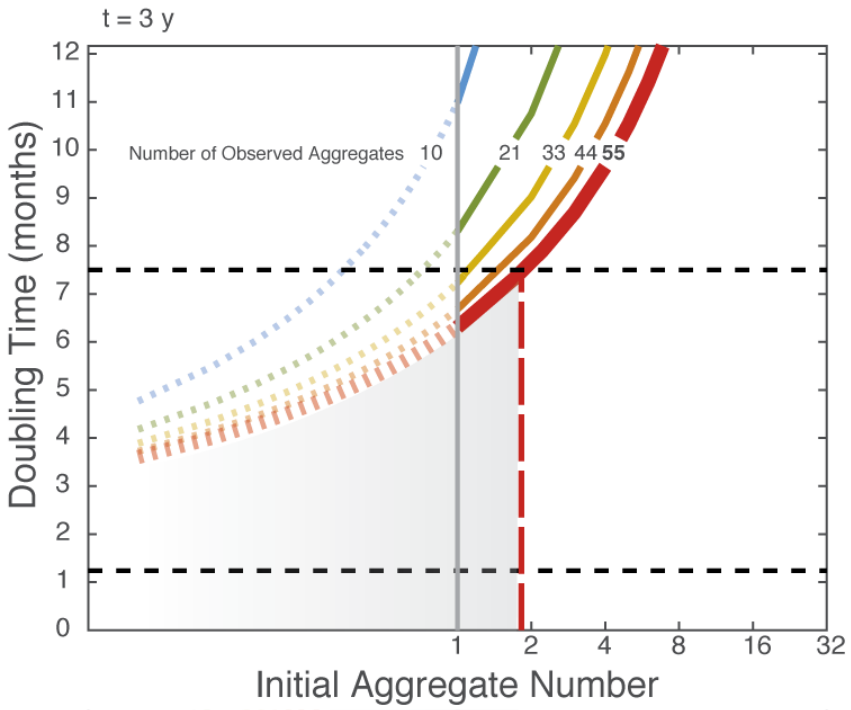

Figure 6. A model calculating initial ANME-SRB consortium number required to produce a given number of consortia observed after 3 years of sediment-free incubation indicates that for previously-calculated consortium doubling times (Girguis et al., 2005; Meulepas et al., 2009; Nauhaus et al., 2007), even the largest consortium clusters must have grown from a small percentage of their current number, assuming consortia observed in a cluster grew from a smaller number of consortia. Thus, silicates observed between consortia must have grown subsequent to inoculation, from media undersaturated with respect to amorphous silica and Si adsorption on aluminosilicate clays (S5).

Together, these lines of evidence disprove the null hypothesis that consortium-attached silicates formed due to passive attachment of detrital silicates on ANME-SRB consortium surfaces or via known mechanisms of abiotic silicate precipitation from solution, implying active local removal of Si from solution during AOM by ANME-2—SRB consortia and suggestive of bona fide silicate biomineralization by ANME-SRB.

The biological mechanism used by ANME-SRB consortia to catalyze orthosilicic acid condensation is currently unknown. Prokaryotic silicate biomineralization of Si-rich phases in undersaturated conditions has been previously observed in experiments examining the Si-bearing spore coat of the *Bacillus subtilis* (Motomura et al., 2016). In this gram-positive bacterium, condensation of dissolved orthosilicic acid was demonstrated to be catalyzed by a particularly serine- and arginine- rich sequence of a spore coat protein (Motomura et al., 2016). The zwitterionic nature of this sequence is similar to that of silacidins and silaffins, proteins that contribute to silica precipitation in diatoms serine- and lysine-rich proteins thought to contribute to silica precipitation in diatoms (Kroger et al., 2001; Wenzl et al., 2008; Richthammer et al., 2011). Following previous work attempting to find silaffin-like proteins in diatom genomes (Scheffel et al., 2011), we performed a search through our seep metagenome database to find proteins with similar, C-terminal zwitterionic sequences rich in serine and lysine or arginine residues. One serine- and arginine-rich hypothetical protein was found in association with a Deltaproteobacteria (SEEP-SRB1) partner of ANME (Desulfobacterales sp. S7086C20, NCBI accession OEU44463; (Skennerton et al., 2017)) predicted to be membrane-associated and localized to the cell surface. Additional support for the extracellular localization of this protein was

suggested by the prediction of a hydrophobic DUF3300 domain in the protein. Related proteins with serine- and lysine/arginine-rich C-terminal sequences were also detected in other Desulfobacterales (Desulfobacterales bacterium SG8_35_2, NCBI accession KPK26241.1) and additional members of the Deltaproteobacteria, including *Geobacter uraniireducens* Rf4 (NCBI accession WP_011939518.1) may be candidates for investigating the degree to which this group of membrane proteins may be involved in silicate biomineralization via interactions between its C-terminal zwitterionic sequence and dissolved orthosilicic acid.

Another notable example of prokaryotic silicate biomineralization with potential relevance to the ANME-SRB syntrophy is the potential link between extracellular Fe reduction of iron-rich clays and concomitant silica precipitation. Observations of silica precipitation in media undersaturated with respect to amorphous silica were reported from experiments in which silica precipitation occurred during the reductive dissolution of Fe-rich clay minerals by iron- and sulfate-reducing bacteria (Dong et al., 2003; Li et al., 2004; O'Reilly et al., 2005; Furukawa and O'Reilly, 2007; Zhang et al., 2007) (Li et al., 2004). Here, silica precipitation was proposed to occur through the activity of polyamines, long-chain forms of which (>7 aminopropyl units) have been proposed to play an important role in silica precipitation in diatoms (Kröger et al., 2000; Belton et al., 2008) and have been shown to precipitate silica in undersaturated conditions from silica oligomers (Patwardhan et al., 2011). Long-chain polyamines, structurally-similar to thermospermine (Kröger et al., 2000), have been proposed to be synthesized in diatoms by aminopropyl transferases with a conserved GGGE motif (Michael, 2011). Prokaryotic aminopropyl transferases with a

conserved GGGE motif related to those in diatoms (Minguet et al., 2008) also produce longer-chain and branched polyamines >4 aminopropyl units long (Hamana et al., 1991; Knott, 2009; Ohnuma et al., 2011). We searched existing ANME-SRB metagenome data for aminopropyl transferases homologous to those known to produce long-chain polyamines. However, no ANME or SRB genome contained homologous aminopropyl transferases; the only homologous sequence was an aminopropyl transferase from a reconstructed Dehalococcoides from methane seeps.

Although the biochemical mechanism catalyzing silicate precipitation mediated by ANME-SRB remains uncertain, observations of silica precipitation resulting from interactions between Fe- or sulfate-reducing prokaryotes and clays may give insight into possible sources of Si precipitated in phases attached to consortium surfaces. Recent evidence strongly suggests ANME performs direct electron transfer to SRB partners through multiheme cytochrome complexes (McGlynn et al., 2015; Wegener et al., 2015), and ANME have been shown to use insoluble Fe, Mn oxides and soluble electron shuttles as electron acceptors (Beal et al., 2009; Sivan et al., 2014; Ettwig et al., 2016; Scheller et al., 2016; Leu et al., 2020). These extracellular electron transfer models of ANME-SRB syntrophy are similar to direct electron transfer by organisms such as *Shewanella oneidensis* and *Geobacter* sp. shown to be capable of reducing clay-bound iron with concomitant removal of Si from clays, driving silicate precipitation in undersaturated conditions as discussed above (Dong et al., 2003; O'Reilly et al., 2005; Furukawa and O'Reilly, 2007; Zhang et al., 2007). The poorly-understood process of silica precipitation occurring as a result of clay interactions with various Fe- and sulfate-reducers could

possibly explain observations of consortium-attached silicates and iron sulfide: silicate precipitation could be driven by auxiliary Fe-reduction of clay-bound Fe by consortia, either by direct transfer of electrons by protein complexes or redox-active shuttles to clays adhered to consortium exteriors or through indirect reduction via sulfide oxidation. However, silica precipitation driven by clay dissolution alone would imply by mass balance the presence of an equally-abundant Al-enriched clay residue in our experiments. While we do not observe such phases attached to ANME-SRB consortium clusters in our experiments, previous study of the mineral products of dissimilatory reduction of iron-bearing clay minerals (O'Reilly et al., 2005) as well as previous study of the mineralogy of silicates attached to ANME-SRB consortia (Chen, et al 2014) documented such Al-rich residues, which in the latter study were identified by TEM as Al-rich silicate crystals of kaolinite and/or nacrite (both $Al_2Si_2O_5(OH)_4$). Future work is necessary to parse the extent of direct silica precipitation from media vs. precipitation via proximal clay dissolution, as this will help resolve these competing hypotheses.

The presence of silicate phases precipitated on consortium surfaces and between consortia suggests the purpose of these phases may be to give structure to consortium exteriors or to polyconsortium clusters as those observed here in sediment-free incubations. If these polyconsortium clusters exist as a major mode of consortium growth in vivo, authigenic silicates may ensure the ability for consortia to share resources, as has been observed within consortia for N_2-fixation (Dekas et al., 2009; Dekas et al. 2016; this thesis, Chapter 1). It remains unknown, however, if the cluster mode of consortium growth is

present in environmental settings; examining positions of consortia directly within the sediment matrix is a promising direction of future research.

The mode of prokaryotic silicate biomineralization described in this study may be additionally important for the preservation of organic carbon in the rock record. Authigenic silicates are well-known to provide excellent preservation potential in rocks of all ages, providing early occlusion of pore space which protects organics from degradation (Callow and Brasier, 2009; Newman et al., 2016). Early silicate cements are important in fossil seep carbonates spanning the Phanerozoic, where silica appears as fibrous and botryoidal cements replacing aragonite or cryptocrystalline void-filling cements (Peckmann et al., 2002; Himmler et al., 2008; Kaim et al., 2008; Kuechler et al., 2012; Smrzka et al., 2015; Miyajima et al., 2016). Early silica precipitation in seep carbonates can entomb organics; in one striking example, preservation of vestimentiferan tube worm chitin by early silicate cements in Late Cretaceous (Campanian) seep carbonates of Japan has been documented (Hikida et al., 2003). In rare cases, silicate cements from both fossil (Miyajima et al., 2016) and modern (Köhler et al., 1999) seep carbonates have even been observed to trap CH_4 in hydrate minerals, suggesting silicate cementation concomitant with CH_4 production (Lazzeri et al., 2017).

Here, we document in seep carbonate samples the presence of Si-rich phases localized to the margins of C-rich domains (Fig. 5). Although we could not exactly correlate these features between SEM and epifluorescent microscopy, these C-rich domains share morphology and spatial distribution with those of DAPI-stained aggregates with morphology suggestive of ANME-SRB consortia (Fig. 5A). On the basis of these

observations, we hypothesized that these domains represent ANME-SRB consortia that precipitated silicates on consortium exteriors. We further speculated that the precipitation of silicates on the exteriors of these putative ANME-SRB consortia served to preserve their biomass. Our hypothesis could be tested by measurement of the carbon isotope compositions of these domains by SIMS. If this hypothesis is confirmed, these features would then present a useful search image for ANME-SRB consortia preserved in fossil seep carbonates.

The importance of early silicate cementation in seep carbonates and in siliciclastic sediments more broadly (Newman et al., 2016) for non-mineralized tissue preservation in the rock record raises the question of the degree to which understudied prokaryotic silicate biomineralization may interact with this process. Silica-precipitating diatom silaffin sequences are highly divergent, implying the evolution of zwitterionic peptides as a method for biological control of silicate mineralization to have occurred multiple times, further demonstrated by the silicate-precipitation activity of a *Bacillus subtilis* spore coat protein (Kroger et al., 2001; Scheffel et al., 2011; Motomura et al., 2016). The possibility that similar convergent evolution may have produced a variety of yet-uncharacterized proteins similar to that discussed here from Desulfobacterales sp. S7086C20 motivates future work to directly test the degree to which this protein can catalyze silicate precipitation in solutions undersaturated with respect to amorphous silica. A demonstration of silicate precipitation in undersaturated conditions catalyzed by this protein would be an important step in improving our understanding of biological mediation of early silicate cementation in the rock record.

CONCLUSIONS

We demonstrate here for silicate precipitation in undersaturated and sediment-free media within the extracellular matrix produced by ANME-SRB consortia. SEM-EDS examination reveals this silicate phases to exhibit authigenic textures similar to those observed on the exteriors of ANME-SRB consortia removed directly from sediment, suggesting that silicates precipitated on the exteriors ANME-SRB consortia grown under sediment-free incubations are representative of those previously discussed in the literature. Additionally, the composition of silicates precipitated in sediment-free, Si-undersaturated conditions are highly similar to those observed on ANME-SRB consortia extracted from environmental samples. These observations indicate bona fide silicate precipitation mediated by ANME-SRB consortia and suggest that authigenic silicates may play an important role in the taphonomy of methane seep ecosystems in the rock record.

REFERENCES

Aloisi, G., Pierre, C., Rouchy, J.-M., Foucher, J.-P., and Woodside, J. (2000). Methane-related authigenic carbonates of eastern Mediterranean Sea mud volcanoes and their possible relation to gas hydrate destabilisation. Earth Planet. Sci. Lett. 184, 321–338. doi:10.1016/S0012-821X(00)00322-8.

Barghoorn, E. S., and Tyler, S. A. (1965). Microorganisms from the Gunflint Chert. Science 147, 563–575. doi:10.1126/science.147.3658.563.

Beal, E. J., House, C. H., and Orphan, V. J. (2009). Manganese- and Iron-Dependent Marine Methane Oxidation. Science 325, 184–187. doi:10.1126/science.1169984.

Belton, D. J., Patwardhan, S. V., Annenkov, V. V., Danilovtseva, E. N., and Perry, C. C. (2008). From biosilicification to tailored materials: Optimizing hydrophobic domains and resistance to protonation of polyamines. Proc. Natl. Acad. Sci. 105, 5963–5968. doi:10.1073/pnas.0710809105.

Boetius, A., Ravenschlag, K., Schubert, C. J., Rickert, D., Widdel, F., Gieseke, A., et al. (2000). A marine microbial consortium apparently mediating anaerobic oxidation of methane. Nature 407, 623. doi:10.1038/35036572.

Braissant, O., Decho, A. W., Dupraz, C., Glunk, C., Przekop, K. M., and Visscher, P. T. (2007). Exopolymeric substances of sulfate-reducing bacteria: Interactions with calcium at alkaline pH and implication for formation of carbonate minerals. Geobiology 5, 401–411. doi:10.1111/j.1472-4669.2007.00117.x.

Cai, C., Leu, A. O., Xie, G.-J., Guo, J., Feng, Y., Zhao, J.-X., et al. (2018). A methanotrophic archaeon couples anaerobic oxidation of methane to Fe(III) reduction. ISME J. 12, 1929–1939. doi:10.1038/s41396-018-0109-x.

Callow, R. H. T., and Brasier, M. D. (2009). Remarkable preservation of microbial mats in Neoproterozoic siliciclastic settings: Implications for Ediacaran taphonomic models. Earth-Sci. Rev. 96, 207–219. doi:10.1016/j.earscirev.2009.07.002.

Case, D. H., Pasulka, A. L., Marlow, J. J., Grupe, B. M., Levin, L. A., and Orphan, V. J. (2015). Methane Seep Carbonates Host Distinct, Diverse, and Dynamic Microbial Assemblages. mBio 6. doi:10.1128/mBio.01348-15.

Chen, Y., Li, Y.-L., Zhou, G.-T., Li, H., Lin, Y.-T., Xiao, X., et al. (2014). Biomineralization mediated by anaerobic methane-consuming cell consortia. Sci. Rep. 4, 1–9. doi:10.1038/srep05696.

Cline, J. D. (1969). Spectrophotometric Determination of Hydrogen Sulfide in Natural Waters1. Limnol. Oceanogr. 14, 454–458. doi:10.4319/lo.1969.14.3.0454.

Cock, P. J. A., Antao, T., Chang, J. T., Chapman, B. A., Cox, C. J., Dalke, A., et al. (2009). Biopython: freely available Python tools for computational molecular biology and bioinformatics. Bioinformatics 25, 1422–1423. doi:10.1093/bioinformatics/btp163.

Decho, A. W. (2010). Overview of biopolymer-induced mineralization: What goes on in biofilms? Ecol. Eng. 36, 137–144. doi:10.1016/j.ecoleng.2009.01.003.

Dekas, A. E. (2013). Diazotrophy in the deep: an analysis of the distribution, magnitude, geochemical controls, and biological mediators of deep-sea benthic nitrogen fixation. Div. Geol. Planet. Sci. Ph.D.

Dekas, A. E., Poretsky, R. S., and Orphan, V. J. (2009). Deep-Sea Archaea Fix and Share Nitrogen in Methane-Consuming Microbial Consortia. Science 326, 422–426. doi:10.1126/science.1178223.

Dixit, S., Van Cappellen, P., and van Bennekom, A. J. (2001). Processes controlling solubility of biogenic silica and pore water build-up of silicic acid in marine sediments. Mar. Chem. 73, 333–352. doi:10.1016/S0304-4203(00)00118-3.

Dong, H., Kostka, J. E., and Kim, J. (2003). Microscopic evidence for microbial dissolution of smectite. Clays Clay Miner. 51, 502–512.

Drever, J. I. (1988). The Geochemistry of Natural Waters. 3rd ed. Upper Saddle River, New Jersey: Prentice Hall.

Ettwig, K. F., Zhu, B., Speth, D., Keltjens, J. T., Jetten, M. S. M., and Kartal, B. (2016). Archaea catalyze iron-dependent anaerobic oxidation of methane. Proc. Natl. Acad. Sci. 113, 12792–12796. doi:10.1073/pnas.1609534113.

Fein, J. B., Scott, S., and Rivera, N. (2002). The effect of Fe on Si adsorption by *Bacillus subtilis* cell walls: insights into non-metabolic bacterial precipitation of silicate minerals. Chem. Geol. 182, 265–273. doi:10.1016/S0009-2541(01)00294-7.

Ferris, F. G., Fyfe, W. S., and Beveridge, T. J. (1987). Bacteria as nucleation sites for authigenic minerals in a metal-contaminated lake sediment. Chem. Geol. 63, 225–232. doi:10.1016/0009-2541(87)90165-3.

Furukawa, Y., and O'Reilly, S. E. (2007). Rapid precipitation of amorphous silica in experimental systems with nontronite (NAu-1) and *Shewanella oneidensis* MR-1. Geochim. Cosmochim. Acta 71, 363–377. doi:10.1016/j.gca.2006.09.006.

G.E. Healthcare Life Sciences (2018). Cell Separation Media: Methodology and applications. Uppsala, Sweden: GE Healthcare Bio-Sciences AB.

Girguis, P. R., Cozen, A. E., and DeLong, E. F. (2005). Growth and population dynamics of anaerobic methane-oxidizing archaea and sulfate-reducing bacteria in a continuous-flow bioreactor. Appl. Environ. Microbiol. 71, 3725–3733. doi:10.1128/aem.71.7.3725-3733.2005.

Glasauer, S., Langley, S., and Beveridge, T. J. (2001). Sorption of Fe (Hydr)Oxides to the Surface of *Shewanella putrefaciens*: Cell-Bound Fine-Grained Minerals Are Not Always Formed De Novo. Appl. Environ. Microbiol. 67, 5544–5550. doi:10.1128/aem.67.12.5544-5550.2001.

Gunnarsson, I., and Arnórsson, S. (2000). Amorphous silica solubility and the thermodynamic properties of H4SiO°4 in the range of 0° to 350°C at Psat. Geochim. Cosmochim. Acta 64, 2295–2307. doi:10.1016/S0016-7037(99)00426-3.

Hamana, K., Niitsu, M., Samejima, K., and Matsuzaki, S. (1991). Polyamine Distributions in Thermophilic Eubacteria Belonging to Thermus and Acidothermus. J. Biochem. (Tokyo) 109, 444–449.

Hikida, Y., Suzuki, S., Togo, Y., and Ijiri, A. (2003). An exceptionally well-preserved fossil seep community from the Cretaceous Yezo Group in the Nakagawa area, Hokkaido, northern Japan. Paleontol. Res. 7, 329–342. doi:10.2517/prpsj.7.329.

Himmler, T., Freiwald, A., Stollhofen, H., and Peckmann, J. (2008). Late Carboniferous hydrocarbon-seep carbonates from the glaciomarine Dwyka Group, southern Namibia. Palaeogeogr. Palaeoclimatol. Palaeoecol. 257, 185–197. doi:10.1016/j.palaeo.2007.09.018.

Hugo, R. C., Cady, S. L., and Smythe, W. (2011). The Role of Extracellular Polymeric Substances in the Silicification of Calothrix: Evidence from Microbial Mat Communities in Hot Springs at Yellowstone National Park, USA. Geomicrobiol. J. 28, 667–675. doi:10.1080/01490451.2010.511983.

Iler, R. K. (1979). The Chemistry of Silica: Solubility, Polymerization, Colloid and Surface Properties, and Biochemistry. New York: Wiley.

Kaim, A., Jenkins, R. G., and WarÉN, A. (2008). Provannid and provannid-like gastropods from the Late Cretaceous cold seeps of Hokkaido (Japan) and the fossil record of the Provannidae (Gastropoda: Abyssochrysoidea). Zool. J. Linn. Soc. 154, 421–436. doi:10.1111/j.1096-3642.2008.00431.x.

Knittel, K., and Boetius, A. (2009). Anaerobic Oxidation of Methane: Progress with an Unknown Process. Annu. Rev. Microbiol. 63, 311–334. doi:10.1146/annurev.micro.61.080706.093130.

Knott, J. M. (2009). Biosynthesis of long-chain polyamines by crenarchaeal polyamine synthases from Hyperthermus butylicus and Pyrobaculum aerophilum. FEBS Lett 583, 3519–24. doi:10.1016/j.febslet.2009.10.014.

Köhler, B., Singer, A., and Stoffers, P. (1994). Biogenic nontronite from marine white smoker chimneys. Clays Clay Miner. 42, 689–701.

Köhler, S., Irmer, G., Kleeberg, R., Monecke, J., Herzig, P. M., and Schulz, B. (1999). Melanophlogite from the Cascadia accretionary prism, offshore Oregon: First occurrence in a cold seep environment. Berichte Dtsch. Mineral. Ges. 11, 129.

Konhauser, K. O., Fyfe, W. S., Ferris, F. G., and Beveridge, T. J. (1993). Metal sorption and mineral precipitation by bacteria in two Amazonian river systems: Rio Solimões and Rio Negro, Brazil. Geology 21, 1103–1106. doi:10.1130/0091-7613(1993)021<1103:MSAMPB>2.3.CO;2.

Konhauser, K. O., Schultze-Lam, S., Ferris, F. G., Fyfe, W. S., Longstaffe, F. J., and Beveridge, T. J. (1994). Mineral precipitation by epilithic biofilms in the speed river, ontario, Canada. Appl Env. Microbiol 60, 549–53.

Konhauser, K. O., and Urrutia, M. M. (1999). Bacterial clay authigenesis: a common biogeochemical process. Chem. Geol. 161, 399–413. doi:10.1016/S0009-2541(99)00118-7.

Krause, S., Liebetrau, V., Gorb, S., Sánchez-Román, M., McKenzie, J. A., and Treude, T. (2012). Microbial nucleation of Mg-rich dolomite in exopolymeric substances under anoxic modern seawater salinity: New insight into an old enigma. Geology 40, 587–590. doi:10.1130/G32923.1.

Kröger, N., Deutzmann, R., Bergsdorf, C., and Sumper, M. (2000). Species-specific polyamines from diatoms control silica morphology. Proc. Natl. Acad. Sci. 97, 14133–14138. doi:10.1073/pnas.260496497.

Kroger, N., Deutzmann, R., and Sumper, M. (2001). Silica-precipitating peptides from diatoms. The chemical structure of silaffin-A from Cylindrotheca fusiformis. J Biol Chem 276, 26066–70. doi:10.1074/jbc.M102093200.

Kuechler, R. R., Birgel, D., Kiel, S., Freiwald, A., Goedert, J. L., Thiel, V., et al. (2012). Miocene methane-derived carbonates from southwestern Washington, USA and a model for silicification at seeps. Lethaia 45, 259–273. doi:10.1111/j.1502-3931.2011.00280.x.

Lalonde, S. V., Konhauser, K. O., Reysenbach, A.-L., and Ferris, F. G. (2005). The experimental silicification of Aquificales and their role in hot spring sinter formation. Geobiology 3, 41–52. doi:10.1111/j.1472-4669.2005.00042.x.

Lazzeri, K. E., Bebout, G. E., and Geiger, C. A. (2017). Nitrogen and carbon concentrations and isotopic compositions of the silica clathrate melanophlogite. Am. Mineral. 102, 686–689. doi:10.2138/am-2017-5876.

Leu, A. O., Cai, C., McIlroy, S. J., Southam, G., Orphan, V. J., Yuan, Z., et al. (2020). Anaerobic methane oxidation coupled to manganese reduction by members of the Methanoperedenaceae. ISME J. 14, 1030–1041. doi:10.1038/s41396-020-0590-x.

Li, Y.-L., Vali, H., Sears, S. K., Yang, J., Deng, B., and Zhang, C. L. (2004). Iron reduction and alteration of nontronite NAu-2 by a sulfate-reducing bacterium1 1Associate editor: J. B. Fein. Geochim. Cosmochim. Acta 68, 3251–3260. doi:10.1016/j.gca.2004.03.004.

Loyd, S. J., Sample, J., Tripati, R. E., Defliese, W. F., Brooks, K., Hovland, M., et al. (2016). Methane seep carbonates yield clumped isotope signatures out of equilibrium with formation temperatures. Nat. Commun. 7, 12274. doi:10.1038/ncomms12274.

Luff, R., and Wallmann, K. (2003). Fluid flow, methane fluxes, carbonate precipitation and biogeochemical turnover in gas hydrate-bearing sediments at Hydrate Ridge, Cascadia Margin: numerical modeling and mass balances. Geochim. Cosmochim. Acta 67, 3403–3421. doi:10.1016/S0016-7037(03)00127-3.

Marlow, J. J., Steele, J. A., Ziebis, W., Thurber, A. R., Levin, L. A., and Orphan, V. J. (2014). Carbonate-hosted methanotrophy represents an unrecognized methane sink in the deep sea. Nat. Commun. 5, 5094. doi:10.1038/ncomms6094.

Mason, O. U., Case, D. H., Naehr, T. H., Lee, R. W., Thomas, R. B., Bailey, J. V., et al. (2015). Comparison of Archaeal and Bacterial Diversity in Methane Seep Carbonate Nodules and Host Sediments, Eel River Basin and Hydrate Ridge, USA. Microb. Ecol. 70, 766–784. doi:10.1007/s00248-015-0615-6.

McGlynn, S. E., Chadwick, G. L., Kempes, C. P., and Orphan, V. J. (2015). Single cell activity reveals direct electron transfer in methanotrophic consortia. Nature 526, 531–535. doi:10.1038/nature15512.

McGlynn, S. E., Chadwick, G. L., O'Neill, A., Mackey, M., Thor, A., Deerinck, T. J., et al. (2018). Subgroup Characteristics of Marine Methane-Oxidizing ANME-2 Archaea and Their Syntrophic Partners as Revealed by Integrated Multimodal Analytical Microscopy. Appl. Environ. Microbiol. 84, e00399-18. doi:10.1128/AEM.00399-18.

Mera, M. U., and Beveridge, T. J. (1993). Mechanism of silicate binding to the bacterial cell wall in *Bacillus subtilis*. J. Bacteriol. 175, 1936–1945.

Meulepas, R. J. W., Jagersma, C. G., Gieteling, J., Buisman, C. J. N., Stams, A. J. M., and Lens, P. N. L. (2009). Enrichment of anaerobic methanotrophs in sulfate-reducing membrane bioreactors. Biotechnol. Bioeng. 104, 458–470. doi:10.1002/bit.22412.

Michael, A. J. (2011). Molecular machines encoded by bacterially-derived multi-domain gene fusions that potentially synthesize, N-methylate and transfer long chain polyamines in diatoms. FEBS Lett. 585, 2627–2634. doi:10.1016/j.febslet.2011.07.038.

Michaelis, W., Seifert, R., Nauhaus, K., Treude, T., Thiel, V., Blumenberg, M., et al. (2002). Microbial Reefs in the Black Sea Fueled by Anaerobic Oxidation of Methane. Science 297, 1013–1015. doi:10.1126/science.1072502.

Michalopoulos, P., and Aller, R. C. (2004). Early diagenesis of biogenic silica in the Amazon delta: alteration, authigenic clay formation, and storage. Geochim. Cosmochim. Acta 68, 1061–1085. doi:10.1016/j.gca.2003.07.018.

Minguet, E. G., Vera-Sirera, F., Marina, A., Carbonell, J., and Blázquez, M. A. (2008). Evolutionary Diversification in Polyamine Biosynthesis. Mol. Biol. Evol. 25, 2119–2128. doi:10.1093/molbev/msn161.

Miyajima, Y., Watanabe, Y., Yanagisawa, Y., Amano, K., Hasegawa, T., and Shimobayashi, N. (2016). A late Miocene methane-seep deposit bearing methane-trapping silica minerals at Joetsu, central Japan. Palaeogeogr. Palaeoclimatol. Palaeoecol. 455, 1–15. doi:10.1016/j.palaeo.2016.05.002.

Moore, D. M., and Reynolds, R. C. (1997). X-Ray Diffraction and the Identification and Analysis of Clay Minerals. New York: Oxford University Press.

Motomura, K., Ikeda, T., Matsuyama, S., Abdelhamid, M. A. A., Tanaka, T., Ishida, T., et al. (2016). The C-Terminal Zwitterionic Sequence of CotB1 Is Essential for Biosilicification of the *Bacillus cereus* Spore Coat. J. Bacteriol. 198, 276–282. doi:10.1128/jb.00447-15.

Naehr, T. H., Eichhubl, P., Orphan, V. J., Hovland, M., Paull, C. K., Ussler, W., et al. (2007). Authigenic carbonate formation at hydrocarbon seeps in continental margin sediments: A comparative study. Deep Sea Res. Part II Top. Stud. Oceanogr. 54, 1268–1291. doi:10.1016/j.dsr2.2007.04.010.

Nauhaus, K., Albrecht, M., Elvert, M., Boetius, A., and Widdel, F. (2007). In vitro cell growth of marine archaeal-bacterial consortia during anaerobic oxidation of methane with sulfate. Environ. Microbiol. 9, 187–196. doi:10.1111/j.1462-2920.2006.01127.x.

Newman, S. A., Mariotti, G., Pruss, S., and Bosak, T. (2016). Insights into cyanobacterial fossilization in Ediacaran siliciclastic environments. Geology 44, 579–582. doi:10.1130/G37791.1.

Ohnuma, M., Ganbe, T., Terui, Y., Niitsu, M., Sato, T., Tanaka, N., et al. (2011). Crystal structures and enzymatic properties of a triamine/agmatine aminopropyltransferase from Thermus thermophilus. J Mol Biol 408, 971–86. doi:10.1016/j.jmb.2011.03.025.

O'Reilly, S. E., Watkins, J., and Furukawa, Y. (2005). Secondary mineral formation associated with respiration of nontronite, NAu-1 by iron reducing bacteria. Geochem. Trans. 6, 67–67. doi:10.1186/1467-4866-6-67.

Orphan, V. J., Hinrichs, K.-U., Ussler, W., Paull, C. K., Taylor, L. T., Sylva, S. P., et al. (2001a). Comparative Analysis of Methane-Oxidizing Archaea and Sulfate-Reducing Bacteria in Anoxic Marine Sediments. Appl. Environ. Microbiol. 67, 1922–1934. doi:10.1128/AEM.67.4.1922-1934.2001.

Orphan, V. J., House, C. H., Hinrichs, K.-U., McKeegan, K. D., and DeLong, E. F. (2001b). Methane-Consuming Archaea Revealed by Directly Coupled Isotopic and Phylogenetic Analysis. Science 293, 484–487. doi:10.1126/science.1061338.

Orphan, V. J., House, C. H., Hinrichs, K.-U., McKeegan, K. D., and DeLong, E. F. (2002). Multiple archaeal groups mediate methane oxidation in anoxic cold seep sediments. Proc. Natl. Acad. Sci. 99, 7663–7668. doi:10.1073/pnas.072210299.

Orphan, V. J., Turk, K. A., Green, A. M., and House, C. H. (2009). Patterns of 15N assimilation and growth of methanotrophic ANME-2 archaea and sulfate-reducing bacteria within structured syntrophic consortia revealed by FISH-SIMS. Environ. Microbiol. 11, 1777–1791. doi:10.1111/j.1462-2920.2009.01903.x.

Peckmann, J., Goedert, J. L., Thiel, V., Michaelis, W., and Reitner, J. (2002). A comprehensive approach to the study of methane-seep deposits from the Lincoln Creek Formation, western Washington State, USA. Sedimentology 49, 855–873. doi:10.1046/j.1365-3091.2002.00474.x.

Pernthaler, A., Dekas, A. E., Brown, C. T., Goffredi, S. K., Embaye, T., and Orphan, V. J. (2008). Diverse syntrophic partnerships from deep-sea methane vents revealed by direct cell capture and metagenomics. Proc. Natl. Acad. Sci. U. S. A. 105, 7052–7057. doi:10.1073/pnas.0711303105.

Pernthaler, J., Glöckner, F.-O., Schönhuber, W., and Amann, R. (2001). "Fluorescence in situ hybridization (FISH) with rRNA-targeted oligonucleotide probes," in Methods in Microbiology Marine Microbiology. (Academic Press), 207–226. doi:10.1016/S0580-9517(01)30046-6.

Phoenix, V. R., Konhauser, K. O., and Ferris, F. G. (2003). Experimental study of iron and silica immobilization by bacteria in mixed Fe-Si systems: implications for microbial silicification in hot springs. Can. J. Earth Sci. 40, 1669–1678. doi:10.1139/e03-044.

Phoenix, V. R., Martinez, R. E., Konhauser, K. O., and Ferris, F. G. (2002). Characterization and Implications of the Cell Surface Reactivity of Calothrix sp. Strain KC97. Appl. Environ. Microbiol. 68, 4827–4834. doi:10.1128/aem.68.10.4827-4834.2002.

Reeburgh, W. S. (2007). Oceanic Methane Biogeochemistry. Chem. Rev. 107, 486–513. doi:10.1021/cr050362v.

Richthammer, P., Börmel, M., Brunner, E., and van Pée, K.-H. (2011). Biomineralization in Diatoms: The Role of Silacidins. ChemBioChem 12, 1362–1366. doi:10.1002/cbic.201000775.

Scheffel, A., Poulsen, N., Shian, S., and Kröger, N. (2011). Nanopatterned protein microrings from a diatom that direct silica morphogenesis. Proc. Natl. Acad. Sci. 108, 3175–3180. doi:10.1073/pnas.1012842108.

Scheller, S., Yu, H., Chadwick, G. L., McGlynn, S. E., and Orphan, V. J. (2016). Artificial electron acceptors decouple archaeal methane oxidation from sulfate reduction. Science 351, 703–707. doi:10.1126/science.aad7154.

Schink, B. (1997). Energetics of syntrophic cooperation in methanogenic degradation. Microbiol. Mol. Biol. Rev. 61, 262–280.

Schreiber, L., Holler, T., Knittel, K., Meyerdierks, A., and Amann, R. (2010). Identification of the dominant sulfate-reducing bacterial partner of anaerobic methanotrophs of the ANME-2 clade. Environ. Microbiol. 12, 2327–2340. doi:10.1111/j.1462-2920.2010.02275.x.

Siever, R., and Woodford, N. (1973). Sorption of silica by clay minerals. Geochim. Cosmochim. Acta 37, 1851–1880. doi:10.1016/0016-7037(73)90146-4.

Sivan, O., Antler, G., Turchyn, A. V., Marlow, J. J., and Orphan, V. J. (2014). Iron oxides stimulate sulfate-driven anaerobic methane oxidation in seeps. Proc. Natl. Acad. Sci. 111, E4139–E4147. doi:10.1073/pnas.1412269111.

Skennerton, C. T., Chourey, K., Iyer, R., Hettich, R. L., Tyson, G. W., and Orphan, V. J. (2017). Methane-Fueled Syntrophy through Extracellular Electron Transfer: Uncovering the Genomic Traits Conserved within Diverse Bacterial Partners of Anaerobic Methanotrophic Archaea. mBio 8, e00530-17. doi:10.1128/mBio.00530-17.

Smrzka, D., Kraemer, S. M., Zwicker, J., Birgel, D., Fischer, D., Kasten, S., et al. (2015). Constraining silica diagenesis in methane-seep deposits. Palaeogeogr. Palaeoclimatol. Palaeoecol. 420, 13–26. doi:10.1016/j.palaeo.2014.12.007.

Stahl, D. A., and Amann, R. (1991). "Development and Application of Nucleic Acid Probes in Bacterial Systematics," in Nucleic Acid Techniques in Bacterial Systematics, eds. E. Stackebrandt and M. Goodfellow (Chichester, U.K.: John Wiley & Sons Ltd.), 205–248.

Teichert, B. M. A., Bohrmann, G., and Suess, E. (2005). Chemoherms on Hydrate Ridge — Unique microbially-mediated carbonate build-ups growing into the water column. Palaeogeogr. Palaeoclimatol. Palaeoecol. 227, 67–85. doi:10.1016/j.palaeo.2005.04.029.

Thiagarajan, N., Crémière, A., Blättler, C., Lepland, A., Kirsimäe, K., Higgins, J., et al. (2020). Stable and Clumped Isotope Characterization of Authigenic Carbonates in Methane Cold Seep Environments. Geochim. Cosmochim. Acta. doi:10.1016/j.gca.2020.03.015.

Tréguer, P. J., and De La Rocha, C. L. (2013). The World Ocean Silica Cycle. Annu. Rev. Mar. Sci. 5, 477–501. doi:10.1146/annurev-marine-121211-172346.

Treude, T., Krüger, M., Boetius, A., and Jørgensen, B. B. (2005). Environmental control on anaerobic oxidation of methane in the gassy sediments of Eckernförde Bay (German Baltic). Limnol. Oceanogr. 50, 1771–1786. doi:10.4319/lo.2005.50.6.1771.

Treude, T., Orphan, V., Knittel, K., Gieseke, A., House, C. H., and Boetius, A. (2007). Consumption of Methane and CO2 by Methanotrophic Microbial Mats from Gas Seeps of the Anoxic Black Sea. Appl. Environ. Microbiol. 73, 2271–2283. doi:10.1128/AEM.02685-06.

Urrutia, M. M., and Beveridge, T. J. (1994). Formation of fine-grained metal and silicate precipitates on a bacterial surface (*Bacillus subtilis*). Chem. Geol. 116, 261–280. doi:10.1016/0009-2541(94)90018-3.

Van Cappellen, P., and Qiu, L. (1997). Biogenic silica dissolution in sediments of the Southern Ocean. I. Solubility. Deep Sea Res. Part II Top. Stud. Oceanogr. 44, 1109–1128. doi:10.1016/S0967-0645(96)00113-0.

Visscher, P. T., Reid, R. P., and Bebout, B. M. (2000). Microscale observations of sulfate reduction: Correlation of microbial activity with lithified micritic laminae in modern marine stromatolites. Geology 28, 919–922. doi:10.1130/0091-7613(2000)28<919:MOOSRC>2.0.CO;2.

Wegener, G., Krukenberg, V., Riedel, D., Tegetmeyer, H. E., and Boetius, A. (2015). Intercellular wiring enables electron transfer between methanotrophic archaea and bacteria. Nature 526, 587–590. doi:10.1038/nature15733.

Wenzl, S., Hett, R., Richthammer, P., and Sumper, M. (2008). Silacidins: Highly Acidic Phosphopeptides from Diatom Shells Assist in Silica Precipitation In Vitro. Angew. Chem. Int. Ed. 47, 1729–1732. doi:10.1002/anie.200704994.

Yee, N., Phoenix, V. R., Konhauser, K. O., Benning, L. G., and Ferris, F. G. (2003). The effect of cyanobacteria on silica precipitation at neutral pH: implications for bacterial silicification in geothermal hot springs. Chem. Geol. 199, 83–90. doi:10.1016/S0009-2541(03)00120-7.

Yu, N. Y., Wagner, J. R., Laird, M. R., Melli, G., Rey, S., Lo, R., et al. (2010). PSORTb 3.0: improved protein subcellular localization prediction with refined localization subcategories and predictive capabilities for all prokaryotes. Bioinformatics 26, 1608–15. doi:10.1093/bioinformatics/btq249.

Zabel, M., Boetius, A., Emeis, K. C., Ferdelman, T. G., and Spieß, V. (2008). RV METEOR Cruise Report M76/L1, M76/L2, M76/L3a+b, PROSA process Studies in the Eastern South Atlantic. DFG Senatskommission für Ozeanographie.

Zhang, G., Dong, H., Kim, J., and Eberl, D. D. (2007). Microbial reduction of structural Fe3+ in nontronite by a thermophilic bacterium and its role in promoting the smectite to illite reaction. Am. Mineral. 92, 1411–1419. doi:10.2138/am.2007.2498.

Zhang, Y., Henriet, J.-P., Bursens, J., and Boon, N. (2010). Stimulation of in vitro anaerobic oxidation of methane rate in a continuous high-pressure bioreactor. Bioresour. Technol. 101, 3132–3138. doi:10.1016/j.biortech.2009.11.103.

Zhang, Y., Maignien, L., Zhao, X., Wang, F., and Boon, N. (2011). Enrichment of a microbial community performing anaerobic oxidation of methane in a continuous high-pressure bioreactor. BMC Microbiol. 11, 137. doi:10.1186/1471-2180-11-137.

SUPPLEMENTAL FIGURES

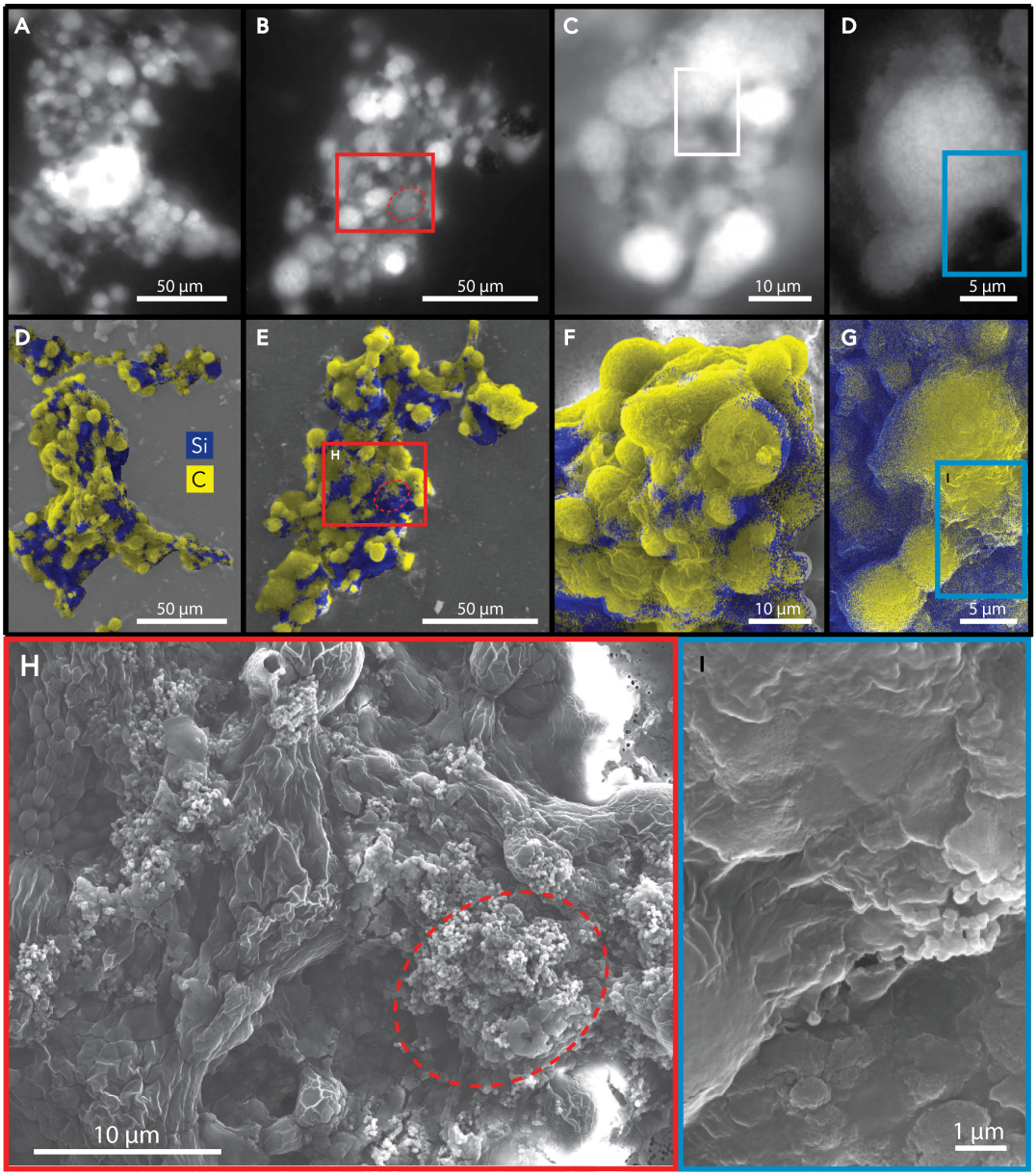

Supplemental Figure 1. Epifluorescence (DAPI-stained) (A-D), SEM-EDS (D-I) imagery documenting spatial distribution of silicates between consortia (consisting of ANME-2a/b and SEEP-SRB1, based on 16S rRNA amplicon sequencing, Fig. S6) grown under sediment-free conditions. SEM-EDS compositional maps demonstrate the common appearance of Si-rich domains between consortia. Detailed SEM imagery (H-I) corroborates other SEM and TEM imagery demonstrating the appearance of consortium-attached silicates as ~200 nm semispherical particles often intergrown and encrusting consortia.

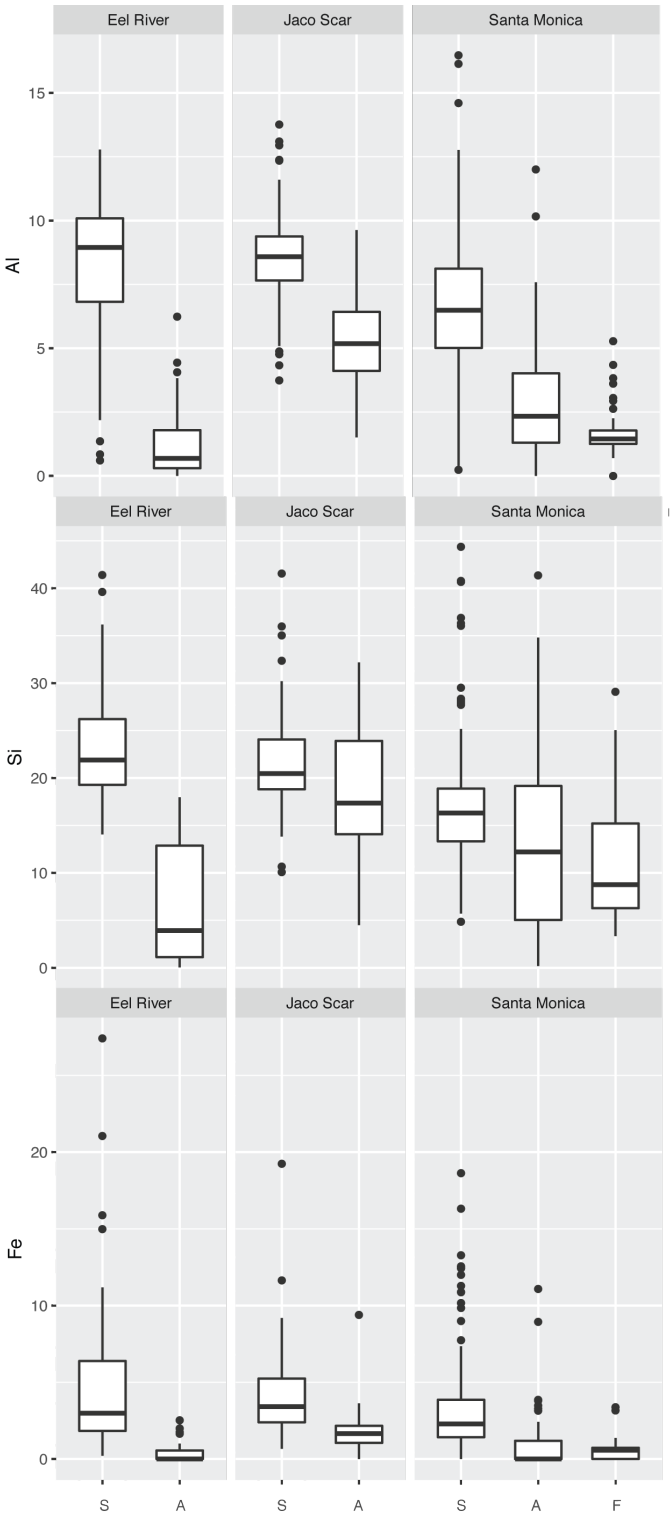

Supplemental Figure 2. EDS compositional data of silicates attached to consortia sourced directly from methane seep sediments (A) or grown under sediment-free conditions (F), demonstrating the Si-rich and Al- and Fe- poor nature of these phases.

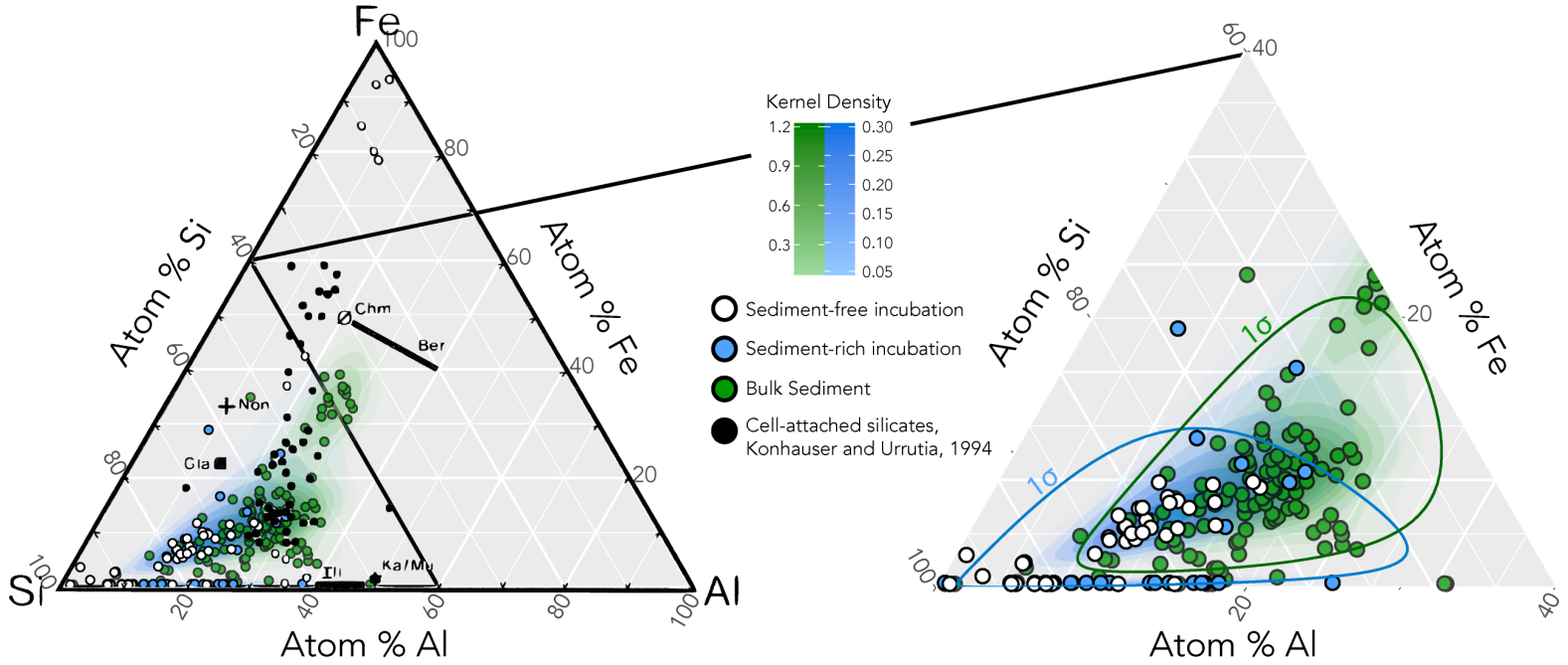

Supplemental Figure 3. EDS compositional data visualized on an Fe-Al-Si ternary plot of silicates attached to consortia sourced from Santa Monica Basin methane seep sediments or sediment-free incubations, demonstrating (left panel) significant compositional differences between these consortium-attached silicates, bulk methane seep sediment, and previously-observed silicates attached to bacterial cell walls (Konhauser and Urrutia, 1999). ANME-SRB consortium-attached silicates are significantly more Si-rich and Fe- and Al- poor than those previously observed attached to bacterial cell exteriors.

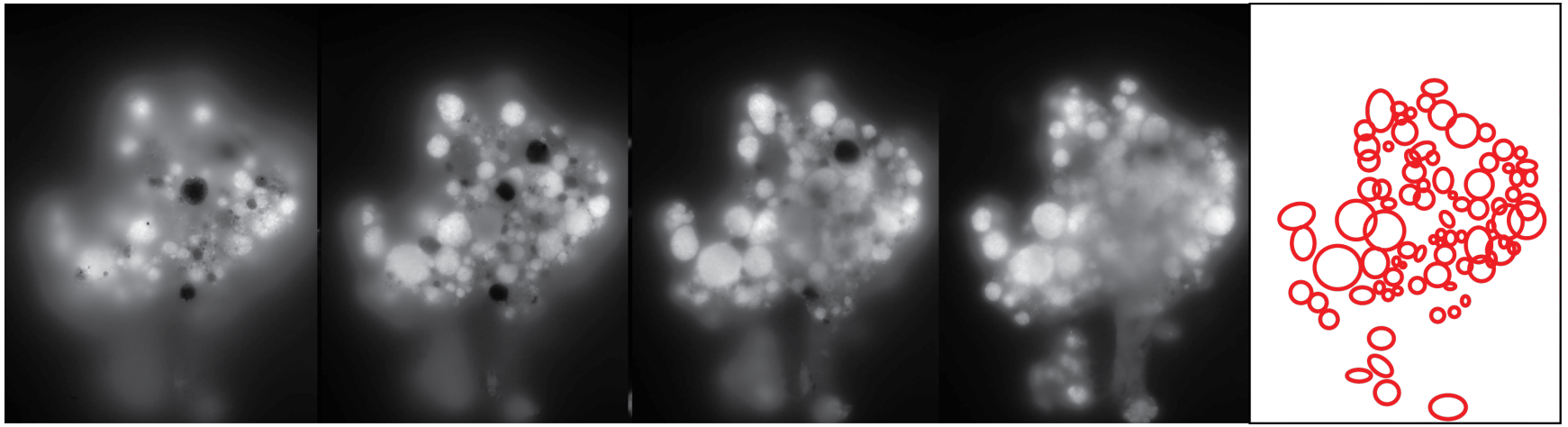

Supplemental Figure 4. Epifluorescence (using DAPI) imagery of a large consortium cluster grown under sediment-free conditions, demonstrating the method by which consortia were counted to use as an input to the growth model (Fig. 6). Consortia were counted by inspection of images taken on different focal planes of the epifluorescence microscope.

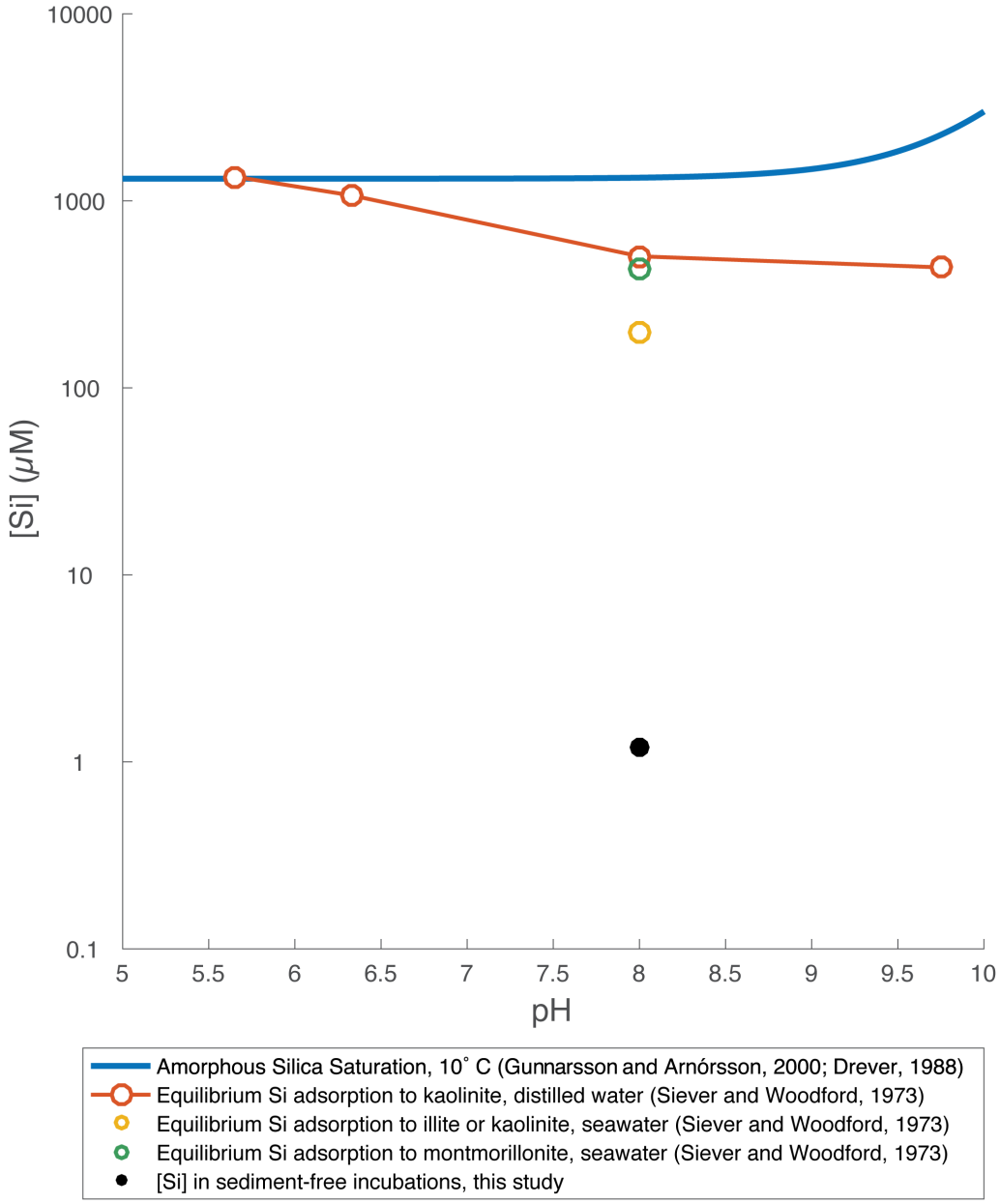

Supplemental Figure 5. Comparison between [Si] measured in media of sediment-free incubations of ANME-SRB consortia examined in this study and theoretical amorphous silica saturation (Drever, 1988; Gunnarsson and Arnórsson, 2000) and equilibrium Si adsorption to aluminosilicate clays (Siever and Woodford, 1973), precluding either abiotic mechanism of Si enrichment of consortium-attached silicates from relevance in the sediment-free incubations examined here.

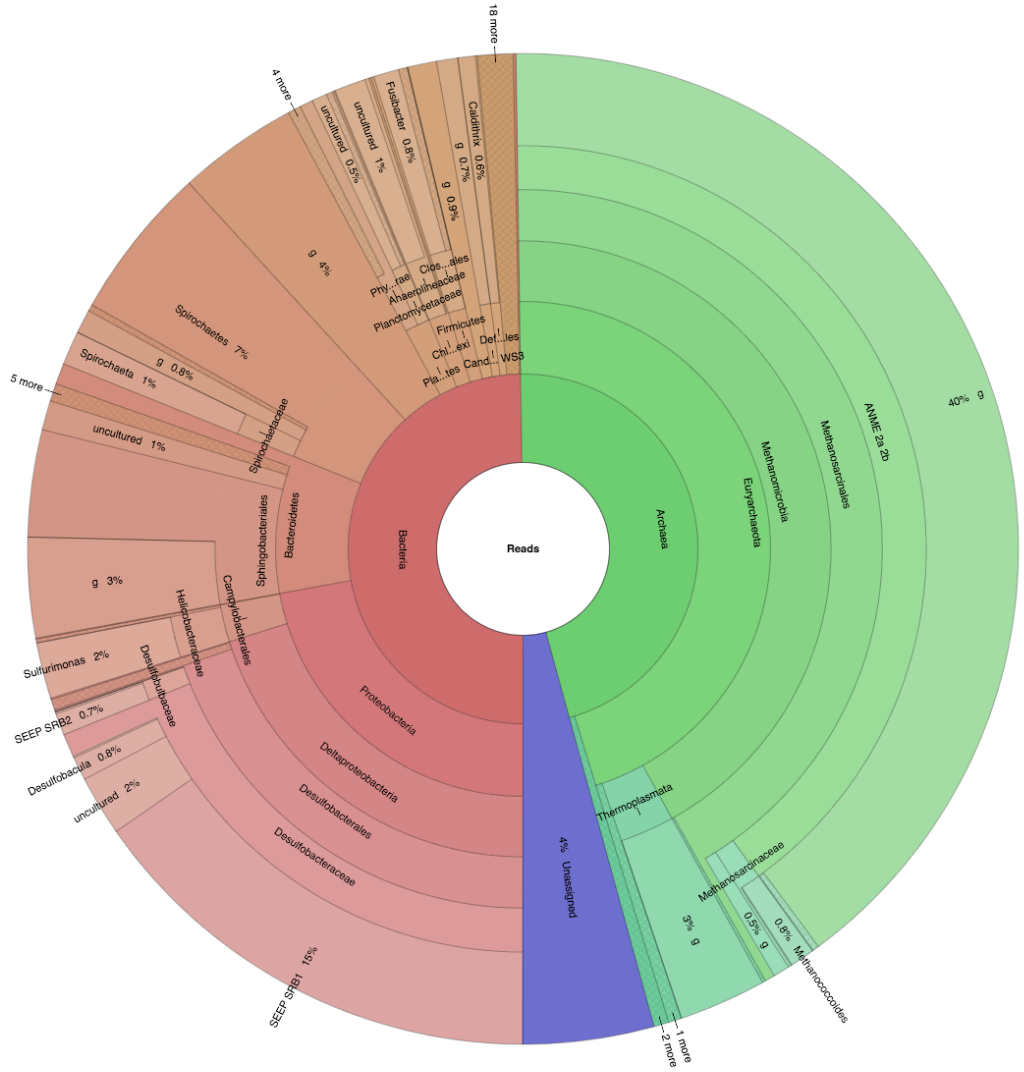

Supplemental Figure 6. Krona chart (Ondov et al., 2011) depicting taxonomic composition of sediment-free incubations based on reads of V4 16S rRNA gene sequences ('iTags'). ANME-2a/b and SEEP SRB1 reads are particularly abundant in this dataset, implying these to be the partner taxa of cell consortia visualized through methods without additional taxonomic resolution (i.e. DAPI stains; Supp. Figs 1,4).

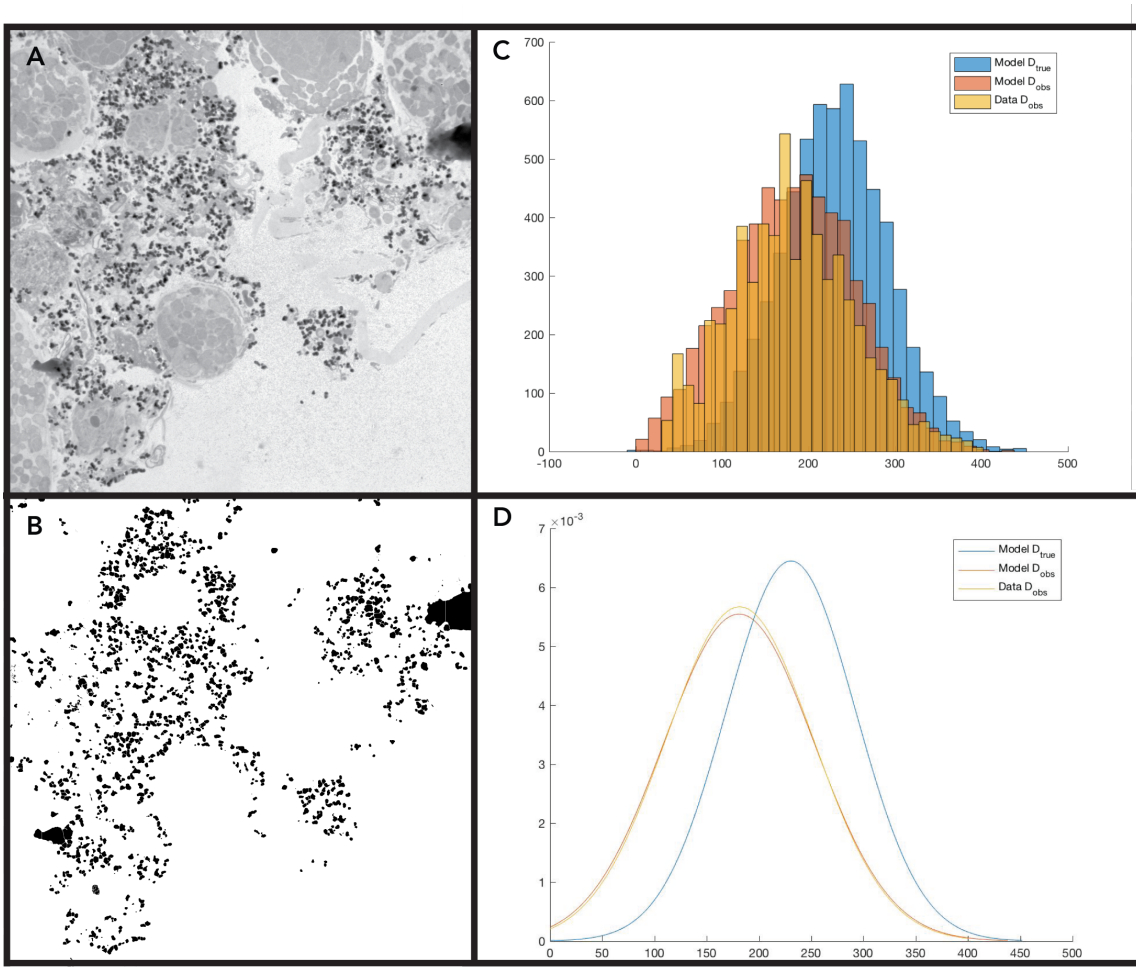

Supplemental Figure 7. TEM imaging of consortium-attached silicates (A) processed in imageJ by thresholding and watershed analysis to obtain raw data (B) for a Markov Chain Monte Carlo (MCMC)-based approach to measure true particle size of subspherical consortium attached silicates. Diameters measured directly from raw TEM data underestimate true particle size, as random cross-sections through spheres with any size distribution are more likely to intersect spheres above or below sphere equators. MCMC estimation of sphere diameter (C-D) is calculated to be (230±62 nm), precluding this phase to be a contaminant such as Percoll (particle size 15-30 nm).

Chapter 4

DIAGENETIC STABILIZATION OF MANGANESE-RICH SEDIMENTARY ROCKS

Kyle S. Metcalfe[1], Jena E. Johnson[2], Samuel M. Webb[3], Woodward W. Fischer[1]

[1] Division of Geological and Planetary Sciences,
California Institute of Technology, Pasadena, California, 91125

[2] Department of Earth and Environmental Sciences,
University of Michigan, Ann Arbor, MI 48109

[3] Stanford Synchrotron Radiation Lightsource,
Stanford University, Menlo Park, CA 94025

ABSTRACT

Precambrian manganese-rich sedimentary rocks comprise prominent portions of the rock record spanning periods of dramatic environmental change, but the imprint of early diagenesis on these deposits partially obscures the processes that produced the primary Mn-rich sediments. We constructed a numerical model simulating early diagenesis of mixed Fe-Mn sediments to ascertain the environmental and geobiological parameters that are important for the diagenetic stabilization of Mn-rich sedimentary rocks. We constrained our model with a case study presented by the vast, classic Mn deposits of Kalahari Manganese Field hosted by the Paleoproterozoic-age Hotazel Formation in the Transvaal Supergroup, South Africa, the largest known Mn deposits in the geological record. We benchmarked model results using synchrotron X-ray fluorescence spectroscopy imaging of the composition and Mn redox states of a sample of iron- and manganese-rich strata of the Hotazel Formation. We found that our model could produce a mineral assemblage

comparable to that of the Hotazel Formation, defined by Mn^{3+} : Mn^{2+} and Fe : Mn ratios. These results demonstrated that the Mn(III)-rich mineralogy of the Hotazel Formation required a significant flux reducing potential, provided by organic carbon, to produce concentrations of $Mn^{2+}_{(aq)}$ sufficient to overcome the thermodynamic threshold for reaction with solid-phase $Mn^{4+}O_2$ and resulting $Mn^{3+}OOH$ precipitation. When the rate constant for metal reduction in our model was reduced by 5-6 orders of magnitude, representing the delivery rate of abiotic reductants, Mn(III) phases were not observed, indicating that for this system, biological catalysis was necessary to produce the abundant Mn(III) phases observed in the Hotazel Formation. These modeling results led us to speculate that the Mn- and Fe-rich strata in the Hotazel Formation reflect deposition of a significant amount of organic carbon contemporaneously with metal oxides in a basin where deposited MnO_2 : $Fe^{3+}OOH$ ratios were determined by changes in the transportation of water masses through a basin in direct communication with high-potential oxidants like those provided by photosystem II or atmospheric O_2.

INTRODUCTION

The history recorded by Precambrian Mn-rich sedimentary rocks is challenging to decipher due to a lack of analogous modern sediments. Although some modern sedimentary environments have produced Mn nodules dispersed on the seafloor (Margolis and Burns, 1976; Post, 1999; Glasby, 2006), modern basins lack thick deposits of Mn-rich sediments such as those produced by some basins of Paleoproterozoic age that contain as much as ~2.7 x 10^{15} g Mn (Gutzmer and Beukes, 1996; Cairncross and Beukes, 2013). Explaining the petrogenesis of Mn-rich sedimentary rocks requires mechanisms that concentrated Mn sufficiently in a water body to produce large volumes of Mn-rich sediments. Mn is present in the crust is typically divalent, producing soluble Mn^{2+} upon dissolution of the original igneous or metamorphic mineral hosts of these metals (Calvert and Pedersen, 1996; Post, 1999). Mn^{2+} is highly soluble, and if not oxidized will be slowly sequestered in carbonate phases at concentrations proportional to its dissolved concentration (Holland, 1984; Mucci, 2004; Johnson et al., 2013; Fischer et al., 2016). Mn concentrations in carbonates indicate seawater Mn concentrations have remained between seven to two orders of magnitude lower than $Ca^{2+}_{(aq)}$ concentrations throughout Earth history (Fischer et al., 2016), demonstrating that a mechanism to concentrate Mn is necessary to produce the Mn-rich carbonates common in Mn-rich sedimentary rocks (Holland, 1984; Veizer et al., 1989; Johnson et al., 2016b; Lingappa et al., 2019).

Prior studies have focused on oxidation and sedimentation of insoluble oxide particles as the primary mechanism of Mn concentration for Mn-rich sediments. In modern environments, Mn is concentrated by oxidation of dissolved Mn^{2+} to insoluble Mn(III) or

Mn(IV) phases, which settle from suspension as particles or accumulate as nodules at the sediment-water interface (Margolis and Burns, 1976; Post, 1999; Glasby, 2006). As oxidation of $Mn^{2+}_{(aq)}$ is crucial for the precipitation and sedimentation of Mn-rich minerals in modern environments, it has been inferred as the process by which Precambrian Mn-rich sediments were emplaced (Johnson et al., 2013, 2016b). Importantly for paleobiological interpretations of Mn-rich sediments, the high redox potential of Mn necessitates either the presence of significant concentrations of O_2 or specialized biochemistry (Johnson et al., 2013) to oxidize $Mn^{2+}_{(aq)}$ and produce Mn-rich sedimentary rocks. The temporal distribution of Mn-rich sedimentary rocks, reaching a maximum in the Paleoproterozoic, has been explained by invoking the evolution of a Mn-oxidizing photosystem (Johnson et al., 2013) as well as oxidation of Mn- and Fe-rich seawater by free O_2 to form large deposits (Beukes, 1983, 1987; Kirschvink et al., 2000; Tsikos et al., 2003; Kopp et al., 2005; Hoffman, 2013).

Although the precursor Mn phases to those observed in Precambrian Mn-rich sedimentary rocks were oxides, these phases are often found in these rocks as Mn(II)- and/or Mn(III)-bearing minerals (Johnson et al., 2016b), implying that primary Mn oxides were subjected to syn- or post-depositional reduction. Examples of these deposits can be found throughout the Precambrian rock record (Johnson et al., 2016b), including the Hotazel Formation of northern South Africa, a massive Late Archaean-Early Paleoproterozoic deposit containing abundant braunite [$Mn^{2+}Mn^{3+}_6SiO_{12}$] and kutnohorite [$CaMn^{2+}(CO_3)_2$] (Schneiderhan et al., 2006; Johnson et al., 2016b), as well as the Neoproterozoic Santa Cruz Formation of southern Brazil, composed of braunite and

rhodochrosite [$Mn^{2+}CO_3$] in well-preserved sections (Johnson et al., 2016b). The process responsible for the stabilization of Mn(III)-bearing minerals such as braunite in Precambrian Mn-rich sedimentary rocks represents a particularly interesting gap in our current understanding of the petrogenesis of these rocks. Braunite has been hypothesized to form during late diagenesis from reaction of a Mn(III) oxyhydroxide/oxide precursors such as bixbyite [α-$Mn^{3+}{}_2O_3$] with silica (Robie et al., 1995; Johnson et al., 2016b), but the conditions leading to the initial stabilization of the Mn(III) oxyhydroxide or Mn(III) oxide precursor are poorly understood.

To investigate the history recorded by Mn(III)-bearing minerals in Precambrian Mn-rich sedimentary rocks, we must first identify whether their Mn(III) precursor phases were the product of early diagenesis or later alteration. Study of the texture and redox states of Mn and Fe minerals in Mn-rich deposits has indicated that these precursor phases to these minerals were the products of early diagenetic processing: facies often contain well-preserved early diagenetic textures, including fine-grained crystals of Mn carbonates and braunite that delineate bedding (Johnson et al., 2016b). Other early diagenetic textures include abundant mm-scale Mn-bearing carbonate nodules that reflect early preferential cementation, where CO_3^{2-} and $Mn^{2+}{}_{(aq)}$ and $Ca^{2+}{}_{(aq)}$ were of sufficient concentrations to precipitate Mn-rich carbonate minerals (Mucci, 2004; Johnson et al., 2016b). Some Mn-rich sedimentary deposits contain crystals of Mn carbonates with Ca- and Mn-rich zones that vary in composition from kutnohorite [$CaMn^{2+}(CO_3)_2$] to Ca-rich rhodochrosite [$Mn^{2+}CO_3$], indicating dynamic geochemical conditions during syn- and/or post-depositional precipitation of these phases from a fluid of time-varying composition

(Schneiderhan et al., 2006; Johnson et al., 2016b). Mn carbonates are found intergrown with Mn(III) minerals including braunite in textures that imply formation of the precursor Mn(III) phase contemporaneous to Mn carbonate precipitation (Nel et al., 1986; Schneiderhan et al., 2006; Johnson et al., 2016b). $\delta^{13}C$ measurements of Mn carbonates document light values (–8.3 to –12.5‰), reflecting the imprint of early diagenesis driven by organic carbon oxidation on these phases (Okita et al., 1988; Tsikos et al., 2003; Maynard, 2010). Organic carbon oxidation coupled to metal reduction by microorganisms has been inferred as a reductive process primarily responsible for the production of $Mn^{2+}_{(aq)}$ available for precipitation as carbonate minerals (Schneiderhan et al., 2006; Johnson et al., 2016b). $Fe^{2+}_{(aq)}$ has also been implicated as a major electron donor for abiotic reduction of sedimentary Mn oxides (Postma, 1985; Van Cappellen and Wang, 1996; Postma and Appelo, 2000), and was likely important for the early diagenesis of Mn-rich sediments given the abundance of hematite [$Fe^{3+}_2O_3$] intergrown with Mn carbonate phases observed in the Hotazel Formation (Schneiderhan et al., 2006). The pervasive imprint of early diagenetic processes on Mn-rich sedimentary rocks thus enables interpretation of the mineral assemblages observed in these formations as reflective of the biogeochemical environment at or near to the time of deposition.

With the relative timing of the precipitation of Mn(III) oxyhydroxides/oxides in Mn-rich sediments constrained to early diagenesis, the processes potentially responsible for the stabilization of these phases can then be identified. Dissolved and solid-phase Mn^{3+} species can be generated as a transient intermediate during microbial reduction of Mn oxides (Kostka et al., 1995; Lin et al., 2012; Madison et al., 2013) or microbial oxidation of

Mn(II) (Webb et al., 2005), and in larger quantities by reaction of $Mn^{2+}_{(aq)}$ with Mn(IV) oxides, a comproportionation reaction thermodynamically favorable at pH > 7 (Elzinga, 2011; Takashima et al., 2012; Lefkowitz et al., 2013; Johnson et al., 2016a):

$$4H^{+} + Mn^{2+}_{(aq)} + MnO_2 \Rightarrow 2Mn^{3+} + 2H_2O \quad (1)$$

Mn^{3+} produced by either pathway may be stabilized by ligand complexes (Duckworth and Sposito, 2005; Madison et al., 2013; Oldham et al., 2015) or by the precipitation of Mn(III) oxyhydroxides/oxides (Elzinga, 2011), the latter being ultimately a necessary requirement to generate Mn(III) minerals. Experimental precipitation of Mn(III) oxyhydroxides/oxides carried out under conditions relevant to the early diagenesis of Mn-rich sediments typically produces a metastable feitknechtite [β-MnOOH], which quickly stabilizes as manganite [γ-MnOOH] (Hem and Lind, 1983; Elzinga, 2011; Lefkowitz et al., 2013; Elzinga and Kustka, 2015) or hausmannite [Mn_3O_4] (Lefkowitz et al., 2013), depending on solution pH and composition. The synthesis route for braunite from Mn(III) precursor phases such as manganite or hausmannite remains uncertain, however. While manganite can be readily dehydrated to γ-Mn_2O_3 by heating to 200-250 ˚C under anoxic conditions (Hernan et al., 1986), the synthesis of bixbyite [α-Mn_2O_3] from manganite is unclear but may require the presence of Fe^{3+} during manganite dehydration, as Fe^{3+} is known to stabilize the bixbyite crystal structure (Waychunas, 1991).

In addition to the comproportionation reaction between Mn^{2+} and Mn(IV) oxides, we can identify three important processes involved in syn- and post-depositional

modification of Mn-rich sediments that determine the stability of Mn(III) oxyhydroxide/oxide precipitates, including 1) reduction of metal oxides by oxidation of co-sedimentary organic carbon, 2) precipitation of carbonates as cements and nodules, and 3) reduction of Mn oxides by dissolved Fe^{2+}:

1. The microbial oxidation of organic carbon provides electrons to reduce primary Mn- and Fe-oxides and consumes H^+, according to equations 2 through 4 below, using formaldehyde to substitute for a complex set of organic carbon compounds that could serve as electron donors for metal reduction:

$$2MnO_{2\,(s)} + CH_2O + 4H^+ \Rightarrow 2Mn^{2+}_{(aq)} + CO_2 + 3H_2O \quad (2)$$

$$4MnOOH_{(s)} + CH_2O + 8H^+ \Rightarrow 4Mn^{2+}_{(aq)} + CO_2 + 7H_2O \quad (3)$$

$$4FeOOH_{(s)} + CH_2O + 8H^+ \Rightarrow 4Fe^{2+}_{(aq)} + CO_2 + 7H_2O \quad (4)$$

Microbial communities present in sediments are known to play a fundamental role in governing the rate, degree, and character of organic carbon oxidation; thus, to understand the stabilization of Mn(III) oxyhydroxide/oxide precipitates, the process and products of microbial metal reduction must be addressed (Froelich et al., 1979; Van Cappellen and Wang, 1996). Eq. 2 assumes MnO_2 reduction via a pathway that simultaneously transfers two e^- to MnO_2 from organic carbon, which has been documented by the model metal-reducing microorganism *Shewanella oneidensis* MR-1 (Kotloski and Gralnick, 2013; Johnson et al., 2016a). One-electron pathways of Mn(IV) oxide reduction have also been observed that produce small concentrations of Mn^{3+} intermediates relative to Mn^{2+} (Kostka et al., 1995; Lin et al., 2012), but the dominant products of microbial Mn- and Fe-

oxide reduction are dissolved Mn^{2+} and Fe^{2+} (Froelich et al., 1979; Myers and Nealson, 1988; Lovley, 1991; Van Cappellen and Wang, 1996). $Mn^{2+}_{(aq)}$ produced from microbial respiration of Mn oxides can then react with Mn(IV) oxides to produce Mn(III) oxyhydroxide/oxide phases (Eq. 1), facilitated by the pH increase driven by Mn oxide reduction.

2. As shown in Eqs. 2-4, microbial metal reduction consumes H^+ and produces inorganic carbon. This in turn increases alkalinity and pH, and catalyzes the precipitation of carbonate cements and nodules (Raiswell and Fisher, 2000):

$$CO_3^{2-}{}_{(aq)} + M^{2+}_{(aq)} \Rightarrow MCO_{3\,(s)} \qquad (5)$$

where M^{2+} can be Ca^{2+}, Mg^{2+}, Mn^{2+}, or Fe^{2+}, depending on solution composition. In Mn-rich sedimentary rocks, observed carbonates include kutnohorite, Mn-rich calcites, ankerite [$Ca(Fe^{2+},Mn^{2+},Mg)(CO_3)_2$] and rarely siderite [$Fe^{2+}CO_3$] (Nel et al., 1986; Maynard, 2010; Johnson et al., 2016b). Precipitation of Mn carbonates consumes $Mn^{2+}_{(aq)}$ otherwise available for reaction with Mn(IV) oxides, and thus is in direct competition for $Mn^{2+}_{(aq)}$ with the Mn^{2+} – Mn^{4+} comproportionation reaction (Eq. 1). However, the kinetics of these processes are significantly different, as Mn carbonate precipitation occurs significantly more slowly than Mn^{2+} – Mn^{4+} comproportionation (Johnson et al., 2016a), but requires significantly lower $Mn^{2+}_{(aq)}$ concentrations to be thermodynamically favorable (Jensen et al., 2002; Lefkowitz et al., 2013).

3. Reactions between Mn and Fe constitute a third process important in early diagenetic processing of Mn-rich sediments (Postma, 1985; Van Cappellen and

Wang, 1996; Postma and Appelo, 2000). $Fe^{2+}_{(aq)}$ can reduce Mn(IV) phases forming a range surface-bound Fe oxide phases depending on solution composition (Schaefer et al., 2017):

$$2H_2O + 2Fe^{2+}_{(aq)} + MnO_2 \Rightarrow 2FeOOH_{(s)} + 2H^+ + Mn^{2+}_{(aq)} \quad (6)$$

This reaction is known to be rapid (Siebecker et al., 2015; Johnson et al., 2016a) but self-limiting, due to the accumulation of Fe oxides that occlude reactive sites on the Mn oxide surface, preventing further reaction with $Fe^{2+}_{(aq)}$ (Villinski et al., 2001, 2003). This process is particularly interesting in the context of the early diagenesis of Mn-rich sediments, as it couples anaerobic Fe oxidation to production of $Mn^{2+}_{(aq)}$ and protons. While the production of $Mn^{2+}_{(aq)}$ from anaerobic Fe oxidation will increase the favorability of Mn(III) oxyhydroxide/oxide precipitation, concomitant acid production will decrease the favorability of this reaction.

Understanding the impact of these intertwined processes on the stability of Mn(III) oxyhydroxides/oxides requires an evaluation of the kinetics of these chemical reaction, which often compete for reactants or couple redox cycling to alkalinity changes in complex and sometimes self-limiting ways. To account for these interactions and to interpret the geochemical conditions responsible for the stabilization of Mn(III) precursor phases in the rock record, we constructed a numerical model simulating the products of early diagenesis for a range of initial compositions of the primary sediments, varying proportions of organic carbon, Mn oxides, and Fe oxides. We then compared the model

outputs to a case study of the Hotazel Formation to constrain the initial sediment composition that stabilized Mn(III) phases in primary sediments of this Mn-rich deposit.

GEOLOGICAL BACKGROUND OF HOTAZEL CASE STUDY

Stratigraphically, the Hotazel Formation is a part of the Late Archaean-Early Paleoproterozoic Transvaal Supergroup (Fig. 1a), a thick package of predominantly well-preserved (Gutzmer and Beukes, 1996; Tsikos et al., 2003, 2010) sedimentary and minor volcanic rocks providing one of few windows into biogeochemistry across a unique interval of Earth history (Beukes, 1987; Condie, 1993; Knoll and Beukes, 2009; Hoffman, 2013; Johnson et al., 2013). Within the Transvaal Supergroup, the Hotazel is a part of the Postmasburg Group, a conformable sequence of glacial, volcanic, and Mn-rich deposits outcropping in western outcrops of the Transvaal Supergroup known as the Griqualand West Basin. The Hotazel Formation is conformably underlain by the volcanic Ongeluk Formation (Schneiderhan et al., 2006), which is in turn conformably underlain by the glaciogenic Makganyene Formation (Evans et al., 1997). In some interpretations, the Makganyene Formation has been correlated to a disconformity within the Duitschland and Rooihoogte formations in eastern outcrops of the Transvaal Supergroup known as the Eastern Transvaal Basin (Guo et al., 2009; Hoffman, 2013; Luo et al., 2016). In other interpretations, the Ongeluk Formation and therefore the underlying Makganyene Formation are significantly older and roughly contemporaneous with carbonates of the Chuniespoort Group in the Eastern Transvaal Basin (Gumsley et al., 2017). In all models, the Hotazel Formation postdates evidence for the first accumulation of atmospheric O_2 in

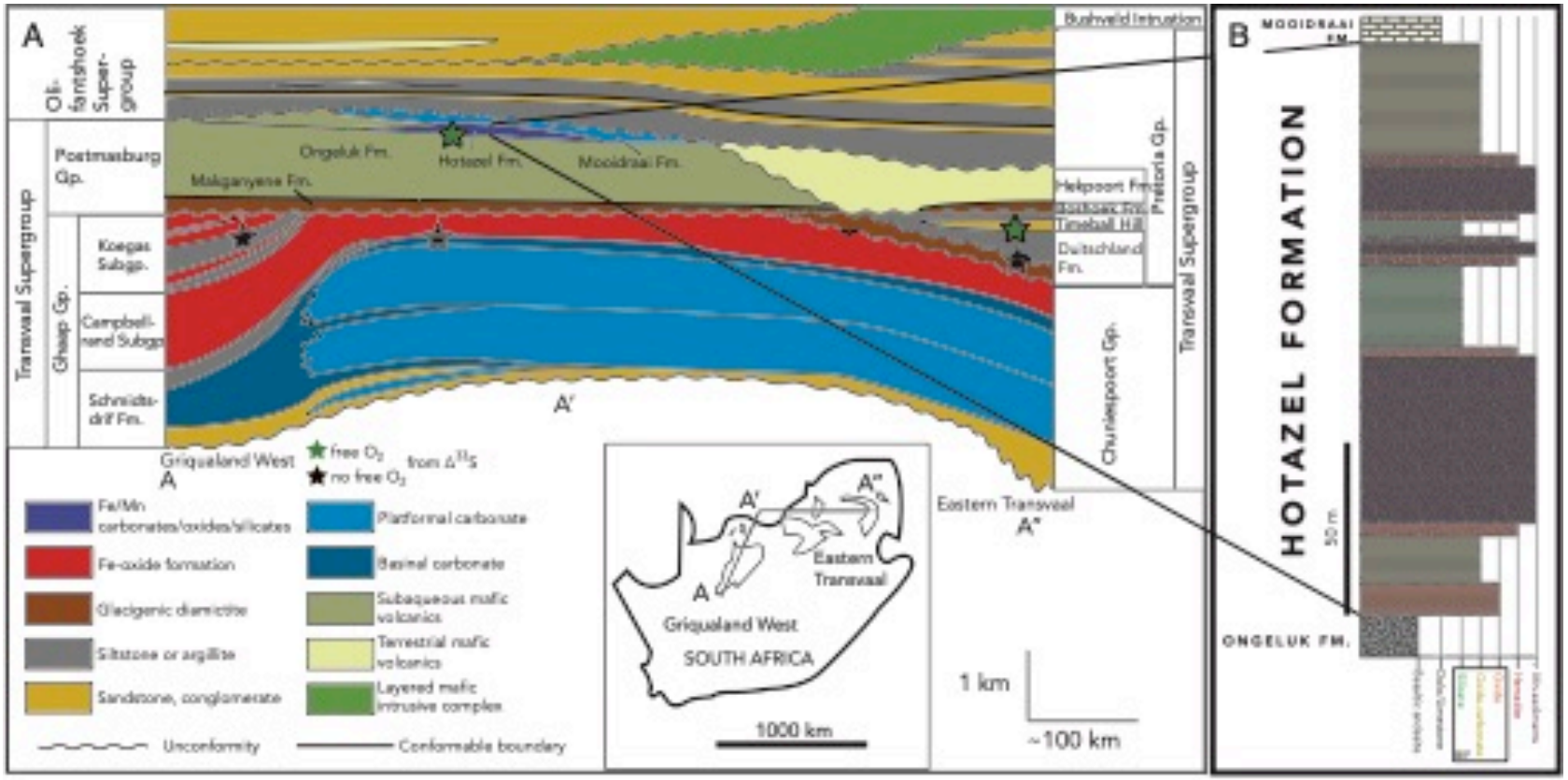

Figure 1.—Summary of the geological context of the Hotazel Formation. **A**) Composite stratigraphy of the Transvaal Supergroup, (after (Beukes, 1983), modified by correlations of (Hoffman, 2013; Luo, Ono, Beukes, Wang, Xie and Summons, 2016)). **B**) Stratigraphy of the Hotazel Formation from a drill core (after (Schneiderhan, Gutzmer, Strauss, Mezger and Beukes, 2006)).

samples of the Transvaal Supergroup from the Eastern Transvaal Basin (Farquhar et al. 2000; Bekker et al., 2001; Guo et al., 2009; Hoffman, 2013; Luo et al., 2016; Gumsley et al., 2017), and thus records an interval of profound change in the Earth system.

Given that the Hotazel Formation was deposited during one of the most dynamic periods of Earth history, several researchers have sought to examine the petrogenesis of these unique Mn-rich sedimentary rocks. That the Hotazel Formation conformably overlies the glaciogenic Makganyene Formation has led to the interpretation that the Hotazel was deposited from oxidation of a water column rich in $Mn^{2+}_{(aq)}$ and $Fe^{2+}_{(aq)}$ that was isolated from atmospheric O_2 by a global glaciation (Beukes, 1983; Kirschvink et al., 2000; Kopp et al., 2005; Schneiderhan et al., 2006). Cornell and Schutte alternatively suggested an alternative model in which the Hotazel Formation was a volcanogenic exhalative deposit related to Ongeluk volcanism (Cornell and Schütte, 1995). However, the presence of multiple paleomagnetic poles recorded by hematite in the Hotazel Formation has contradicted this hypothesis, supporting instead an origin from sedimentation of primary metal oxides precipitated from seawater (Evans et al., 2001). In this study, we use the petrogenetic framework for the deposition of the Hotazel wherein primary Fe and Mn oxides sediments were generated from oxidation of seawater $Mn^{2+}_{(aq)}$ and $Fe^{2+}_{(aq)}$ (Schneiderhan et al., 2006; Johnson et al., 2016b), and further consider the early diagenesis and kinetic constraints on the deposition of the Hotazel Formation.

The Hotazel Formation itself comprises a ~100 m thick package of Fe- and Mn-rich facies that record in their mineral assemblages a complex history. Outcrops of the Hotazel Formation in the Griqualand West Basin feature several Mn- and Fe-rich facies (Fig. 1b)

characterized in some outcrops by low-grade, minimally-metamorphosed 'Mamatwan-type' deposits (Gutzmer and Beukes, 1996) that are the focus of this study. Fe-rich lithologies, as classified by James, 1954 and arranged in order of increasing oxidation state of Fe minerals, include silicate-, oxide-carbonate, and oxide-facies iron formation as well as thin, microcystalline beds rich in hematite (Fig. 1b, Tsikos and Moore, 1997; Schneiderhan et al., 2006). Fe-rich lithologies are symmetrically stacked around three Mn-rich sedimentary units: hematite beds sit directly above and below Mn-rich units consisting of braunite, kutnohorite, and hematite, and above and below these hematite beds lie silicate-faces IF containing greenalite [$Fe_6^{2+}Si_4O_{10}(OH)_8$] (Schneiderhan et al., 2006). Previous work has interpreted this symmetric stacking pattern of facies to reflect differences in seawater redox potential, with Mn-rich facies representing precipitation from a stratified water column with higher redox potential than that responsible for the emplacement of Fe-rich facies (Schneiderhan et al., 2006).

As the world's largest deposits of Mn-rich sedimentary rock, hosting approximately 13500 Mt of Mn ore containing >20% Mn (Beukes, 1983; Gutzmer and Beukes, 1996), the Mn-rich facies of the Hotazel Formation are unique within the formation for the wealth of their Mn minerals. Petrographic analysis of the Mn-rich units documented a matrix of microcrystalline braunite and hematite intergrown with kutnohorite hosting abundant ~1 mm carbonate nodules (Tsikos and Moore, 1997; Schneiderhan et al., 2006; Johnson et al., 2016b). Kutnohorite crystals in the matrix are compositionally-zoned and are cross-cut by euhedral braunite (Schneiderhan et al., 2006; Johnson et al., 2016b). Carbonate nodules, consisting mostly of microsparitic kutnohorite, cross-cut the kutnohorite-braunite matrix

and rarely contain small inclusions of Mn(IV) oxides interpreted to represent unreacted residues of the primary Mn oxides (Johnson et al., 2016b). While the textures and light $\delta^{13}C$ values preserved in these deposits reflect extensive early diagenetic processing, no organic carbon remains in the Hotazel Formation today, indicating full remineralization of co-deposited organic carbon. The presence of abundant Fe in Mn-rich (28-52 wt. % Mn) units of the Hotazel, constituting 5-24 wt. % Fe of these deposits (Schneiderhan et al., 2006), further suggests the importance of anaerobic Fe cycling in the petrogenesis of these deposits. These petrographic observations imply that the stabilization of Mn(III) phases in the Mn-rich sediments of the Hotazel Formation occurred contemporaneously to complex cycling of Mn and Fe during early diagenesis. Reactions central to Mn and Fe cycling in this deposit, such as anaerobic Fe oxidation by Mn oxides and $Mn^{2+} – Mn^{4+}$ comproportionation, can compete for reactants, requiring consideration of reaction kinetics to predict the initial conditions of organic carbon, Fe oxides and Mn oxides that stabilize Mn(III) precipitates. To address this, we constructed a numerical model describing the kinetics of the involved reactions, calibrated by experimental measurements of the rate constants of these reactions. We then compared our model results to petrographic study of Mn-rich sediments of the Hotazel Formation to evaluate the precise fluxes of organic carbon and Mn-Fe-oxides necessary to stabilize the observed mineral assemblage, providing deeper insight into these ancient and enigmatic rocks.

METHODS

Petrography

A fresh hand sample of Mamatwan-type deposits of the stratigraphically-lowest Mn-rich sedimentary unit of the Hotazel Formation was collected from an open-pit mine in the Kalahari Mn field selected due to its recent exposure and thus lack of oxidative weathering (Johnson et al., 2013, 2016b). A circular ~15 μm ultra-flat thin section was prepared by High Mesa Petrographics and examined using transmitted visible light microscopy as well as spectroscopic X-ray mapping to characterize the mineralogy and petrographic textures of the sample. Prior to this study, this sample had been examined for Mn mineralogy and geochemistry (Johnson et al., 2016b). Transmitted visible light microscopy was performed using a Leica polarizing microscope. For chemical imaging of the Hotazel Formation, we used synchrotron-based X-ray mapping spectroscopic mapping at beamline 10-2 of the Stanford Synchrotron Lightsource in Menlo Park, CA. Maps were created by collecting the X-ray fluorescence generated by incident X-ray light on the thin section, with fluorescence collected by a Vortex SII International Si drift detector for 80 × 80 μm pixels rastered across the thin section. An X-ray energy of 13.5 keV was rastered across the thin section for measurement of elemental abundances. After data collection, each pixel contained information about the energies of fluorescence produced from incident 13.5 keV X-rays proportional to the presence of a given element, allowing for the spatial resolution of different element abundances (Johnson et al., 2016b). The fluorescence maps produced were processed using the MicroAnalysis Toolkit software (Webb, 2006) to produce maps of elemental abundance in mol/cm^3. An

HDF5 file from this processed image was produced and analyzed in Python to calculate Mn^{3+}/Mn^{2+}. This calculation assumed these Mn-rich sediments of the Hotazel Formation are primarily composed of two Mn-bearing phases, kutnohorite and braunite, consistent with previous reports (Johnson et al., 2016b).

Scanning electron microscopy (SEM) and energy-dispersive spectroscopy (SEM-EDS) were used to corroborate and provide additional textural and mineralogical context synchrotron X-ray mapping mapping, and were conducted at Caltech using a Zeiss 1550VP Field Emission SEM equipped with an Oxford INCA Energy 300 X-ray EDS system. Samples were carbon-coated prior to analysis.

Modeling

A numerical model of ordinary differential equations was constructed and solved in MATLAB describing the processes relevant for early diagenesis of Mn-rich sediments. The model tabulated the rate of change of 9 species (MnO_2, MnOOH, $MnCO_3$, Mn^{2+}, FeOOH, $FeCO_3$, Fe^{2+}, lactate, and acetate) and three parameters of the carbonate system:

$$\text{Alkalinity} = [HCO_3^-] + 2[CO_3^{2-}] \quad (7)$$

$$\text{DIC} = [H_2CO_3] + [HCO_3^-] + [CO_3^{2-}] \quad (8)$$

$$\text{pH} = -\log[H^+] \quad (9)$$

The full system of equations is presented in Supplemental Information, but below we describe the rate expressions for components of early diagenesis to facilitate discussion of the results.

The first of the processes relevant for early diagenesis of Mn-rich sediments is microbially-catalyzed remineralization of organic carbon (Eqs. 1, 2). An expression from the literature (Tang et al., 2007) describing the rate of anaerobic oxidation of lactate to acetate and CO_2 by model Mn-reducing bacterium *S. oneindensis* (Myers and Nealson, 1988; Lovley, 1991; Johnson et al., 2016a) was used to represent remineralization of organic carbon by metal-reducing microbes in Mn-rich sediments generally:

$$\frac{d}{dt} = k_3 \cdot \min\left(\left[\mathrm{lac^-}\right], [Metal\ oxide]\right)\right) \frac{k_4}{k_4 + [\mathrm{ace^-}]} \qquad (10)$$

k_3 is an empirically-derived rate constant relating the product of the limiting electron donor or acceptor and a term describing rate attenuation due to accumulation of the metabolic end-product of the metabolism, acetate. For each species interacting with microbial metal reduction (Mn/Fe-oxide, Mn^{2+}/Fe^{2+}), electron flow to a given electron acceptor (MnO_2, FeOOH, or MnOOH) was modeled as proportional to its concentration. The use of a rate expression derived for *S. oneidensis* to represent generalized rates of microbial metal reduction is predicated upon the observation that the extracellular electron transport (EET) logic employed by different metal-oxide-reducing microbes appears to be the product of convergent evolution, despite the fact that sequences encoding metal-reducing biomachinery in extant taxa are highly divergent (cf. (Butler et al., 2009; Richardson et al., 2012)). Critically for the analysis of mixed Fe-Mn

formations, however, many these organisms are capable of reducing both Fe and Mn oxides with relatively similar affinity (Lovley, 1991), implying that the physiologies contained within the Fe/Mn-oxide reducing metabolic guild are governed by common chemical logic, even if the biochemical pathways to metal reduction are divergent. In *S. oneidensis*, this moderate indifference to metal-oxide terminal electron acceptor has been demonstrated through studies of metal reduction in a wide range of Fe- and/or Mn-bearing minerals (Lovley, 1991), providing support as well for the acceptor-proportional electron-flow assumption.

The second early diagenetic process contained in the model is the precipitation of carbonates—idealized as two endmembers infrequently observed in Hotazel Formation Mn-rich sediments: siderite and rhodochrosite. Although the Hotazel Formation features prominent kutnohorite rather than rhodochrosite, empirical rate constants for the latter, as well as siderite, were extracted from the literature (Jensen et al., 2002) given the availability of the data. Additionally, the experimental method used by Jensen and coworkers accounts for the kinetic inhibition by Fe^{2+} and Mn^{2+} on Ca-carbonate precipitation hypothesized to be important for Archean carbonates (Sumner and Grotzinger, 1996). Data from Jensen and coworkers were fitted to the common empirical relation (Morel and Hering, 1993), assuming a linear relationship between precipitation rate and the degree of saturation:

$$\frac{d}{dt} = k_{5,6}\left(\frac{\left[Mn^{2+},Fe^{2+}\right]\left[CO_3^{2-}\right]}{k_{sp_{rd,sd}}} - 1\right) \qquad (11)$$

The literature contains a range of k_{sp} values for Fe- and Mn-carbonates (Sternbeck, 1997; Jensen et al., 2002; Xu et al., 2004; Bénézeth et al., 2009) due to complexities of carbonate precipitation (Mucci, 2004), but for consistency the k_{sp} values for rhodochrosite and siderite calculated by (Jensen, Boddum, Tjell and Christensen, 2002) were used in this model. The concentration of carbonate ion in the model was calculated for every time step using a modified version of a script solving the carbonate system given dynamic alkalinity and DIC (Zeebe and Wolf-Gladrow, 2001):

$$K_1^{'} = \frac{[HCO_3^-][H^+]}{[H_2CO_3]} \qquad (12)$$

$$K_2^{'} = \frac{[CO_3^{2-}][H^+]}{[HCO_3^-]} \qquad (13)$$

Together with Eqs. 6 and 7, Eqs. 11 and 12 formed a system of 4 equations and 4 unknowns that could be readily solved given DIC and alkalinity from the model and values for $K_1^{'}$ *and* $K_2^{'}$ from the literature. Initial values of 2300 and 2000 meq were assigned for alkalinity and DIC, respectively, selected due to the plausibility that Precambrian seawater had carbonate chemistry broadly similar to that of the modern (Grotzinger and Kasting, 1993; Grotzinger and James, 2000; Hardie, 2003; Sumner and Beukes, 2006; Higgins et al., 2009; Spear et al., 2014; Halevy and Bachan, 2017).

Reduction of MnO_2 by $Fe^{2+}_{(aq)}$ was studied in the model; this process was inferred to be important in Mn-rich sediments given the co-occurence of hematite with kutnohorite throughout the Hotazel Formation and in close (µm-scale) petrographic association (Schneiderhan, Gutzmer, Strauss, Mezger and Beukes, 2006). This reaction is

known to be rapid (Villinski, Saiers and Conklin, 2003; Siebecker, Madison and Luther, 2015; Johnson, Savalia, Davis, Kocar, Webb, Nealson and Fischer, 2016) but self-limiting, due to the accumulation of Fe-oxides such as lepidocrocite, which occludes reactive sites on the MnO_2 surface, preventing further reaction with dissolved Fe^{2+}. The reaction between Fe^{2+} and MnO_2 is modeled here (after (Villinski, Saiers and Conklin, 2003)) as second-order with respect to the two reactants:

$$\frac{d}{dt} = k_1[\mathrm{MnO_2}][\mathrm{Fe^{2+}}] \qquad (14)$$

The final modeled component of the early diagenesis system was the comproportionation reaction between Mn^{2+} and MnO_2 to produce Mn(III) phases (Eq. 4). Work on the kinetics of this reaction has documented the complexity of the reaction pathways involved (Lefkowitz, Rouff and Elzinga, 2013), but the equilibrium stability of these phases can be generally described by the relation:

$$K_{eq} = \frac{[\mathrm{H^+}]^2}{[\mathrm{Mn^{2+}}]} \qquad (15)$$

For the comproportionation reaction to proceed, the thermodynamic threshold described above must be exceeded, i.e. $[Mn^{2+}] > [H^+]^2 / K_{eq}$. Although the nanoparticulate nature of initial Mn^{3+} precipitates creates significant uncertainties in estimates of these thresholds (Navrotsky et al., 2010; Lefkowitz et al., 2013), for the purposes of modeling here, a K_{eq} for feitknechtite of $10^{-10.2}$ calculated by Lefkowitz and coworkers was used, given experimental observations of feitknechtite as a primary precipitate of the Mn^{2+}–MnO_2 comproportionation reaction. Data from a kinetic experiment conducted by

Lefkowitz and coworkers that produced hausmannite (no data was available for feitknechtite) was fitted assuming a first-order reaction with respect to [Mn^{2+}]:

$$\frac{d}{dt} = k_2[\mathrm{Mn}^{2+}] \qquad (16)$$

The four component rate relations outlined above were assembled into a system of 9 ordinary differential equations according to the network topology of early diagenetic chemical reactions diagrammed in Fig. 2. With initial organic carbon (represented in the model by lactate) set to 1 mM, initial FeOOH and MnO_2 concentrations were each varied between 0.01–15 mM, and the system of differential equations was solved using the Runge-Kutta method of MATLAB's *ode45* solver (Shampine and Reichelt, 1997), producing a 75x75x11 matrix with entries representing the steady-state concentrations of each of the 9 species, alkalinity and DIC. At every timestep, pH was calculated from carbonate alkalinity and DIC using the equations of Zeebe and Wolf-Gladrow. The dimensions of the matrix were set by the length of the respective vectors describing independent variables of initial [FeOOH], [MnO_2], and [lactate].

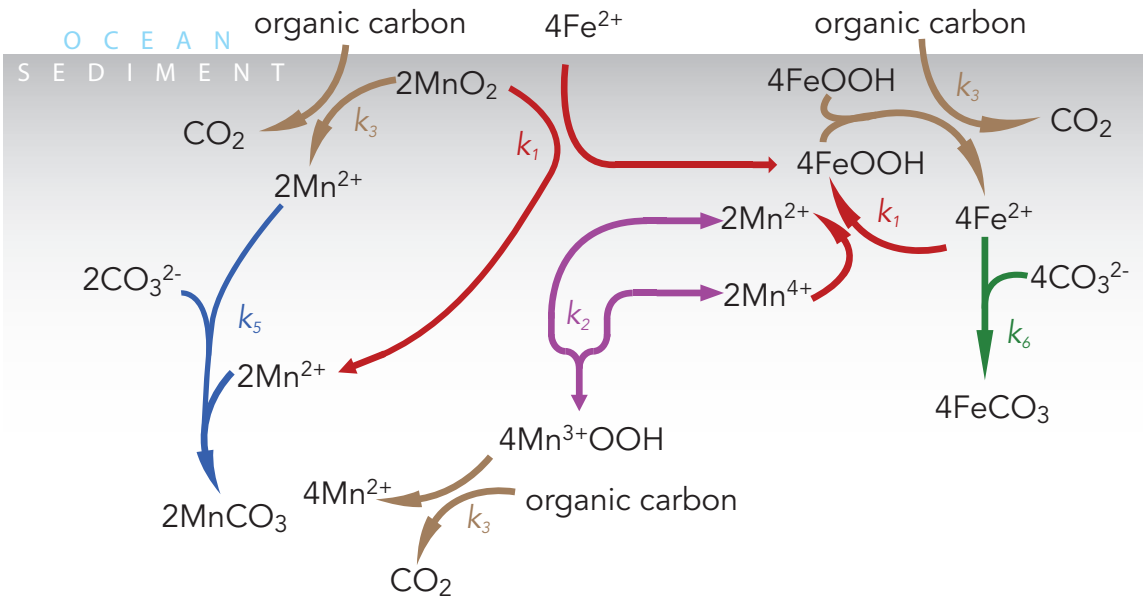

Figure 2. Schematic representation of chemical reactions in the early diagenesis of Mn-rich sediments modeled in this study. Corresponding rate constants were placed in Table 1.

Constant	Value	Citation
k_1	5500	Villinski, et al. 2003
k_2	140	Elzinga, et al. 2011
k_3	0.33	Tang, et al. 2007
k_4	0.0126	Tang, et al. 2007
k_5	7×10^{-11}	Jensen, et al. 2002
k_6	1×10^{-8}	Jensen, et al. 2002
k_7	2×10^{-6}	Jensen, et al. 2002
k_{sprd}	6.3×10^{-13}	Jensen, et al. 2002
k_{spsd}	1.4×10^{-11}	Jensen, et al. 2002
k_{spcc}	$1 \times 10^{-8.5}$	Jensen, et al. 2002

Table 1. Values for rate constants and other parameters used in the numerical model of the early diagenesis of Mn-rich sediment. Rate constant indices correspond to those depicted in Figure 1.

RESULTS

Microscopy

Optical microscopy, synchrotron X-ray mapping, and SEM-EDS analysis of a thin section sample of the Hotazel Formation corroborated earlier reports characterizing this facies of the formation as dominated by mixed Fe and Mn phases and mm-scale carbonate nodules (Fig. 3). Optical microscopy indicated the presence of pervasive nodules with diffuse margins throughout these Mn-rich sediments. Nodule centers contained drusy crystals with larger crystal sizes near their centers, decreasing in size toward more finely crystalline and nodule margins (Fig. 3A).

SEM imaging exhibited several intergrown phases within the nodules and matrix distinguished by the intensity of the backscatter and their elemental composition inferred from SEM-EDS (Fig. 3b). 100 μm-scale textures are characterized by phases with higher (located in the matrix) or lower (localized in nodules) backscatter signatures. Rare euhedral high-backscatter phases were observed in nodules, high-backscatter phases were predominantly found in the matrix. Minerals appearing darkest under SEM backscatter were typically cross-cut by euhedral crystals of a brighter (higher-backscatter) phase, which were in turn cross-cut by yet brighter phases. SEM-EDS mapping indicates these three phases correspond to minerals rich in Ca+Mn, Mn+Si, and Fe+O, respectively (Fig. 3b). These mineralogical and textural observations are consistent with descriptions in the literature (Schneiderhan et al., 2006; Johnson et al., 2016b) of kutnohorite, braunite, and hematite in this unit of the Hotazel Formation.

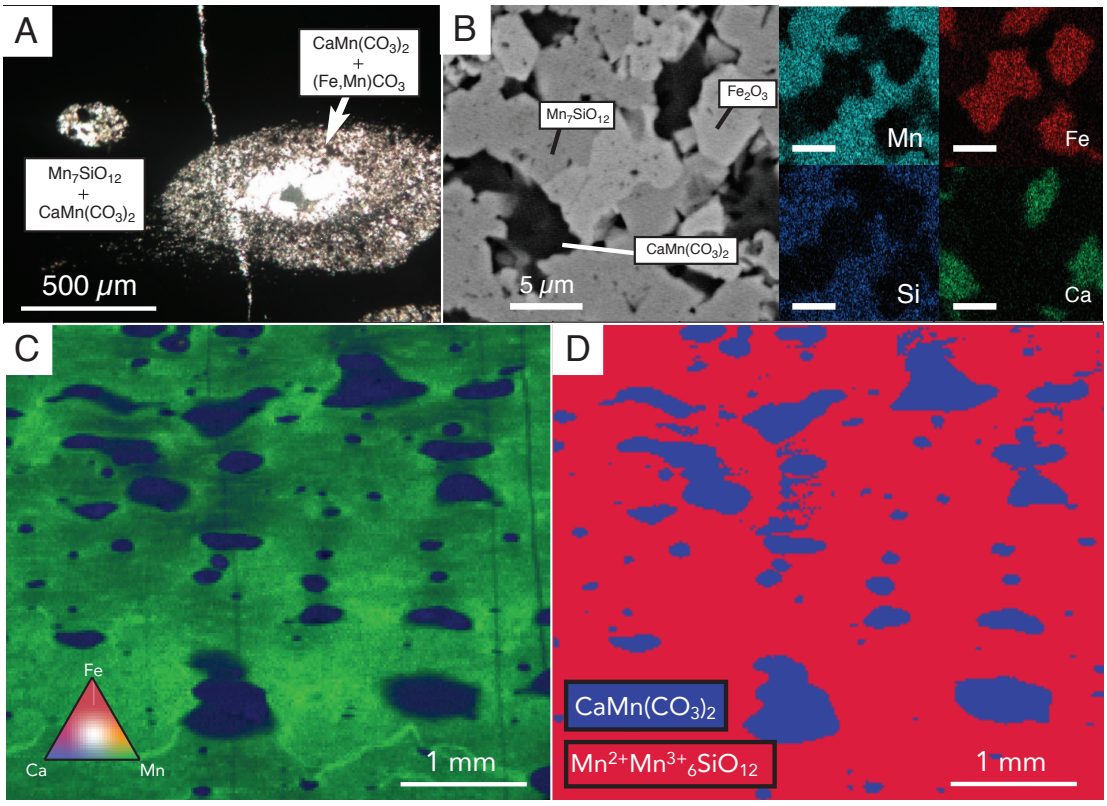

Figure 3.—SEM-EDS microscopy and synchrotron XRF and XAS analyses of a thin section of Mn-rich sedimentary rock from the Hotazel Formation. **A**) Transmitted-light optical microscopy. **B**) SEM (left panel) and EDS (right) showing intergrown braunite, hematite, and kutnohorite in Mn-rich sediments of the Hotazel Formation. **C**) Synchrotron XRF mapping at a beam energy of 13.5 keV, showing fluorescence detected from Mn, Fe, and Ca. **D**) Segmented image of Mn fluorescence from synchrotron XRF mapping, showing distribution of kutnohorite (blue) and braunite (red). See text for details. Figure 4.—Steady-state mineral assemblages calculated by the numerical model of early diagenesis of Mn-rich sediments with initial C_{org} = 1 mM. Notable initial conditions (A-C) were highlighted.

Larger-scale textural relationships were revealed and quantified through synchrotron-based X-ray microprobe spectroscopy mapping. High-energy X-ray mapping at 13500 eV documented the relative spatial distribution of Fe, Mn, and Ca in the sample (Fig. 3C). Fe and Mn were found at higher concentrations in the matrix (up to 2.3 and 9.5 mol/cm^2, respectively) and Ca was found at higher concentrations in nodules (Fig. 3C). Elevated Fe relative to Mn was detected around nodule margins, appearing on 3-color maps of Fe, Mn and Ca concentrations as lighter green areas, with darkest green describing areas richest in Mn. Mapping of relative Fe, Mn, and Ca revealed the abundance of Mn relative to these other two important cations throughout the sample, corroborating earlier geochemical reports characterizing elemental abundances in hand samples of this unit of the Hotazel via bulk rock XRF methods (Schneiderhan et al., 2006). This previous work described bulk Mn, Fe, and Ca abundances from this unit ranging from 5.1-24.1%, 28.2-51.6%, and 6.1-22.9% by weight, respectively; on average, Mn, Fe, and Ca abundances average 10.2%, 40.7%, and 17%, respectively (Schneiderhan et al., 2006). These data, reflecting bulk Mn/Fe ≈ 4 averaged over 12 hand samples from the lowest Mn-sediment unit of the Hotazel, strongly agree with our measurement of Mn/Fe ≈ 4.4 averaged over the thin section collected from this unit, reinforcing our confidence in the quantitative capabilities of our synchrotron-based methods.

After characterizing the spatial distribution and relative abundance of Fe, Mn, and Ca in the sample, we quantified the distribution of Mn redox states in this sample of Mn-rich sediments of the Hotazel Formation, leveraging previous observations that matrix-hosted Mn is contained in braunite (Mn^{3+}/Mn^{2+} = 6), while nodules contain Mn in

kutnohorite ($Mn^{3+}/Mn^{2+} = 0$) (Schneiderhan et al., 2006; Johnson et al., 2016b). Pixels representing Mn fluorescence from nodules, and therefore from kutnohorite-bound Mn, appeared as a distinct population of pixels with lower fluorescence from Mn, and thus lower Mn concentration. This bimodal distribution of Mn fluorescence intensities was used to segment the image using a threshold intensity value, yielding two pixel populations (Fig. 3D). Two sums of the pixel intensities in these two populations was weighted by Mn^{2+} and Mn^{3+} content of each phase, and the ratio of these sums yielded $Mn^{3+}/Mn^{2+} = 4.2$.

Numerical Modeling

The presence of co-occurring ferrous Fe species with Mn oxides defines a disequilibrium mineral assemblage that combats simple thermodynamic treatment, and therefore a model was constructed that could evaluate the kinetics required to explain this complex deposit. This model varied initial [FeOOH], [MnO_2], and [lactate]. The last parameter is a stand-in that represents reactive organic carbon, selected due to the abundance of kinetic data on lactate oxidation by metal-oxide reducing microbes (Tang et al., 2007). The model produced steady state values of [$MnCO_3$], [$FeCO_3$], [FeOOH], [$Mn^{3+}OOH$], and [MnO_2], creating mineral assemblages *in silico* that could be compared to the observed assemblage in the Hotazel Formation. (Figs. 4-6). Initial [FeOOH] and [MnO_2] values were varied between 0.01-15 mM and initial [lactate] was set to 1 mM. The range of final mineral stable mineral assemblages were visualized using contour

plots that depicted the dominant mineral phases (i.e. $MnCO_3$, $FeCO_3$, FeOOH, $Mn^{3+}OOH$, and MnO_2) for a given initial [lactate] across a 2D space defined by a range of initial [FeOOH] and [MnO_2].

Modeling results depicted two broad behavior domains of the system, producing a final mineral assemblage dominated by $MnCO_3$ and $FeCO_3$ and one dominated by FeOOH, MnOOH, and MnO_2, divided by a line with slope corresponding to the stoichiometry of MnO_2 and FeOOH reduction via 4 e^- transfer by oxidation of lactate to acetate (Fig. 4). The relative concentrations of $MnCO_3$ and $FeCO_3$ in the domain corresponding to a $MnCO_3$ – $FeCO_3$ mixture reflected amounts that were directly proportional to initial [MnO_2]/[FeOOH]. The proportionality of these final carbonate phases to the relative amount of initial oxide phases was apparent from the slope of the contours of each respective phase, radiating outwards from the origin (Fig. 4). The domain corresponding to a final mineral assemblage dominated by FeOOH, MnOOH, and MnO_2 was broadly characterized by a maximum final MnOOH content representing balance between relative C_{org} and MnO_2 supply. A set of initial conditions with relatively low initial FeOOH and higher MnO_2 produced abundant final MnOOH, the relative lack of Fe allowing for higher % Mn phases, but insufficient initial MnO_2 to result in mineral assemblages without sufficient electron donors to reduce a significant amount of MnO_2.

Estimates of initial conditions corresponding to the observed steady-state mineral assemblage in the Hotazel Formation were made by contouring [Mn]/[Fe] and MnOOH/$MnCO_3$ ratios–measured using synchrotron X-ray mapping–in initial [MnO_2] – [FeOOH] space as calculated by the numerical model. Values for these contours—

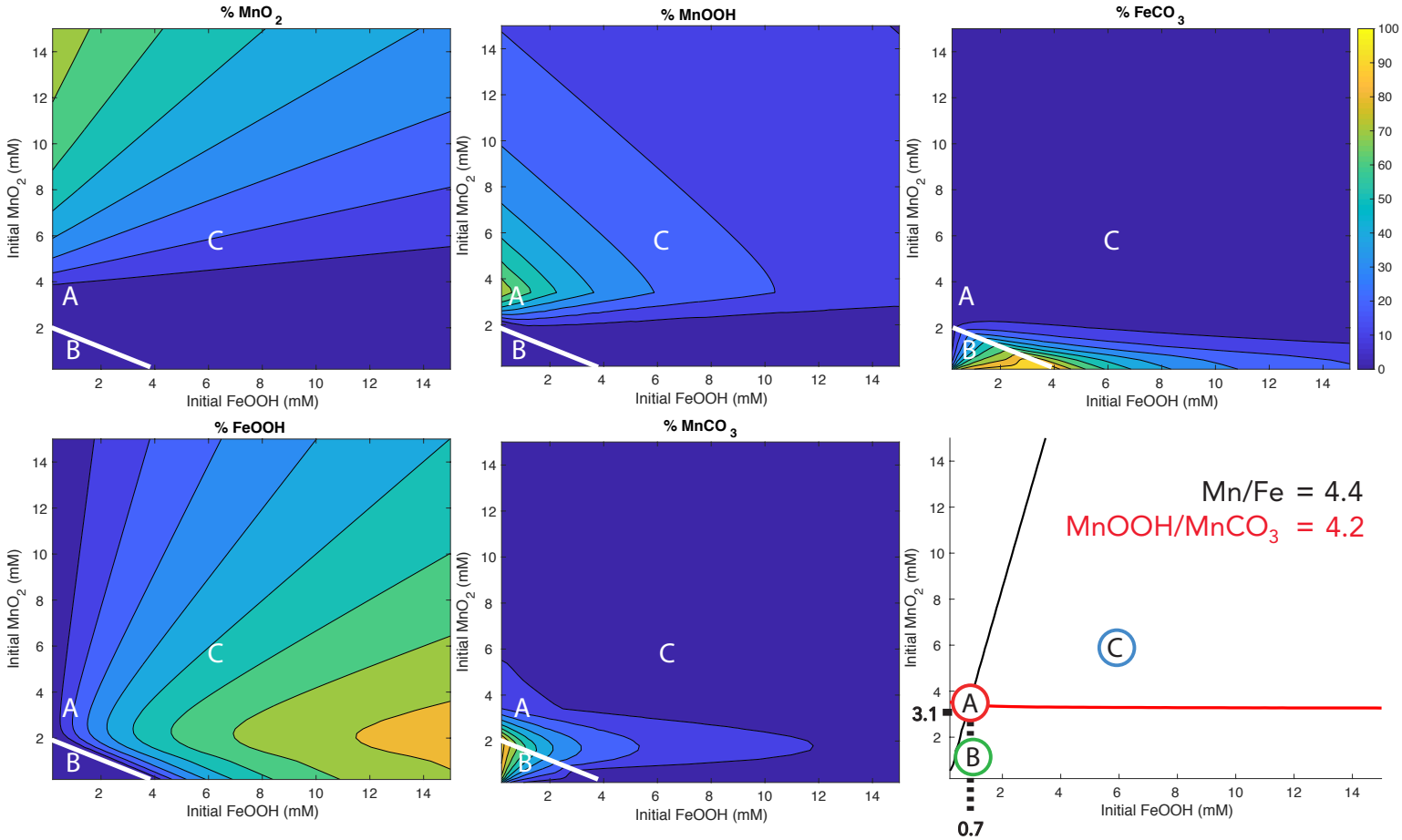

Figure 4.—Steady-state mineral assemblages calculated by the numerical model of early diagenesis of Mn-rich sediments with initial C_{org} = 1 mM. Notable initial conditions (A-C) were highlighted.

describing the set of solutions for mapping a range of initial [MnO_2], [FeOOH], and [lactate] to a [Mn]/[Fe] or $FeCO_3$ per total Fe—were determined from quantification of synchrotron observations of a sample of the Hotazel Formation, giving values of [Mn]/[Fe] ≈ 4.4 and MnOOH/$MnCO_3$ ≈ 4.2 (Fig. 4). Intersection of the contours indicated that the initial conditions capable of reproducing the observed mineral assemblage in the Hotazel Formation was only possible for initial [FeOOH] : [MnO_2] : [lactate] ≈ 0.7 : 3.1 : 1 (Fig. 4, point A). The contour describing [Mn]/[Fe] traced out a line from the origin with an approximate slope of ~4, reflecting the absence of removal of dissolved Mn^{2+} or Fe^{2+} via advective or diffusive transport processes in this model. The contour describing solutions corresponding to Fe_2O_3 per total solid phase Fe displayed a sharp kink at higher initial [FeOOH] that resulted from the decreasing degree of FeOOH reduction with higher initial [FeOOH], resulting in increasing residual FeOOH and decreasing final $FeCO_3$.

Two other points of interest (points B and C) were also selected, representative of initial [Mn]/[Fe] = 1 in domains corresponding to $MnCO_3$+$FeCO_3$- and FeOOH+MnO_2+MnOOH-dominated mixtures. A ternary plot summarizing solutions to the model for initial [lactate] = 1 mM was also constructed (Fig. 5). The model proved incapable of producing solutions containing MnO_2 residues for $MnCO_3$: MnOOH lower than ~1:4. The model, however, was able to produce $MnCO_3$-rich solutions in cases where no MnO_2 residues remained. An overlay of % $FeCO_3$ per total Fe onto these data revealed correlation between the relative abundance of reduced Fe species and that of reduced Mn (Fig. 5).

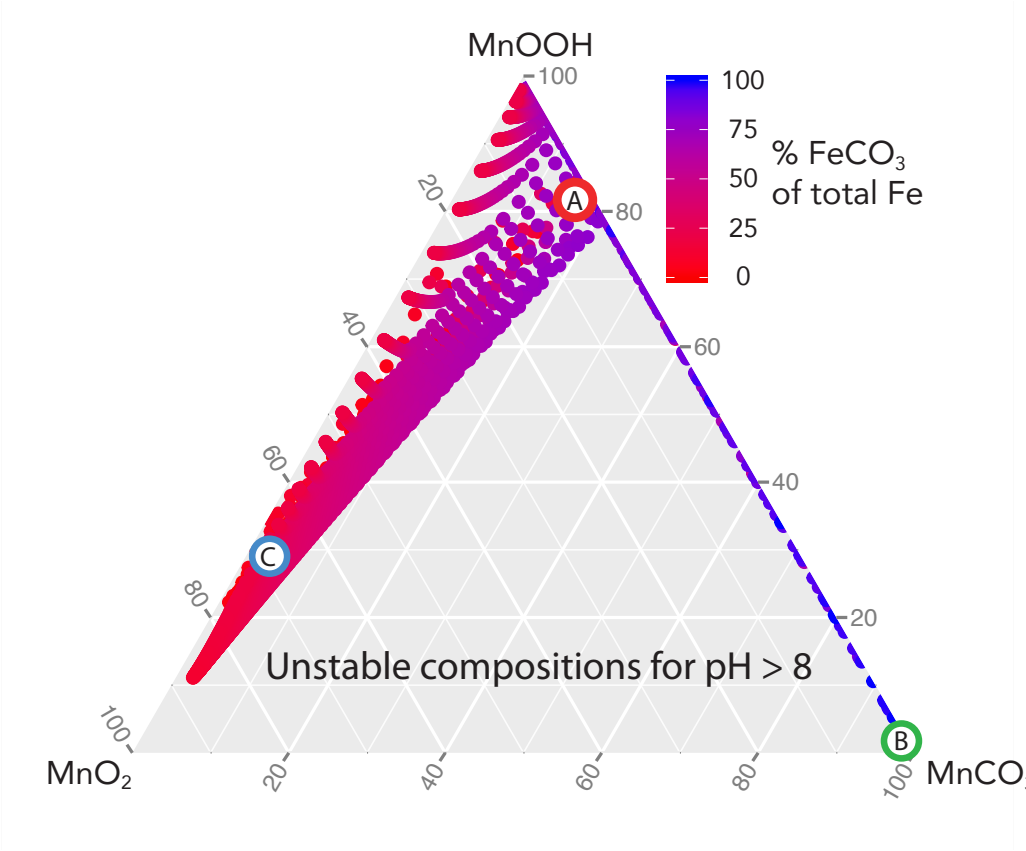

Figure 5.—Ternary plot summarizing steady-state mineral assemblages calculated by the numerical model of early diagenesis of Mn-rich sediments with initial C_{org} = 1 mM. Notable initial conditions (A-C) were highlighted as detailed in the text and in Fig. 4.

The time-dependent behavior of this system, for three selected representative initial conditions corresponding to points A, B, and C in initial [MnO_2] – [FeOOH] space (cf. Fig. 4), exhibited a clear bifurcation in the products generated by this system (Fig. 6). For initial condition A, % MnOOH increased logistically and simultaneously with % $FeCO_3$ and % $MnCO_3$ while % MnO_2 and % FeOOH decreased symmetrically with % MnOOH and % $FeCO_3$. Initial condition B, corresponding to [Mn]/[Fe] = 1 within the set of $MnCO_3$+$FeCO_3$-dominated solutions, displayed complex behavior in which % MnOOH increased until % MnO_2 reaches zero, after which % MnOOH decreased to zero. Subsequently, % $MnCO_3$ increased while $FeCO_3$ fell significantly. Initial condition C depicted small logistic increases in % $FeCO_3$, % MnOOH, and % $MnCO_3$ at the expense of % FeOOH and % MnO_2 (Tang et al., 2007).

Varying the rate constant describing metal oxide reduction via lactate (representative of sedimentary organic carbon) oxidation (k_3) across 8 orders of magnitude while initial FeOOH : MnO_2 : C_{org} was held constant at 0.7 : 3.1 : 1 revealed a bifurcation of steady-state solutions to the early diagenesis system with respect to solid phase Mn species, i.e. MnO_2, MnOOH, and $MnCO_3$ (Fig. 7). For k_3 values >5 orders of magnitude slower than initially modeled (cf. Figs. 4-6), MnOOH as a percentage of total solid phase Mn decreased to near zero, replaced instead by an MnO_2+$MnCO_3$ mixture. Decreases in MnOOH and $MnCO_3$ as a proportion of solid phase Mn were accompanied by MnO_2 increases in steady-state solutions corresponding to small ($<10^{-6}$) k_3.

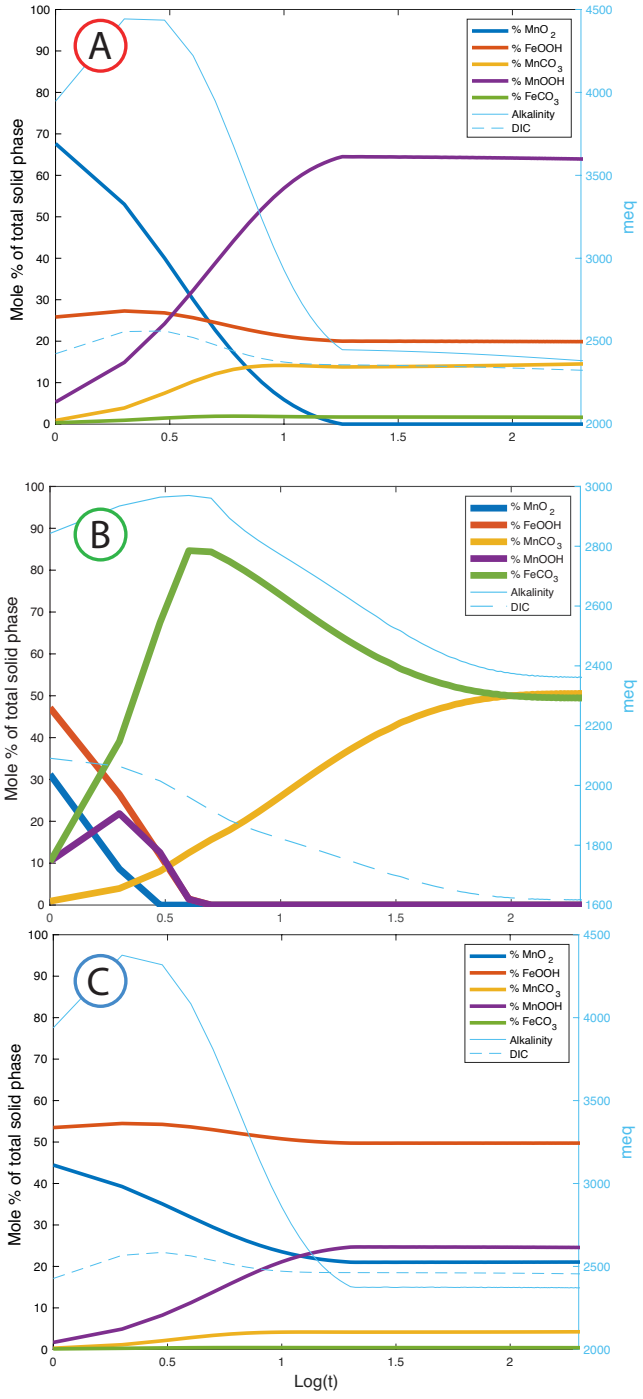

Figure 6.—Time-dependent behavior of three runs of the numerical model corresponding to initial conditions A-C annotated in Figs. 4, 5.

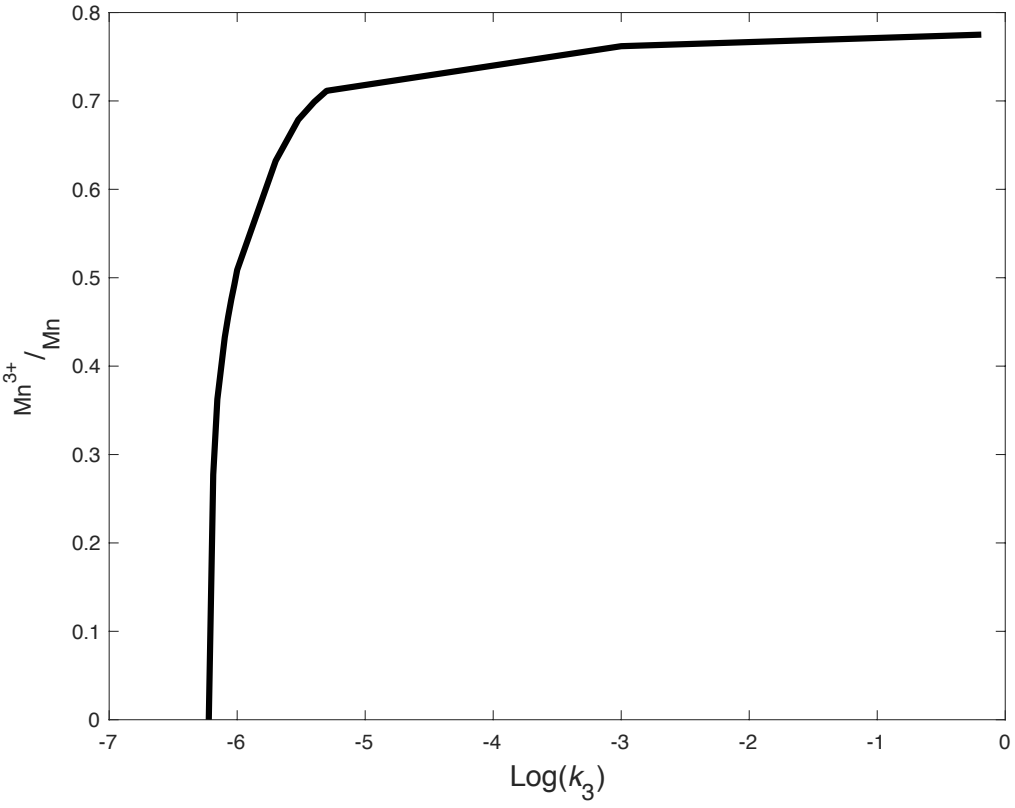

Figure 7.—Dependency of final MnOOH/$MnCO_3$ ratio of mineral assemblage on rate constant for microbial metal reduction (k_3). For $k_3 < \sim 6 \times 10^{-6}$, MnOOH cannot be precipitated by the early diagenetic system as modeled here (dashed line).

DISCUSSION

Petrographic characterization of this sample of the Hotazel Formation by SEM-EDS and synchrotron-based XRF mapping revealed a complex early diagenetic history recorded by this deposit. SEM-EDS documented braunite, kutnohorite, and hematite phases dispersed in a matrix and cross-cut by carbonate nodules containing kutnohorite (Fig. 3). Kutnohorite-bearing carbonate nodules were in turn cross-cut by later braunite and hematite phases, reflecting a diagenetic history with multiple stages of carbonate and silicate/oxide precipitation. These observations corroborate previous work identifying chemical zoning in kutnohorite of the Hotazel Formation, interpreted as representative of dynamic early diagenetic processes responsible for the precipitation of kutnohorites with variable cation concentrations (Johnson, Webb, Ma and Fischer, 2016). Our quantification of Mn^{3+}/Mn^{2+} (≈ 4.2) in the Hotazel Formation corroborated previous reports of the abundance of the Mn^{3+}-rich phase braunite, interpreted to represent an earlier $Mn^{3+}OOH$ phase which subsequently reacted with porewater Si to form braunite (Johnson et al., 2016b).

The presence of a Mn^{3+} phase thought to be stabilized by reactions between $Mn^{4+}O_2$ phases and $Mn^{2+}_{(aq)}$ (Lefkowitz et al., 2013), required the evaluation of the kinetics of reactions relevant for Mn and Fe phases constituting the primary Mn-rich sediments, which would allow for time-varying and disequilibrium processes that we postulated might stabilize the observed mineral assemblage. These kinetics were evaluated by a numerical model describing processes relevant for early diagenesis of Mn-rich sediments, and produced stable mineral assemblages grouped into $MnCO_3$+$FeCO_3$ -

rich and $MnOOH+MnO_2+FeOOH$-rich assemblages, divided by a line with slope corresponding to the stoichiometric oxidation of lactate (used in the model as a substitute for organic carbon) coupled to the reduction of MnO_2 or FeOOH, and mediated by a metal-reducing microbe (e.g. *S. oneidensis*). Varying initial [lactate] translated this stoichiometric line outwards from the origin without changing slope (data not shown), demonstrating the insensitivity of this modeling approach to differing absolute concentrations; although the concentrations modeled here (with maxima = 15 mM) are clearly lower than those in a package of primary Mn- and Fe-oxide sediments, changes in absolute concentrations do not change the behavior of the system. Instead, these results showed that insight into the early diagenetic dynamics of mixed Fe- and Mn-oxide sediments using this modeling approach could be obtained by varying the relative concentrations of three inputs: FeOOH, MnO_2, and lactate.

Solutions to the $MnCO_3+FeCO_3$ -rich and $MnOOH+MnO_2+FeOOH$-rich domains correspond to those with electron-acceptor-limiting and electron-donor-limiting initial conditions, respectively (Fig. 4). Within the electron-acceptor-limiting domain, solutions describe a mixture of Mn and Fe carbonates with $MnCO_3$: $FeCO_3$ varying in direct proportion to initial MnO_2 : FeOOH. Thus, this domain retains no information to constrain the proportion of initial organic carbon required to produce the deposit, as the final composition of the mineral assemblage is entirely dependent on initial FeOOH and MnO_2. Contours for carbonate phases above the electron-donor-limiting frontier change slope from contours within the electron-acceptor-limiting initial conditions set, reflecting the presence of partially- or non-reduced oxide phases above this stoichiometric line. The

set of solutions dominated by MnOOH (up to 92.5%) are of particular note, as these contain solutions analogous to that of the Hotazel Formation, consisting of significant Mn^{3+} species proposed (Johnson, Webb, Ma and Fischer, 2016) to have formed from comproportionation of Mn^{2+} and Mn^{4+} through an analogous mechanism to that modeled here using experimental constraints (Elzinga, 2011; Lefkowitz, Rouff and Elzinga, 2013; Johnson, Savalia, Davis, Kocar, Webb, Nealson and Fischer, 2016). Indeed, it is in this region that the contours–describing the set of solutions corresponding to ratios constrained by synchrotron XRF–intersected, indicating initial relative concentrations of FeOOH, MnO_2, and organic carbon were likely near 0.7 : 3.1 : 1 (Figs. 4-6, point A). Additionally, for large (>6 times the initial concentration of electron-donor) initial electron acceptor concentrations, the behavior of the system resembles that of the set of electron-acceptor-limiting solutions, reflecting insufficient electron donor concentrations to produce final $MnCO_3$: $FeCO_3$ ratios that differ from initial MnO_2 : $FeCO_3$.

Visualizing solutions for this system with initial [lactate] = 1 mM in ternary space illustrated important aspects of the general behavior of Mn-rich sediments undergoing microbially-catalyzed early diagenesis (Fig. 5). Stable mineral assemblages fell within a field on the ternary diagram clearly demarcated by a line from the 100% MnO_2 corner describing a constant ratio of 1:4 $MnCO_3$: MnOOH that the set of solutions with remaining unreduced MnO_2 residue cannot exceed. This is a direct result of the importance of the Mn^{2+}-Mn^{4+} comproportionation reaction in the early diagenesis of Mn-rich sediments, which for porewater pH ≥ 8 (reflecting syn-depositional conditions for the Hotazel Formation) is favorable as long as $Mn^{2+}_{(aq)}$ and MnO_2 are both in excess of

~100 μM (Lefkowitz et al., 2013). Relatively acidic porewater (pH < 8) were required to drive MnOOH disproportionation, producing mineral assemblages dominated by co-existing $MnCO_3$ and MnO_2. Thus, for likely syn-depositional pH conditions and sufficient Mn^{2+} and MnO_2, Mn^{2+}-Mn^{4+} comproportionation- was strongly favored, producing Mn mineral assemblages dominated by Mn(III).

The time-dependent behavior of this system was then examined, allowing for direct comparison between the behavior of the model and the history of the retrieved sample of the Hotazel Formation as inferred by investigation of cross-cutting relationships (Fig. 6). For initial [FeOOH], [lactate], and [MnO_2] found to produce in the model a mineral assemblage similar to that of the Hotazel, the time-dependent behavior delineated a history in which early MnOOH precipitation was followed by later precipitation of $MnCO_3$ and $FeCO_3$ (Fig. 6A). This somewhat contradicts textural observations of the Hotazel Formation in which the Mn^{3+} phase both cross-cuts and is cross-cut by kutnohorite, the former as a cement and the latter as nodules. The modeling performed here did not account for localized precipitation of nodules around nuclei, which could ameliorate this problem. Additionally, braunite has been interpreted to result from silica uptake by a MnOOH precursor (Johnson et al., 2016b), suggesting that primary cross-cutting relationships may not have been preserved in the rock record.

The time-dependent behavior of one set of initial conditions corresponding to electron-acceptor limitation (Fig. 6B) further demonstrated the importance of time-resolved understandings of these processes. For conditions corresponding to electron acceptor limitation and initial [MnO_2] : [FeOOH], the model produced a metastable

initial mineral assemblage with ~20% MnOOH that subsequently dissolved as MnO_2 is depleted by reductive dissolution. Without MnO_2 to react with $Mn^{2+}_{(aq)}$, MnOOH disproportionated as $MnCO_3$ decreased $[Mn^{2+}_{(aq)}]$ below the K_{eq} for the comproportionation reaction, dissolving the metastable phase. Additionally, a small deviation from the 1:1 $[MnCO_3]$: $[FeCO_3]$ expected for initial 1:1 $[MnO_2]$: [FeOOH] and electron-acceptor-limited conditions was observed, resulting from the fast precipitation of $FeCO_3$ relative to $MnCO_3$. Rapid sequestration of CO_3^{2-} in $FeCO_3$ reduced DIC and resulted in $[Mn^{2+}_{(aq)}]/[Fe^{2+}_{(aq)}] > 1$.

Mn^{4+}–Mn^{2+} comproportionation was observed in these numerical experiments to be crucial for the production of solid-phase Mn(III) in analogous abundance to that observed in the Hotazel Formation. Abundant carbonate anion in marine environments has provided a sink for Mn^{2+} throughout much of Earth history, implying that $[Mn^{2+}_{(aq)}]$ was unlikely to have exceeded the ~100 μM requirement for spontaneous Mn^{4+}–Mn^{2+} comproportionation on the basis of fluxes from the solid earth alone. Production of Mn^{2+} from reductive dissolution of MnO_2, however, might have provided sufficient Mn^{2+} to drive Mn^{4+}–Mn^{2+} comproportionation and thus precipitate abundant MnOOH. Without rapid production of Mn^{2+} from reductive dissolution, $[Mn^{2+}_{(aq)}]$ could not have reached concentrations sufficient for comproportionation with solid-phase Mn(IV). This was demonstrated quantitatively in our model results by a bifurcation of model solutions across a threshold value for the metal reduction rate constant parameter $k_3 \leq 6 \times 10^{-6}$ (Fig. 7), five orders of magnitude slower than the rate constant determined from experimental studies of *S. oneidensis* (Tang et al., 2007).

Invoking reductive dissolution of MnO_2 as a crucial aspect in the petrogenesis of the Hotazel Formation requires a significant supply of reductant to the precursor sediments. As modeled here, this reductant was likely organic carbon as other titrants (e.g. sulfide) would have resulted in the accumulation of insoluble products not observed in the Hotazel Formation (e.g. elemental sulfur). In contrast, a flux of organic carbon into precursor sediments of the Hotazel Formation would have ultimately produced CO_2 upon complete remineralization, leaving the stable mineral assemblage devoid of organic carbon. Additionally, the possibility that $Fe^{2+}_{(aq)}$ could have served as a reductant is also precluded by our kinetic approach to modeling Hotazel Formation petrogenesis, as the weathering flux of $Fe^{2+}_{(aq)}$ to the ocean would not have provided a sufficient flux of electron equivalents to drive Mn^{4+}–Mn^{2+} comproportionation. Using the numerical experiments presented here as a comparison, estimates of a weathering flux of ~10^{12} mol Fe yr^{-1} (Canfield, 1998; Holland, 2006) would represent a flux of ~10^{-6} – 10^{-9} mmol e^- yr^{-1} from $Fe^{2+}_{(aq)}$ into a 1 L volume of seawater depending on the estimated volume of seawater into which the $Fe^{2+}_{(aq)}$ efflux entered and is mixed on an annual timescale. In contrast, the transfer of electrons from 1 mM C_{org} occurred at a rate equivalent to 6x10^3 mmol e^- yr^{-1} in our numerical experiments. Reducing the metal reduction rate parameter k_3 to a value insufficient to produce MnOOH by comproportionation ($k_3 \leq 10^{-6}$) was equivalent to an electron transfer rate of 10^{-2} mmol e^- yr^{-1}, still several orders of magnitude faster than estimates of electron flux via $Fe^{2+}_{(aq)}$ from weathering, thus precluding $Fe^{2+}_{(aq)}$ from weathering as a potential source of reductant to produce MnOOH precursor phases of braunite in the Hotazel Formation.

It was clear from these results that catalyzed Mn-oxide reduction (usually performed in modern sediments by microbial dissimilatory metal reduction) was necessary to accumulate sufficient Mn^{2+} to drive comproportionation and therefore produce abundant Mn(III) phases. The insight that Mn(III) phases suggest a history of microbially-mediated reductive dissolution of MnO_2 may provide a framework to interpret potential biosignatures in Mn-rich martian rocks (Lanza et al., 2014). If these martian units share a chemical sedimentary petrogenesis with Mn-rich sedimentary rocks of the Hotazel Formation, they may record a history of microbially-catalyzed Mn reduction if the presence of Mn(III) phases were to be discerned.

The inference that a ratio of initial FeOOH : MnO_2 : C_{org} = 0.7 : 3.1 : 1 was required to produce the mineral assemblage observed in the Hotazel Formation enabled further interpretation of the paleoenvironment recorded by the Hotazel Formation. Previous studies have characterized the stacking pattern of iron- and manganese-rich facies of the Hotazel Formation as the result of fluctuating seawater redox conditions, given the necessity for highly oxidizing conditions to oxidize $Mn^{2+}_{(aq)}$ relative to that required for oxidation of $Fe^{2+}_{(aq)}$ (Beukes, 1983; Schneiderhan et al., 2006; Lantink et al., 2018). However, the significant excess of seawater $Mn^{2+}_{(aq)}$ relative to $Fe^{2+}_{(aq)}$ necessary to produce sedimentary metal oxides of a similar ratio required a mechanism by which Mn is enriched in seawater relative to Fe, as Fe from the solid earth is in significant excess relative to Mn (Fe : Mn in upper continental crust ≈ 60 : 1, (Taylor and McLennan, 1995)). Differing oxidation kinetics between $Fe^{2+}_{(aq)}$ and $Mn^{2+}_{(aq)}$ offer an explanation. $Fe^{2+}_{(aq)}$ is readily oxidized relative to Mn^{2+} (Millero et al., 1987; Morgan,

2005; Luther, 2010), resulting in depletion of Fe relative to Mn as a parcel of metal-rich, upwelling seawater reacts with atmospheric O_2. Transport of this water parcel in communication with atmospheric O_2 would result in progressively Mn-dominated metal oxide sediments, resulting finally in the deposits analyzed here, with primary FeOOH : MnO_2 ratios of 1 : 4.4. Changes of facies in the Hotazel Formation from Fe- to Mn-dominated could thus be reinterpreted to result from changing proximity of the Hotazel Formation depocenter with respect to an initial upwelling zone, with Mn-rich facies corresponding to a greater distance to the upwelling zone.

More broadly, the precipitation and stabilization of phases in the numerical model not predicted by thermodynamics demonstrated the importance of kinetic parameters (Elzinga, 2011) in reconstructing paleoenvironments and active pathways which were likely to have processed manganese formations in the deep past. In particular, the stable mineral assemblage represented by point A (analogous to that in the Hotazel Formation), consisting of >50% of a braunite-precursor Mn(III) phase, demonstrates the importance of rapid accumulation of $Mn^{2+}_{(aq)}$ and the subsequent comproportionation reaction with Mn^{4+} in determining the outcome of early diagenesis of these Fe-Mn sediments. The capacity for this numerical model to reproduce the mineral assemblage of the Hotazel Formation indicates the importance of examining reaction kinetics in systems where fluxes may be modulated by biology. Differences in reaction products from a model variant excluding biological Fe and Mn reduction further underscores the importance of evaluating effects of biological modification of manganese formations when examining Fe and Mn formations.

CONCLUSIONS

The Hotazel Formation—though notably devoid of significant concentrations of organic carbon today—records a rich history of active interaction with organic carbon, demonstrated here by the diagenetically stabilized, disequilibrium mineral assemblage constrained through coupled spectroscopic and modeling efforts. Synchrotron X-ray mapping of a Mn-rich facies of the Hotazel Formation with prominent early diagenetic textures (e.g. nodules) revealed the coexistence of Mn and Fe phases out of thermodynamic equilibrium, requiring kinetic explanations. A numerical model of the early diagenesis of Mn-rich sediments was used to invert for initial concentrations of electron donor and electron acceptors (FeOOH and MnO_2) required to produce the mineral assemblage measured by synchrotron X-ray techniques, and indicated that initial [FeOOH] : [MnO_2] : [C_{org}] = 0.7 : 3.1 : 1. These ratios reflect an input of significant C_{org} to the precursor sediments that is today absent due to remineralization during early diagenesis. Additionally, the model demonstrated that rapid Mn^{2+} production from reductive dissolution of MnO_2 by C_{org} was necessary to produce final concentrations of solid-phase Mn^{3+} matching that measured in the Hotazel Formation by synchrotron XRF. The kinetically controlled reactions resulting from C_{org} remineralization increased Mn^{2+} concentrations in porewaters fast enough to drive comproportion with Mn^{4+}, ultimately resulting in an abundant Mn^{3+} phase that would later become braunite after diagenetic reactions with porewater Si. These results indicate these Mn deposits are very much geobiological in nature—not just requiring the impact of photosynthesis in the oxidation and accumulation of the metals, but also in their diagenetic stabilization through microbially mediated organic diagenesis. Results showed that the precursor sediment had

high Mn : Fe ratios—values significantly above that typical of the solid Earth, implying kinetic control of facies stacking patterns in the Hotazel Formation. Future work on understanding the paleoredox conditions required to produce certain types of sedimentary rocks might benefit from similar approaches that seek to quantify the convolution of initial sediment composition and the time-dependent properties of diagenetic reactions that can lead to geologically stable, disequilibrium mineral assemblages. This type of approach might also be useful in evaluating the unexpected and common manganese mineralization observed in ancient sedimentary rocks on Mars (Lanza et al., 2014; Stamenković et al., 2018).

ACKNOWLEDGEMENTS

Support for this work was provided by the Simons Foundation Collaboration on the Origins of Life, the Agouron Institute, and David and Lucille Packard Foundation, and a NSF GRFP to KSM. Portions of this research were carried out at the Stanford Synchrotron Radiation Lightsource, SLAC National Accelerator Laboratory, a DOE Office of Science User Facility.

REFERENCES

BEKKER, A., KAUFMAN, A.J., KARHU, J.A., BEUKES, N.J., SWART, Q.D., COETZEE, L.L., AND ERIKSSON, K.A., 2001, Chemostratigraphy of the Paleoproterozoic Duitschland Formation, South Africa: Implications for Coupled Climate Change and Carbon Cycling: American Journal of Science, v. 301, p. 261–285, doi: 10.2475/ajs.301.3.261.

BÉNÉZETH, P., DANDURAND, J.L., and HARRICHOURY, J.C., 2009, Solubility product of siderite (FeCO3) as a function of temperature (25–250 °C): Chemical Geology, v. 265, p. 3–12, doi: 10.1016/j.chemgeo.2009.03.015.

BEUKES, N.J., 1987, Facies relations, depositional environments and diagenesis in a major early Proterozoic stromatolitic carbonate platform to basinal sequence, Campbellrand Subgroup, Transvaal Supergroup, Southern Africa: Sedimentary Geology, v. 54, p. 1–46, doi: 10.1016/0037-0738(87)90002-9.

BEUKES, N.J., 1983, Palaeoenvironmental Setting of Iron-Formations in the Depositional Basin of the Transvaal Supergroup, South Africa, *in* Trendall, A.F. and Morris, R.C., eds., Iron-Formation: Facts and Problems: Developments in Precambrian Geology, Elsevier, Amsterdam, p. 558.

BUTLER, J.E., YOUNG, N.D., and LOVLEY, D.R., 2009, Evolution from a respiratory ancestor to fill syntrophic and fermentative niches: comparative genomics of six Geobacteraceae species: BMC Genomics, v. 10, p. 1–10, doi: 10.1186/1471-2164-10-103.

CAIRNCROSS, B., and BEUKES, N.J., 2013, The Kalahari Manganese Field: the adventure continues: Struik Nature, Cape Town.

CALVERT, S.E., and Pedersen, T.F., 1996, Sedimentary geochemistry of manganese; implications for the environment of formation of manganiferous black shales: Economic Geology, v. 91, p. 36–47, doi: 10.2113/gsecongeo.91.1.36.

CANFIELD, D.E., 1998, A new model for Proterozoic ocean chemistry: Nature, v. 396, p. 450–453, doi: 10.1038/24839.

CONDIE, K.C., 1993, Chemical composition and evolution of the upper continental crust: Contrasting results from surface samples and shales: Chemical Geology, v. 104,

p. 1–37, doi: 10.1016/0009-2541(93)90140-E.

CORNELL, D.H., and SCHÜTTE, S.S., 1995, A volcanic-exhalative origin for the world's largest (Kalahari) Manganese field: Mineralium Deposita, v. 30, p. 146–151, doi: 10.1007/bf00189343.

DUCKWORTH, O.W., and SPOSITO, G., 2005, Siderophore−Manganese(III) Interactions. I. Air-Oxidation of Manganese(II) Promoted by Desferrioxamine B: Environmental Science & Technology, v. 39, p. 6037–6044, doi: 10.1021/es050275k.

ELZINGA, E.J., 2011, Reductive transformation of birnessite by aqueous Mn(II): Environ Sci Technol, v. 45, p. 6366–72, doi: 10.1021/es2013038.

ELZINGA, E.J., and KUSTKA, A.B., 2015, A Mn-54 Radiotracer Study of Mn Isotope Solid–Liquid Exchange during Reductive Transformation of Vernadite (δ-MnO2) by Aqueous Mn(II): Environmental Science & Technology, v. 49, p. 4310–4316, doi: 10.1021/acs.est.5b00022.

EVANS, D.A., BEUKES, N.J., and KIRSCHVINK, J.L., 1997, Low-latitude glaciation in the Palaeoproterozoic era: Nature, v. 386, p. 262–266, doi: 10.1038/386262a0.

EVANS, D., GUTZMER, J., BEUKES, N., and KIRSCHVINK, J., 2001, Paleomagnetic constraints on ages of mineralization in the Kalahari manganese field, South Africa: Economic Geology, v. 96, p. 621–631.

FARQUHAR, J., BAO, H., and THIEMENS, M., 2000, Atmospheric Influence of Earth's Earliest Sulfur Cycle: Science, v. 289, p. 756, doi: 10.1126/science.289.5480.756.

FISCHER, W.W., HEMP, J., and VALENTINE, J.S., 2016, How did life survive Earth's great oxygenation? Current Opinion in Chemical Biology, v. 31, p. 166–178, doi: 10.1016/j.cbpa.2016.03.013.

FROELICH, P.N., KLINKHAMMER, G.P., BENDER, M.L., LUEDTKE, N.A., HEATH, G.R., CULLEN, D., DAUPHIN, P., HAMMOND, D., HARTMAN, B., and MAYNARD, V., 1979, Early oxidation of organic matter in pelagic sediments of the eastern equatorial Atlantic: suboxic diagenesis: Geochimica et Cosmochimica Acta, v. 43, p. 1075–1090, doi: 10.1016/0016-7037(79)90095-4.

GLASBY, G.P., 2006, Manganese: Predominant Role of Nodules and Crusts, *in* Schulz, H.D. and Zabel, M., eds., Marine Geochemistry: Springer Berlin Heidelberg,

Berlin, Heidelberg, p. 371–427. https://doi.org/10.1007/3-540-32144-6_11.

GUMSLEY, A.P., CHAMBERLAIN, K.R., BLEEKER, W., SÖDERLUND, U., DE KOCK, M.O., LARSSON, E.R., and BEKKER, A., 2017, Timing and tempo of the Great Oxidation Event: Proceedings of the National Academy of Sciences, v. 114, p. 1811, doi: 10.1073/pnas.1608824114.

GUO, Q., STRAUSS, H., KAUFMAN, A.J., SCHRÖDER, S., GUTZMER, J., WING, B., BAKER, M.A., BEKKER, A., JIN, Q., KIM, S.-T., and FARQUHAR, J., 2009, Reconstructing Earth's surface oxidation across the Archean-Proterozoic transition: Geology, v. 37, p. 399–402, doi: 10.1130/g25423a.1.

GUTZMER, J., and BEUKES, N.J., 1996, Mineral paragenesis of the Kalahari manganese field, South Africa: Ore Geology Reviews, v. 11, p. 405–428.

HEM, J.D., and LIND, C.J., 1983, Nonequilibrium models for predicting forms of precipitated manganese oxides: Geochimica et Cosmochimica Acta, v. 47, p. 2037–2046, doi: 10.1016/0016-7037(83)90219-3.

HERNAN, L., MORALES, J., and TIRADO, J.L., 1986, Relationships between composition and surface properties of the dehydration products of synthetic manganite: Surface and Coatings Technology, v. 27, p. 343–350, doi: 10.1016/0257-8972(86)90074-5.

HOFFMAN, P.F., 2013, The Great Oxidation and a Siderian snowball Earth: MIF-S based correlation of Paleoproterozoic glacial epochs: Chemical Geology, v. 362, p. 143–156, doi: 10.1016/j.chemgeo.2013.04.018.

HOLLAND, H.D., 1984, Chemical Evolution of the Atmosphere and Oceans: Princeton University Press, Princeton, NJ, 582 p.

HOLLAND, H.D., 2006, The oxygenation of the atmosphere and oceans: Philosophical transactions of the Royal Society of London. Series B, Biological sciences, v. 361, p. 903–915, doi: 10.1098/rstb.2006.1838.

JAMES, H.L., 1954, Sedimentary facies of iron-formation: Economic Geology, v. 49, p. 235–293, doi: 10.2113/gsecongeo.49.3.235.

JENSEN, D.L., BODDUM, J.K., TJELL, J.C., and CHRISTENSEN, T.H., 2002, The solubility of rhodochrosite (MnCO3) and siderite (FeCO3) in anaerobic aquatic environments:

Applied Geochemistry, v. 17, p. 503–511, doi: 10.1016/S0883-2927(01)00118-4.

JOHNSON, J.E., SAVALIA, P., DAVIS, R., KOCAR, B.D., WEBB, S.M., NEALSON, K.H., and FISCHER, W.W., 2016a, Real-Time Manganese Phase Dynamics during Biological and Abiotic Manganese Oxide Reduction: Environmental Science & Technology, doi: 10.1021/acs.est.5b04834. http://dx.doi.org/10.1021/acs.est.5b04834.

JOHNSON, J.E., WEBB, S.M., MA, C., and FISCHER, W.W., 2016b, Manganese mineralogy and diagenesis in the sedimentary rock record: Geochimica et Cosmochimica Acta, v. 173, p. 210–231, doi: 10.1016/j.gca.2015.10.027.

JOHNSON, J.E., WEBB, S.M., THOMAS, K., ONO, S., KIRSCHVINK, J.L., and FISCHER, W.W., 2013, Manganese-oxidizing photosynthesis before the rise of cyanobacteria: Proceedings of the National Academy of Sciences of the United States of America, v. 110, p. 11238–11243, doi: 10.1073/pnas.1305530110.

KIRSCHVINK, J.L., GAIDOS, E.J., BERTANI, L.E., BEUKES, N.J., GUTZMER, J., MAEPA, L.N., and STEINBERGER, R.E., 2000, Paleoproterozoic snowball Earth: Extreme climatic and geochemical global change and its biological consequences: Proceedings of the National Academy of Sciences of the United States of America, v. 97, p. 1400–1405.

KNOLL, A.H., and BEUKES, N.J., 2009, Introduction: Initial investigations of a Neoarchean shelf margin-basin transition (Transvaal Supergroup, South Africa): Precambrian Research, v. 169, p. 1–14, doi: 10.1016/j.precamres.2008.10.009.

KOPP, R.E., KIRSCHVINK, J.L., HILBURN, I.A., and NASH, C.Z., 2005, The Paleoproterozoic snowball Earth: A climate disaster triggered by the evolution of oxygenic photosynthesis: Proceedings of the National Academy of Sciences of the United States of America, v. 102, p. 11131–11136, doi: 10.1073/pnas.0504878102.

KOSTKA, J.E., LUTHER, G.W., and NEALSON, K.H., 1995, Chemical and biological reduction of Mn (III)-pyrophosphate complexes: Potential importance of dissolved Mn (III) as an environmental oxidant: Geochimica et Cosmochimica Acta, v. 59, p. 885–894, doi: 10.1016/0016-7037(95)00007-0.

KOTLOSKI, N.J., and GRALNICK, J.A., 2013, Flavin electron shuttles dominate extracellular electron transfer by Shewanella oneidensis: MBio, v. 4, doi: 10.1128/mBio.00553-12. http://mbio.asm.org/content/4/1/e00553-12.full.pdf.

LANTINK, M.L., OONK, P.B.H., FLOOR, G.H., TSIKOS, H., and MASON, P.R.D., 2018, Fe isotopes of a 2.4 Ga hematite-rich IF constrain marine redox conditions around the GOE: Precambrian Research, v. 305, p. 218–235, doi: 10.1016/j.precamres.2017.12.025.

LANZA, N.L., FISCHER, W.W., WIENS, R.C., GROTZINGER, J., OLLILA, A.M., COUSIN, A., ANDERSON, R.B., CLARK, B.C., GELLERT, R., MANGOLD, N., MAURICE, S., LE MOUELIC, S., NACHON, M., SCHMIDT, M., et al., 2014, High manganese concentrations in rocks at Gale crater, Mars: Geophysical Research Letters, v. 41, p. 5755–5763.

LEFKOWITZ, J.P., ROUFF, A.A., and ELZINGA, E.J., 2013, Influence of pH on the Reductive Transformation of Birnessite by Aqueous Mn(II): Environmental Science & Technology, v. 47, p. 10364–10371, doi: 10.1021/es402108d.

LIN, H., SZEINBAUM, N.H., DICHRISTINA, T.J., and TAILLEFERT, M., 2012, Microbial Mn(IV) reduction requires an initial one-electron reductive solubilization step: Geochimica et Cosmochimica Acta, v. 99, p. 179–192, doi: 10.1016/j.gca.2012.09.020.

LINGAPPA, U.F., MONTEVERDE, D.R., MAGYAR, J.S., VALENTINE, J.S., and FISCHER, W.W., 2019, How manganese empowered life with dioxygen (and vice versa): Free Radic Biol Med, v. 140, p. 113–125, doi: 10.1016/j.freeradbiomed.2019.01.036.

LOVLEY, D.R., 1991, Dissimilatory Fe(III) and Mn(IV) reduction: Microbiological Reviews, v. 55, p. 259–287.

LUO, G., ONO, S., BEUKES, N.J., WANG, D.T., XIE, S., and SUMMONS, R.E., 2016, Rapid oxygenation of Earth's atmosphere 2.33 billion years ago: Science Advances, v. 2, doi: 10.1126/sciadv.1600134. http://advances.sciencemag.org/content/advances/2/5/e1600134.full.pdf.

LUTHER, G.W., 2010, The Role of One- and Two-Electron Transfer Reactions in Forming

Thermodynamically Unstable Intermediates as Barriers in Multi-Electron Redox Reactions: Aquatic Geochemistry, v. 16, p. 395–420, doi: 10.1007/s10498-009-9082-3.

MADISON, A.S., TEBO, B.M., MUCCI, A., SUNDBY, B., and LUTHER, G.W., 2013, Abundant Porewater Mn(III) Is a Major Component of the Sedimentary Redox System: Science, v. 341, p. 875–878, doi: 10.1126/science.1241396.

MARGOLIS, S.V., and BURNS, R.G., 1976, Pacific Deep-Sea Manganese Nodules: Their Distribution, Composition, and Origin: Annual Review of Earth and Planetary Sciences, v. 4, p. 229–263, doi: 10.1146/annurev.ea.04.050176.001305.

MAYNARD, J.B., 2010, The Chemistry of Manganese Ores through Time: A Signal of Increasing Diversity of Earth-Surface Environments: Economic Geology, v. 105, p. 535–552, doi: 10.2113/gsecongeo.105.3.535.

MILLERO, F.J., SOTOLONGO, S., and IZAGUIRRE, M., 1987, The oxidation kinetics of Fe (II) in seawater: Geochimica et Cosmochimica Acta, v. 51, p. 793–801.

MOREL, F.M.M., and HERING, J.G., 1993, Principles and Applications of Aquatic Chemistry: Wiley. https://books.google.com/books?id=Rs31PfkeBaIC.

MORGAN, J.J., 2005, Kinetics of reaction between O2 and Mn(II) species in aqueous solutions: Geochimica et Cosmochimica Acta, v. 69, p. 35–48, doi: 10.1016/j.gca.2004.06.013.

MUCCI, A., 2004, The Behavior of Mixed Ca–Mn Carbonates in Water and Seawater: Controls of Manganese Concentrations in Marine Porewaters: Aquatic Geochemistry, v. 10, p. 139–169, doi: 10.1023/B:AQUA.0000038958.56221.b4.

MYERS, C.R., and NEALSON, K.H., 1988, Microbial reduction of manganese oxides: Interactions with iron and sulfur: Geochimica et Cosmochimica Acta, v. 52, p. 2727–2732, doi: 10.1016/0016-7037(88)90041-5.

NAVROTSKY, A., MA, C., LILOVA, K., and BIRKNER, N., 2010, Nanophase Transition Metal Oxides Show Large Thermodynamically Driven Shifts in Oxidation-Reduction Equilibria: Science, v. 330, p. 199–201, doi: 10.1126/science.1195875.

NEL, C.J., BEUKES, N.J., and DE VILLERS, J.P.R., 1986, The Mamatwan manganese mine of the Kalahari Manganese Field, *in* Anhaeusser, C.R. and Maske, S., eds.,

Mineral Deposits of Southern Africa: Geological Society of South Africa.

OKITA, P.M., MAYNARD, J.B., SPIKER, E.C., and FORCE, E.R., 1988, Isotopic evidence for organic matter oxidation by manganese reduction in the formation of stratiform manganese carbonate ore: Journal Name: Geochimica et Cosmochimica Acta; (USA); Journal Volume: 52:11, p. Medium: X; Size: Pages: 2679-2685.

OLDHAM, V.E., OWINGS, S.M., JONES, M.R., TEBO, B.M., and LUTHER, G.W., 2015, Evidence for the presence of strong Mn(III)-binding ligands in the water column of the Chesapeake Bay: Marine Chemistry, v. 171, p. 58–66, doi: 10.1016/j.marchem.2015.02.008.

POST, J.E., 1999, Manganese oxide minerals: Crystal structures and economic and environmental significance: Proceedings of the National Academy of Sciences, v. 96, p. 3447–3454, doi: 10.1073/pnas.96.7.3447.

POSTMA, D., 1985, Concentration of Mn and separation from Fe in sediments—I. Kinetics and stoichiometry of the reaction between birnessite and dissolved Fe(II) at 10°C: Geochimica et Cosmochimica Acta, v. 49, p. 1023–1033, doi: 10.1016/0016-7037(85)90316-3.

POSTMA, D., and APPELO, C.A.J., 2000, Reduction of Mn-oxides by ferrous iron in a flow system: column experiment and reactive transport modeling: Geochimica et Cosmochimica Acta, v. 64, p. 1237–1247, doi: 10.1016/S0016-7037(99)00356-7.

RAISWELL, R., and FISHER, Q.J., 2000, Mudrock‐hosted carbonate concretions: a review of growth mechanisms and their influence on chemical and isotopic composition: Journal of the Geological Society, v. 157, p. 239–251, doi: 10.1144/jgs.157.1.239.

RICHARDSON, D.J., BUTT, J.N., FREDRICKSON, J.K., ZACHARA, J.M., SHI, L., EDWARDS, M.J., WHITE, G., BAIDEN, N., GATES, A.J., MARRITT, S.J., and CLARKE, T.A., 2012, The “porin-cytochrome” model for microbe-to-mineral electron transfer: Mol Microbiol, v. 85, p. 201–12, doi: 10.1111/j.1365-2958.2012.08088.x.

ROBIE, R.A., HUEBNER, J.S., and HEMINGWAY, B.S., 1995, Heat capacities and thermodynamic properties of braunite (Mn7SiO12) and rhodonite (MnSiO3): American Mineralogist, v. 80, p. 560–575, doi: 10.2138/am-1995-5-616.

SCHAEFER, M.V., HANDLER, R.M., and SCHERER, M.M., 2017, Fe(II) reduction of

pyrolusite (β-MnO 2) and secondary mineral evolution: Geochemical Transactions, v. 18, p. 1–11, doi: 10.1186/s12932-017-0045-0.

SCHNEIDERHAN, E.A., GUTZMER, J., STRAUSS, H., MEZGER, K., and BEUKES, N.J., 2006, The chemostratigraphy of a Paleoproterozoic MnF-BIF succession - the Voëlwater Subgroup of the Transvaal Supergroup in Griqualand West, South Africa: South African Journal of Geology, v. 109, p. 63–80.

SHAMPINE, L.F., and REICHELT, M.W., 1997, The MATLAB ODE Suite: SIAM J. Sci. Comput., v. 18, p. 1–22, doi: 10.1137/s1064827594276424.

SIEBECKER, M., MADISON, A.S., and LUTHER, G.W., 2015, Reduction Kinetics of Polymeric (Soluble) Manganese (IV) Oxide (MnO2) by Ferrous Iron (Fe2+): Aquatic Geochemistry, v. 21, p. 143–158, doi: 10.1007/s10498-015-9257-z.

STAMENKOVIĆ, V., WARD, L.M., MISCHNA, M., and FISCHER, W.W., 2018, O2 solubility in Martian near-surface environments and implications for aerobic life: Nature Geoscience, v. 11, p. 905–909, doi: 10.1038/s41561-018-0243-0.

STERNBECK, J., 1997, Kinetics of rhodochrosite crystal growth at 25°C: The role of surface speciation: Geochimica et Cosmochimica Acta, v. 61, p. 785–793, doi: 10.1016/S0016-7037(96)00379-1.

SUMNER, D.Y., and GROTZINGER, J.P., 1996, Were kinetics of Archean calcium carbonate precipitation related to oxygen concentration? Geology, v. 24, p. 119–122, doi: 10.1130/0091-7613(1996)024<0119:wkoacc>2.3.co;2.

TAKASHIMA, T., HASHIMOTO, K., and NAKAMURA, R., 2012, Mechanisms of pH-Dependent Activity for Water Oxidation to Molecular Oxygen by MnO2 Electrocatalysts: Journal of the American Chemical Society, v. 134, p. 1519–1527, doi: 10.1021/ja206511w.

TANG, Y.J., MEADOWS, A.L., and KEASLING, J.D., 2007, A kinetic model describing Shewanella oneidensis MR-1 growth, substrate consumption, and product secretion: Biotechnology and Bioengineering, v. 96, p. 125–133, doi: 10.1002/bit.21101.

TAYLOR, S.R., and MCLENNAN, S.M., 1995, The Geochemical Evolution of the Continental Crust: Reviews of Geophysics, v. 33, p. 241–265.

TSIKOS, H., BEUKES, N.J., MOORE, J.M., and HARRIS, C., 2003, Deposition, Diagenesis, and Secondary Enrichment of Metals in the Paleoproterozoic Hotazel Iron Formation, Kalahari Manganese Field, South Africa: Economic Geology, v. 98, p. 1449–1462, doi: 10.2113/gsecongeo.98.7.1449.

TSIKOS, H., MATTHEWS, A., EREL, Y., and MOORE, J.M., 2010, Iron isotopes constrain biogeochemical redox cycling of iron and manganese in a Palaeoproterozoic stratified basin: Earth and Planetary Science Letters, v. 298, p. 125–134, doi: 10.1016/j.epsl.2010.07.032.

TSIKOS, H., and MOORE, J.M., 1997, Petrography and geochemistry of the Paleoproterozoic Hotazel Iron-Formation, Kalahari manganese field, South Africa; implications for Precambrian manganese metallogenesis: Economic Geology, v. 92, p. 87–97, doi: 10.2113/gsecongeo.92.1.87.

VAN CAPPELLEN, P., and WANG, Y., 1996, Cycling of iron and manganese in surface sediments; a general theory for the coupled transport and reaction of carbon, oxygen, nitrogen, sulfur, iron, and manganese: American Journal of Science, v. 296, p. 197–243, doi: 10.2475/ajs.296.3.197.

VEIZER, J., HOEFS, J., LOWE, D.R., and THURSTON, P.C., 1989, Geochemistry of Precambrian carbonates: II. Archean greenstone belts and Archean sea water: Geochim Cosmochim Acta, v. 53, p. 859–71.

VILLINSKI, J.E., O'DAY, P.A., CORLEY, T.L., and CONKLIN, M.H., 2001, In Situ Spectroscopic and Solution Analyses of the Reductive Dissolution of MnO2 by Fe(II): Environmental Science & Technology, v. 35, p. 1157–1163, doi: 10.1021/es001356d.

VILLINSKI, J.E., SAIERS, J.E., and CONKLIN, M.H., 2003, The Effects of Reaction-Product Formation on the Reductive Dissolution of MnO2 by Fe(II): Environmental Science & Technology, v. 37, p. 5589–5596, doi: 10.1021/es034060r.

WAYCHUNAS, G.A., 1991, Crystal Chemistry of Oxides and Oxyhydroxides, *in* Lindsay, D.H., ed., Oxide Minerals: Petrologic and Magnetic Significance: Reviews in Mineralogy, Mineralogical Society of America, p. 55.

WEBB, S.M., 2006, SMAK: Sam's Microprobe Analysis Kit: Stanford Synchrotron

Radiation Laboratory, Menlo Park, CA.

WEBB, S.M., DICK, G.J., BARGAR, J.R., and TEBO, B.M., 2005, Evidence for the presence of Mn(III) intermediates in the bacterial oxidation of Mn(II): Proceedings of the National Academy of Sciences, v. 102, p. 5558–5563, doi: 10.1073/pnas.0409119102.

XU, T., APPS, J.A., and PRUESS, K., 2004, Mineral sequestration of carbon dioxide in a sandstone–shale system: Chemical Geology, v. 217, p. 295–318, doi: 10.1016/j.chemgeo.2004.12.015.

A p p e n d i x A

HIGH-GRADIENT MAGNETIC SEPARATION METHODS FOR ANAEROBIC EXTRACTION OF MAGNETIC MINERALS FROM MARINE SEDIMENTS

Kyle S. Metcalfe and Victoria J. Orphan

Division of Geological and Planetary Sciences,
California Institute of Technology, Pasadena, California, 91125

ABSTRACT

Evidence suggests microorganisms inhabiting marine sediments may use magnetic minerals as conduits for extracellular electron transfer (EET). However, existing techniques to extract magnetic minerals do not maintain anoxic conditions necessary for downstream culturing of obligately anaerobic microorganisms. Here, I present anaerobic methods for the extraction of magnetic minerals from marine sediments, with the aim of using these extracted minerals for culturing of the attached microorganisms.

INTRODUCTION

Conductive magnetic minerals such a magnetite (Fe_3O_4) present in marine sediments may serve as a conduit for electron transfer between microorganisms living in these sediments. Experimental work with anaerobic enrichment cultures has shown that magnetite amendments can stimulate the metabolic activity of syntrophic microorganisms [1–6]. This suggests microorganisms employing EET may associate *in situ* with conductive minerals as a way to

facilitate electron transfer between syntrophic partners. Indeed, microorganisms known to employ EET as a core part of their metabolism such as *Geobacter* sp. have been shown to precipitate fine-grained magnetite [7, 8] although the degree of physical association between these authigenic phases and the cell is unclear. To examine microbial communities attached to magnetic minerals *in situ*, extraction of such minerals from the bulk sediment matrix must be performed.

Previous methods for extraction of magnetic minerals from marine sediment have primarily been performed under aerobic conditions [9]. These techniques employed high-gradient magnetic separation (HGMS) to extract magnetic minerals from marine sediment, as HGMS is effective for extracting fine-grained (< 100 μm) magnetic minerals [10–12] with crystal sizes similar to those of magnetite often observed in marine sediments [13]. These techniques have been primarily developed for paleomagnetic study of sediments, and thus have typically been unconcerned with maintaining anaerobic conditions. Also, methods developed for compatibility with downstream molecular biology work (e.g. [9]) also were not primarily concerned with maintaining anaerobic conditions, as a priority was placed on molecular study. However, this precludes the culturing of obligate anaerobes from these separation techniques. Syntrophic microorganisms found to be stimulated by magnetite enrichments (e.g. *Geobacter* sp. and *Methanosarcina* sp.) are sensitive to O_2, and thus using these techniques to extract such microorganisms for culturing would be ineffective.

Here, we present methods for the extraction of fine-grained magnetic minerals from marine sediments, while maintaining anaerobic conditions and other considerations necessary for downstream culturing work.

METHODS

Briefly, HGMS was performed on marine sediments by use of an apparatus in which a peristaltic pump circulated a diluted marine sediment sample through a magnetic column of nickel foam placed inside a magnetic field generated by a Frantz L-1 Isodynamic Separator (S.G. Frantz Co., Trenton, NJ). The methods described here were developed further from those detailed by Harrison and Orphan, particularily their use of a magnetic column (in their case using steel wool as the magnetic matrix) inside a Frantz separator. The methods presented here differ from previously-published methods in several respects. This method focuses on highly magnetic minerals (cheifly, magnetite), given the strength of the evidence for the capability for this mineral to stimulate syntrophic EET. This method also maintains anaerobic conditions in the separation apparatus, useful for downstream culturing.

HGMS Apparatus Assembly

Before assembly of the main apparatus, 2 butyl stoppers penetrated each by 4 sharp 17G 3.5” nickel-plated cannulas with Luer hubs (Cadence Science, Cranston, RI) were prepared for subsequent sterilization by autoclave. The apparatus consisted of 11 lengths of Cole-Parmer Masterflex® silicone tubing, 95802-05, ID = 0.125”, OD = 0.25” (Vernon Hills, IL) and were autoclave-sterilzed along with the butyl stoppers, Cole-Parmer polypropylene Luer fittings, 1x 250 mL and 1x 1 L Pyrex bottles with a magnetic stir bar placed in the 250 mL bottle, 1x 125 mL serum vial, and nickel foam for the magnetic column (see “HGMS Column” below). Tubing was connected with fittings (fittings were wrapped in Parafilm to aid in preventing O_2 leaking into the

line) to create 3 parallel circuits (Figs. 1, 2) for use in circulating in sequence 1) the diluted sediment sample through the magnetic column to collect magnetic minerals in the column while the Frantz was active , 2) 3X PBS for removal of residual non-magnetic minerals from the line, and for 3) elution of magnetic minerals into a 125 mL serum vial after the Frantz was turned off. Circulation was controlled by a Cole-Parmer Masterflex L/S peristaltic pump.

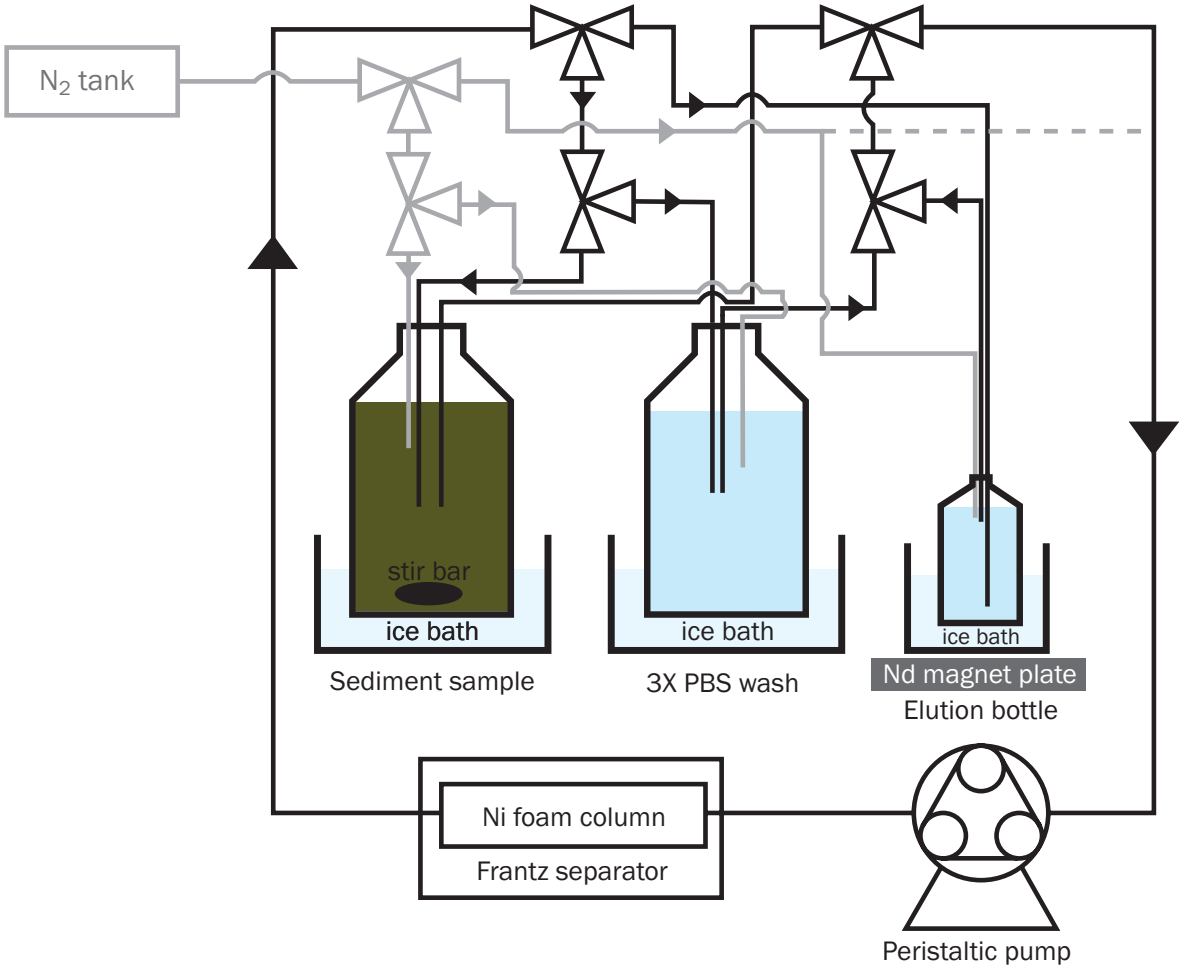

Figure 1. Schematic of anaerobic HGMS apparatus. N_2 vents for bottle sparging are omitted for clarity. Dashed line indicates temporary connection to sparge line with N_2.

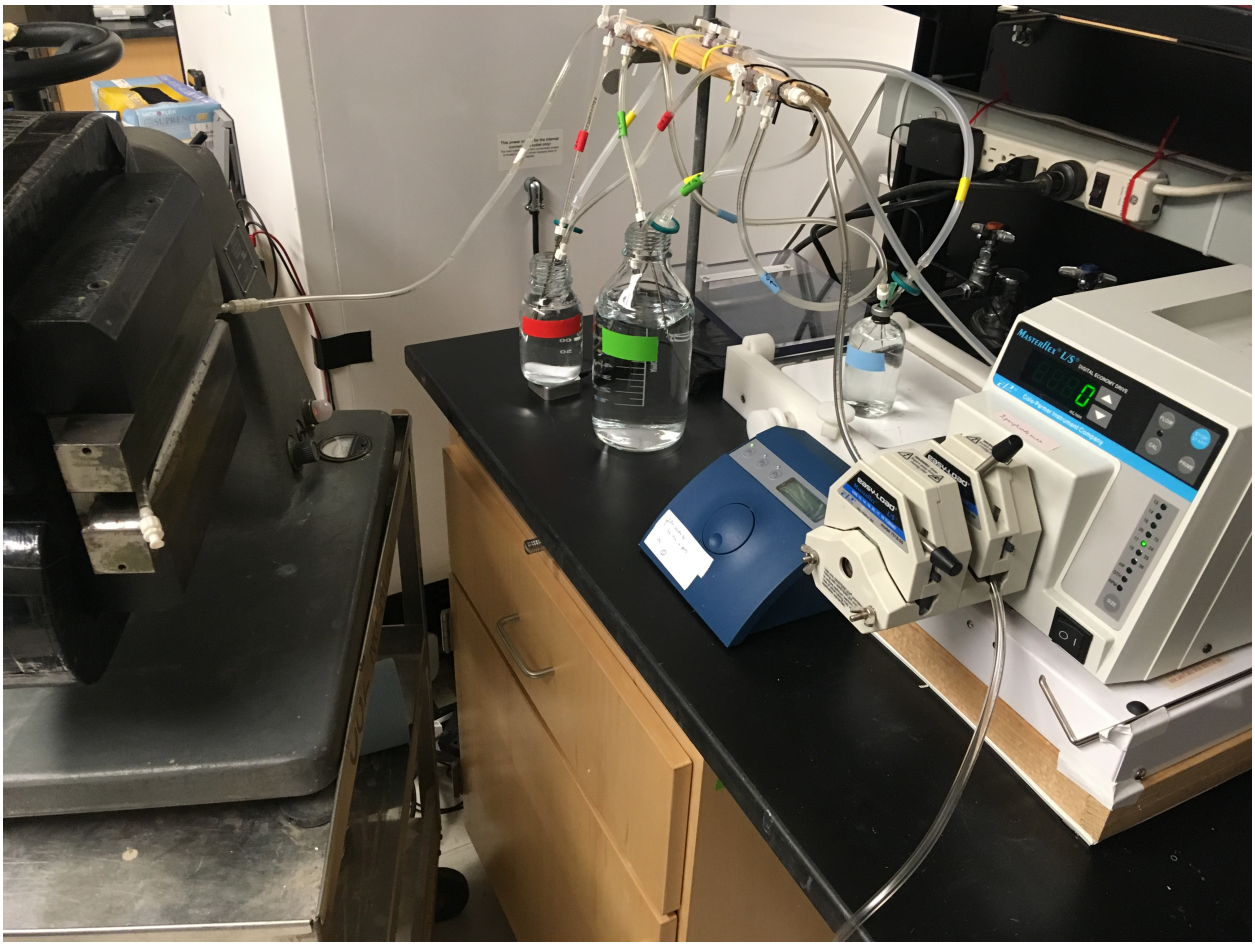

Figure 2. Picture of the apparatus during an early stage of development. Omitted in this image are the prepared butyl stoppers with sharp cannulas and the ice baths. The connection between the peristaltic pump and the column was removed to position the Frantz separator at an angle as to easily image the full apparatus. Lines are labeled in accordance to a correponding bottle color label. Lines labeled with yellow are N_2 sparging lines.

HGMS Column

One autoclaved segment of tubing, cut to the length of the Frantz separator chute, was prepared for use as the magnetic column. Nickel foam (Item no. EQ-bcnf-16m-2, 80-110 pores per inch, pore diameter = 0.25 mm, MTI Corporation, Richmond, CA) was used as the magnetic matrix for the column, selected for its similar filament size but superior porosity to steel wool or thin wire used in previous studies to extract fine-grained magnetic minerals [9]. Ni foam was prepared for use in the column using a 0.125" diameter hole punch (Mayhew Steel Products, Turners Falls, MA) to create 50 Ni foam discs. These discs were placed in a small beaker and autoclaved. NiO produced on Ni foam surfaces from autoclaving (which reduces recovery of magnetic minerals by ~50%) was removed by cleaning Ni discs within the beaker in a sonication bath of 37% HCl for 5 min. The hazardous $NiCl_4^{2-}$ complex produced from this sonication was disposed in an appropriate waste container, and Ni foam was then cleaned by three 5 min washes of 100% ethanol in a sonication bath. Waste ethanol was placed in a separate hazardous waste container. Ni foam was dried under UV-C light and added to the autoclaved tubing segment by use of a sterile cannula. The cannula was magnetized by a Nd magnet through the wall of a sterile glass test tube and used to pick up Ni foam discs for placement in the column under a sterile flame. Fittings were placed on the ends of the column and the column was then connected with the rest of the apparatus.

HGMS Operation

After the apparatus was constructed, 1x 250 mL, 1x 1 L, and 1x 125 mL 3X PBS were filter-sterilized (0.2 μm) into the sterile Pyrex bottles and serum vial and N_2 sparged for 15 min in an ice bath. These vessels were sealed with butyl stoppers and 400 mM Na_2S was added to each vessel to obtain 4 mM Na_2S to remove residual O_2. These bottles were placed in a 10˚C cooler until use. Three ice baths were placed on the lab bench adjacent to the Frantz separator for placement of the Pyrex bottles and serum vial. A submersible stirrer with external control was placed in the water bath.

The Pyrex bottles were then prepared and attached to the apparatus, taking care to quickly perform these next steps as to maintain anaerobic conditions in the bottles. First, the two autoclaved butyl stoppers prepared with sharp cannulas were placed in a Coy anaerobic chamber along with the 250 mL and 1 L bottles retrieved from the 10˚C cooler. The butyl stoppers sealing the Pyrex bottles were quickly exchanged for the stoppers prepared with sharp cannulas, and the top of the Pyrex bottles were wrapped in Parafilm to provide a temporary seal. Bottles were then removed from the chamber, placed in the ice baths, and connected to the apparatus via Luer fittings (Fig. 1). These bottles were then continuously sparged with N_2 during the operation of the apparatus. Additionally, the N_2 line for sparging the 125 mL bottle during elution was temporarily reconnected to the segment of the apparatus including the column to remove as much O_2 as possible from the line (Fig. 1). The immersed stirrer was set to 750 RPM.

10 mL of sediment sample (~2:1 water:sediment) was then injected into the 250 mL Pyrex bottle containing the stir bar. N_2 sparging of the column and connected lines was stopped and

circulation of the sediment sample through the apparatus was initiated by switching three-way valves to only circulate through the sample bottle. The peristaltic pump was then set to a flow rate of 40 mL/min and the Frantz separator was switched on and set to 0.3 A, targeting magnetite [14]. Sample was circulated through the apparatus for 13 min, equivalent to >2 complete circulations of the sample bottle volume.

After 13 min, the 'wash' step was performed to dilute contaminating minerals in the line from the first magnetic capture step. The peristaltic pump was paused and the three-way valves swiched to only circulate through the 1 L 'wash' bottle of 3X PBS with 4 mM Na_2S. Circulation of the wash bottle then commenced at the same flow and magnetic parameters as used in the initial magnetic capture step.

After 13 min of circulation of the wash bottle, the elution step was performed. The 125 mL serum vial for capturing eluted magnetic minerals was retrieved from the 10˚C cooler, placed in an ice bath, and attached to the apparatus using 1x 7 cm 22G needle (inflow to vial) and 1x 2.5 cm 22G needle (outflow from vial). Sparging with N_2 was initiated using 2x 2.5 cm 22G needles. The peristaltic pump was again paused, three-way valves switched appropriately, and the Frantz separator was switched off. Elution was initiated by setting the peristaltic pump to a flow rate of 40 mL/min. Circulation proceeded for 7 min, after which the peristaltic pump was shut off and the bottle was detached from the apparatus by needle removal. The bottle was then placed in a 4˚C cooler for downstream culturing efforts.

Results from Control Experiments

To test the efficacy of the methods presented here, a control experiment was performed in which recovery of fine-grained magnetite synthesized following published protocols [15] mixed with nonmagnetic clay (ISCz-1, Clay Minerals Society, Chantilly, VA) was measured. A mixture of 34.7 mg synthetic fine-grained magnetite and 500 mg ISCz-1 was suspended in 250 mL DI and circulated through the apparatus following the protocol detailed above. The mass of magnetic particles recovered in the elution bottle was measured by filtration of the elution bottle through a 0.4 μm polycarbonate filter. After drying and weighing, 26.3 mg material was recovered on the filter, corresponding to >70% recovery; no more than ~0.5 mg of the material remaining on the filter was estimated to be ISCz-1, as this is approximate mass of ISCz-1 per mL after dilution from the volume of the wash bottle. Negligible magnetite was retained on the magnetic stir bar, as observed with natural sediment samples.

Preliminary Results

Recovery of magnetic minerals and attached microbial communities using the HGMS apparatus detailed here was performed on a methane seep sediment sample from bottle PC-KD (see Chapter 2 of this thesis for sampling details). The elution bottle was prepared using artificial seawater media from published work [16] and was pressurized to 2 bar with CH_4. Epifluorescence microscopy was performed on PFA-fixed samples from the elution bottle, revealing the presence of microbial aggregates with morphology similar to that of ANME-SRB consortia (Fig. 3). Reflected light microscopy revealed the presence of reflective domains ~2-3 μm in diameter,

potentially representing magnetite attached to ANME-SRB exteriors. 16S rRNA amplicon sequencing of these incubations documented abundant reads assigned to the Heimdallarchaeota. These incubations were maintained at 4˚C for future experimental work.

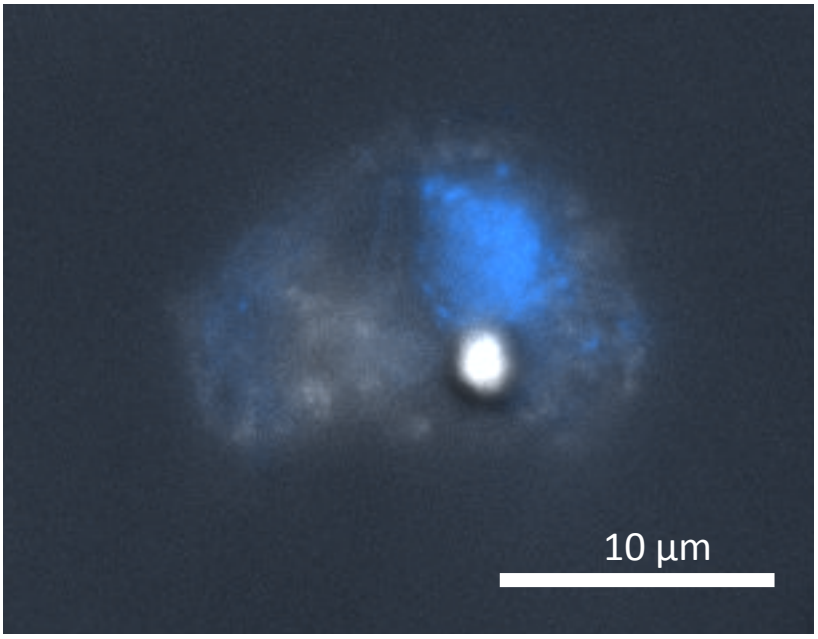

Figure 3. Epifluorescence microscopy of microorganisms recovered from HGMS separation of methane seep sediment. Putative ANME-SRB consortia were stained by DAPI (*blue*) and were observed attached to reflective particles (*white*).

REFERENCES

1. Liu F, Rotaru AE, Shrestha PM, Malvankar NS, Nevin KP, Lovley DR. Magnetite compensates for the lack of a pilin-associated c-type cytochrome in extracellular electron exchange. *Env Microbiol* 2015; **17**: 648–55.
2. Kato S, Hashimoto K, Watanabe K. Microbial interspecies electron transfer via electric currents through conductive minerals. *Proc Natl Acad Sci* 2012; **109**: 10042.
3. Kato S, Hashimoto K, Watanabe K. Methanogenesis facilitated by electric syntrophy via (semi)conductive iron-oxide minerals. *Env Microbiol* 2012; **14**: 1646–54.
4. Li H, Chang J, Liu P, Fu L, Ding D, Lu Y. Direct interspecies electron transfer accelerates syntrophic oxidation of butyrate in paddy soil enrichments. *Environ Microbiol* 2015; **17**: 1533–47.
5. Tang J, Zhuang L, Ma J, Tang Z, Yu Z, Zhou S. Secondary Mineralization of Ferrihydrite Affects Microbial Methanogenesis in Geobacter-Methanosarcina Cocultures. *Appl Environ Microbiol* 2016; **82**: 5869–5877.
6. Rotaru A-E, Calabrese F, Stryhanyuk H, Musat F, Shrestha PM, Weber HS, et al. Conductive Particles Enable Syntrophic Acetate Oxidation between Geobacter and Methanosarcina from Coastal Sediments. *mBio* 2018; **9**.
7. Lovley DR, Stolz JF, Nord GL, Phillips EJP. Anaerobic production of magnetite by a dissimilatory iron-reducing microorganism. *Nature* 1987; **330**: 252–254.
8. Vali H, Weiss B, Li Y-L, Sears SK, Kim SS, Kirschvink JL, et al. Formation of tabular single-domain magnetite induced by Geobacter metallireducens GS-15. *Proc Natl Acad Sci* 2004; **101**: 16121–16126.
9. Harrison BK, Orphan VJ. Method for Assessing Mineral Composition-Dependent Patterns in Microbial Diversity Using Magnetic and Density Separation. *Geomicrobiol J* 2012; **29**: 435–449.
10. Chang S-BR, Kirschvink JL. Possible Biogenic Magnetite Fossils from the Late Miocene Potamida Clays of Crete. In: Kirschvink JL, Jones DS, MacFadden BJ (eds). *Magnetite Biomineralization and Magnetoreception in Organisms: A New Biomagnetism*. 1985. Springer US, Boston, MA, pp 647–669.
11. Schulze DG, Dixon JB. High Gradient Magnetic Separation of Iron Oxides and other Magnetic Minerals from Soil Clays. *Soil Sci Soc Am J* 1979; **43**: 793–799.
12. Oberteuffer J. Magnetic separation: A review of principles, devices, and applications. *IEEE Trans Magn* 1974; **10**: 223–238.
13. Roberts AP. Magnetic mineral diagenesis. *Earth-Sci Rev* 2015; **151**: 1–47.
14. Rosenblum S, Brownfield IK. Magnetic susceptibilities of minerals. *Magnetic susceptibilities of minerals* . 2000. U.S. Geological Survey, Reston,VA.
15. Kang YS, Risbud S, Rabolt JF, Stroeve P. Synthesis and Characterization of Nanometer-Size Fe3O4 and γ-Fe2O3 Particles. *Chem Mater* 1996; **8**: 2209–2211.
16. Scheller S, Yu H, Chadwick GL, McGlynn SE, Orphan VJ. Artificial electron acceptors decouple archaeal methane oxidation from sulfate reduction. *Science* 2016; **351**: 703–707.